Turbulence et écoulements multiphasiques

mémoire d'habilitation à diriger les recherches

Turbulence et Écoulements Multiphasiques

Turbulence et Écoulements Multiphasiques

Particules, Bulles et Interfaces

Mémoire d'Habilitation à Diriger les Recherches

Djamel Lakehal

Ecole Polyetchnique Fédérale de Zurich

Octobre 2004

Ce mémoire a été rédigé pour la soutenance d'une

Habilitation à Diriger les Recherches

le 26 novembre 2004 à l'Ecole Centrale de Lyon

devant le **jury** composé de

J. Bataille, G. Yadigaroglu, J-M. Delhaye, M. Lance,
F. Leboeuf, P. Sagaut, A. Cartellier

Rapporteurs:

G. Yadigaroglu, M. Lance, P. Sagaut

Remerciements

Je tiens à remercier Georges Yadigaroglu, Michel Lance et Pierre Sagaut qui ont accepté de rapporter sur les travaux présentés dans ce mémoire. C'est grace à Georges que ces travaux ont été initiés; je lui serai reconnaissant de m'avoir donné tant de liberté dans mes choix scientifiques. Je remercie Michel qui m'a encouragé à rédiger ce mémoire.

Je remercie également Jean-Marc Delhaye, Jean Bataille, Francis Leboeuf et Alain Cartellier d'avoir accepté de participer au jury.

Les travaux présentés dans ce mémoire ont été réalisés grâce à la précieuse collaboration de "Chidu" Narayanan, Marco Fulgosi, Petar Liovic, Sanjoy Banerjee, Valerio de Angelis, Massimo Milelli, Michel Lance et Brian Smith, sans oublier Markus Meier, Lorenzo Botto, Pascale Buchel et Sylvain Reboux.

Contents

Résumé

Ce document fait la synthèse des activités de recherche de notre équipe Simulation des Écoulements Multifluides (CMFD). Cette équipe faisait partie entre 1999 et 2004 du Laboratoire de Génie Nucléaire (LKT) de l'EPF Zurich, sous la direction du Pr. Georges Yadigaroglu. Les recherches menées dans cette unité se sont essentiellement centrées autour de l'étude de la dynamique des écoulements multi-phasiques et des transferts. Les motivations s'inscrivaient dans un cadre de recherche fondamentale, ayant pour objectif de faire avancer les connaissances sur les mécanismes microphyisiques qui controllent les échanges interfaciaux, et leur rapport avec le comportement macroscopique des écoulements dans les systèmes energétiques. L'élément essentiel de nos recherches porte sur la structure de la turbulence à l'échelle du mélange et à l'échelle interfaciale, ainsi que sur le développement et l'application de méthodes de calcul adéquates. L'approche suivie a été élaborée il y a cinq ans avec la création du groupe CMFD. Elle consiste à traiter cette classe d'écoulements sur trois fronts complémentaires: faire recours aux méthodes de suivi d'interfaces pour les écoulements interfaciaux, traiter les mélanges hétérogènes avec l'approche multi-fluide, et utiliser le suivi Lagrangien pour la dispersion particulaire. La turbulence est traitée dans le cadre de la simulation numérique directe et des grandes échelles. Les modèles requis pour le traitement des échelles sous-mailles et des échanges interfaciaux sont developpés sur la base de résultats fournis par la simulation directe d'écoulements stratifiés diphasiques. Ces axes de recherche sont résumés dans ce document, qui présente également une synthèse des différentes approches analytiques basées sur leur origine connue, les lois de conservation exprimées sous différentes formes.

Nous n'exposerons pas nos travaux les plus récents dans ce manuscrit sur la DNS des écoulements cisaillés en présence de condensation, ni sur la LES des écoulements à surfaces libres, ni sur la dispersion de particules dans les couches de mélange, ni sur le traitement de la ligne triple. Les résultats obtenus auront besoin de plus de temps avant d'être dépouilleées et analysées.

1

Introduction

1.1 POSITION DU PROBLÈME

L'étude des écoulements multiphasiques est devenue de plus en plus importante pour plusieurs types d'installations industrielles aussi bien dans le cadre de l'optimisation de leur conception que dans celui des considérations de sûreté. Il est cependant important de ne pas perdre de vue que les phénomènes étudiés ne sont pas nés de l'industrialisation et des technologies nouvelles puisqu'un bon nombre d'entre eux existaient déja "à l'état naturel". Aux applications classiques des écoulements multiphasiques aux systèmes de conversion d'énergie ou au transport des hydrocarbures, s'ajoute aujourd'hui un intérêt croissant envers leur utilisation pour des applications "micro-échelles". La maitrise de ces écoulements s'avére très utile pour de nombreuses technologies émergeantes, en microélectronique pour le refroidissement par micro-canaux, comme dans les opérations pharmaceutiques pour le micro séquencage, le micro dosage, la séparation de phase, etc.

La science des écoulements multiphasiques permet la synthèse de plusieurs éléments de réponse à des questions aussi fondamentales que l'instabilité des surfaces libres, le mouvement des bulles, le mélange des panaches gaz-liquide, le comportement des particules solides et des gouttelettes dans les champs turbulents, la transition de régime d'écoulement dans les conduites, etc. Ces éléments constituent ce qui devrait être défini comme "physique macroscopique", occupant l'état le plus élevé dans la hiérarchie des échelles spatio-temporelles présentes dans un écoulement multiphasique type. L'échelle intégrale est généralement reprśentative l'échelle caractéristique de l'écoulement.

A ce premier pilier viennent s'ajouter les éléments d'échanges interfaciaux, regroupant des phénomènes physiques locaux plus subtils tels que la rupture et la reconnections des interfaces, le changement de phase, les tensions superficielles, la dynamique de la ligne triple, l'effet Marangoni, etc. Ceux-ci, avec les échanges pariétaux, pourraient être désignés par "physique mésoscopique", agissant au niveau intermédiaire de la cascade des échelles. Les échelles caractéristiques se comparent alors à la taille des inclusions (diamètre des bulles), au rapport amplitude-longueur d'onde des interfaces cisaillées ou aux échelles de Kolmogorov si celles-ci sont plus grandes que les inclusions elles-mêmes.

Le plus bas niveau de la hiérarchie des échelles spatio-temporelles relève de la "physique moléculaire" où les enjeux sont centrés autour de la "continuité des milieux", la variation des propriétés matérielles (viscosité, conductivité thermique, etc.), la singularité de la ligne triple, et même l'épaisseur de la sous-couche interfaciale sur laquelle le gradient de densité n'est pas nul. Ici, l'ordre de l'échelle de longueur caractéristique peut se comparer au libre parcours moyen.

1.2 ÉCHELLES DE PHASE ET ÉCHELLES DE TURBULENCE

Pour mieux appréhender le sujet que nous nous proposons de développer dans ce mémoire, il convient d'insister sur ce qu'à notre avis distingue les écoulements turbulents multiphasiques d'autres écoulements, c'est-à-dire l'interaction entre les structures turbulentes et les inclusions (bulles, particules, interfaces) de tailles et de propriétés matérielles variables. On sera donc contraint de parler de deux types d'échelles évoluant simultanément, sinon conjointement: les échelles de phase et les échelles de turbulence. De même qu'il existe une cascade d'énergie cinétique en turbulence, on parlera désormais d'une hiérarchie ou d'une cascade d'échelles de phase. Aussi, à l'instar de la turbulence, les échelles de phase sont-elles encore fortement hétérogènes et non-locales. Il faut souligner que l'exercise qui consiste à faire une distinction entre les échelles des phénomènes multiphasiques est très utile sinon nécéssaire, quand on sait l'ambiguité des méthodes de prédictions établies à cet égard. En effet, seules la simulation directe et la simulation des grandes échelles, qui représentent aujourd'hui le niveau le plus fin et le plus sophistiqué de la simulation, sont capables justement de différencier entre les échelles de turbulence et de phase. Nous exposerons dans les chapitres suivants les idées maitresses de ces méthodes; les détails sont par ailleurs présentés dans Lakehal (2004).

La première question qui s'impose est de savoir si l'ordre de grandeur des échelles de phase (des inclusions) peut être affecté par la turbulence des écoulements en question, ou ce sont les écoulements qui peuvent etre menés à une transition de régime par les interactions entre phases ? Le meilleur exemple en est la turbulence induite par le passage de bulles dans un écoulement initialement au repos, ou, à l'opposé, celui d'un champ turbulent qui se modifie par la présence des particule (Lance & Bataille, 1991). Dans le premier cas, la turbulence est créée dans le sillage des inclusions, contrairement au second cas où c'est de la dissipation qui se produit à la suite de la rupture des structures de vorticité par les particules solides (Narayanan, 2004).

Indépendamment du régime d'écoulement (laminaire ou turbulent), la probabilité d'interaction entre les phases est d'autant plus forte que la multitude des échelles dans la hiérarchie n'est pas négligeable. Ceci nous conduit à la clarification conceptuelle suivante: la complexité des écoulements multiphasiques se mesure à la variabilité des échelles spatio-temporelles présentes. Elle reflète le comportement des inclusions en interaction, et se manifeste par leur distribution spatiale ("dynamique de phase"). Modéliser les écoulements multiphasiques est précisément synonyme de la prédiction de cette dynamique; les comprendre signifie être en mesure de prédire les mécanismes qui en sont responsables. Il convient alors de distinguer entre prédire et comprendre les écoulements multiphasiques. Seule la simulation fine –expérimentale ou numérique– peut combler les lacunes de connaissance, dans les limites de la perception théorique. Prétendre donc pouvoir "modéliser" un problème tel que l'évaporation sur une plaque plane est illusoire tant que les enjeux fondamentaux ne sont pas bien compris.

1.3 CHOIX DE MÉTHODE DE PRÉDICTION

Aujourd'hui la recherche emprunte deux voies complémentaires: les études à "échelle spécifique" et les études "multi-échelles", intégrant toutes les dimensions du problème, sans distinction. Bien qu'il existe plusieurs problèmes dont la solution n'exige qu'un traitement ciblé à une échelle, nous sommes de plus en plus confrontés à des problèmes complexes où la séparation d'échelles est manifeste.

Pour répondre aux particularités des études à échelle spécifique, plusieurs techniques de modélisation ont été développées au cours des dernières années: l'approche des milieux discontinus, regroupant la dynamique moléculaire (MD), les particules dissipatives (DPD) et les Lattice-Boltzmann (LB), et l'approche des milieux continus, englobant les méthodes Euleriennes et Euleriennes-Lagrangiennes sur lesquelles nous reviendrons dans le chapitre suivant. Un modèle de calcul "multi-échelles" devrait ainsi pouvoir intégrer différentes techniques à la fois, selon le problème en considération. A l'heure actuelle les études à "échelle spécifique" qui ne ciblent qu'une échelle de phase prcise à la fois sont censées répondre à des questions relevant de la compréhension, et non de la prédiction. Dans ce qui suit, il ne sera question que de l'approche des milieux continus.

Pour mieux comprendre la logique de séparation d'échelles et les moyens de simulation disponibles aujourd'hui, observons l'exemple du déferlement d'une vague illustré dans la Fig. 1.1. Au plus haut de la hiérarchie des échelles, il y a la discontinuité interfaciale air-eau. Il y a ensuite des structures turbulentes créées par le cisaillement à la surface (côté air), et celles qui remontent des fonds marins (côté eau), responsables du renouvellement surfacique. Au niveau intermédiaire, les vagues déferlent et forment une couche de mélange à bulles (whitecaps), source d'embruns marins, dont la dynamique est contrôlée par la rupture des vagues suivie par leur cisaillement. Ces inclusions occupent l'état le plus bas de la hiérarchie des échelles. Les échanges qui s'en suivent s'opèrent aussi à des échelles spécifiques: l'absorption des gaz solubles (CO_2) par l'océan à lieu au niveau des discontinuités

interfaciales, et est accentué par le renouvellement surfacique. En contre partie, l'échange inverse eau-atmosphère est due à l'évaporation des embruns marins, modifiant remarquablement les bilans de conservation massique et thermo-hygrométrique.

Figure 1.1 Exemple d'un écoulement multiphasique multi échelles.

La discontinuité interfaciale peut instinctivement être approchée par une méthode de suivi d'interface ou en imposant une condition de pression sur la surface libre. La zône de mélange air-eau est mieux traitée par un modèle à deux fluides, moyennant les interactions entre les phases par le biais de la fonction de distribution ou la probabilité de présence des constituants (ou fonction identificatrice de phase), χ, qui vaut alternativement 0 et 1, comme nous le verrons plus loin. La dynamique des embruns marins génŕés par le déferlement des vagues peut-elle être étudiée par une approche Eulerienne-Lagrangienne, décrivant la trajectoire de chaque gouttelette dans le champ de vent. Les échanges de chaleur et de masse sont intègrés selon le choix fait pour la dynamique de phase. Dans tout les cas de figure, on émet des hypothèses à partir du formalisme equationnel exact (lois de conservation) pour arriver à des équations simplifiées écrites en grandeurs globales statistiques, conduisant aux modélisations les plus courantes des écoulements multiphasiques.

Les possibilités offertes pour traiter la cascade des échelles de turbulence sont: (i) la modélisation statistique basée sur la fermeture en un point (RANS), (ii) la simulation des grandes échelles (LES) basée sur le filtrage spatial des variables indépendantes, et (iii) la simulation numérique directe (DNS) qui ne requiert aucun niveau de modélisation ni d'approximation. L'approche RANS est sans doute la plus couramment utilisée pour les écoulements multiphasiques, et va notamment de pair avec le modèle à deux fluides. Ce type de modèle de fermeture est aussi souvent combiné avec les méthodes de suivi de particules pour la dispersion particulaire.

La percée des deux nouveaux outils de simulation pure (LES/DNS) dans la science des écoulements multiphasiques est restée confinée aux études de la dispersion particulaire, dans le cadre de l'approche Eulerienne-Lagrangienne. S'il est vrai que la DNS n'est pas applicable aux écoulements multiphasiques fortement mélangées tels que l'exemple porté sur la Fig 1.1, elle peut néanmoins être envisagée pour des écoulements à bulles ou pour des écoulements à larges discontinuités interfaciales, tels que les écoulements stratifiés gaz-liquide. Il faut noter en passant que la communauté utilise souvent 'abusivement' le sigle DNS pour faire référence au suivi d'interface (méthodes VOF, Level Sets, etc.).

Dans la science des milieux multiphasiques, le type de simulation où la plut part des paramètres sont des solutions du problème porte à présent un nom: CMFD, ou Computational Multi-Fluid Dynamics (Yadigaroglu, 2003).

1.4 APPLICATIONS PRATIQUES

Toujours est-il que la recherche sur les écoulements multiphasiques serait stérile si elle n'était pas inscrite dans un cadre pratique bien défini où la compréhension des enjeux fondamentaux est capitalisée au profit de l'impact industriel ou environnemental. Ceci est particulièrement vrai pour toutes disciplines qui entrent en compte pour répondre à des questions aussi sensibles que l'énergie nucléaire; la thermo-hydraulique des réacteurs nucléaires en est un exemple.

Précisément, les progrès de la science des écoulements multiphasiques et de la technologie thermo-hydraulique des systèmes nucléaires vont souvent de pair, et c'est dans ce cadre que les recherches menées au LKT sous la direction du Pr. G. Yadigaroglu se sont inscrites.

Ces recherches étaient essentiellement centrées autour de l'étude de la dynamique des écoulements multiphasiques et des transferts. Les motivations avaient pour objectif de faire avancer les connaissances sur les mécanismes microphysiques qui controllent les échanges interfaciaux, et leur rapport avec le comportement macroscopique des écoulements présents dans les systèmes de production d'énergie nucléaire. L'élément essentiel de nos recherches portait sur l'étude de la turbulence à l'échelle du mélange et à l'échelle interfaciale. L'approche suivie consistait à traiter ces écoulements sur trois fronts complémentaires: faire recours aux méthodes de suivi d'interfaces pour les écoulements interfaciaux, traiter les mélanges hétérogènes avec l'approche multi-fluide, et utiliser le suivi Lagrangien pour la dispersion particulaire, le tout dans un cadre de simulation directe ou des grandes echelles de la turbulence, DNS et LES.

Les paragraphes qui suivent font la synthèse de ces applications, dans un ordre précis; les méthodes de prédiction pour chacune d'entre elles sont décrites dans le chapitre suivant.

Les modèles requis pour le traitement des échelles sous-mailles et des échanges interfaciaux sont developpés sur la base de résultats fournis par la simulation directe d'écoulements stratifiés diphasiques.

1.4.1 Ecoulements à bulle: thermo-hydraulique des réacteurs nucléaires

Le schéma de cette synergie peut se résumer ainsi: les essais expérimentaux sont effectués à grandes échelles, alors que la modélisation est réservée aux phénomènes à plus petites échelles. Et pourtant, si les expériences du type PANDA (Yadigaroglu *et al.*, 2003) illustrent bien les études expérimentales à grandes échelles, la classification est plus abstraite en matière de modélisation. Par exemple, on ne sait pas encore très bien ce qui des phénomènes thermo-hydrauliques est accessible aux codes système à une dimension utilisés couramment pour étudier les transitions dans les systèmes nucléaires, et ce qui nécessite des simulations plus sophistiquées. Pour simplifier, on entend par méthodes numériques sophistiquées les approches basées sur la résolution des équations de transport en multi-dimensions, faisant notamment moins recours aux modèles. Au contraire, les codes systèmes réduisent les problèmes à une dimension, et les décrivent en fonction de paramètres moyennés –notamment en fonction de la fraction volumique ou taux de vide– par exemple, sur la section de la conduite.

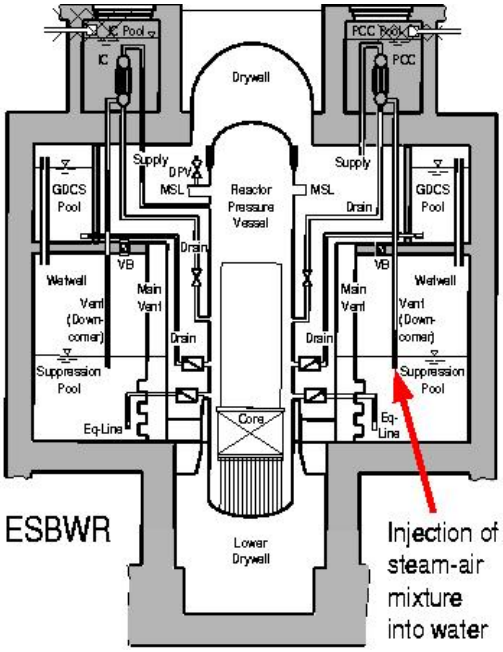

Figure 1.2 Schéma d'un réacteur ESBWR à refroidissement de secours passif.

1.4.1.1 Systèmes de sûreté passifs Au cours des accidents réels ou postulés dans les réacteurs nucléaires refroidis à l'eau (réacteurs à eau légère LWR, réacteurs CANDU, réacteurs WWER), plusieurs phénomènes multi-

phasiques peuvent avoir lieu, dont la complexité dépend de la nature et de la gravité de l'incident. La recherche vise surtout à s'assurer du contrôle des procèdes d'évacuation de l'énergie du système –lors d'une brèche, par exemple. Ces opérations peuvent être accomplies de facon efficace par condensation de vapeur injectée dans des bassins de dépressurisation dans l'enceinte de confinement, ou par le refroidissement du milieu ambiant par des échangeurs de chaleur.

Les recherches poursuivies entre le Laboratoire de Génie Nucléaire de l'ETH (LKT) et le Laboratoire de Thermo-Hydraulique du PSI (LTH), sous la direction du Pr. Georges Yadigaroglu, ont été justement motivées par le besoin de développer des systèmes de sûreté passifs pour la nouvelle génération de réacteurs LWR.

Dans la conception de ces réacteurs, pour l'évacuation de la chaleur résiduelle de l'enceinte de confinement, soit de la vapeur est condensée dans des condensateurs spécifiques, soit les parois de l'enceinte de confinement sont refroidies de l'extérieur (Yadigaroglu *et al.*, 2003). Dans les réacteurs à eau bouillante simplifiés (SBWR et ESBWR, voir Fig. 1.2), par exemple, ces systèmes passifs sont concus pour évacuer sous certaines conditions la chaleur résiduelle par condensation de vapeur dans des bassins de dépressurisation.

Afin de placer le thème "interactions entre échelles" en perspective, on s'intéresse aux moyens de séquestration d'énergie par condensation cités plus haut, ou plutôt à la prédiction de l'échelonnement des processus dans l'enceinte de confinement (distribution de pression, de température et de concentration des espèces). Précisons qu'il s'agit d'une étape nécessaire dans l'analyse de sûreté, et c'est à ce titre que les outils de simulation futurs sont censés être en mesure de prédire la dynamique des transferts à tous les niveaux de la hiérarchie évoquée plus haut: du changement de phase par condensation de bulles, au mélange des phases et à la destratification thermique des bassins et des espèces. Il s'agit donc de l'accident le plus étudié qui est celui de la rupture des conduites principales du circuit de refroidissement (LOCA: Loss of Coolant Accident).

1.4.1.2 Séquestration de vapeur par injection de bulles

Dans le système primaire de sûreté passif concu pour les réacteurs du type SBWR et ESBWR (voir Fig. 1.2), les conduites de suppression de vapeur verticales sont immergées (à peu près à 1 mètre) dans le bassin de dépressurisation. De grosses bulles formées de mélange vapeur et non-condensables peuvent être injectées par ces conduites. Les essais en laboratoire ont montré qu'une grande portion de vapeur se condense bien avant le détachement des bulles, mais l'effet d'échelle reste incertain et seule la simulation numérique pourrait pallier l'absence de mesures à plus grandes échelles. L'un des paramètres de conception critiques qui reste à déterminer est le niveau d'immersion des conduites dans le bassin à même de favoriser la fragmentation des bulles avant leur montée à la surface, et donc l'accélération du processus de condensation.

La première étude numérique et expérimentale menée dans ce sens a été l'oeuvre de Meier (1999*a*), qui a développé une méthode VOF axisymétrique robuste. Les travaux qui s'en suivirent au LKT ont porté sur la généralisation du modèle, en intégrant la composante turbulence du problème par le biais des simulations à grandes échelles (LES). Le chapitre 4 est un résumé des tentatives de simulation LES. Une autre composante importante du sujet en rapport avec la condensation de vapeur a été traitée d'une manière originale, c'est-à-dire par le biais de la simulation directe. Les résultats de la première 'vague' d'exploration de ce sujet sont résumés dans les Chapitres 5, 6 et 7, où il est question de transport turbulent passif uniquement. Les résultats obtenus pour la condensation n'ont pas été encore entièrement traités. L'idée est que l'étude DNS fournisse des modèles de changement de phase prenant en compte la turbulence à l'interface et le cisaillement et la déformation de celle-ci. Ces modèles sont censés être incorporées dans des outils de calcul basés sur le suivi d'interface (VOF), dans un cadre de modélisation LES.

1.4.1.3 Destratification par les panaches à bulles

Le principe de l'opération est illustré dans le schéma de l' ESBWR porté sur la Fig. 1.2. Le "Drywell" (l'espace gazeux du système de dépressurisation de l'enceinte) est directement connecté aux unités de refroidissement passifs (PCC), qui sont placées sur le toit de l'enceinte de confinement abritant le réacteur. La vapeur condensée dans ces unités est alors reversée dans le système primaire, tandis que la vapeur non-condensée est déchargée dans le bassin de dépressurisation. La pression ambiante au-dessus du bassin est un paramètre vital pour la conception du réacteur, et est la somme des pressions partielles du non-condensable et de la vapeur. Il est clair que la condensation partielle de vapeur et la stratification thermique du bassin sont des conditions non-favorables, d'où la nécessite de bien comprendre les mécanismes de transfert en jeu. On sait déjà qu'un mélange parfait empêchant la stratification thermique se produit durant la phase initiale d'un accident de rupture de brèche, lorsque le déchargement dans le bassin de dépressurisation est très violent. Ceci n'est cependant pas garanti dans des conditions d'injection beaucoup moins violentes; le bassin d'eau peut devenir thermiquement stratifié et l'on cherche les effets tendant d'inverser le processus. L'injection d'un panache à bulles en est un.

Dans le cadre de l'amélioration des connaissances par simulation numérique des panaches à bulles, les premières études menées au PSI et au LKT ont porté sur l'application du modèle à deux fluides. Plusieurs modèles de turbulence ont été testés, et de nouvelles approches pour la dispersion turbulente ont été développées (Milelli & Smith, 1998). Les résultats des simulations ont montré que l'élément essentiel n'était pas pris en considération, c'est-à-dire les interactions instantanées entre les structures énergétiques de grande échelle et la phase dispersée. Les recherches ont alors pris un autre tournant, en collaboration avec Michel Lance, où l'on a commencé à s'intéresser à la simulation des grandes échelles (LES). Le principe et l'application de cette idée sont résumées dans le Chapitre 3 de ce manuscrit.

1.4.2 Dispersion particulaire

A l'origine, les études menées au LKT sur la dispersion des particules des gouttelettes dans les écoulements turbulents ont été motivés par le besoin de comprendre les mécanismes de mélange et de destratification dans les bassins de dépressurisation des réacteurs à eau bouillante. Il était question en premier lieu de développer un outil de simulation capable de prédire la dispersion des particules et des bulles et de comparer les résultats aux essais qui devaient être menés au PSI. Des essais sont encore en cours (octobre 2004), alors que les travaux DNS ont été realisés un an auparavant. C'est ce déphasage entre expérience et simulation qui nous a conduit à emprunter un chemin plus classique, moins appliqué à la thermo-hydraulique.

Nos travaux se sont centrés sur les écoulements turbulents chargés de particules et ont finalement porté sur trois thèmes complémentaires: l'analyse de stabilité des écoulements cisaillés libres (Narayanan *et al.*, 2002; Narayanan & Lakehal, 2002), les mécanismes de déposition et de dispersion Narayanan *et al.* (2003) dans les écoulements confinés, et l'influence des particules sur la turbulence (Lakehal & Narayanan, 2003).

Les écoulements turbulents chargés de particules sont généralement étudiés aux faibles taux de présence (écoulements dilués). Dans de telles conditions, les particules n'affectent que très légèrement la dynamique de la phase continue, contrairement aux écoulements à fort taux de présence, où les modifications imposées par les inclusions peuvent être très importantes. Notre équipe a fait de l'analyse de l'influence des particules sur la turbulence de la phase porteuse une priorité dans ses recherches (Narayanan, 2004). L'équipe s'est intéressée aux agitations générées par un nuage de particules solides à "fort" taux de présence. Pour mieux appréhender le sujet, on s'est d'abord focalisé sur un écoulement cisaillé libre dominé par la présence de structures cohérentes dans les zônes de mélange. L'influence des particules est en effet plus visible, s'agissant de structures de basses fréquences. Mais en permettant à la couche de mélange d'évoluer à l'infini, on a pu élargir l'étude aux petites structures de turbulence générées par la fragmentation des structures de Kelvin-Helmholtz après leur mise en paire. Dans chaque cas, l'analyse numérique vise à clarifier le rôle des particules dans le changement de la structure de l'écoulement

L'analyse de stabilité de la couche de mélange chargée de particules s'est imposée comme une étude préliminaire aux simulations numériques directes détaillées (Narayanan *et al.*, 2002; Narayanan & Lakehal, 2002). Le but était de savoir initialiser les calculs DNS et de définir l'étendue du domaine fluide en fonction du taux de réponse ou de relaxation des particules (le nombre de Stokes) et de leur taux de chargement. Nous avons comparés les résultats de l'analyse des équations de Orr-Sommerfeld aux résultats de la simulation Eulerienne-Lagrangienne.

Le deuxième volet des recherches, portant sur les mécanismes de déposition et de dispersion dans les écoulements confinés (Narayanan *et al.*, 2003), s'est centré autour d'un écoulement turbulent dans un canal ouvert. Il s'agissait d'enrichir le débat sur le rôle des structures turbulentes proches de la paroi dans la déposition et la concentration préférentielle des particules. Une étude parallèle s'est intéressée aux même mécanismes, mais dans un écoulement stratifié air-liquide; l'objectif était de clarifier le rôle des déformations interfaciales sur les deux mécanismes qui contrôlent la déposition, soit la diffusion turbulente et le libre envol des particules (papier en cours de révision, Botto *et al.*, IJMF, 2004). La dernière partie qui a fait l'objet de la thèse de Narayanan (2004) fut consacrée à l'étude de l'effet des particules sur la désintégration des structures de Kelvin-Helmholtz en petites structures dissipatives. On ne fait pas mention de ce travail dans ce document.

1.4.3 Ecoulements à surfaces libres – turbulence aux interfaces

Ce travail devait s'inscrire dans le cadre du problème précédant, c'est-à-dire dans le sillage de l'étude des mécanismes de transport passifs et actifs (avec changement de phase) aux interfaces cisaillées. L'itinéraire choisi nous a conduit vers ce but, mais en passant d'abord par deux éléments incontournables, (i) le comportement de la turbulence aux interfaces, et (ii) le transport passif de chaleur ou de masse. Dans le paragraphe qui suit, on parlera davantage du problème d'échanges océans-atmosphere (le lecteur peut s'en offusquer), mais force est de constater que les modèles d'échanges interfaciaux sont les mêmes, qu'il s'agisse de problèmes de thermo-hydraulique ou, paradoxalement

de problèmes de l'environnement. La présentation de cette section est conçue, par mesure de cohérence, comme si l'on devait traiter le problème de l'absorption des gaz peu solubles par les océans.

1.4.3.1 Position du problème Les phénomènes de transport aux interfaces gaz-liquide sont impliqués dans de nombreux domaines industriels et environnementaux. Dans le cadre des échanges eaux-atmosphère, les recherches avaient d'abord porté sur l'étude de l'absorption de gaz par les rivières et les lacs dont le besoin naturel en oxygène est important. L'absorption des substances dissoutes, telles que les PCB, à partir de la terre ferme et des zônes cotières, est ensuite devenu un sujet d'intérêt majeur. Mais ce sont les transferts des gaz à effet de serre (CO2 et méthane) et de l'humidité à la surface des océans qui ont focalisé les regards vu l'impact qu'ils ont sur le réchauffement de la planète. On estime à près de 30-40 pourcent la part du CO2 produit par l'homme qui est absorbé par les océans. Mais ces estimations sont remises en question du fait des incertitudes qui entourent la prédiction du taux de transfert de gaz aux surfaces libres. Par exemple, l'absorption océanique du CO2 peut varier d'un facteur 3, selon qu'on se refère au modèle de Liss & Merlivat (1986) ou à celui de Wanninkhof & McGillis (1999*a*). On comprend dès lors l'intêret des scientifiques pour cette branche de recherche, et le besoin d'améliorer l'état des connaissances fondamentales sur le sujet des transferts turbulents à travers les surfaces libres.

Le transfert aux interfaces est traditionnellement traité en deux volets. Dans le premier on trouve les processus de transport aux surfaces libres non cisaillées, c'est-à-dire les situations où le vent est faible et où la turbulence est générée ailleurs qu'à l'interface, par exemple au fonds de l'écoulement ou dans la zône de mélange comprise entre les courants en dessous de la surface; les structures turbulentes viendraient après se distordre sur la surface de l'eau. Dans la seconde catégorie, on trouve les situations où le cisaillement imposé par le vent est significatif à l'interface, de sorte que la production de la turbulence à lieu à l'interface. Comme dans le cas précédent, le transfert de chaleur pourrait être important à l'interface, s'exacerbant davantage avec la chaleur latente d'évaporation qui augmente avec le cisaillement, ce qui se traduit par une contribution à la production de turbulence par convection naturelle du côté liquide. Mais ce point n'est pas le sujet de ce travail.

Dans la réalité, l'interface se déforme sous l'action du vent et des mouvements du fluide. Ceci augmente la complexité du problème et rend les mesures et les simulations difficiles, en particulier dans la zône proche de l'interface. C'est pour cette raison que ce sujet n'a pas connu le même essor que les études traitant du transport aux surfaces solides. Considérons le cas où la vitesse du vent sur un film d'eau augmente progressivement. La turbulence est générée à la surface quand le cisaillement imposé par le vent devient important, ce qui, par ailleurs, peut arriver à des vitesses relativement faibles. Des ondulations commencent alors à apparaitre sur la surface, s'amplifiant sous l'effet du vent pour former des ondes capillaires d'abord, suivies d'ondes de gravité ensuite. Quand la vitesse du vent (mesurée à 10 m en dessus de la surface) est de l'ordre de 3 à 5 m/s, les vagues deviennent houleuses et commence alors le phénomène de micro-fragmentation, dont les échelles caractéristiques sont de l'ordre du O(1 cm) en amplitude et O(10 cm) en longueur d'onde. Les caractéristiques de la turbulence sous les vagues différent selon l'intensité du vent imposé.

Avant la rupture de la surface, la turbulence à l'interface est vraisemblablement générée, comme aux parois solides, par le cisaillement imposé, ce que l'on a pu par ailleurs constater en analysant les résultats de la DNS (Fulgosi *et al.*, 2003). On peut observer des macro-structures turbulentes organisées, dont l'empreinte sur l'interface laisse entrevoir des zônes de grandes et de faibles vitesses. Ces mouvements sont à l'origine d'un processus intermittent de migration de masse du fluide autour de l'interface (bursts), formé d'éjections du fluide hors de la région interfaciale vers l'extérieur, et du mécanisme inverse (sweeps), ramenant le fluide vers l'interface. Ces structures évoluent avec l'intensité du cisaillement d'une manière similaire à ce qui se produit aux voisinage des parois, et la périodicité du processus de migration de masse de fluide autour de l'interface qui s'en découle contrôle le renouvellement de la surface.

La combinaison de l'échelle de vitesse de frottement (ou de cisaillement) et de la fréquence d'éjections et d'absorption de fluide de et vers l'interface est au centre du modèle de renouvellement surfacique. Nos travaux basés sur le calcul DNS du transfert à travers une interface cisaillée ont bien mis en évidence cette corrélation entre transfert de masse, vitesse de frottement et fréquence d'éjections et d'absorption (Lakehal *et al.*, 2003). Ce scénario reste en fait valable tant que la micro-fragmentation n'a pas encore eu lieu; le début de ce processus marque évidemment un changement important de la structure de la turbulence à l'interface. L'observation expérimentale montre que si la vitesse du vent 10 m au-dessus de l'eau augmente encore (12-13 m/s), la fragmentation avec entrainement d'air prendrait place (wind-driven whitecapping), s'accompagnant de la formation d'embruns marins, qui reste localisée dans les zônes de très grande activité turbulente, puisque la vitesse moyenne du vent au-dessus des océans est de l'ordre de 7.5 m/s. De ce fait, la micro-fragmentation reste le phénomène qui domine le processus global des échanges entre les eaux et l'atmosphère.

1.4.3.2 Modèles de renouvellement surfacique

Les pionniers de la modélisation des transferts aux surfaces libres, Lewis & Whitman (1924), ont posé le problème tel que le transport de masse s'effectuait à travers un film fluide laminaire, d'épaisseur δ, adjacent à l'interface, indépendamment du régime d'écoulement amont. Ceci donna naissance au premier modèle de transfert massique, selon lequel le coefficient de transfert β est directement proportionnel à la diffusion moléculaire, D. Mais les expériences qui s'en suivirent ont montré que la proportionnalité suivait plutôt $\beta \sim D^{2/3}$ pour les interfaces fluide-solide, et $\beta \sim D^{1/2}$ pour les surfaces libres, au moins pour des valeurs de nombre de Schmidt $Sc = \nu/D$ assez grandes (ou ν est la viscosité cinématique). L'idée proposée plus tard par Higbie (1935) stipule que la turbulence transportant le fluide vers les interfaces entraine le renouvellement surfacique après un laps de temps, τ, durant lequel l'absorption de gaz formant par le film liquide à lieu. Selon la théorie de Lewis et Whitman, le coefficient de transfert est donc

$$\beta = D/\delta \tag{1.1}$$

alors que selon Higbie

$$\beta = [D/(\pi\tau)]^{1/2} \tag{1.2}$$

Inspiré par les travaux de Higbie, Danckwerts (1951*a*) proposa un modèle de transfert de masse selon lequel le renouvellement surfacique se manifeste d'une manière aléatoire, donnant lieu du côté liquide à l'approximation suivante

$$\beta = (D/\overline{\tau})^{1/2} \tag{1.3}$$

où $\overline{\tau}$ pourrait être défini comme le temps moyen entre deux renouvellements successifs. Il faut noter que le modèle de renouvellement de Higbie-Danckwerts prédit la dépendance du transfert du côté liquide, β, en fonction de D, comme $D^{1/2}$, ce qui a été confirme plus tard par les mesures expérimentales. Cependant, le temps entre renouvellements, est resté non-specifié, et c'est là que réside toute la faiblesse du modèle.

Plusieurs modèles ont été alors proposés pour τ, notamment le modèle des "grandes échelles" (LE, ou Large-Eddy) de Fortescue & Pearson (1967), et le modèle des "petites échelles" (SE, ou Small-Eddy) de Banerjee *et al.* (1968). Selon le modèle LE, l'échelle caractéristique des échanges est directement reliée à la turbulence de l'écoulement non-perturbé, et est définie par $\overline{\tau} \approx \Lambda/u$, d'où $\beta\ Sc^{1/2} = u\ Re_t^{-1/2}$, ou Λ représente l'échelle intégrale de la turbulence, u l'échelle de vitesse associée, et $Re_t = u\Lambda/\nu$ le nombre de Reynolds turbulent.

Partant de l'idée que le transfert est plutôt contrôlé par les petites échelles de turbulence, le modèle SE de Banerjee *et al.* (1968) donne l'expression pour l'échelle de temps caractéristique $\overline{\tau} \approx (v/\varepsilon)^{1/2}$, où ε est le taux de dissipation de l'énergie cinétique turbulente proche de l'interface. Celle-ci peut être, soit mesurée soit estimée, par exemple, $\varepsilon \approx u^3/\Lambda$, de sorte que $\beta\ Sc^{1/2} = u\ Re_t^{-1/4}$. Il y a cependant une ambiguïté quant à la détermination du nombre de Reynolds turbulent. Plus précisément, ε représente le taux de dissipation proche de l'interface, et de ce fait il est préférable que cette quantité soit directement évaluée. Il s'avère aussi que, sous certaines conditions, les modèles LE et SE produisent des résultats considérablement différents, une dissonance clarifiée plus tard par Theofanous (1984), en unifiant les deux modèles de sorte qu'ils puissent prédire le comportement asymptotique du taux de transfert pour les petits et les grands nombres de Reynolds, respectivement.

1.4.3.3 Modèles de divergence surfacique pour les interfaces non-cisaillées

Une autre idée s'est développe dans le sillage des modèles de renouvellement LE et SE, et qui consiste à relier le taux de transfert à une quantité locale à l'interface, traduisant le taux de déformation de celle-ci par étirement ou contraction, plutôt qu'aux échelles de turbulence. A l'origine de cette hypothèse, Campbell & Hanratty (1983) et McCready & Hanratty (1984), qui ont étudié le comportement de la turbulence au voisinage d'une paroi solide et d'une interface libre cisaillée, ont mis en évidence l'importance des fluctuations normales aux interfaces w' dans le processus de transfert. Banerjee (1990) a par la suite eu l'idée d'utiliser le résultat de McCready en l'occurrence pour dériver une expression pour le taux de transfert de masse, valable pour une interface cisaillée et une turbulence homogène et isotrope pour des nombres de Schmidt élevés:

$$\frac{\beta\ Sc^{1/2}}{u} \approx \frac{C}{Re_t^{1/2}} \left[\left(\frac{\partial u'}{\partial x} + \frac{\partial v'}{\partial y} \right)^2 \right]_{int}^{1/4} \tag{1.4}$$

Dans l'expression plus haut, int désigne l'interface, et les quantités entre parenthèses sont normalisées par les échelles intégrales caractéristiques du champ non-perturbé. L'idée en est, qu'au voisinage d'une interface cisaillée, l'activité de transfert induite par les fluctuations normales se traduit par une divergence des vitesses tangentielles à la surface, du fait que w' croit suivant z ($w' \propto \partial w'/\partial z|_{int} + \cdots$) et non pas suivant z^2 comme pour une paroi

solide ($w' \propto \partial^2 w'/\partial z^2|_{wall} z^2/2 + \cdots$); c'est-à-dire que sa derivée normale à l'interface est non nulle. On notera que la quantité entre parenthèses dans l'expression plus haut représente le carré de la divergence de surface due aux fluctuations turbulentes, qui, sous cette forme adimensionelle $\beta \approx (D\gamma)^{1/2}$ fait apparaitre le paramètre γ, la divergence de surface, et D la diffusivité moléculaire.

Mais ce modèle reste inapplicable en pratique sans une théorie reliant γ à une quantité qu'on peut estimer à partir de l'écoulement mesuré ou calculé. Le recours par Banerjee à la théorie de Graham (1998) tient précisément au fait que celle-ci relie les caractéristiques de la turbulence amont au spectre des fluctuations normales à la surface w', et donc à celui de γ, ce que l' expression (1.4) ne peut délivrer seule. En quelque sorte, la mesure de la déformation interfaciale par étirement ou contraction remplacerait le paramètre de renouvellement dans le modèle de Danckwerts (1951*a*), à la différence près que γ est plus facilement mesurable. En remaniant les résultats de Brumley & Jirka (1987), qui se sont basés sur la théorie de Graham (1998) afin de déterminer la distorsion des spectres de w' sur une surface rigide, Banerjee (1990) est arrivé à l'expression suivante pour β

$$\frac{\beta\, Sc^{1/2}}{u} \approx \frac{C}{Re_t^{1/2}} \left[0.3 \left(2.83\, Re_t^{3/4} - 2.14\, Re_t^{2/3}\right)\right]^{1/4} \tag{1.5}$$

Cette expression constitue la base du modèle de divergence de surface (SD model); elle recoupe avec l'hypothèse de Theofanous et al., selon laquelle le taux de transfert suit bien $Re_t s^{-1/2}$ pour les nombres de Reynolds turbulents relativement petits et $Re_t^{-1/4}$ autrement, réconciliant les modèles de renouvellement LE et SE. Il ne faut cependant pas perdre de vue que cette expression n'était destinée qu'aux interfaces non cisaillées – en conformité avec la théorie de Graham (1998), et sans effets de contamination par les surfactants ou par la convection naturelle. Une surface libre est cependant mobile et peut de ce fait se déformer par l'action du fluide sous-jacent. Dans ce cas, la divergence de la surface serait moins importante, se traduisant dans le modèle par une réduction de la constante de proportionnalité 'C'.

On a longtemps pensé que dans le cas d'un cisaillement imposé par le vent, la structure de la turbulence au voisinage de la surface se trouverait modifiée, empruntant plutôt les caractéristiques de la turbulence pariétale. Les modèles de renouvellement et de divergence surfacique pourraient s'appliquer, mais seulement pour les processus de transport contrôlés par le liquide, même si la turbulence reste régie par la production au voisinage de l'interface. Seule la normalisation des variables devrait dans ce cas se baser sur le cisaillement interfacial et sur la viscosité cinématique du fluide (variables internes). La situation se compliquerait davantage si la surface cisaillée était aussi libre de se déformer, ce qui contrairement à une paroi rigide, permettrait à une partie de l'énergie transmise par le vent de former les vagues, et à une autre portion de produire de la turbulence. L'interaction entre les vagues et la turbulence n'est toujours pas bien comprise.

1.4.3.4 Modèles de divergence surfacique pour les interfaces cisaillées Nos plus récents travaux (en collaboration avec S. Banerjee) basés sur la DNS des écoulements stratifiés viennent de montrer que le modèle SD s'applique aussi bien aux surfaces cisaillées qu'aux interfaces déformables. Les détails des simulations et des résultats sont présentes dans l'article paru très récemment (Banerjee *et al.*, 2004), où l'on montre comment, en présence de cisaillement, les résultats DNS de la divergence surfacique normalisée par les variables internes et tenant compte de la courbure de l'interface suivent bien les prédictions du modèle, même sous les conditions qui ne sont pas celles pour lesquelles la théorie de Hunt et Graham fut élaborée. Ce résultat ouvre en effet une nouvelle voie pour l'utilisation de cette classe de modèles pour des applications pratiques, où la divergence surfacique et les échelles de turbulence ne sont pas facilement déterminables.

En résume, l'idée de tester le modèle de divergence surfacique pour une interface déformable, cisaillée, et une turbulence amont homogène a germé alors qu'on se posait la question si le nombre de Reynolds turbulent pouvait aussi être utilisé pour la parametrisation de la turbulence, même si celle-ci est générée à l'interface. Nous avons donc considéré le cas d'une tension interfaciale imposée par le vent externe, ce qui est le contexte de toutes nos études DNS. Dans ce cas précis, l'expression (1.4) fut reformulée en employant les variables internes comme paramètres de normalisation (*i.e.* $\beta_w^+ = \beta^w\, u_{\star,frict}$ et $u_i^{'+} = u'/u_{\star,frict}$), de sorte que

$$\beta_w^+\, Sc_w^{1/2} = C \left[(\gamma^+)^2\right]_{int}^{1/4}; \quad \gamma^+ = \nabla^+ \cdot \mathbf{u}_{tang}^{'+} - 2w^{'+}\, \nabla^+ \cdot \mathbf{n} \tag{1.6}$$

où toutes les quantités contenues dans le terme de droite de (1.6) sont normalisées par $u_{\star,frict}$ et ν. Les résultats du modèle plus haut (1.6) ont été comparés aux simulations pour différentes valeurs de Sc et de $u_{\star_L}$. Il est avèré que le modèle et la DNS sont en accord jusqu'à un nombre de Schmidt $Sc = 200$, mais le désaccord observé par

les modèles LE et SE pour $Sc = 1.0$ persiste dans ce cas aussi. La DNS a donc permis le calibrage du modèle SD pour les surfaces libres cisaillées et en présence d'une turbulence homogène.

2

Représentations Mathématiques

Résumé

Ce chapitre traite de l'utilisation de la simulation numérique directe et de la simulation des grandes échelles (DNS et LES) pour une catégorie précise d'écoulements multiphasiques. On présentera différents concepts de simulations des écoulements multiphasiques: les méthodes Euleriennes et Euleriennes-Lagrangiennes, le modèle à deux fluides et la variante à fluide unique. La DNS, qui reste hors de portée des applications pratiques, est très utile pour la compréhension des processus de transport et la dérivation de modèles. Bien que sa maitrise en dehors de la dispersion particulaire n'est pas encore prouvée, on peut aujourd'hui utiliser la DNS pour certaines catégories d'écoulements diphasiques simples, tels que les écoulements stratifiés gaz-liquide (Fulgosi *et al.*, 2003). L'approche LES qui s'avère potentiellement prometteuse pour les écoulements dispersés à bulles et pour les écoulements interfaciaux[1] est basée sur une moyenne spatiale sur la grille. Son formalisme mathématique est dans ce contexte basé sur un filtrage pondéré par la fonction indicatrice de phase, interprétée différemment selon qu'on se refère à la formulation a deux-fluides ou aux méthodes de suivi d'interfaces (à fluide unique). La variante basée sur les équations à deux-fluides filtrées est bien adaptée, par exemple, aux panaches à bulles. L'approche fluide unique qui en est une version traitant plus de détails sous-mailles, peut prédire la dynamique simultanée des échelles de turbulence et des échelles interfaciales jusqu'à la sous-couche visqueuse; elle est conçue pour traiter les écoulements interfaciaux. Nous toucherons aussi à l'approche Eulerienne basée sur la moyenne d'entité de Prosperetti et Zhang pour les écoulements chargés de particules solides que nous avons adaptée en introduisant les moyennes spatiales pour les écoulements laminaires homogènes, et le filtrage des variables pour les écoulements turbulents.

2.1 INTRODUCTION

A l'instar des écoulements monophasiques, la turbulence joue un rôle prépondérant dans la séparation des échelles dans les écoulements multiphasiques. Cependant, la dynamique des interfaces et des inclusions peut modifier la cascade d'énergie cinétique turbulente, telle qu'elle est définie conventionnellement. L'enjeu primordial dans le contexte des écoulements multiphasiques turbulents tient donc à la nature de la relation ambiguë entre les échelles de turbulence d'une part, et les échelles caractéristiques des interfaces et des inclusions (par exemple, taille des bulles, rayon de courbure de l'interface) d'autre part. Cette interdépendance ne peut être bien comprise qu'avec l'aide de la simulation numérique directe ou des grandes échelles (DNS et LES).

Pour bien illustrer notre propos, reprenons l'exemple de l'écoulement turbulent homogène à bulles étudié par Lance & Bataille (1991). Ce travail pionnier a clairement montré que sous certaines conditions, la présence des

[1] Les écoulements interfaciaux regroupent toutes les configurations dans lesquelles les fluides évoluent en contact directe à travers une interface bien dèfinie et moins fragmentèe (de plus grande échelle) que dans les écoulements dispersés, par exemple.

bulles peut changer la pente du régime inertiel de la cascade des échelles de turbulence de $-5/3$ à $-8/3$. Ce résultat tangible a permis de savoir un peu plus sur la pseudo-turbulence, un phénomène qui a tenu le haut de l'affiche dans la recherche depuis longtemps. On sait, par exemple, que les petites bulles peuvent ramener les plus petites échelles de turbulence à leur taille, c'est-à-dire que l'échelle de Kolomogorov n'est pas la plus petite échelle dans les écoulements multiphasiques. Ce que l'on ignore, par contre, est si la déformation de l'interface est affectée par la turbulence ou vice versa, et dans quelles proportions.

Dans ce qui suit, nous allons précisément revenir sur nos récents travaux qui ont porté sur l'utilisation des techniques DNS et LES pour la classe d'écoulements multiphasiques la plus étudiée dans la littérature, c'est à dire les écoulements particulaires, les panaches à bulles, et les écoulements interfaciaux (stratifiés). Le choix est évidemment délibéré, étant donné que les algorithmes développés pour simuler la dynamique de chaque classe d'écoulements a atteint un certain degré de maturité: les méthodes Euleriennes et Eulero-Lagrangiennes, le modèle à deux fluides, et les méthodes de suivi d'interfaces. Il faut préciser que dans le cas des panaches à bulles, nous ne considérerons pas les écoulements hétérogènes fortement mélangés (2.1 gauche), mais plutôt ceux chargés de bulles presque sphériques et de tailles plus ou moins identiques (2.1 droite), pour lesquels il existe au moins un consensus quant à la forme des forces interfaciales à considérer. Pour les écoulements semblables à ceux présentés dans la partie gauche de la figure, ces forces sont difficiles sinon impossibles à dériver.

Dans les écoulements chargés de micro bulles ou de particules présents dans les applications industrielles telles que dans le génie des procèdés, la métallurgie et les systèmes de conversion d'énergie, ce qui importe le plus c'est de prédire correctement la dynamique des phases en interaction. Le spectre dénergie cinétique du mélange résultant de ces interactions peut montrer l'effet de la présence des inclusions sur la phase de transport. Par contre, dans les écoulements interfaciaux séparés par une interface bien définie, tels que les écoulements de conduite ou les surfaces océaniques, on peut au contraire trouver des spectres propres à chaque phase des deux côtés de l'interface. Il convient alors de prédire ces échelles jusqu'aux interfaces, pour chacune des phases, un peu comme dans les écoulements de paroi.

La DNS des écoulements multiphasiques a essentiellement porté sur l'étude de la dispersion de particules par le biais de la méthode des points-particules massiques. Il est clair que la DNS des écoulements tels que ceux montrés dans la Figure 2.1 n'est pas à la portée des moyens actuels, à l'exception de quelques tentatives comme celle de Bunner & Tryggvason (2003) qui ont simulé la dynamique de 27 bulles montantes dans un canal. Si la dynamique des interfaces des bulles a bien été simulée dans ce travail, rien n'est moins sûr quant à la turbulence du système. L'écoulement stratifie gaz-liquide étudié conjointement par l'UCSB et l'EPF Zurich (DeAngelis, 1998*a*; Fulgosi *et al.*, 2003; Lakehal *et al.*, 2003) est l'une des rares exceptions ou les solutions de deux phases turbulentes –obtenues par une méthode pseudo-spectrale– sont directement couplées à l'interface, celle-ci étant libre de se déformer dans la limite des ondes capillaires et de gravité. Cette étude (c.f. Chapitres 5, 6 et 7) a servi à l'exploration de plusieurs mécanismes de transports turbulents à l'interface.

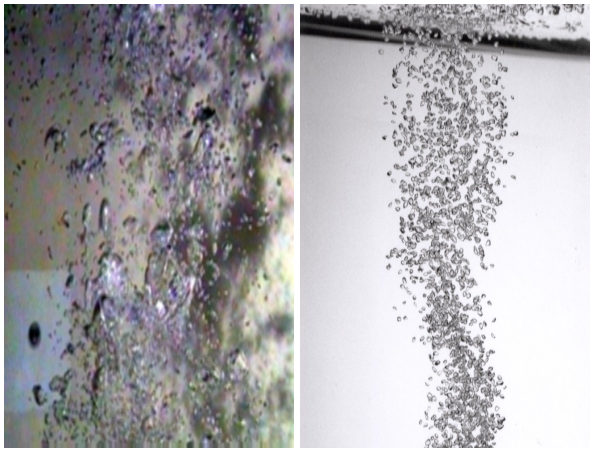

Figure 2.1 écoulements à bulles; (à gauche) écoulement fortement mélangé, (à droite) écoulement à bulles sphériques

Toutes les tentatives, ou presque, visant à l'extension des modèles de turbulence conventionnels basés sur l'équation de dissipation de l'énergie cinétique (RANS) aux écoulements à bulles se sont montrées peu concluantes. Très peu d'études ont porté sur l'extension des modèles RANS aux écoulements interfaciaux; on ne sait donc pas très bien les évaluer. Les raisons de l'échec des modèles en un point sont sans doute liées à la moyenne temporelle

sur laquelle ils se basent, filtrant la plus grande partie du spectre énergétique et, par ricochet, les interactions entre les grosses structures et la phase dispersée. Il est très peu probable que des modèles, aussi élaborés qu'ils puissent l'être, arrivent à reproduire les effets des interactions entre phases, même en combinaison avec des modèles de dispersion turbulente de plus en plus sophistiqués (de Bertodano *et al.*, 1994; Sadatomi *et al.*, 1981; Smith, 1998*a*; Carrica *et al.*, 1999). La modélisation RANS des écoulements à particules solides par l'approche Eulerienne-Lagrangienne dépend énormément du modèle de turbulence appliqué à la phase porteuse. Les limitations des modèles à deux équations sont à présent bien établies.

L'alternative "naturelle" aux modèles RANS pour les écoulements dispersées à bulles et à particules est la simulation des grandes échelles, qui consiste à prédire directement les structures turbulentes plus larges que l'échelle caractéristique de la phase dispersée. La dynamique associée aux échelles non-résolues sera modélisée à l'aide d'un modèle sous-maille. Les grandes échelles sont en effet responsables de la dynamique des phases et des interactions qui en résultent, alors que les échelles sous-mailles jouent plutôt un rôle dissipatif local, sinon aux interfaces. Néanmoins, l'effet dissipatif induit par la dynamique des inclusions au niveau sous-maille reste encore obscur; nos tentatives, en collaboration avec l'École Centrale de Lyon, pour les panaches à bulles n'ont pas apporté de réponses définitives (Lance *et al.*, 1999; Milelli *et al.*, 2001*b*,*a*; Lakehal *et al.*, 2002*b*).

Pour ce qui est des écoulements interfaciaux, on peut procéder en faisant le parallèle avec les écoulements cisaillés pariétaux, tant l'analogie entre les comportements asymptotiques aux parois et aux interfaces est évidente (Fulgosi *et al.*, 2003). Ce point sera développé en détail dans le Chap. 5. Partant de cette hypothèse, il apparait nécessaire de traiter la sous-couche interfaciale de la même manière qu'en turbulence pariétale, c'est à dire par le biais d'une fonction d'amortissement des échelles de longueur. Nous montrerons plus loin comment celles-ci peuvent être dérivées des résultats de simulations numériques directes.

On peut donc appliquer la même stratégie LES pour ce type d'écoulements, sachant que dans le cadre des méthodes de suivi d'interfaces la physique peut être simulée jusqu'à l'interface. La grille représente alors le plus petit rayon de courbure de l'interface résolu, par référence à la turbulence, où l'échelle sous-maille représente la plus petite échelle résolue de la cascade. La modélisation sous-maille qui s'ensuit est en quelque sorte similaire. Les travaux initiés au sein de notre groupe (Lakehal *et al.*, 2004; Liovic & Lakehal, 2004) sont précurseurs dans ce domaine, où l'on a pour la première fois réussi à incorporer l'approche LES dans un solveur volumes finis basé sur une reconstruction d'interfaces du second ordre. L'algorithme VOF (volume de fluide) a été préfère pour sa capacité de prédire la fragmentation massive des interfaces et leur reconnection (Liovic *et al.*, 2002), mais surtout pour sa capacité à conserver la masse et la quantité de mouvement et à preserver les symmetries topologiques lors de la reconstruction.

2.2 DESCRIPTIONS INSTANTANÉES DES ÉCOULEMENTS MULTIPHASIQUES (DNS)

Nous introduisons dans ce paragraphe les différentes options éxistantes pour la description instantanée des écoulements multiphasiques. Ces méthodes dépendent bien évidemment de la nature des écoulements en considération. Nous commencons par les écoulements chargés de particules solides, avant de passer aux panaches à bulles et aux écoulements interfaciaux, stratifiés. Nous introduisons les différentes formulations pré-moyennées, sans trop de détails sur les fondements mathématiques de celles-ci.

Commençons par considérer un système occupé par deux phases distinctes (k) de densité ρ^k et de viscosité μ^k. Pour simplifier, considérons que ce système est incompressible et isotherme, et que les effets de changement de phase et de Marangoni sont absents. Les différentes descriptions du système peuvent concerner un mélange comprenant une phase continue et une phase dispersée à bulles ou à particules ($k = C$ et $k = D$ ou $k = p$), où bien un système formé de deux phases continues immiscibles, par exemple un mélange gaz-liquide ($k = L$ et $k = G$).

2.2.1 L'approche Eulerienne–Lagrangienne

Dans l'approche Eulerienne-Lagrangienne de suivi de particules ou de micro-bulles, les équations de mouvement des particules sont celles de Maxey & Riley (1983*a*). Pour les particules solides, les conditions et restrictions suivantes s'imposent: (1) les particules sont plus petites que l'échelle de Kolomogorov, (2) elles sont rigides, et (3) ont un rapport de densité avec la phase continue de l'ordre de $1/1.000$. Cette dernière condition, qui ne s'applique pas aux micro-bulles, permet de ne retenir que la force de trainée pour les particules; les forces de flottabilité ne sont considérées que pour les micro-bulles. Dans tous les cas de figure, le nombre de Reynolds des particules ou des micro-bulles doit être inférieur à l'unité afin d'adhérer à la condition du fluide Stokesien. L'équation de mouvement d'une particule solide, qui est dérivée par l'intégration de léquation de quantité de mouvement autour d'une forme

sphérique, s'écrit sous la forme conventionnelle suivante

$$\frac{d\mathbf{u}_p}{dt} = -\frac{9\mu}{2\rho_D a^2}(\mathbf{u}_p - \mathbf{u}[\mathbf{x}_p(t)]), \tag{2.1}$$

ou $\mathbf{u}_p$ est la vitesse de la particule, $\mathbf{x}_p$ sa position, et $\mathbf{u}$ la vitesse du fluide interpolée à la position de la particule. Pour les micro-bulles, les forces de masse ajoutée et de flottabilité doivent être rajoutées. Les forces de Basset sont généralement négligées.

La phase continue est representée par les équations de Navier–Stokes pour un écoulement incompressible d'un fluide Newtonien:

$$\frac{\partial u_j}{\partial x_j} = 0, \qquad \text{et} \tag{2.2}$$

$$\frac{\partial u_i}{\partial t} + u_j \frac{\partial u_i}{\partial x_j} = -\frac{1}{\rho_f}\frac{\partial p}{\partial x_i} + \frac{1}{Re}\frac{\partial^2 u_i}{\partial x_j^2} + F_i^{fp}, \tag{2.3}$$

ou F_i^{fp} est la force d'interaction fluide–particule par unité de volume. Le couplage entre le fluide et les particules est complété par la projection de la force agissant sur chaque particule sur le support fluide. Le vecteur de force d'interaction fluide–particule $\mathbf{F}^{fp}$ a la forme nodale suivante (au point 'm'):

$$\mathbf{F}_m^{fp} = \sum_{\alpha=1}^{N_p} \frac{\rho_p v_p}{\rho_f V_m} \mathbf{f}^\alpha W(\mathbf{x}^\alpha, \mathbf{x}^m), \tag{2.4}$$

ou α est l'indice de particule, N_p le nombre de particules dans l'écoulement, $\mathbf{f}^\alpha$ la force sur une particule isolée centerée au point $\mathbf{x}^\alpha$, et W le support de projection de la force sur le noeud 'm'. Ce dernier est calculé en se basant sur la distance de la particule des noeuds attribués à celle-ci. V_m est le volume fluide autour de chaque noeud.

2.2.2 La formulation Eulerienne à deux fluides

Reprenons le schéma type (Fig. 2.2) du système multiphasique comprenant des entités de nature et de tailles différentes. L'espace $\Omega^C(t)$ occupé par la phase continue est chargé d'inclusions (bulles ou particules) présentes sous forme de N entités distinctes:

$$\Omega^D(t) = \sum_{j=1}^{N} \omega_j^D(t) \tag{2.5}$$

Pour distinguer les deux phases présentes dans le domaine $\Omega \equiv \Omega^C(t) \cup \Omega^D(t)$, on a le choix entre une identification exacte des inclusions non-déformables par une fonction de Dirac $\delta(\mathbf{x} - \mathbf{x}_p)$, et le recours à une fonction indicatrice de phase (ou distribution), définie par $\chi^k(\mathbf{x}, t) = 1$ pour $\mathbf{x} \in \mathbf{\Omega^k(t)}$, et $\chi^k(\mathbf{x}, t) = 0$ sinon, pour les fluides déformables. On déduira facilement que la fonction $\chi^k(\mathbf{x}, t)$ n'est rien d'autre que la somme des fonctions de Dirac $\delta^n(\mathbf{x} - \mathbf{x}_p^n)$:

$$\chi^k(\mathbf{x}, t) = \sum_{n=1}^{N_p} \delta^n(\mathbf{x} - \mathbf{x}_p^n), \tag{2.6}$$

ou "n" est le nombre de particules dans le volume considéré.

2.2.2.1 Inclusions déformables Il s'agit ici de dériver les équations pour un écoulement à bulles, sans limitation à priori quant à leur taille ou à leur forme. Dans ces conditions, la fonction indicatrice de phase $\chi^k(\mathbf{x}, t)$ peut être interprétée différemment selon que l'on se positionne dans un cadre de moyenne d'ensemble, de moyenne temporelle ou de moyenne spatiale. Elle peut autant signifier une probabilité de présence de phase, comme elle peut désigner une fonction de distribution spatiale. On parlera alors de concept de "moyennes de phase" pour les phases continue et dispersée. Dans tout les cas de figure, si cette fonction est utilisée pour marquer des surfaces matérielles, alors l'invariance Lagrangienne (Truesdell & Toupin, 1960) s'applique pour $\chi^k(\mathbf{x}, t)$, ce qui se traduit par l'équation de convection suivante:

$$\frac{D\chi^k}{Dt} = \frac{\partial \chi^k}{\partial t} + \mathbf{u}_I \cdot \nabla \chi^k = 0, \tag{2.7}$$

Il faut noter qu'en l'absence de changement de phase, la vitesse de l'interface $\mathbf{u}_I$ se réduit à $\mathbf{u}^k$. Dans les conditions simplifiées ci-dessus, en utilisant (2.7), les équations de conservation instantanées pour chaque phase marquée par χ peuvent être écrites sous la forme ci-dessous

$$\frac{\partial}{\partial t}(\chi^k \rho^k) + \nabla \cdot \chi^k \rho^k \mathbf{u}^k = 0 \tag{2.8}$$

$$\frac{\partial}{\partial t}(\chi^k \rho^k \mathbf{u}^k) + \nabla \cdot \chi^k \rho^k \mathbf{u}^k \mathbf{u}^k = \nabla \cdot \chi^k \Pi^k - \Pi^k \cdot \nabla \chi^k + F_g^k \tag{2.9}$$

où F_g^k est la force de gravité, et $\Pi^k = -P^k \mathbf{I} + \sigma^{\mathbf{k}}$ le tenseur de Cauchy contenant la pression et les tensions visqueuses $\sigma = \mu(\nabla \mathbf{u} + \nabla \mathbf{u}^{\mathbf{T}})$. L'inter-pénétration des phases et les interactions interfaciales associées est mise en évidence par l'application d'une moyenne de phase aux équations instantanées (2.7), (2.8) et (2.9). Ceci est à la base du modèle à deux-fluides, décrivant la présence simultanée de deux phases en un point (Ishii, 1975; Achard & Delhaye, 1977; Chan & Banerjee, 1980; Drew & Lahey, 1988*a*; Zhang & Prosperetti, 1997) en résolvant le système des équations de phase moyennées. Les équations de phase moyennées en question sont obtenues par moyenne du système 2.8 sur des échelles temporelles ou spatiales plus larges que celles caractéristiques de la phase dispersée, pour $N > 1$ inclusions et $k = L$ et $k = G$ (Fig. 2.2 (gauche)). Indépendamment de la nature de la moyenne de phase employée et du régime d'écoulement, l'opération fait systématiquement apparaître des corrélations non-fermées qui auront besoin d'être modélisées.

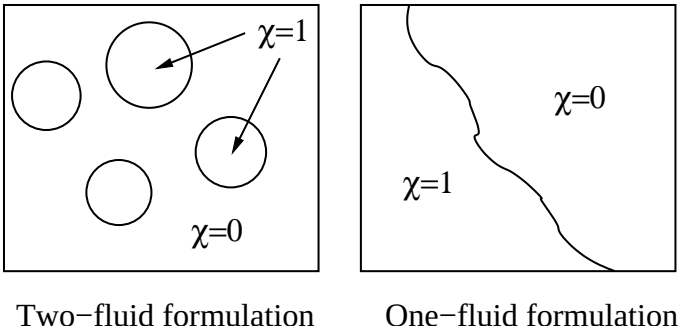

Figure 2.2 Echelle de séparation dans les deux formulations

2.2.2.2 Inclusions non-déformables Il s'agit ici de particules solides de très petites tailles, pouvant former un nuage dense proche d'un milieu continu. Dans ce cas, il est plus naturel et préférable de déterminer des quantités pour la phase dispersée équivalentes à des "densités particulaires" ("number density") plutôt qu'à des fractions volumiques. On peut alors définir une "moyenne d'entité" ou "moyenne particulaire" pour dériver les équations de la phase dispersée, au lieu de "moyennes de phase"; celle-ci sera retenue pour la phase continue. La "moyenne d'entité" s'applique à n'importe quelle quantité caractéristique ou propriété de la particule. Par exemple, la vitesse de centre de masse ou la densité matérielle.

Si l'échelle de longueur de la variation (L) des quantités moyennées est plus large que le rayon des particules (a), la fraction volumique β_D et la vitesse "moyenne de phase" $\langle \mathbf{u}_D \rangle$ de la phase dispersée peuvent être approximées par le "densité particulaire" n et la vitesse de centre–de–masse $\overline{\mathbf{w}}$ (Prosperetti & Zhang, 1995),

$$\beta_D = n v_p + \mathcal{O}\left(\frac{a}{L}\right)^2 \quad \text{et} \quad \langle \mathbf{u}_D \rangle = \overline{\mathbf{w}} + \mathcal{O}\left(\frac{a}{L}\right)^2, \tag{2.10}$$

ou $v_p = 4\pi a^3/3$ est le volume de la particule.

L'approche de constituée de "moyenne de phase" pour le fluide et de "moyenne d'entité" pour la phase dispersée, proposée par Prosperetti & Zhang (1995) et Zhang & Prosperetti (1997), a été adoptée dans nos travaux, à la différence près qu'au lieu d'appliquer une moyenne d'ensemble nous avons reformulé les équations de sorte qu'on puisse moyenner dans l'espace si l'écoulement est homogène dans une direction, et filtrer (sur la grille) dans le cas turbulent général. En s'inspirant de la procédure introduite par Zhang & Prosperetti (1997), nous obtenons les équations de conservation suivantes pour la phase continue (incompressible) et la phase dispersée:

$$\rho_C \frac{\partial \beta_C}{\partial t} + \rho_C \frac{\partial}{\partial x_j}(\beta_C \langle u_{Cj} \rangle) = 0, \tag{2.11}$$

$$\rho_C \frac{\partial}{\partial t}(\beta_C \langle u_{Ci} \rangle) + \rho_C \frac{\partial}{\partial x_j}(\beta_C \langle u_{Cj} \rangle \langle u_{Ci} \rangle) = \frac{\partial}{\partial x_j}(\beta_C \langle \sigma_{ij} \rangle) + \rho_C \frac{\partial}{\partial x_j}(\beta_C \tau_{C,ij}) - \beta_D f_{i,CD} + \rho_C \beta_C g_i, \tag{2.12}$$

$$\rho_D \frac{\partial n}{\partial t} + \rho_D \frac{\partial}{\partial x_j}(n \overline{w}_j) = 0, \qquad \text{et} \tag{2.13}$$

$$\rho_D \frac{\partial}{\partial t}(n \overline{w}_i) + \rho_D \frac{\partial}{\partial x_j}(n \overline{w}_j \overline{w}_i) = \rho_D \frac{\partial}{\partial x_j}(n \tau_{D,ij}) + n f_{i,DC} + \rho_D n g_i, \tag{2.14}$$

où

$$\tau_{C,ij} = \langle u_{Ci} \rangle \langle u_{Cj} \rangle - \langle u_{Ci} u_{Cj} \rangle, \qquad \text{et} \tag{2.15}$$

$$\tau_{D,ij} = \overline{w_i}\ \overline{w_j} - \overline{w_i w_j} \tag{2.16}$$

représente les tenseurs non-résolus provenant du processus de moyenne. Ces termes qui ne dépendent pas directement du régime d'écoulement, sont appelés ici "tensions de moyennes", afin de ne pas confondre avec les tensions de Reynolds sous-mailles. Dans le cas d'un écoulement laminaire homogène dans la direction latérale (par ex. couche limite), ces quantités représentent l'effet des fluctuations de vitesse du fluide induites par les particules pour la phase continue, et la variation de la vitesse de particule dans la direction latérale pour la phase dispersée. Notons que ces équations ne considèrent ni les effets d'interactions ni de collisions entre particules.

Dans ces équations, (2.11) représente le transport de la fraction volumique du fluide par la vitesse de moyenne de phase, et (2.13) le transport de densité particulaire de la phase dispersée par la vitesse de moyenne d'entité. Les équations (2.12) et (2.14) gouvernent l'évolution des quantités de mouvements respectives. β_C, la fraction volumique de la phase continue est telle que $\beta_C + \beta_D = 1$, et ρ_C et ρ_D sont les densités des phases continue et dispersée, respectivement. Le tenseur des forces visqueuse de la phase continue est representé par σ_{ij}, et la force interfaciale moyenne par unité de volume de particule par f_i. On notera que les équations (2.3) peuvent aussi être derivées à partir de (2.11) et (2.12) en avançant l'hypothèse que la phase dispersée est diluée ($\beta_D \ll 1$ or $\beta_C \approx 1$). En d'autres termes, l'effet de déplacement (ou de masse ajoutée) des particules est négligeable. Cette limitation est par ailleurs imposée par l'hypothèse de "point massique" inhérente aux algorithmes de suivi de particules.

La somme des deux forces interfaciales dans les équations de quantité de mouvement n'est pas nulle (comme dans le modèle à deux fluides pour les inclusions déformables) du fait des différences entre la moyenne de phase et la moyenne d'entité $f_{i,CD}$ est en effet la force interfaciale moyenne due à toutes les surfaces contenues dans le volume de moyenne, alors que $f_{i,DC}$ est la moyenne sur la surface de toutes les particules centrées autour du volume.

La force interfaciale moyenne peut être approximée par celle de l'écoulement autour d'une particule isolée (Maxey & Riley, 1983*a*; Zhang & Prosperetti, 1997). Pour les petites particules, rigides et lourdes, seule la trainée et les forces de gravité entrent en jeu (Elghobashi & Truesdell, 1992). Sous l'hypothèse de l'écoulement de Stokes la force de trainée st définie par

$$f_{i,DC} = -9\mu(\overline{w}_i - \langle u_{Ci} \rangle)/2a^2, \tag{2.17}$$

ou μ est la viscosité du fluide.

L'argument essentiel avancé permettant de négliger les quantités (2.15) et (2.16) est que le fluide est dominé par les fluctuations turbulentes. Pour les écoulements laminaires ce terme n'apparaît qu'aux travers des perturbations de vitesse induites par les particules; il peut être negligé pour les suspensions diluées évoluant dans une régime de Stokes (Zhang & Prosperetti, 1997). En ce qui concerne la phase dispersée, rien n'est moins sur quant à sa suppression, une décision qui fut longtemps adoptée par manque d'options plus fiables (Dimas & Kiger, 1998; DeSpirito & Wang, 2001). Ceci est d'autant plus vrai pour les particules dont l'effet inertiel est significatif. Nous avons justement prouvé que ces termes ne peuvent pas être négligés sans conséquences (Lakehal & Narayanan, 2003).

2.2.3 La formulation fluide unique

2.2.3.1 Méthodes de suivi d'interface Reprenons l'exemple type du système diphasique, mais en considérant maintenant l'existence d'interfaces ou de fronts à plus grandes échelles que les bulles. Rien n'empêche aussi d'augmenter la résolution spatiale de sorte qu'une portion d'inclusion ($N = 1$) soit présente dans le volume

de contrôle $\Omega(t)$, comme indiqué sur la Fig. 2.2 (b). On peut, comme avant, distinguer les phases continues immiscibles $\Omega^L(t)$ et $\Omega^G(t)$ par la fonction indicatrice de phase $\chi^L(\mathbf{x},t)=1$ et $\chi^G(\mathbf{x},t)=0$.

En réduisant l'échelle de longueur sur laquelle la moyenne de phase s'applique on peut contourner l'idée de mélange des phases postulée dans les deux formulations (deux fluides) précédentes. Les conditions de saut à l'interface peuvent alors être directement incorporées, de sorte que les équations de phase (2.8 et 2.9) sont remplacées par un système d'équations unique, dans lequel les propriétés matérielles varient dans l'espace et dans le temps (Kataoka, 1986). La position du front est déterminée par (2.7), que l'on peut résoudre par une variété de schémas, tels que les méthodes Volume-of-Fluid, Level Sets, Front Tracking, etc. La somme des équations (2.8) et (2.9) sur l'indice de phase k dans la limite de $N=1$ donne

$$\frac{\partial \rho}{\partial t}+\nabla\cdot\rho\mathbf{u} = 0 \tag{2.18}$$

$$\frac{\partial}{\partial t}(\rho\mathbf{u})+\nabla\cdot\rho\mathbf{u}\mathbf{u} = \nabla\cdot\Pi+\rho\mathbf{g}-\mathbf{F}_\gamma \tag{2.19}$$

La dernière quantité qui apparait dans le terme de droite de (2.19) représente la condition de saut entre deux fronts fluides (Landau & Lifshitz, 1987):

$$F_\gamma \equiv \sum_k \Pi^k\cdot\nabla\chi^k = (\gamma\,\nabla\cdot\mathbf{n})\;\mathbf{n}\,\delta(\mathbf{x}-\mathbf{x}_I), \tag{2.20}$$

Loin des parois solides, cette condition reflète l'équilibre entre le tenseur des contraintes à l'interface et les tensions de surface. γ est le coefficient des tensions de surface, considéré comme constant dans le contexte présent. Afin de pouvoir exprimer (2.20) sous la forme plus haut nous avons utilisé la relation

$$\nabla\chi^k = -\mathbf{n}^k\delta(\mathbf{x}-\mathbf{x}_I), \tag{2.21}$$

en notant que $\mathbf{n}^k=\nabla\chi^k/|\nabla\chi^k|$ est le vecteur unitaire normal à l'interface (avec $\mathbf{n^L}=-\mathbf{n^G}\equiv\mathbf{n}$); δ étant la fonction de Dirac permettant d'identifier l'interface par $\mathbf{x}_I$. La tension de surface est généralement exprimée en termes de courbure de l'interface $\kappa\equiv-\nabla\cdot\mathbf{n}$, ce qui conduit à $F_\gamma=\gamma\,\kappa\,\nabla\chi$. La densité locale ρ est alors définie par

$$\rho=\sum_k\rho^k\chi^k=\rho^G+(\rho^L-\rho^G)\chi, \tag{2.22}$$

une procédure qui s'applique aussi bien à d'autres propriétés matérielles telle que la conductivité thermique, bien qu'une moyenne pondérée est préferée pour la viscosité μ.

2.2.3.2 Méthodes "Boundary Fitting"

La possibilité de prédire les écoulements interfaciaux turbulents avec la même fidèlité que la DNS spectrale des écoulements monophasiques est probablement un but inaccessible. La raison en est que les méthodes de suivi d'interface ne sont pas assez précises pour cet objectif. Dans le cadre des méthodes volumes/différences finies, on peut envisager d'utiliser des schémas compacts d'ordre supérieur pour les termes de convection, mais on ne resout pas le problème d'identification exacte de la topolgie, ni celui des courants parasitaires issus de la discrétisation des tensions de surface (Meier *et al.*, 2002; Lakehal *et al.*, 2002*a*). Afin de contourner ces difficultés, nous avons opté pour une méthode pseudo-spectrale qui résout séparément deux domaines de fluides différents, avant de les coupler à l'interface par le biais des conditions de saut. Cette méthode apellée "Boundary Fitting" dans la littérature anglo-saxone fut developpée par DeAngelis (1998*a*). Nous l'avons étendue aux transferts passifs et actifs (condensation directe).

Dans l'absence de changement de phase, les conditions de saut à l'interface s'écrivent

$$\begin{cases} ((\tau^L-\tau^G)\cdot\mathbf{n})\cdot\mathbf{n}+p^G-p^L+\sigma\,\kappa\,\nabla\cdot\mathbf{n}=0 \\ ((\tau^L-\tau^G)\cdot\mathbf{n})\cdot t_i=0\;\;,\;\; i=1,2 \\ \mathbf{u}^G=\mathbf{u}^L \end{cases} \tag{2.23}$$

où t_1 et t_2 denotent les deux vecteurs unitaires tangents à l'interface. La topologie de l'interface est determinée par l'équation (2.7), qui représente dans ce contexte l'élévation de l'interface $\chi(\mathbf{x},t)\equiv f(\mathbf{x},t)$ autour du niveau de référence. Bien que la méthode soit plus rigoureuse que les méthodes VOF ou Level Sets, elle reste confinée à des géometries simples et à des nombres de Reynolds limités. De plus, elle ne permet pas à l'interface de se déformer au-delà des ondes capillaires ou de gravité. Les paramètres de contrôle des tensions de surface et de la gravité (les nombres de Weber et de Froude) doivent être choisis en conséquence.

2.3 EQUATIONS MULTIFLUIDES FILTRÉES (LES)

2.3.1 Les équations à deux fluides filtrées pour inclusions déformables

Pour mettre la dérivation dans son contexte, nous nous limitons à la situation simplifiée décrite plus haut, où l'écoulement est composé de N inclusions, occupant chacune une proportion volumétrique égale à $\Omega^D(t)/\Omega(t)$. Pour des raisons évidentes, ce volume doit être plus large que l'échelle caractéristique de la phase dispersée, λ^d. Celle-ci peut être associée au diamètre des bulles D comme à leur espacement Γ (c.f. Fig. 2.3). La procédure de filtrage utilisée dans le contexte LES est une opération linéaire définie par

$$\overline{f(\mathbf{x})} \equiv G \otimes f(\mathbf{x}) = \int_\Omega G(\mathbf{x}-\mathbf{x}';\overline{\Delta})\, f(\mathbf{x}')\, d\mathbf{x}' \tag{2.24}$$

où G représente un filtre spatial obéissant à la condition de normalisation suivante:

$$\int_\Omega G(\mathbf{x}-\mathbf{x}';\overline{\Delta})\, d\mathbf{x}' = 1 \tag{2.25}$$

Les échelles plus petites que la taille du filtre $\overline{\Delta}$, notées par $f'(x) = f(x) - \overline{f(\mathbf{x})}$, sont éliminées par le produit de convolution. Dans ce qui suit, nous limitons la dérivation aux grilles équidistantes pour lesquelles la commutativité entre filtrage et opérateurs différentiels est valide:

$$\overline{\nabla f(\mathbf{x})} = \nabla \overline{f(\mathbf{x})}; \quad \overline{\partial_t f(\mathbf{x})} = \partial_t \overline{f(\mathbf{x})}$$

La fraction volumétrique filtrée $\alpha^k(\mathbf{x})$ peut être définie par

$$\alpha^k(\mathbf{x}) = \overline{\chi^k(\mathbf{x})} = G \otimes \chi^k(\mathbf{x}) \tag{2.28}$$

Les équations multifluides filtrées sont obtenues par l'application d'une opération de pondération par la fonction indicatrice de phase (component-weighted volume-averaging), CWVA, pour une variable $f(x,t)$:

$$\widetilde{f^k}(\mathbf{x}) \equiv \frac{\overline{\chi^k f^k(\mathbf{x})}}{\alpha^k(\mathbf{x})} \tag{2.29}$$

Si l'écoulement est compressible la pondération CWVA devrait être reformulée en fonction de la densité, de sorte que

$$\widetilde{f^k} = \overline{\rho^k \chi^k f^k}/\overline{\rho^k \chi^k} \tag{2.30}$$

L'application de (2.29) au système d'équations (2.8) et (2.9) aboutit aux équations multifluides filtrées:

$$\frac{\partial \overline{\rho}^k}{\partial t} + \nabla \cdot \overline{\rho}^k\, \widetilde{\mathbf{u}}^k = \mathcal{R}_m, \tag{2.31}$$

$$\begin{aligned} \frac{\partial}{\partial t}(\overline{\rho}^k \widetilde{\mathbf{u}}^k) + \nabla \cdot \overline{\rho}^k\, \widetilde{\mathbf{u}}^k \widetilde{\mathbf{u}}^k &= -\nabla \alpha^k \overline{P} + \nabla \cdot \alpha^k \widetilde{\sigma}^k + \overline{\rho}^k \mathbf{g} \\ &\quad \underbrace{-\nabla \cdot \tau^k}_{I} + \underbrace{\mathcal{R}_c}_{II} \underbrace{- \overline{\Pi^k \cdot \nabla \chi^k}}_{III} \end{aligned} \tag{2.32}$$

ou $\overline{\rho}^k \equiv \alpha^k\, \widetilde{\rho}^k$ représente la densité de phase apparente. L'erreur dans l'équation de conservation de la masse résulte de la non-linéarité du terme de convection, $\mathcal{R}_m \equiv (\widetilde{\rho \mathbf{u}}^k - \widetilde{\rho}^k \widetilde{\mathbf{u}}^k)$, et peut être négligée pour les écoulements incompressibles, c'est-à-dire $\overline{\rho}^k \equiv \alpha^k\, \widetilde{\rho}^k = \alpha^k\, \rho^k$. La non-linéarité du terme de convection dans (2.32) fait apparaitre les deux quantités suivantes:

$$\tau_{ij}^k \equiv \overline{\rho}^k (\widetilde{\mathbf{u}\mathbf{u}}^k - \widetilde{\mathbf{u}}^k \widetilde{\mathbf{u}}^k), \tag{2.33}$$

$$\mathcal{R}_c \equiv (\widetilde{\rho \mathbf{u}\mathbf{u}}^k - \widetilde{\rho}^k \widetilde{\mathbf{u}\mathbf{u}}^k). \tag{2.34}$$

Le premier terme (I) est la divergence des tensions de Reynolds sous-mailles, alors que le second (II) représente l'erreur induite par la conservation de masse. Les tensions sous-mailles doivent être modélisées en termes de quantités résolvables pour chaque phase. Le dernier terme (III) est la somme des **forces interfaciales** résultantes du filtrage du tenseur de Cauchy Π_{ij}.

Il est évident que contrairement à la formulation LES des écoulements monophasiques, le filtrage dans ce contexte soulève des questions quant au rapport entre l'échelle de coupure $\overline{\Delta}$ et l'échelle caractéristique de la phase dispersée λ^d (Figure 2.3). Conceptuellement, $\overline{\Delta}$ devrait être plus large que λ^d, mais le dilemme persiste quant à la taille du filtre appropriée permettant la plus grande résolution d'échelles possible sans pour autant violer la restriction $\overline{\Delta}/\lambda^d > 1$.

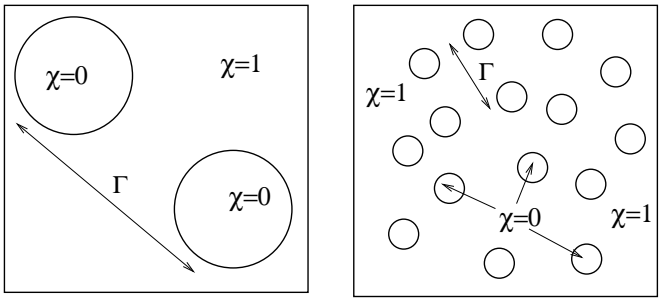

Figure 2.3 Représentations sous-maille des inclusions. Le rapport de l'échelle caractéristique de la phase dispersée à la taille du filtre est plus grande à gauche.

Le terme d'interactions interfaciales filtré $F^k \equiv G \otimes \Pi^k_{ij} n^k_j \delta(\mathbf{x} - \mathbf{x}_I)$ signifie qu'une partie des forces exercées par une phase sur l'autre est lissée par l'opération de filtrage. Dans le cas particulier d'une bulle isolée ou d'un panache à bulles, ces forces englobent la traînée, la portance, la masse ajoutée, et les forces de Basset: F_d, F_l, F_a and F_h. Les lois de fermeture pour ces forces sont bien documentées dans la littérature (Auton *et al.*, 1988; Fabre *et al.*, 1995). On notera seulement que ces forces doivent entre exprimées en fonction des vitesses résolues $\widetilde{\mathbf{u}}^k$.

2.3.2 Les équations filtrées du système fluide unique

Le système d'équations (2.18–2.19) est une description microscopique de deux fluides immiscibles, incompressibles et Newtoniens. La description meso–échelle du système peut être obtenue par la procédure de produit de convolution définie par (2.24).

La fonction indicatrice de phase filtrée, $\overline{\chi} = G \otimes \chi$, est dans ce contexte interprétée comme un volume de fluide (VOF), que l'on notera sous une forme indicielle par $C_{ij} \equiv \overline{\chi} = 1/V \int_V \chi(\mathbf{x}, t) dV$, si un filtre 'top-hat' devait être appliqué. La dérivation des équations filtrées du système fluide unique est aussi basée sur la pondération CWVA introduite plus haut, bien que sous une forme qui s'adapte à la présence d'interfaces plutôt qu'à des inclusions. Dans la formulation précédante (2.31 et 2.32), les variables sont pondérées dans les zones de fluide mélangées par la fraction phasique résolue $\alpha^k(x)$. Mais comme ces zones se réduisent à des interfaces aigues dans la formulation d'un fluide unique, la pondération ne peut être effectuée que par le biais de la densité locale (2.22). Il vient alors

$$\widetilde{f}(\mathbf{x}) \equiv \frac{G \otimes [f(\mathbf{x})\,\rho(\mathbf{x})]}{G \otimes \rho(\mathbf{x})} = \frac{\overline{\rho(\mathbf{x}) f(\mathbf{x})}}{\overline{\rho(\mathbf{x})}} \tag{2.35}$$

Cette opération est empruntée à la moyenne de Favre, mais au lieu de l'équation d'état pour la densité locale résolue, celle-ci est déterminée par

$$\overline{\rho}(\mathbf{x}) = \overline{\chi}(\mathbf{x})\rho^L + (1 - \overline{\chi}(\mathbf{x}))\rho^G \tag{2.36}$$

L'équation de conservation de masse filtrée s'écrit alors

$$\frac{\partial \overline{\rho}}{\partial t} + \nabla \cdot \overline{\rho}\,\widetilde{\mathbf{u}} = 0 \tag{2.37}$$

La substitution de (2.36) dans (2.37) permet d'exprimer les équations filtrées de continuité et de topologie interfaciale:

$$\nabla \cdot \widetilde{\mathbf{u}} = 0 \tag{2.38}$$

$$\frac{\partial \overline{\chi}}{\partial t} + \widetilde{\mathbf{u}} \cdot \nabla \overline{\chi} = 0, \tag{2.39}$$

dans lesquelles la densité locale a été éliminée. L'application de (2.24) et (2.35) aux équations de quantité de mouvement (2.19) donne

$$\begin{aligned}\frac{\partial}{\partial t}(\widetilde{\rho}u) + \nabla\cdot\overline{\rho}\,\widetilde{\mathbf{u}}\,\widetilde{\mathbf{u}} &= -\nabla\overline{P} + \nabla\cdot\widetilde{\sigma} + \overline{\rho}\mathbf{g} + \gamma\,\overline{\kappa}\,\overline{\mathbf{n_i}} \\ &\underbrace{-\nabla\cdot\tau}_{I} + \underbrace{\mathcal{R}_d}_{II} + \underbrace{\mathcal{R}_\gamma}_{III}\end{aligned} \tag{2.40}$$

ou

$$\tau_{ij} \equiv \overline{\rho}\,(\widetilde{\mathbf{uu}} - \widetilde{\mathbf{u}}\widetilde{\mathbf{u}}) \tag{2.41}$$

Les termes (II) et (III) qui apparaissent dans (2.40) sont le résultat de la non-linéarité du tenseur visqueux et de la courbure d'interface κ (ou du vecteur unitaire normale à l'interface $\mathbf{n}$), soit.

$$\mathcal{R}_d \equiv \nabla\cdot\left[\overline{\sigma}_{ij} - \widetilde{\sigma}_{ij}\right], \tag{2.42}$$

$$\mathcal{R}_\gamma \equiv \gamma\,\overline{\kappa\,n_i} - \gamma\,\overline{\kappa}\,\overline{n_i}. \tag{2.43}$$

Ces quantités dénotent les contributions sous-mailles des forces de trainée et de tension interfaciale non-résolues. La modélisation de ces termes est moins évidente que le tenseur de Reynolds sous-mailles. En turbulence la plus petite échelle de l'écoulement –l'échelle de Kolmogorov– peut être reliée au nombre de Reynolds des échelles intégrales. Au contraire, les échelles d'interface non-résolues sont difficiles sinon impossibles à caractériser. Une façon de progresser consisterait à étudier par le biais de la DNS la relation entre les tensions de Reynolds sous-maille (ou plutôt ses composantes L_{ij}, C_{ij} et R_{ij}) et $\mathcal{R}_d$. Mais pour être pragmatique et lucide, il ne sert à rien de chercher à modéliser $\mathcal{R}_d$ tant que l'on n'a pas encore su améliorer la discrétisation du terme des tensions de surface, résolu lui même.

La modélisation du tenseur de Reynolds sous-mailles peut être effectuée par référence à la mécanique des fluides monophasiques, c'est à dire soit par des modèles à viscosité turbulente, soit par le biais d'approches plus élaborées, telles que le principe de déconvolution ou les modèles multi-échelles. Mais le fait que la phase légère percoive le liquide comme une paroi solide suggère qu'un traitement semblable est nécessaire. Le détail de la modélisation sous-maille se trouve aux chapitres 3 et 4. Cependant, nous néxposerons pas nos travaux sur le traitement des zones proches des interfaces.

3

LES of a Vertical Mixing Layer Laden with Bubbles

Le contenu de ce Chapitre est extrait du papier "*Large Eddy Simulation of bubbly turbulent shear flows*", paru dans *Journal of Turbulence*, 3(25), pp. 1-21, 2002. [1]. by Djamel Lakehal, Brian Smith and Massimo Milelli

Abstract

The paper reports on recent advances in the application of the Large-Eddy Simulation (LES) approach to turbulent, vertical mixing layers containing bubbles at low void-fraction. The method is based on the filtered muti-fluid equations derived from the application of a single component-weighted volume-averaging process. The subgrid-scale modelling is based on the Smagorinsky kernel in both its original form and the dynamic procedure of Germano. Parameter studies have been undertaken to determine the effects of the ratio of the *cut-off* filter to the typical length scale characterizing the dispersed phase, the influence of the lift coefficient, the performance of the subgrid-scale models, and the importance of inlet turbulence levels. A new model is proposed for possible bubble-induced turbulence modulation in which the mixing length of the dispersed phase at the subgrid-scale is inferred dynamically from the resolved flow field. By averaging over times longer than the dynamic time scales of the turbulent fluctuations, mean quantities, including phase velocities and void fractions, are derived, which are then compared against experimental data. A critical discussion of the usefulness of LES approaches in this context is given. Overall, the LES approach shows considerable promise in regard to predicting mean quantities including phase velocities and void fractions.

3.1 INTRODUCTION

Three-dimensional mixing of two-phase bubbly flows occurs in many industrial applications, including gas stirring of liquid metal ladles in several metallurgical processes, bubble-column mixers in chemical processing, and venting of vapour mixtures to liquid pools in nuclear reactors. Bubbly flows also play an important role in environmental processes, such as the aeration of lakes, mixing of stagnant water, and destratification of water reservoirs. For all these applications the basic need is to determine the currents induced by the gaseous phase evolving in the surrounding liquid and the subsequent mixing and partition of energy, or species concentration, in the core flow.

The interface topology in this class of flow is intermittent to a considerable degree and also heterogeneous – compared, for example, to the simple situation of a rising bubble or a falling liquid film. This explains why the prediction strategies must rely on a certain form of averaged transport equations with additional unclosed interfacial

[1] Reprinted with the permission of the publisher, *AOP Pub.*.

interaction terms. These are *smoothly* distributed over the computational domain since they are proportional to a continuous function known as the void fraction, reflecting the rate of occurence of one phase within a defined control volume (or during a defined interval of time). The solution methods may be based on the Eulerian-Lagrangian approach or on the Eulerian-Eulerian variant, depending on the flow under consideration. In the Lagrangian reference frame, individual bubbles, or clouds of bubbles, are treated in a discrete way. The reference frame moves with the bubbles and the instantaneous location of each discrete entity is determined by reference to its origin and the time elapsed. In the Eulerian-Eulerian approach, also known as the *multi-fluid* or *interpenetrating media* formulation, the liquid and gas phases are treated as interpenetrating, continuous media, each separately satisfying their own conservation and constitutive laws, and coupled by phase interaction relations. The method has the advantage that two-way coupling between phases can easily be represented, but does require the appropriate mass, momentum and energy exchanges between the phases to be readily quantified.

A key point in modelling bubbly flows is related to the representation of the local turbulence phenomena, and how these dictate the way the local exchanges take place in the mixture. Turbulence modulation due to the presence and motion of the bubbles is also to be expected, even at low void fractions. Until recently, most modelling strategies in this context have relied on extensions of single-phase turbulence models based on the Reynolds Averaged Navier-Stokes Equations (RANS); see, for example, (de Bertodano *et al.*, 1994); (Sadatomi *et al.*, 1981); (Milelli *et al.*, 2001*b*); (Carrica *et al.*, 1999). Models based on the RANS framework have generally proved disappointing in the multi-phase flow context, even in reproducing the global characteristics of the flow. But, even beyond this aspect, it is questionable whether the RANS concept is suitable for this class of flow since, by relying on time averaging, the models tend to filter out both the small-scale turbulence and the instantaneous interactions between the eddies and the dispersed phase. This is the reason why a multitude of models, known as *Turbulent Dispersion Models*, have been advanced to approximate this two-way effect, in addition to closure laws for the Reynolds stresses within each phase. In practice, this idea was most often realized in terms of a superposition of shear-induced and bubble-induced stress tensors in the equations for the liquid phase; the latter being constructed on the basis of scaling arguments.

The necessity of a global strategy, dispensing with previous RANS-based approaches is evident. In the present work we explore the use of the Large-Eddy Simulation (LES) method in which the large-scale motions are solved directly, and the smallest motions, including the interaction of the bubble motion with the surrounding turbulence, are represented in terms of subgrid models. The rationale behind the approach derives from the expectation that large-scale motions will interact strongly with the bubbles themselves, and will therefore be largely responsible for the macroscopic bubble motion, including dispersion, whereas the subgrid scales will be less important, affecting mainly the small-scale bubble oscillations. Consequently, the interfacial momentum forces will be accounted for at the resolved supergrid level only. The subgrid-scale (SGS) turbulence modelling strategy is based on the Smagorinsky (1963) kernel, both in its original form and via the dynamic procedure (DSM) of (Germano *et al.*, 1991), in which the non-resolved scales are approximated from the resolved velocity field. The SGS global dissipative effect, including the modulation induced by the dispersed phase, is modelled via a novel *hybrid* strategy, in which the typical length scale characterizing the dispersed phase is inferred dynamically from the resolved velocity field rather than involving the bubble diameter. This idea reflects the following physical mechanism: the rate of turbulence dissipation at the SGS level due to the liquid and bubble-induced fluctuations is entirely dictaed by the motion of the large-scale, energetic eddies.

In a first step, before investigating bubble-driven flows (plumes), the test case selected here to pursue these ideas is the vertical bubbly shear layer studied experimentally by (Masbernat *et al.*, 1997). One advantage of opting for this case study is that the flow may be considered as being statistically two-dimensional, which helps in conducting sensitivity runs to determine the influence of the ratio of the cut-off filter to the typical length scale characterizing the dispersed phase, the effect of varying the lift coefficient, the predictive performance of specific physical and SGS models, and the effect of initial turbulence levels. A second advantage is the fact that bubbles are of small, uniform diameter (typically $3mm$), and void fractions are small ($\approx 2-3$ percent), so that bubble-bubble interaction effects are negligible.

3.2 GOVERNING EQUATIONS AND SUBGRID-SCALE MODELLING

3.2.1 The two-fluid approach: basic concept

Describing the motion of multi-phase flow systems in terms of model transport equations is fundamentally subject to a certain degree of approximation due to the phase averaging required by the presence of more than one phase. In the present context, use is made of the *multi-fluid* formulation to describe the simultaneous presence of various phases

at each point in the mixture. Without exploring this concept in detail, it suffices to say that it has been presented in various forms[2] (e.g. (Ishii, 1975); (Achard & Delhaye, 1977); (Banerjee & Chan, 1980); (Delhaye, 1987); (Drew & Lahey, 1988*b*);(Besnard & Harlow, 1988)). In all cases, a rigorous formalism requires the two-phase continuum equations to be derived by averaging over length or time scales large compared to typical length or time scales characteristics of the dispersed phase motions, but small compared to those characterizing the mean flow (Λ and Θ).

The starting point is the exact, or microscopic instantaneous equations governing each phase evolving in the system. This preliminary *microscale description* involves the smallest possible length and time scales (λ and θ) compatible with the continuum formulation (Bataille, 1981). The standard conservation laws for each phase can thus formally be written using the phase indicator function $\chi(\mathbf{x}, t)$ at time t and point x defined by

$$\chi^k(\mathbf{x}, t) = 1 \quad \text{for} \quad x \in k, \quad \text{and} \quad 0 \quad \text{otherwise} \tag{3.1}$$

to demarcate volumes occupied by each phase k. In the absence of heat and mass transfer, the balance equations for each phase are multiplied by χ (see, for example, (Delhaye, 1987)):

$$\chi^k \frac{\partial}{\partial t}(\rho^k) + \chi^k \frac{\partial}{\partial x_j}(\rho^k u_j^k) = 0 \tag{3.2}$$

$$\chi^k \frac{\partial}{\partial t}\left(\rho^k u_i^k\right) + \chi^k \frac{\partial}{\partial x_j}(\rho^k u_i^k u_j^k) = \chi^k \frac{\partial}{\partial x_j}\Pi_{ij}^k + \chi^k \rho^k g_i \tag{3.3}$$

where ρ^k is the phase density, g denotes gravity, and the superscript k refers either to the dispersed phase (k=d) or to the continuous phase (k=c). The phase net stress composed of the pressure contribution and the viscous stress, σ_{ij}^k, is defined by

$$\Pi_{ij}^k = -p^k \delta_{ij} + \sigma_{ij}^k \tag{3.4}$$

At this stage, the above system of equations only reflects the presence of multiple components within the system. The inter-penetration of the phases and the subsequent interfacial interactions stem from applying *phase averaging* to the pre-averaged microscopic equations (3.2) and (3.3). Whether it is performed over time, space, or an ensemble, phase averaging always gives rise to extra unclosed quantities that require modelling. This *macroscale description* of the flow is precisely what leads to the instantaneous *phase averaged multi-fluid equations* describing each component as a continuum, regardless of whether the flow regime is laminar or turbulent. But again, proper model derivation requires the averaging to be performed over intermediate length or time scales larger than λ and θ and smaller than Λ and Θ.

Further, the direct numerical simulation (DNS) of this system of equations should resolve most of the relevant turbulent scales, but since this is not realistic in practice, a further averaging of the *phase averaged multi-fluid equations* can then be performed leading to averaged turbulent quantities for each phase, analogous to Reynolds stresses. This additional flow decomposition, which we shall refer to as *turbulence averaging*, may either be a non-weighted time average or a Favre-weighted average based on α^k, the volume fraction. This is rigorously defined as the ratio of the volume of component k in an arbitrary small region to the total volume of the region in question, i.e. $\alpha^k \equiv \langle \chi^k \rangle$. Once adopted, Reynolds averaging ($f = \overline{f} + f'$) generates extra second and third-order correlations involving variable fluctuations α' and f', which also require appropriate modelling. Note that this complication can easily be avoided by use of Favre-weighted averaging (Elghobashi, 1994*a*).

The present formulation aims at unifying the micro- and macroscale descriptions discussed above by adopting a single *component-weighted volume averaging* procedure, which directly leads to a system of *filtered two-fluid equations*. The main difference with earlier formulations is the use of a unique large spatial filter instead of doubling the averaging procedure, e.g. ensemble then space or space then space. This is synonymous to the large-eddy simulation approach in which scales larger than the space filter (represented in this case by the grid size) are solved directly, and the smaller (subgrid) scales will be modelled.

3.2.2 The filtered two-fluid equations

Instead of resorting to the usual volume averaging procedure (Ishii, 1975; Achard & Delhaye, 1977; Drew & Lahey, 1988*b*), the present work relies on translating this into a generalized convolution product as it was first applied to

[2]We exclude reference to the variants based on ensemble averaging.

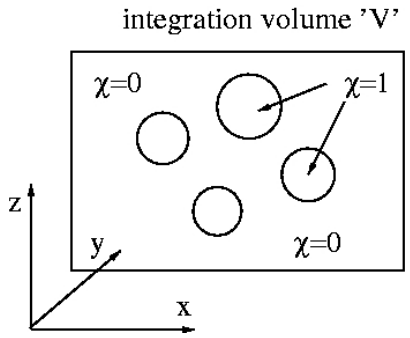

Figure 3.1 Definition of the control volume for phase averaging

multiphase flows by Bataille (1981). The topological equation reflecting the material derivative of χ^k following the interface can be written as

$$\frac{D\chi^k}{Dt} = \frac{\partial \chi^k}{\partial t} + u_j^k \frac{\partial \chi^k}{\partial x_j} = 0, \tag{3.5}$$

By use of the above equation the system of instantaneous equations (3.2) and (3.3) can be recast into a more convenient form:

$$\frac{\partial}{\partial t}(\chi^k \rho^k) + \frac{\partial}{\partial x_j}(\chi^k \rho^k u_j^k) = 0 \tag{3.6}$$

$$\frac{\partial}{\partial t}\left(\chi^k \rho^k u_i^k\right) + \frac{\partial}{\partial x_j}(\chi^k \rho^k u_i^k u_j^k) = \chi^k \frac{\partial}{\partial x_j}\Pi_{ij}^k + \chi^k \rho^k g_i \tag{3.7}$$

For flow systems involving immiscible continuous phases we start the derivation by assuming the domain of the flow (D) to be composed of control volumes (V) containing both fluids, each occupying a volumetric proportion equal to V^k/V (c.f. Fig. 3.1). For obvious reasons this volume has to be larger than the characteristic length scale of the dispersed phase λ^d, denoting the bubble diameter and/or spacing. The volume averaging procedure employed here derives from the filtering process utilized within the LES framework, conventionally defined by

$$\overline{f(\mathbf{x})} = \int_D G(\mathbf{x} - \mathbf{x}'; \Delta)\, f(\mathbf{x}')\, d\mathbf{x}' \tag{3.8}$$

where $G(\mathbf{x} - \mathbf{x}'; \Delta)$ represents an appropriate spatial filter defined such that

$$\int_D G(\mathbf{x} - \mathbf{x}'; \Delta)\, d\mathbf{x}' = 1 \tag{3.9}$$

with Δ being the filter width. For the sake of simplicity, the convolution product represented by equation (3.8) is denoted by

$$\overline{f(\mathbf{x})} = G \otimes f(\mathbf{x}) \tag{3.10}$$

The wavelength of the smallest scale retained by the filtering operation corresponds to the filter width defined here as $\Delta = (\Delta x \Delta y \Delta z)^{1/3}$, where Δx denotes the cell size in the streamwise direction, etc. Within the multi-fluid approach it is conceptually desirable to identify each phase k by defining a quantity reflecting the averaged volumetric fraction of that phase within volume V, i.e. the void fraction in the present context:

$$\alpha^k(\mathbf{x}) = \overline{\chi^k(\mathbf{x})} = G \otimes \chi^k(\mathbf{x}) \tag{3.11}$$

The *filtered multi-fluid equations* are obtained by resorting to the *component-weighted volume-averaging* process[3], in which

$$\widetilde{f^k} = \frac{\overline{\chi^k f^k}}{\overline{\chi^k}} \equiv \frac{G \otimes f^k(\mathbf{x})\, \chi^k(\mathbf{x})}{G \otimes \chi^k(\mathbf{x})} \tag{3.12}$$

[3]This is similar to Favre averaging in which the weighting function is the density ρ. In connection to this, if the flow is compressible on each side of the interface, the density is no longer constant, in which case the above defined filter should be phrased as a *component and density weighted volume-averaging* process and expressed as $\widetilde{f^k} = \overline{\rho^k \chi^k f^k}/\overline{\rho^k \chi^k}$.

Without explicitly assuming commutativity of the filtering operation with respect to the differential operators (in contrast to LES for single phase flows), applying now the above variable definition to equations (3.6) and (4.27) results in the filtered multi-fluid equations:

$$\frac{\partial}{\partial t}(\alpha^k \rho^k) + \frac{\partial}{\partial x_j}(\alpha^k \rho^k \widetilde{u}_j^k) = 0, \quad \sum \alpha^k = 1, \tag{3.13}$$

$$\frac{\partial}{\partial t}\left(\alpha^k \rho^k \widetilde{u}_i^k\right) + \frac{\partial}{\partial x_j}\left(\alpha^k \rho^k \widetilde{u}_i^k \widetilde{u}_j^k\right) = \frac{\partial}{\partial x_j}\alpha^k \left[\widetilde{\Pi_{ij}^k} - \tau_{ij}^k\right] + \alpha^k \rho^k g_i + \mathcal{M}^k \tag{3.14}$$

The above set of equations has the same form as those derived by Tran (1997) and Bataille *et al.* (1999). Note, too, that use was made of the conventional decomposition of the stress tensor into resolved and subgrid-scale (SGS) components, i.e.

$$\tau_{ij}^k = \rho^k \left(\widetilde{u_i u_j}^k - \widetilde{u_i}^k \widetilde{u_j}^k\right) \tag{3.15}$$

The SGS tensor τ_{ij}^k needs to be modelled in terms of determinable (filtered) quantities for each phase. The last term in the filtered momentum equations is a pure interfacial force resulting from filtering the diffusive flux $\Pi_{ij}^k \partial_j(\chi^k)$:

$$\mathcal{M}^k \equiv G \otimes \Pi_{ij}^k n_j^k \delta(\mathbf{x} - \mathbf{x}_I) \tag{3.16}$$

where n_j^k stands for the normal unit vector pointing outward of phase k, and δ for the Dirac distribution identifying the interface location with $\mathbf{x}_I$. Indeed, the first term on the right-hand side of equation (4.27) can be written as

$$\chi^k \frac{\partial}{\partial x_j}\Pi_{ij}^k = \frac{\partial}{\partial x_j}\chi^k \Pi_{ij}^k + \Pi_{ij}^k n_j^k \delta(\mathbf{x} - \mathbf{x}_I) \tag{3.17}$$

noting that

$$\frac{\partial \chi^k}{\partial x_j} = -n_j^k \frac{\partial \chi^k}{\partial n_j^k} = -n_j^k \delta(\mathbf{x} - \mathbf{x}_I). \tag{3.18}$$

More important to note is that, in contrast to the filtered single-phase equations, a conceptual restriction arising in the present approach is that the cut-off filter Δ should strictly be larger[4] than the length-scale characteristic of the dispersed phase λ^d. The dilemma posed is in determining an appropriate choice of the ratio Δ/λ^d providing a sufficient large-scale resolution while not violating this restriction. The non-resolved subgrid scales, $u_i'^k = u_i^k - \widetilde{u_i}^k$, represent the portion of flow details of wavelength smaller than Δ smoothed out by applying equation (3.12); these scales include possible bubble-induced fluctuations. The conjuncture suggests that the subgrid-scale motion of the continuous phase in particular may be affected by bubble-induced agitation, and as such it needs to be represented by the subgrid-scale (SGS) model.

3.2.3 Interfacial momentum forces

The simultaneous presence of the phases also imposes an approximation for the interfacial term $\mathcal{M}^k$ reflecting the global force exerted by the phases on each other, but at the supergrid level. Let us assume that each control volume V forming the flow domain D is populated by n_b bubbles of volume V_b. If G is taken as a top-hat or boxcar filter of width $\Delta \equiv V^{1/3}$ and height $1/\Delta$ we may write the interfacial force $\mathcal{M}^k$ as

$$G \otimes \Pi_{ij}^k n_j^k \delta(\mathbf{x} - \mathbf{x}_I) \equiv \frac{1}{V} \sum_{l=1}^{n_b} \int_S \Pi_{ij}^k \, n_j^k \, dS \tag{3.19}$$

where S is the surface of the bubble. If we now explicitly separate the filtered stress divergence term $\alpha^k \partial_j(\widetilde{\Pi_{ij}^k})$ from the first term on the right-hand side of equation (3.14) and use the Gauss' theorem to transform its volume integral into a surface integral, equation (3.19) may be transformed into a filtered interfacial force of the form

$$\mathcal{M}'^k = \alpha^k \int_S \left[\Pi_{ij}^k - \widetilde{\Pi_{ij}^k}\right] \, n_j^k \, dS \tag{3.20}$$

[4]Both the filter width Δ and the length-scale characteristic of the dispersed phase λ^d should be defined such that $\lambda < \lambda^d < \Delta < \Lambda$.

where the integral represents the forces per unit dispersed phase volume. In the particular case of a single bubble rising in a quiescent pure fluid, the force exerted by the continuous phase on the bubble encompasses the drag, lift, virtual or added mass and Basset history forces, i.e. F_d, F_l, F_a and F_h. The Basset history contribution is often neglected. Assuming a dilute-loading limit, the filtered interfacial force given by equation (3.20) can be equally formulated:

$$\mathcal{M}'^d = -\mathcal{M}'^c = \alpha^d \left(\widetilde{F_d} + \widetilde{F_l} + \widetilde{F_a} \right) \tag{3.21}$$

The closure laws for these three components are well documented in the literature (Banerjee & Chan, 1980; Drew & Lahey, 1988*b*; Auton *et al.*, 1988; Smith, 1998*b*; Zhang & Prosperetti, 1997). In the present case, however, each filtered contribution is naturally expressed in terms of resolved velocities $\widetilde{u_j}^k$. For example, invoking small-to-negligible SGS effects on the global drag force, $\widetilde{F_d}$ can be approximated by

$$\widetilde{F_d} \approx \frac{3}{4} \frac{C_d^*}{d_b} \rho^c \left| \widetilde{\mathbf{u}}^c - \widetilde{\mathbf{u}}^d \right| \left(\widetilde{\mathbf{u}}^c - \widetilde{\mathbf{u}}^d \right) \tag{3.22}$$

where ρ^c denotes the density of the continuous phase, d_b the bubble diameter, and C_d^* the modified drag coefficient which should slightly deviate from the *true* (valid for a non-deformable sphere immersed in a Stokes flow) coefficient C_d. Beyond the Stokes regime C_d can be determined from

$$C_d = \frac{24}{Re_d} \left(1 + 0.1 Re_d^{0.75} \right); \quad Re_d = \frac{d_b |\widetilde{\mathbf{u}}^c - \widetilde{\mathbf{u}}^d|}{\nu^c} \tag{3.23}$$

The modified drag coefficient C_d^* is proposed to account for the SGS effects, but in the absence of experimental or firmer numerical evidence its value was taken equal to that of C_d determined from equation (3.23). The filtered virtual mass force, which appears because the bubble acceleration also requires acceleration of the surrounding fluid, is also approximated by

$$\widetilde{F_a} \approx \rho^c C_a^* \left(\frac{D\widetilde{u}_i^d}{Dt} - \frac{D\widetilde{u}_i^c}{Dt} \right) \tag{3.24}$$

in which the value of the modified added mass coefficient C_a^* is taken here equal to that (exact) for a single sphere rising in an infinite fluid (Drew & Lahey, 1987), i.e. C_a = 0.5, assuming dilute suspensions of spheres in a fluid,

The filtered lift force acting on the bubble is expressed herein as follows

$$\widetilde{F_l} \approx \rho^c C_L^* \, \epsilon_{ijk} \left(\widetilde{u}_j^c - \widetilde{u}_j^d \right) \widetilde{\omega}_j^c \tag{3.25}$$

where $\widetilde{\omega}_j^c$ stands for the liquid filtered vorticity and ϵ_{ijk} denotes the permutation tensor. Again, the modified lift coefficient C_L^* is supposed to account for the subgrid-scale effects. Note that there is no generally accepted value of the lift coefficient for a swarm of bubbles, although $0.25 < C_L < 0.5$ is most often used. More than the other two terms, the flow is extremely sensitive to the lift force affecting most the distribution of the phases in the flow, essentially because of the presence of the vorticity in equation (3.25). The value assigned to its coefficient may therefore play a key role in the simulation. A sensitivity study to this parameter has been carried out and results are presented in this paper.

3.2.4 Subgrid-scale modelling

The dissipative scales of motion, including the bubble-induced ones for the continuous phase, are not resolved and require as such a model reproducing energy transfer from the resolved scales. The SGS stress tensor τ_{ij}^k in equation (3.15) is approximated by applying the eddy viscosity concept in which the deviatoric part is linearly related to the resolved rate of strain tensor $\widetilde{S_{ij}}^k$ according to

$$\tau_{ij}^k = -2\mu_{sgs}^k \widetilde{S_{ij}}^k + \frac{1}{3}\delta_{ij}\tau_{kk}^k; \quad \widetilde{S_{ij}}^k = \frac{1}{2}\left(\frac{\partial \widetilde{u_i}^k}{\partial x_j} + \frac{\partial \widetilde{u_j}^k}{\partial x_i} \right) \tag{3.26}$$

Unlike in compressible flows, the trace of τ_{ij}^k is often embodied into the modified pressure. The coefficient of proportionality, μ_{sgs}^k, is known as the turbulent viscosity. Assuming that the dissipative scales are in equilibrium, μ_{sgs} may be scaled in a conventional way via a length scale and a time scale. According to Smagorinsky (1963), the turbulent viscosity can be written as

$$\mu_{sgs} = (C_s \Delta)^2 \rho |\widetilde{S}|; \quad |\widetilde{S}| = \sqrt{2\widetilde{S}_{ij}\,\widetilde{S}_{ij}} \tag{3.27}$$

More specifically in the multi-fluid context the presence of the dispersed phase is known to contribute together with the unresolved scales of motion to the process of energy removal (or dissipation, $\varepsilon_{sgs} \equiv \mu_{sgs}^3/\lambda^4$) from the resolved scales of the liquid phase (Lance & Bataille, 1991). In the context of equation (3.26), this two-way coupling effect can be interpreted as a modulation of μ_{sgs} by its bubble-induced counterpart, μ^d. By assuming the dispersed phase to follow the liquid motion at the SGS level, Tran (1997) developed a model for μ_{bub} in which it was assumed that the velocity scales of the smallest resolved motion and the dispersed phase were identical, which is probably true for micro-bubbles. The effective viscosity for the continuous phase $\mu_{sgs}^c + \mu_{bub}^c$ was of the form

$$\mu_{eff}^c = \mu_{sgs}^c \left[1 + C_f \alpha^d 6\pi \frac{d_b \mu^c}{\Delta \mu_{sgs}^c}\right]^{\frac{1}{3}}, \tag{3.28}$$

in which μ^c is the molecular viscosity and $C_f = 0.17$ is a model constant. The model is in effect grossly dissipative since the coefficient C_f is assigned a fixed value.

Lakehal *et al.* (2002*c*) advanced another idea according to which it is the mixing length of the dispersed phase, λ^d, that may be comparable to the smallest resolved scales, since the bubbles are known to have a tendency to break the eddies into scales of similar size (Lance & Bataille, 1991). Support for this argument can be found in the Scale-Similarity Principle of Bardina *et al.* (1980), which states that the smallest resolved scales are similar to the largest modelled ones; the latter in the present context are the bubbles themselves. The eddy viscosity can then be scaled as the superposition of shear-induced and bubble-induced SGS energy dissipation mechanisms:

$$\mu_{eff}^c = (C_s\Delta)^2 \rho^c |\widetilde{S_{ij}}^c| + (C_s\Delta)\rho^c \alpha^d |\widetilde{\mathbf{u}}^c - \widetilde{\mathbf{u}}^d| \tag{3.29}$$

where we have set λ^d equal to $(C_s\Delta)$ and the velocity scale of the dispersed phase equal to the slip velocity, $|\widetilde{\mathbf{u}}^c - \widetilde{\mathbf{u}}^d|$. Note that in an earlier RANS-based work, Sadatomi *et al.* (1981) incorporated the bubble diameter d_b as a length scale together with the slip velocity to account for the same effect. In the LES context, however, both Sadatomi *et al.* (1981)'s proposal and the above model (3.29) with constant C_s would make the SGS model grossly dissipative. It would therefore make more sense to use equation (3.29) in connection with the DSM approach so as to accommodate the mutual transfer of dissipated momentum between the phases, from the bubbles to the surrounding fluid whenever $C_s > 0$, and vice-et-verca whenever $C_s < 0$. Note also that the difference between the proposed idea and that of Tran (1997) is in the scaling arguments adopted: The similarity between the resolved scales and the dispersed phase in terms of velocity scale can only apply to micro-bubbles, which indeed tend to follow the liquid motion.

For the present application the standard SGS model (3.26) was employed both with the Smagorinsky constant C_s = 0.12 and using the DSM approach of Germano *et al.* (1991). A top-hat filter was employed and the ratio of the test filter to the grid filter was taken equal to two. And as written above, the bubble-induced dissipation model (3.29) was combined with the DSM approach only.

3.3 SIMULATION SET-UP

The experimental facility of Masbernat *et al.* (1997), shown schematically in Fig. 3.2, consists of a vertical square-channel air-water loop. The convergent channel is divided at the bottom into two parts by a splitter plate, each side being supplied independently by a mixture of bubbles and water at specified rates.

In the sensitivity part of the investigation the flow was calculated in two dimensions, taking the risk of violating the LES method which conceptually is three-dimensional. The three-dimensional computational domain was deliberately truncated compared with the experiment (30cm width, 60cm height, and 4cm depth), and slip boundary conditions were imposed on the lateral planes. This measure was found to be equivalent to extending the domain and imposing non-slip wall conditions using the wall-function approach of Wengle & Werner (1989). On top of the domain a constant pressure boundary condition was imposed. At the bottom, the phases were injected with the profiles measured at the end of the splitter plate (at x=-1cm), a level corresponding to the inlet boundary in the present simulations. Two sets of grids were employed for the two-dimensional sensitivity calculations. The finest one consists of 100×200 nodes, and the coarse one of 30×40 nodes. The three-dimensional grid, consisting of $200,000$ nodes, was uniformly distributed ($\Delta x = 3.5mm$, $\Delta y = 3mm$, $\Delta z = 4mm$) to maintain a constant filter width over the entire domain. The inlet void fraction ($\alpha^d = 1.9\%$, with bubbles of $3mm$ diameter), liquid and gas mean velocities (0.22m/s in the slow channel, and 0.54m/s in the fast channel), and the rms velocity profiles, were all taken from the experiment. Both two- and three-dimensional calculations were carried out for

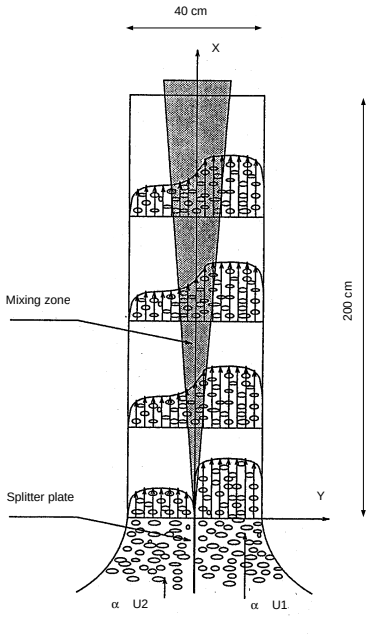

Figure 3.2 Experimental set-up (adapted from (Masbernat *et al.*, 1997))

about 5000 time steps (with $\Delta t = 0.001s$) to reach statistically steady-state solutions. The calculations were performed using an unstructured, multi-block, multi-grid, finite-volume code employing a fully co-located storage arrangement. A second-order central differencing scheme was used for the spatial discretization, and a second-order, fully implicit, backward differencing scheme for the time marching. The solution was iterated to convergence using a pressure-correction approach.

3.4 TWO-DIMENSIONAL SIMULATIONS: PARAMETRIC STUDY

3.4.1 On the value of the lift coefficient and cut-off filter width

The implications on the results of both the filter width Δ and the value assigned to the modified lift coefficient C_L^* were examined within the context of the standard Smagorinsky SGS model with $C_s = 0.12$. In the dispersed-phase context the typical length scale could either be the bubble diameter, $\lambda^d \equiv d_b$, or the the inter bubble-spacing, $\lambda^d \equiv I_b$. These are in fact tied by the void fraction α (assuming spherical bubbles) via $\alpha \approx (d_b/I_b)^3$. This implies that addressing the impact of the ratio Δ/λ^d makes more sense if λ^d could be represented by the inter bubble-spacing. For the sake of clarity, however, the results are presented in what follows based on Δ/d_b.

Results for the u_{rms} distributions obtained with varying C_L^* for the coarse and fine grids are compared against experimental data in Fig. 3.3. They clearly indicate that independently of the value assigned to C_L^* rigorous resolution requires the cut-off filter Δ to be comparable to the bubble size. With the coarse grid, the rms velocities were generally grossly exaggerated, and the void fraction and velocity profiles were rather flat (results not shown here). More precise indications of the effect of varying the lift coefficient can be seen in the context of Fig. 3.4, comparing the void fraction distributions at two elevations using the fine grid. But Fig. 3.3 already suggests that without the lift force the simulation misrepresents the lateral spreading of the plume at the expense of a strong oscillation in the rms magnitude. Figure 3.4 confirms this result through the ragged profiles of void fraction for $C_L^* = 0$, but it also shows overpredicted peaks for $C_L^* = 0.5$. Judging from this figure in particular one is tempted to conclude that $C_L^* = 0.25$ is the best compromise for this class of flow, in conformity with the recommendations of Drew & Lahey (1987).

In summary, it appears that with this level of void fraction (1.9%) and a cut-off length-scale significantly larger than the characteristic length of the dispersed phase ($\Delta/d_b = 3.33$) the simulation cannot capture all the important

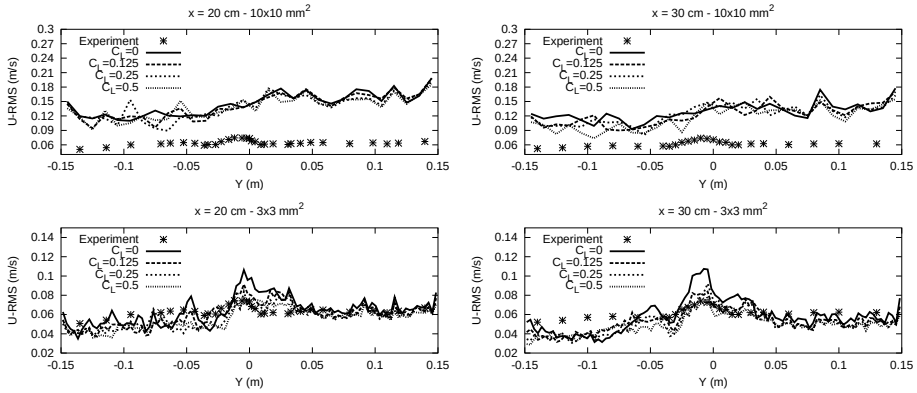

Figure 3.3 u_{rms} distributions for the coarse and fine meshes. Calculations with variable C_L^* and standard SGS model with C_s = 0.12

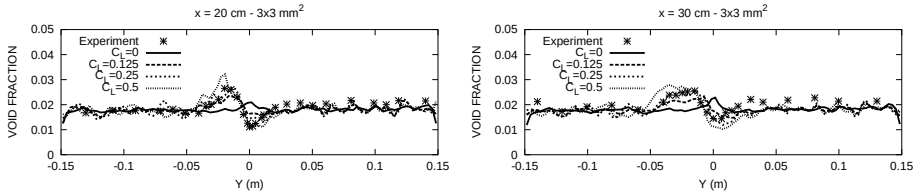

Figure 3.4 Void fraction distributions for the fine mesh ($\Delta/d_b = 1.5$). Calculations with variable C_L^* and standard SGS model with C_s = 0.12

scales involved in the flow; the best results are obtained with $\Delta/d_b = 1.5$. On the other hand, it is likely that in the absence of bubbles a rigorous LES of this flow would require an equal grid resolution owing to the low void fraction (1.9% only). But apart from that, a large ratio of Δ/λ^d will leave an unresolved gap of intermediate length-scales interacting with the bubbles still needing to be modelled.

A further optimization exercise, in which $\Delta/d_b = 1.6$ and C_L^* = 0.25, led to the results displayed in Fig. 3.5. There it is shown that both the velocity distributions and void fraction distributions compare well with the experiment, but not the rms values away from the mixing zone. This points to two plausible reasons: either the three-dimensionality of the flow has an appreciable *global* effect on the fluctuating field, in which case a 2D idealization is restrictive, or the bubble-induced fluctuations at the large-scale level in weak-shear regions are not well captured.

3.4.2 On the SGS modelling

The predictive performance of the employed SGS models is discussed within the context of Fig. 3.6 comparing the liquid velocity fluctuations with the experiments. Immediately after the injection location, at x=6cm, the standard SGS model with constant C_s delivers an overpredicted level of u_{rms} as compared with the DSM. The panel also shows that the performance of the DSM is better in the shear region, and in the rapid channel, than in the slow channel away from the mixing zone. The tendency is somewhat inverted at the next location, in the sense that results of the standard SGS model are the closest to the experiment. The misrepresentation of the rms values away from the shear region is equally shared by both models; the possible explanations for this behaviour have already been described.

The reason why at x=6cm the velocity fluctuations are more pronounced in the standard model is probably due to the flow there still being affected by the proximity of the injection, in which case the actual C_s level is well above the value of 0.12 (it has actually a space average of 0.147). This naturally leads to a pronounced effective viscosity that attenuates further the fluctuating field compared with the standard model. Looking at the next location (x=20cm) reveals that the level of u_{rms} is generally underpredicted, more with use of the DSM than by the standard model. This is a misleading result since at that location the values of C_s were on average smaller than 0.12. At x=30cm, where the averaged C_s value was found to converge towards 0.121, the standard and modified SGS models deliver almost the same result (results not shown).

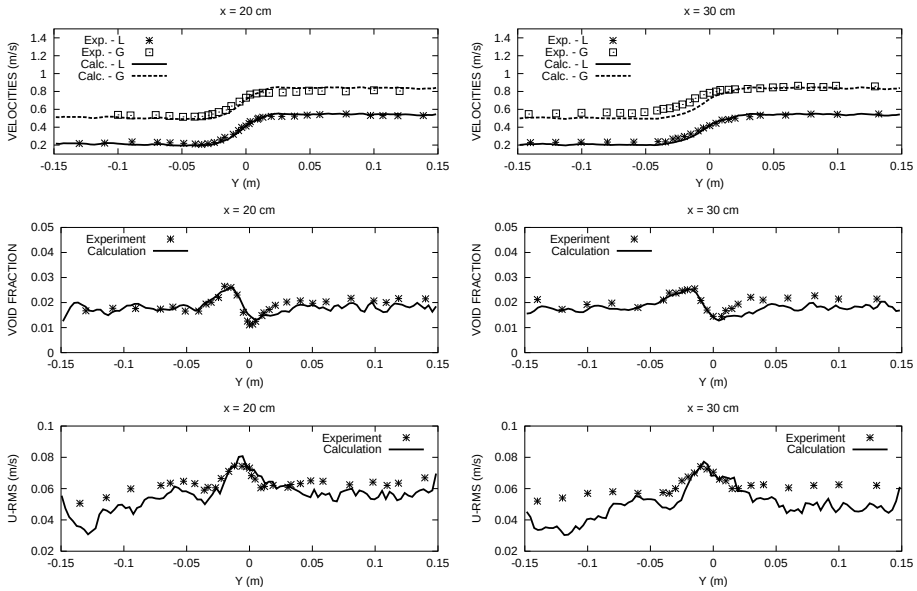

Figure 3.5 Distributions of mean velocities, void fraction and u_{rms}. Calculations (2D) with $\Delta/d_b = 1.6$ and C_L^* = 0.25, and standard SGS model with $C_s = 0.12$

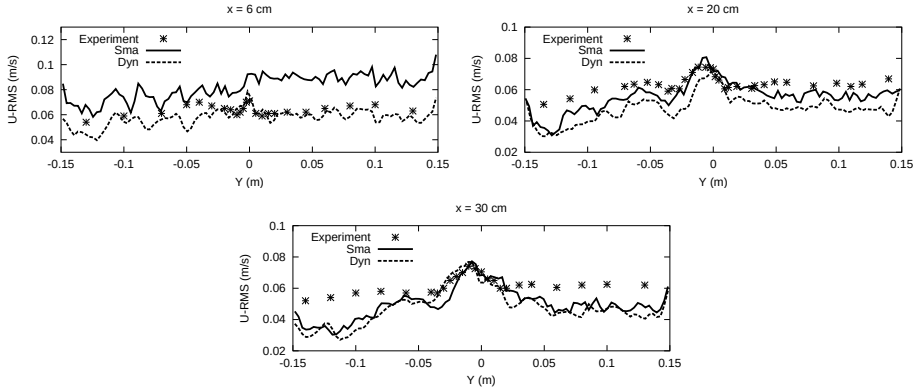

Figure 3.6 u_{rms} distributions obtained with the standard and DSM SGS models. Calculations with $\Delta/d_b = 1.6$ and C_L^* = 0.25

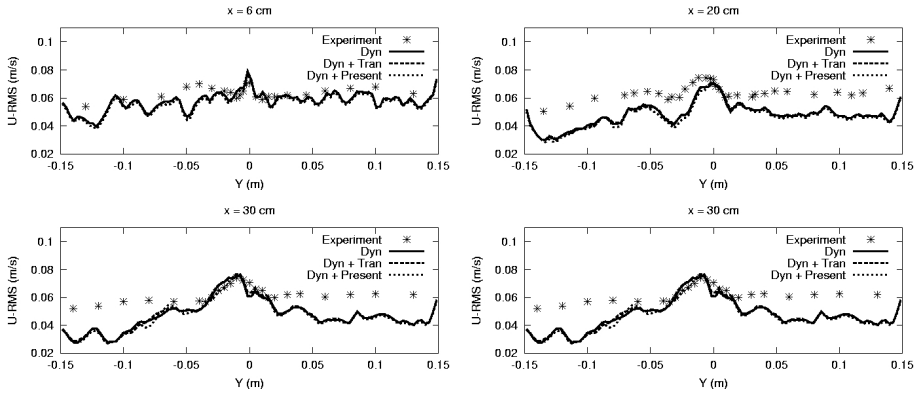

Figure 3.7 u_{rms} distributions obtained with various DSM-based models. Calculations with $\Delta/d_b = 1.6$ and C_L^* = 0.25

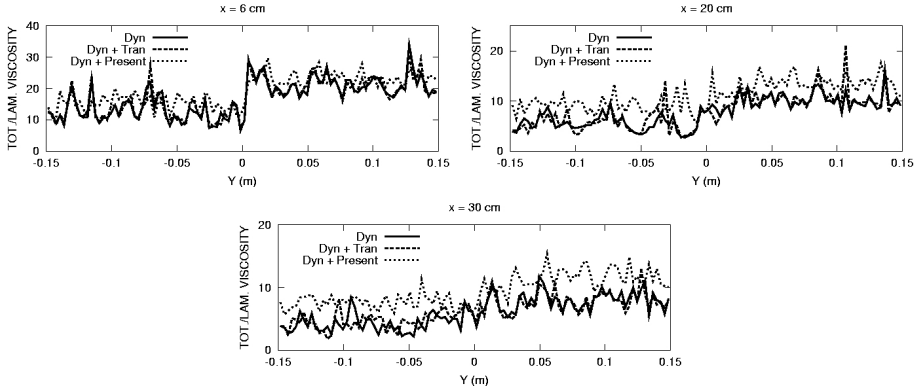

Figure 3.8 Distributions of μ_{eff}/μ obtained with various DSM-based models. Calculations with $\Delta/d_b = 1.6$ and C_L^* = 0.25

Comparison of the time-averaged liquid and gas velocity and volume fraction α^d distributions delivered by the DSM approach, combined with the Tran model (3.28) and the present one (3.29) for bubble-induced dissipation, revealed that these quantities are not sensitive to either of the two models (results not included here). Overall, these predicted quantities agreed very well with the experiment. The u_{rms} distributions plotted in Fig. 3.7 are in line with the conclusion drawn from the previous analysis, i.e. the fluctuating field perceives the effect of promoting the eddy viscosity as a secondary effect only. When looking at Fig. 3.8, displaying the distributions of the ratio μ_{eff}/μ, the previous remark may sound somewhat misleading, since the effective viscosity seems now to be enhanced (by a factor of 2 at x=20 and x=30cm), particularly away from the mixing zone. But obviously, the shear stresses are important only in the regions where appreciable velocity gradients occur. In summary then, in the context of an idealized 2D simulation it seems that representing the bubble-induced rms velocity field in terms of a pure shear-type model is not sufficient. But a final conclusion cannot be drawn without looking at three-dimensional calculations. Also, a close inspection of Fig. 3.8 raises an additional point: At both elevations around the mixing zone the magnitudes of μ_{eff}/μ are comparable to those delivered by the DSM alone. This could *tentatively* be interpreted as the capacity of the proposed model to allow the shear stress to be solely dictated by the strength of the rate of strain $\widetilde{S}_{ij}$, wherever appropriate. Finally, it is worth noting from Fig. 3.8 that the Tran (1997) model seems to have negligible impact compared with the proposed one, which is not surprising (from a formulation point of view, at least) since the presence of the power $1/3$ in equation (3.28) tends to smooth this term out.

3.5 THREE-DIMENSIONAL SIMULATIONS

3.5.1 On the flow structure

Results are presented from three-dimensional simulations with various SGS model combinations and are compared against the data of Masbernat *et al.* (1997). However, prior to that, it is perhaps worth recapitulating the main conclusions drawn from the sensitivity analysis: For the level of void fraction employed here, the optimum grid concentration has to be such that the ratio of the cut-off filter to the bubble diameter is ≈ 1.5; a good compromise can be obtained with a lift coefficient of $C_L^* = 0.25$; the Smagorinsky model performs quite well and gives results comparable to those of the dynamic procedure of Germano; modifying the subgrid-scale model to account for the bubble-induced effect has not yet been conclusive.

The one-dimensional streamwise turbulent energy spectrum taken at a point located in the mixing zone is displayed in Fig. 3.9. The spectrum exhibits a broad range turbulence with a slope oscillating between the single-phase $-5/3$ and the two-phase $-8/3$ power laws in the inertial sub-range. Previous experimental studies have actually attributed the more dissipative spectrum to the presence of the dispersed phase, this being responsible for eddy disintegration. The present result indicates, however, that at this low void fraction the effect of the bubbles on the surrounding turbulence may be negligible.

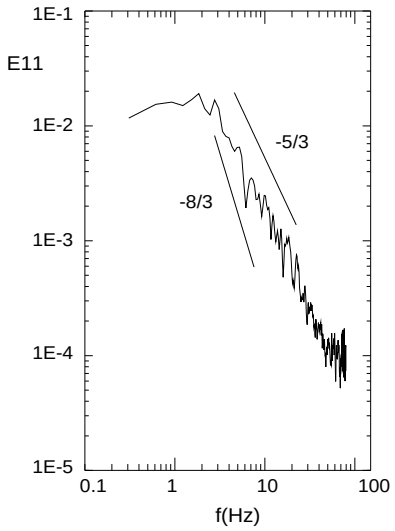

Figure 3.9 One-dimensional streamwise turbulent kinetic energy spectrum

Snapshots of the velocity vectors taken in the middle of the domain at two time steps ($t = 5s$ and $7s$) are shown in Fig. 3.10. The flow clearly exhibits the low speed and high speed regions. Note, too, the formation of large-scale motions visible in the slow channel in particular. The mixing zone between the two channels, identified by a high shear, appears to be oscillating along the flow direction. Figure 3.11 shows two snapshots of volume fraction distributions taken in the mid-plane of the domain. The structure of the flow observed in the previous figure is also reproduced by these contours. The figure clearly shows the smooth inter-penetration of the phases, without a clear distinction of the interface. More important to note is the separation between two distinct flow regions: immediately after the injection the bubbly phase is still sparsely distributed with a clear presence of the small scales, whereas far downstream these structures seem to be smoothed out in favor of the large-scale motions. The oscillation of the mixing zone at the centre of the domain is also clearly shown.

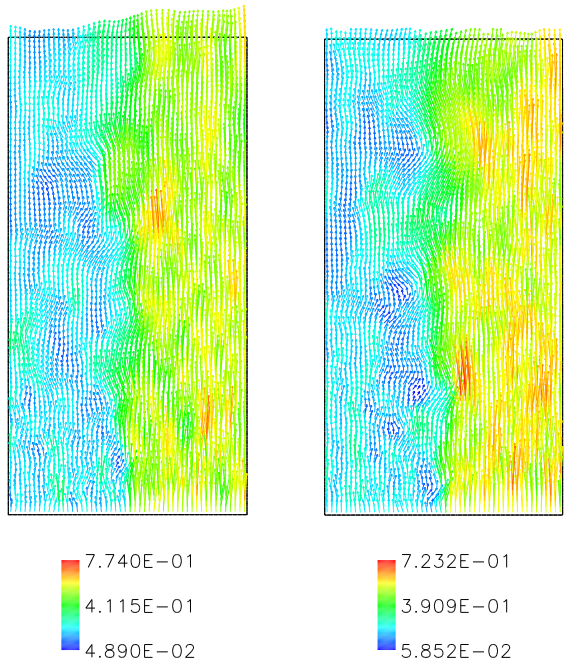

Figure 3.10 Instantaneous resolved velocity vectors in the mid-plane of the domain

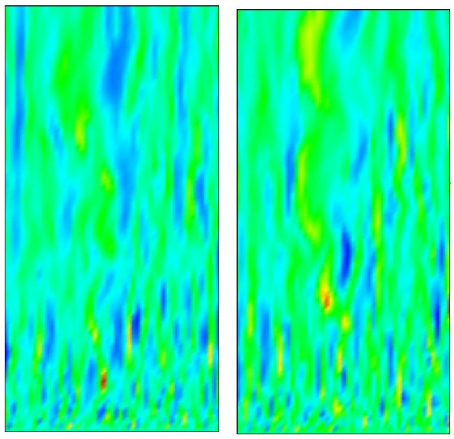

Figure 3.11 Contours of volume fraction distribution in the mid-plane

3.5.2 Averaged and rms quantities: 2D v.s 3D calculations

Two- and three-dimensional calculations are discussed within the context of Figs. 3.12 and 3.13, comparing the time-averaged streamwise velocities and void fractions, respectively. Figure 3.12 shows almost no differences between the two sets of calculations. It also indicates that the LES results do reproduce fairly well the self-preserving behaviour of the plume, in accordance with the data. This supports the idea that the flow is statistically two-dimensional and can therefore be simulated as such. Note in particular that at $x = 40cm$ in the slow channel the predictions are underestimated. In fact, the results have often been observed to begin systematically to deviate from the measurements for $x > 40cm$, in particular in the slow (left) channel. This was attributed by the authors of the experiment to the lack of precision in measuring the inlet profile of the void fraction in that channel. The distribution

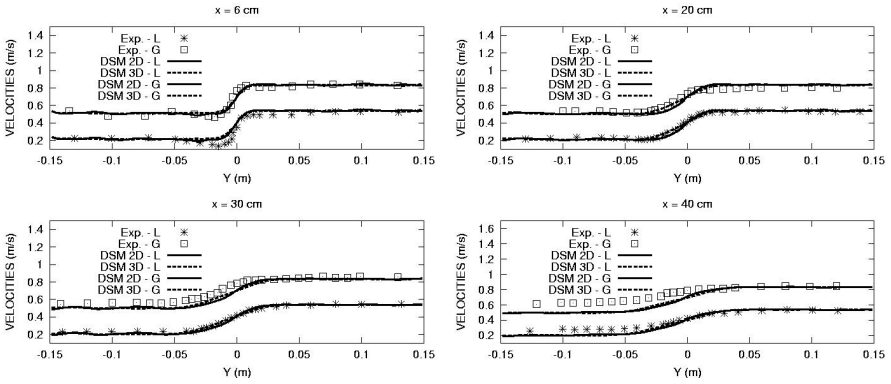

Figure 3.12 Two- and three-dimensional time-averaged liquid and gas velocities

of void fractions reported in Fig. 3.13 is consistent with the discussion in connection with the mean velocities in the sense that only minor differences are perceptible in the two simulations. Also, the peaks at $x = 6cm$, where the flow is still affected by the proximity of the injection, are misrepresented by the same amount. Again, one notes that the agreement between the simulations and measurements is rather good, but slight deviations start to appear further downstream.

3.5.3 On the SGS modelling

The rms streamwise velocities resulting from the standard SGS model and the DSM variant combined with equation (3.29) are plotted in Fig. 3.14 at two cross-flow locations. The figure includes results of both two- and three-dimensional simulations; the latter are spatially averaged over each cross-flow plane. The upper two panels compare the two- and three-dimensional simulations obtained from the standard SGS model with $C_s = 0.12$. Unlike the time-averaged quantities, the panels show a surprising underestimate of the rms velocities in the three-dimensional calculation, but more in the slow channel (left) than in the high speed one. This result also supports what has been observed previously in connection with time-averaged predictions, in that there is evidence for an uncertainty regarding the experimental data at the slow channel. It may also be true that the dissipative behaviour of the standard model affects the results in the low speed region more than in the high speed one. The lower two panels indicate that the more elaborate DSM model grossly underpredicts this turbulence quantity, in particular away from the zone of strong shear. Comparison indicates that results are actually worse when the flow is simulated in three dimensions. Again, the fact that the difference is more pronounced in the slow channel suggests that the experimental inflow conditions are not well reproduced, in particular the profile of void fraction and turbulence intensity. The other source of error may be related to the truncated size of the computational domain, in particular in the third direction, which was taken too narrow, and the boundary conditions applied at the outer boundaries. Results (not included here) of the length scale obtained with the dynamic procedure employed in three dimensions show that the parameter C_s is strongly overpredicted compared to the Smagorinsky value, while in two dimensions its value was always close to 0.12.

The predictive performance of both SGS models is discussed within the context of Fig. 3.15, displaying both time-averaged and rms quantities obtained in three dimensions. The models result in almost identical time-averaged velocities and volume fractions, in accordance with the data. In line with previous discussions, the DSM approach of Germano underpredicts the fluctuating velocity field compared to the standard model, in particular away from the mixing zone. The fact that results of both SGS models significantly deviate from the data reinforces the conclusion that turbulence is more sensitive to the computational details, including the size of the domain and the inflow conditions, than to the subgrid-scale modelling. The new proposal for bubble-induced turbulence modulation seems not to produce the expected results, probably because the dispersed phase in this case is very dilute, so that its role is minimized in the turbulence dissipation mechanism at the SGS level. The turbulence energy spectrum shown in Fig. 3.9 has already shown evidence for little impact of the dispersed phase on the liquid. On the other hand, because the computational domain was not sufficiently dimensioned, the large scales were not adequately resolved, in which case the DSM model combined with the model for bubble-induced dissipation turns out to be more dissipative than the standard model. In this case, modifying the eddy viscosity via equation (3.29)

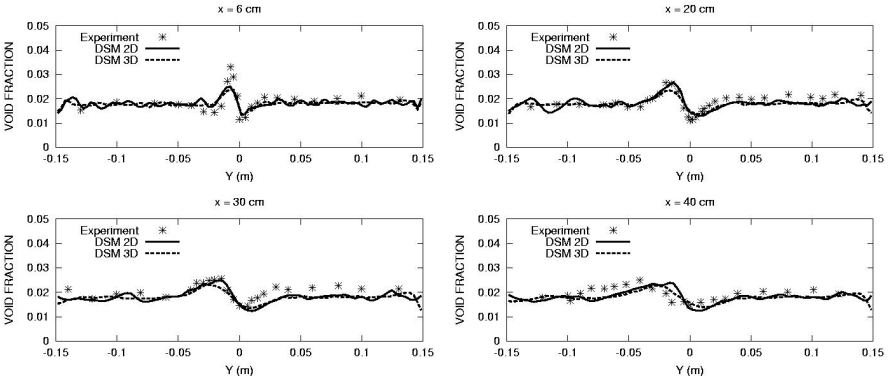

Figure 3.13 Two- and three-dimensional time-averaged void fractions

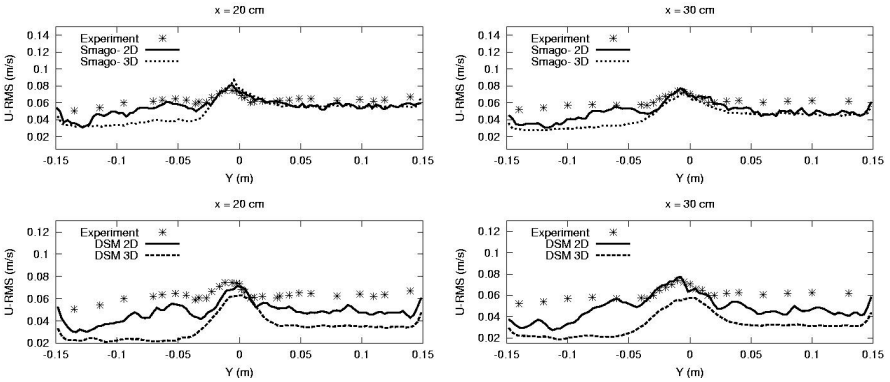

Figure 3.14 Two- and three-dimensional u_{rms} velocities obtained with two SGS models

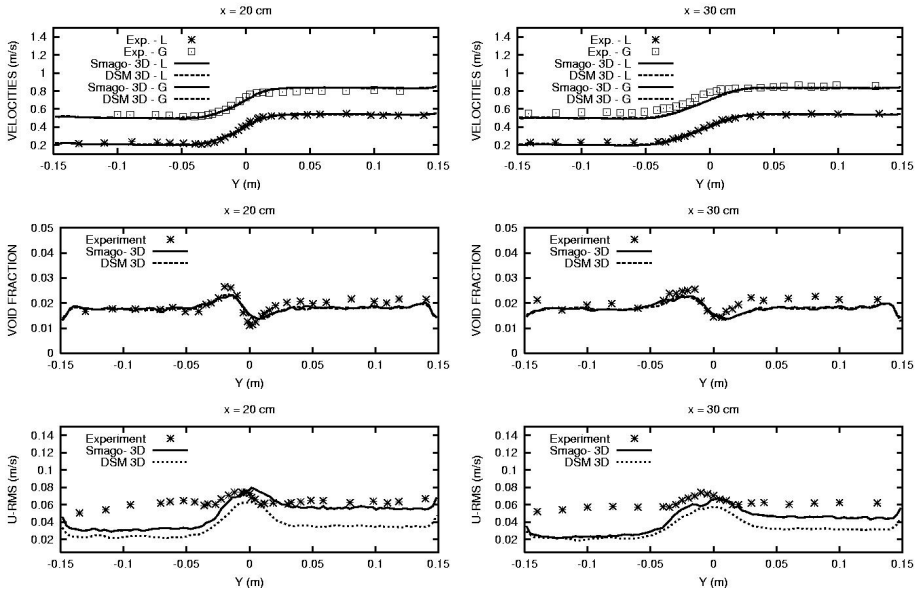

Figure 3.15 Time-averaged velocity and void fraction profiles and rms quantities obtained with two SGS models

corresponds to a counter effect. This issue is clearly not yet conclusive and needs further clarification through a systematic sensitivity study focusing on the influence of the computational domain.

3.6 CONCLUDING REMARKS

Large-eddy simulation of an isothermal, highly turbulent, vertical shear layer laden with bubbles at very low void fraction has been performed. The method is based on the filtered multi-fluid equations derived by the application of a single component-weighted volume-averaging process. The subgrid-scale modelling is based on the Smagorinsky kernel in both its original form and in the form of the dynamic procedure of Germano, in which the length scale is inferred from the resolved scale motion. The test case was investigated experimentally by Masbernat *et al.* (1997). Although the experiment is well documented, most of the available data are time-averaged quantities, and little information is given on turbulence statistics that could be utilized for validating the proposed model for bubble-induced turbulence.

Parameter studies have been undertaken to determine the effects of the ratio of the cut-off filter to the length scale characteristic of the dispersed phase, the influence of the lift coefficient, the performance of the subgrid-scale models, and the importance of inlet turbulence levels. Two-dimensional calculations have revealed that for an inlet void fraction of about 2%, the optimum grid concentration has to be such that the ratio of the cut-off filter to the bubble diameter is ≈ 1.5. A good compromise can be obtained with a lift coefficient of $C_L^* = 0.25$, and the Smagorinsky model performs quite well and gives results comparable to those of the dynamic procedure of Germano.

The simulations have also shown that the flow is statistically two-dimensional; two- and three-dimensional time-averaged quantities were virtually the same. Three-dimensional simulations have also confirmed that the dynamic approach of Germano does not perform better than the Smagorinsky model. The DSM strategy has even proved disappointing in predicting turbulence intensities, most probably because the dimensions of the computational domain were not adequate. Modifying the SGS model to account for bubble-induced dissipation did not bring the expected results, probably because at low void fractions the bubbles only have a minor influence on the turbulence level in the liquid, as revealed by the energy power spectrum. It is suspected that modifying the shear-induced dissipation may result in a counter effect if the large-scale motions are not rigorously resolved. More important to note is that in contrast to single-phase flow experiments (including DNS) there is an inherent difficulty in measuring turbulence quantities in two-phase flows, making direct meaningful comparison with the calculations difficult. In this respect, the data taken for validation in this work present obvious uncertainties. Finally, this novel LES strategy for multi-fluid components, supposed to surpass the conventional RANS approach, needs to be further validated before applying it to flows where the overall motion is buoyancy driven, such as in bubble plumes.

4

Interface Turbulence Interactions in Bubbling

Le contenu de ce Chapitre est extrait du papier *Interface–Turbulence Interactions in Large-scale Bubbling Processes*", soumi a *Phys. of Fluids*, 2004 by Petar Liovic et Djamel Lakehal, 2004.

4.1 ABSTRACT

The paper introduces a novel Large–Eddy Simulation (LES) approach based on the component–weighted filtered single–fluid equations for incompressible, multi–fluid flows involving immiscible fluids. The method has been applied to a turbulent bubbling process driven by constant flow–rate downward injection of air through a pipe into a water pool at $Re_{pipe} \approx 17,000$. A moderate–sized mesh and domain decomposition–based parallelism were used for a $O(10^6)$–time–step computation to extract turbulence statistics representative of fully–developed flow. The bubbling exhibits a substantially cyclic transient behaviour, as well as irregular oscillation between symmetric and lop–sided bubble growth. These dominant flow events, including the $7-8$ Hz bubbling frequency, are predicted in accord with experiment. Turbulence is found to assume its highest intensity in the bulk of the gas flow, and to decay as the interface is approached, in much the same way as in wall–bounded flows. An effective -5/3–slope kinetic energy decay rate prevails throughout a large portion of the flow, but a substantial bubble–induced -8/3 energy decay rate is found to prevail in buoyancy–driven flow regions. Distinct regions of turbulent flow prevail: shear flow associated with "air jetting" in the area just below the pipe tip, buoyancy–driven flow away from the jetting region, and a third region of vigorous bubble break–up a couple of pipe diameters above the tip. Cascading of turbulent kinetic energy is also seen to be accompanied by an instability–induced linear cascading of interface length scales (i.e. azimuthal modes), transferring energy from the most unstable mode to the smallest interface deformation scales, referred to as interface wrinkling. The LES also shows the out–scatter of energy from the large–scale gas–side vortices down to interface wrinkling scales, suggesting the existence of a strong correlation between turbulence and interface deformations. This has been further confirmed by examining strain and vorticity interface–curvature autocorrelations.

4.2 INTRODUCTION

Bubbling mechanisms and induced mixing occur in a large range of multi–phase flow systems, with a significant subset of these processes featuring large bubble injection to sustain the flow. This type of flow is used in a broad range of engineering applications, including the aeration of pools to sustain organisms in waste–water treatment operations, gas–liquid separation in process industries, emergency venting passive safety systems in nuclear power plants, and gas injection for chemical processes in bath smelting. These flows, driven by high–volume, moderate

velocity gas injection into liquid baths, feature flow that is often chaotic and turbulent, and can also feature a wide spectrum of interfacial length scales. Common configurations for gas injection in engineering applications include bottom injection upwards through orifice plates and nozzles, side injection, and top injection downwards through pipes.

Bubble motion in bubbling processes has, for the most part, been inferred from idealized flows such as single bubble formation and the rise of single or pairs of bubbles. Additionally, the effect of this bubble motion on liquid phase bulk flow has been the subject of simplified studies involving a homogeneous liquid phase and a highly inter–dispersed bubbly phase. For turbulent bubbling processes, relatively little has been done so far experimentally or numerically to elucidate the relative importance of single bubbling events in arbitrary bubbling processes, and the mechanisms promoting or suppressing certain sequences of events. In bubble rise, Bunner & Tryggvason (2003) have simulated the rise of 27 identically–sized bubbles in a periodic cell in homogeneous flow, in what they describe as Direct Numerical Simulation (DNS) of bubbly flow. The behaviour of deformed and spherical bubbles differed significantly in terms of alignment of bubbles and their dispersion. Deformed bubbles were associated with significantly different flow structures as compared to spherical bubbles, but modified energy decay due to pseudo–turbulence was ubiquitous. van den Akker (2003) investigated various experimental and numerical databases to identify coherent structures in multi–phase flows, with a focus on bubble column flows. In that paper, "phase locking" was proposed as a possible cause of coherent structure generation, and an analogy was drawn between the von Karman vortex sheet behind a blunt body and the staggered arrangement of vortices in the liquid phase on either side of a meandering bubble plume.

A feature of the flow in bubbling processes that, to date, has been beyond the consideration of simulation models, is bubble break–up. In a study of the oscillation and break–up of bubbles in a turbulent field in micro–gravity, Risso & Fabre (1998) demonstrated turbulence to be potentially responsible for the deformation and break–up of individual bubbles. Kolev (1993) reviewed the numerous models for bubble break–up, in particular those based on a force balance between shear stress around the bubble and surface tension. In particular, the force balance concept forms the basis of the theory of Kolmogorov (1949); Hinze (1975), postulating a critical Weber number for bubble break–up. The theory identifies resonance oscillation, in which eddy excitation and bubble oscillation are in phase, as an additional mechanism for bubble break–up. Martinez-Bazan *et al.* (1999*a*,*b*) injected air bubbles into fully developed turbulent water flow, and measured the resulting bubble size probability density function (p.d.f.). Bubble break–up frequency was determined as a function of bubble size and a critical diameter, depending on the surface tension and the dissipation rate. Break–up frequencies were shown to scale differently for large bubbles, as compared to bubbles sized in the order of the critical diameter. This result led to the identification of two distinct bubble size regimes. In addition, Martinez–Bazan *et al.* proposed statistical models describing the size p.d.f. of the daughter bubbles resulting from break–up.

A common feature of the studies discussed above is that turbulence is active in the liquid phase flow only, because the dispersed phase is formed by small size bubbles. Thus, extending the relevance of these studies to large–scale bubbling processes cannot be justified. Liquid–side turbulence in bubbly flow is important (for mixing) in regions far away from the source of bubble generation, where upstream flow events such as bubble formation and detachment can be ignored. In reality, vigorous break–up of large bubbles is a precursor to idealized bubbly flow. Additionally, in the case of bubbling processes, the establishment of a turbulent liquid–side flow is necessarily the result of a turbulent jet flow issuing from the pipe. Much of the analytical description of bubble formation is too simplistic for meaningful extension to turbulent large–scale bubbling processes, and interface/turbulence interactions as well as the physics involved in the break–up process are poorly understood. This means that a description of bubbling by means of simplified models for bubble formation, individual bubble–rise, bubble break–up, etc., will not properly represent such processes.

Traditionally, turbulent multi–phase flows have been simulated assuming inter–penetrating media, using the averaged "two–fluid" representation for void fraction distribution and the Reynolds–averaged Navier–Stokes (RANS) framework for turbulence modeling. In comparison between topology and turbulence modeling, the two–fluid and RANS approximation approaches are equivalent, in that interface and turbulence structure are not generated as part of the solution, but rather modeled. For the purpose of correctly capturing interface–turbulence interactions, phase–averaging in the two–fluid formalism is not ideal, because interface jump conditions cannot be correctly captured if phases are considered to be homogeneously mixed and inter–penetrated. Fulgosi *et al.* (2003) showed, using their pseudo–spectral boundary–fitting method, that the correct capturing of interface–turbulence interactions in counter–current stratified flow requires careful implementation of jump conditions. In the case of non–dispersed, interfacial, multi–fluid flows, interface location can be tracked only by means of the single–fluid representation. Assuming that large interfacial length scales prevail in the bubbling processes (as will be demonstrated later), modern *interface tracking* methods are capable of providing accurate solutions for interface dynamics

within finite–volume/difference simulations, with the premise of tackling interface–turbulence interactions in flow scenarios much more complex than that considered by Fulgosi *et al.*.

In this paper, we introduce a new LES approach for interfacial, turbulent multi–fluid flows, based on the filtered single–fluid Navier–Stokes equations, in which the super–grid interface kinematics and turbulence are fully resolved. The description is more detailed than in the original contribution (Liovic *et al.*, 2003). To the best of our knowledge, this study represents a first attempt at capturing gas–side turbulence and interface/turbulence interactions, knowing that at this stage it is impossible to resolve the entire spectrum of turbulence and interfacial deformation scales. LES is therefore adopted for capturing turbulence within the framework of the single fluid formalism. We first introduce the filtered governing equations within the single–fluid formalism, and the resulting sub–grid scale terms that need to be modeled. Specific issues in translating the formalism into robust numerics are also addressed. Our main purpose is to demonstrate the feasibility of a combined interface tracking/LES approach for flows that cannot be tackled otherwise. The method is applied to a specific turbulent large–scale bubbling process. Results are discussed and compared to the available data from the experiment of Meier (1999*b*) and Meier *et al.* (2000).

4.3 NUMERICAL METHOD

4.3.1 The filtered one–fluid equations

For flows consisting of immiscible fluid parcels of length scales larger than the grid size, phase inter–penetration is not presumed. Rather, jump conditions between the two phases are directly incorporated, such that the separate equations for each phase k can be replaced by a single set of equations describing the system. This is the starting point of the simplification from a multi–field to a single–field representation of the flow, in which the phases are identified locally using the indicator (or *color*) function C. In the continuous limit, color function C is the Heaviside function

$$C = \begin{cases} 1 & if\ \mathbf{x}\ occupied\ by\ phase\ k = G \\ 0 & if\ \mathbf{x}\ occupied\ by\ phase\ k = L \end{cases} \tag{4.1}$$

such that the C–weighted local density defined by

$$\rho = C\rho^G + (1 - C)\rho^L \tag{4.2}$$

reduces to liquid density ρ^L or gas density ρ^G. Separate species mass conservation equations can then be described using the local density ρ:

$$\frac{\partial \rho}{\partial t} + \frac{\partial \rho u_j}{\partial x_j} = 0\ . \tag{4.3}$$

Assuming incompressibility of each fluid, the continuity equation

$$\frac{\partial u_j}{\partial x_j} = 0 \tag{4.4}$$

is valid as a statement of volume conservation in the single–field representation.

For momentum conservation, we propose a local viscosity μ that similarly takes the form of equation 4.2. The constitutive relation between the rate–of–strain tensor S_{ij} and viscous stress tensor σ_{ij} presumes both fluid species to be Newtonian, i.e.

$$\sigma_{ij} = 2\,\mu S_{ij}, \qquad \text{with} \qquad S_{ij} = \frac{1}{2}\left(\frac{\partial u_i}{\partial x_j} + \frac{\partial u_j}{\partial x_i}\right). \tag{4.5}$$

The single–field momentum equations may thus be written as

$$\frac{\partial (\rho u_i)}{\partial t} + \frac{\partial (\rho u_i u_j)}{\partial x_j} = -\frac{\partial p}{\partial x_i} + \frac{\partial \sigma_{ij}}{\partial x_j} + \rho g_i + \gamma \kappa n_i\ . \tag{4.6}$$

The surface tension term here is $\gamma\kappa n_i$, where γ is the surface tension, κ is the interfacial curvature, and n_i is the unit interface normal, while p denotes incompressible total pressure.

The one–field equations (Eqs. 4.2–4.6) are a micro–scale description of immiscible, incompressible, Newtonian two–phase flow. The macro–scale description (at the super–grid level) of the flow suggests all dependent variables

contain sub–grid scale (SGS) components $f' = f - \overline{f}$, where the resolvable quantities $\overline{f}$ are obtained by convolution using a spatial filter G:

$$\overline{f}(x) = G \otimes f = \int_D G(\mathbf{x} - \mathbf{x}') f(\mathbf{x}') d\mathbf{x}' \,, \tag{4.7}$$

verifying the normalization property

$$\int_D G(\mathbf{x} - \mathbf{x}') d\mathbf{x}' = 1 \,. \tag{4.8}$$

The filtered phase indicator function, $\overline{C} = G \otimes C$, is subsequently interpreted as a volume or mass fraction indicator function. The derivation of the filtered one–fluid equations is based on the use of the Component–Weighted Volume Averaging (CWVA) procedure (Lakehal *et al.*, 2002*b*). In the filtered two–fluid formulation of the momentum equations that was the subject of Lakehal *et al.* (2002*b*), the separate solutions generated for each phase k were weighted in inter–penetrating–phase regions by the resolved volume fraction. In the single–field description of the flow, the coupling of $\overline{C}$ to the flow solution is instead represented through the local density (equation 4.2). Therefore, as a basis for CWVA in the single–field formulation, it is most appropriate to use the local density ρ, which in essence is analogous to Favre averaging for compressible flows:

$$\widetilde{f}(\mathbf{x}) = \frac{\overline{\rho(\mathbf{x}) f(\mathbf{x})}}{\overline{\rho(\mathbf{x})}} \,. \tag{4.9}$$

In using CWVA, the property established by Leonard (1974) that filtering and differentiation commute can be extended to the multi–fluid flow context, too, provided the discretization is performed over uniform meshes. Applying relation 4.7 to the local density yields

$$\overline{\rho} = \overline{C} \rho^L + (1 - \overline{C}) \rho^G \,. \tag{4.10}$$

For mass conservation, filtering of equation 4.3 via relation 4.7 then performing CWVA yields

$$\frac{\partial \overline{\rho}}{\partial t} + \frac{\partial \overline{\rho} \widetilde{u}_j}{\partial x_j} = \varepsilon_c^\rho \,, \tag{4.11}$$

where ε_c^ρ denotes the commutation errors, which will be neglected henceforth. By virtue of incompressibility of the flow on each side of the interface and using relation 4.10, equation 4.11 reduces to the system of filtered continuity and interface topology equations, in which the local density has been eliminated:

$$\frac{\partial \widetilde{u}_j}{\partial x_j} = 0 \tag{4.12}$$

$$\frac{\partial \overline{C}}{\partial t} + \widetilde{u}_j \frac{\partial \overline{C}}{\partial x_j} = 0 \,. \tag{4.13}$$

Performing the convolution product on the momentum equations and applying the local density based CWVA yields

$$\begin{aligned} \frac{\partial \overline{\rho} \widetilde{u}_i}{\partial t} + \frac{\partial}{\partial x_j} \left(\overline{\rho}\, \widetilde{u}_i \widetilde{u}_j \right) &= -\frac{\partial \overline{p}}{\partial x_i} + \frac{\partial \widetilde{\sigma}_{ij}}{\partial x_j} + \overline{\rho} g_i + \gamma\, \overline{\kappa}\, \overline{n_i} \\ &\underbrace{-\frac{\partial \tau_{ij}}{\partial x_j}}_{I} + \underbrace{\varepsilon_c^u}_{II} + \underbrace{\varepsilon_d}_{III} + \underbrace{\varepsilon_\gamma}_{IV} \,, \end{aligned} \tag{4.14}$$

where we have made use of the identity

$$\varepsilon_d \equiv \frac{\partial}{\partial x_j} \left[\overline{\sigma}_{ij} - \widetilde{\sigma}_{ij} \right] \,, \tag{4.15}$$

and introduced the local (phase–specific) SGS tensor, defined as

$$\tau_{ij} \equiv \overline{\rho} \left(\widetilde{u_i u_j} - \widetilde{u}_i \widetilde{u}_j \right) \,. \tag{4.16}$$

Term II designates the sum of errors which appears if commuting between the filtering and differencing operators were not assumed explicitly. Similar to ε_d, the last term (IV) appears as a non–linearity error, which vanishes away from the interface, i.e.

$$\varepsilon_\gamma = \gamma\, \overline{\kappa\, n_i} - \gamma\, \overline{\kappa}\, \overline{n_i} \,. \tag{4.17}$$

It denotes the non–resolved counterpart of surface tension, which has been washed out by filtering. The SGS modeling of non–resolved interfaces is less clear than that of the non–resolved turbulence. In turbulence, the smallest length scale of the problem is the Kolmogorov length scale. In contrast, the non–resolvable interfacial scales are difficult to characterize, even if there exists an approximate scale based on the critical length (l_c) determined from the balance between surface forces and local turbulence intensity. However, the main reason for not modeling the SGS interfacial scales is that the super–grid surface tension force itself cannot be computed accurately enough with current schemes. Surface tension discretization schemes often lead to parasitic currents – a non–physical numerical forcing that, in a range of multi–phase flows, can be as great a contribution to a velocity–field update as advection–scheme numerical dissipation. In other words, it does not suffice to again split the curvature or the normal vector into resolved and SGS components – ultimately giving rise to extra unresolved quantities – before clarifying the interaction mechanisms between non–resolved turbulence and non–resolved interfacial scales.

Having introduced relations for closure of the momentum equation, the filtered single–fluid equations for turbulent, immiscible, multi–fluid flow read:

$$\frac{\partial \widetilde{u}_j}{\partial x_j} = 0 \tag{4.18}$$

$$\frac{\partial \overline{C}}{\partial t} + \widetilde{u}_j \frac{\partial \overline{C}}{\partial x_j} = 0 \tag{4.19}$$

$$\frac{\partial \overline{\rho}\widetilde{u}_i}{\partial t} + \frac{\partial}{\partial x_j}\left(\overline{\rho}\,\widetilde{u}_i\widetilde{u}_j\right) = -\frac{\partial \overline{p}}{\partial x_i} + \frac{\partial \widetilde{\sigma}_{ij}}{\partial x_j} + \overline{\rho} g_i + \gamma\,\overline{\kappa}\,\overline{n_i} - \frac{\partial \tau_{ij}}{\partial x_j} + \sum \varepsilon\,, \tag{4.20}$$

where ε consists of all the non–linearity and commutation errors that arise from the filtering. The local density is determined from expression 4.10, and similarly for the local viscosity.

4.3.2 Numerical Schemes

4.3.2.1 Velocity versus momentum formulation Having presented the filtered equations for immiscible, incompressible two–fluid flow within the single–field framework, we note that the numerical method that was implemented features spatial discretization based on a momentum equation that differs slightly from filtered governing equation (4.20). In practice, instead of using the momentum formulation as presented above, the commonly–used velocity formulation was preferred,

$$\frac{\partial \widetilde{u}_i}{\partial t} + \frac{\partial}{\partial x_j}\left(\widetilde{u}_i\widetilde{u}_j\right) = -\frac{1}{\overline{\rho}}\frac{\partial \overline{p}}{\partial x_i} + \frac{1}{\overline{\rho}}\frac{\partial \widetilde{\sigma}_{ij}}{\partial x_j} + g_i + \frac{1}{\overline{\rho}}\gamma\,\overline{\kappa}\,\overline{n_i} - \frac{1}{\overline{\rho}}\frac{\partial \tau_{ij}}{\partial x_j} \tag{4.21}$$

where the non–linearity and non–commutativity errors $\sum \varepsilon$ have been neglected. This alternative formulation was previously adopted in (Meier, 1999*b*; Meier *et al.*, 2000; Liovic *et al.*, 2001, 2002)) to promote robustness for high density–ratio flows. Use of the velocity formulation in the current work comes at the cost of a departure from rigorous momentum conservation.

4.3.2.2 SGS modeling In the present study, centered differencing is used for momentum advection, and stability is preserved with the help of the dissipation contribution from explicit SGS modeling. The standard Smagorinsky–kernel based SGS model was employed using a value of the damping constant C_s = 0.1 – a value inferred from earlier LES computations of a turbulent bubbly flow (Lakehal *et al.*, 2002*b*) using the dynamic approach (DSM) of Germano *et al.* (1991). The DSM approach could not be used because, in contrast to mixing layers and wall bounded–flows, there is no homogeneous direction over which the constant C_s could be averaged in bubbling processes. Three–dimensional averaging of C_s would lead to very small values because turbulence is essentially concentrated in the bubbling region, as will be shown later. Turbulence near–wall damping was achieved by incorporating the van Driest expression into wall functions. Note finally that for interfacial flows separated by well–defined continuous fronts, any well–established SGS model for single–phase flow could be applied, since the Reynolds stresses are density–weighted for each phase. Both the class and width of the space filter could vary from one phase to the other, too. Models more elaborate than eddy viscosity–based SGS models could also be employed, including, for example, those based on the deconvolution principles. However, the fact that the lighter phase perceives interfaces as evolving rigid boundaries (Fulgosi *et al.*, 2003) suggests that a near–interface treatment is required, in a similar manner to wall flows. Interface functions are thus needed, which could be incorporated into models based on distance function to the interface.

4.3.2.3 Interface Tracking

Vigorous bubbling imposes special requirements for interface tracking methods, in that any particular method must robustly and accurately capture all stretching, fragmentation and coalescence phenomena induced by gas injection. The range of interface length scales and high–curvature interfaces generated in bubble break–up, liquid elongation, bubble coalescence and other phenomena represent a major challenge to particle–based and level–set methods, in that rigorous local volume conservation becomes necessary, and the breaking of a closed surface into multiple closed surfaces must be captured. Ultimately, volume tracking (or Volume–of–Fluid (VOF) methods) based on piecewise planar interface reconstruction (commonly known as PLIC–VOF (Piecewise Linear Interface Calculation) (Kothe & Rider, 1997)) is currently the best interface tracking scheme for robustly and accurately tracking the kinematics, creation and destruction of all resolvable interfaces in such flow problems. In the implementation used here, the 3D PLIC–VOF scheme features piecewise planar interface reconstruction based on the Youngs gradient (Youngs, 1982), and on direction splitting to extend one–dimensional flux updates to 3D (i.e. a three–step update of $\overline{C}$). With this scheme, bulk–property distributions such as density and viscosity are geometrically extracted from the interface reconstructions. The location of the interface described by the color function is used to model surface tension, using the fully kernel–based variant of the Continuum Surface Force (CSF) method (Brackbill *et al.*, 1992).

4.3.2.4 Other numerics and code issues

Meaningful LES requires long computational times, and as such simulating all the transients in interface tracking–based LES requires adequate computing power. The computer code employed here simulates transient 3D flows in complex geometries on distributed–memory platforms, with MPI–facilitated parallelism based on domain decomposition. The flow solver is based on a standard projection method and second–order Euler time–stepping (Liovic *et al.*, 2002). Using domain decomposition, the computation is subdomain–based, thus helping achieve scalable parallel performance. An additional contribution to scalable parallel performance is provided by a Krylov subspace–based Poisson solver featuring Additive Schwarz preconditioning, in which rudimentary interface conditions between sub–domains are used in order to minimize interprocessor communication.

4.4 AIR VENTING THROUGH A DOWNWARD–FACING PIPE

In the bubbling process investigated here, air is vented downwards through a vertical pipe into a water bath. The pipe is referred to as a "downcomer" in the thermal hydraulics lexicon and as a "lance" in extractive metallurgy. Previous to this work, Hirt & Nichols (1980) had considered this problem with a weak–compressibility hydrodynamics solver, but as a demonstration application, without providing enough insight into the phenomena and physics of the flow. In more recent studies, Meier (1999*b*); Meier *et al.* (2000) and Liovic *et al.* (2001, 2002) have had success in predicting this class of flow using VOF under laminar flow conditions. This flow has been deliberately selected for having dual dynamical aspects: the inertia–dominated jetting from the pipe tip is in the opposite direction to the buoyancy force associated with free bubble rise, such that the prevailing flow physics can be distinguished to a substantial extent. From the turbulence point of view, the presence of the pipe wall results in shear flow that is further complicated by the dynamics associated with a highly deformable interface. From the interface dynamics point of view, the presence of the pipe obstructing the detachment and rise of formed bubbles results in a variety of phenomena, e.g. instability of annular bubbles and the formation of vortex rings taking the form of "mushroom–cloud" bubble inversions (Meier, 1999*a*).

4.4.1 Problem Setup

To correspond with the experiments performed by Meier *et al.* (2000), the computational domain of height and breadth $450\ mm$ was discretized using an orthogonal, non–uniform 64^3 mesh. The pipe (inner diameter $50\ mm$, outer diameter $72\ mm$), was centrally located, with its tip $180\ mm$ above the bottom of the domain. The xy–plane (where z is vertical) was refined in a "core bubbling " region ($225\ mm\ \times\ 225\ mm$) using spacing corresponding to a 96×96 mesh, and the pipe diameter was resolved by 10 cells. Except for the inflow area, the top boundary was represented as an outflow boundary. Free–slip boundary conditions were applied to the bottom surface and to the vertical planes of the domain.

In the present study, air venting occurs at $10\ l/s$, and is not choked i.e. the injection flow–rate is constant. This is a particular case documented by Meier *et al.*. The Reynolds number of the pipe flow is 17,000. Within the range of air venting flow rates considered in Meier (1999*b*), the $10\ l/s$ case represents a transition between lop–sided and symmetric bubble rise, as well as between laminar and turbulent gas–side flow. Gaussian perturbations were

superimposed on the initially quiescent bulk flow, providing a turbulence intensity of 0.5 percent relative to the mean inflow velocity. Simulations were performed on a 16–CPU parallel computer, using a Courant number of 0.2 and signal sampling at $1000\ Hz$.

	Simulation	Experiment
First bubble spread at tip level (mm)	48	45
Bubbling frequency (Hz)	7	7

Table 4.1 Measurements generated from simulation and experiment of the 10 l/s air venting experiment of Meier (1999*b*); Meier *et al.* (2000), during start–up and in the establishing of steady–state bubbling.

4.4.2 Transient large–scale bubbling phenomena

Figure 4.1 shows sample frames of bubble interfaces captured during the simulation. For qualitative comparison, the figure also shows sample frames of bubble surfaces captured on video at the same flow rate. Noteworthy phenomena include almost symmetric bubble growth and rise, "fingering" of the upper bubble surface during rise, and lop–sided bubble detachment and free–rise. The simulation of the observed bubble fragmentation demonstrates the ability of VOF to robustly capture the most challenging interface kinematics in a realistic manner, even down to generating and preserving the satellite bubbles.

From commencement of air venting, the frames presented in Figure 4.1 correspond to a time interval of $1.1\ s$. Of the $10\ l/s$ Meier experimental frames shown in the figure, the first two occur within the simulated time interval, while the others correspond to steady–state bubbling beyond this interval. Steady–state bubbling from the tip is established early on in the $1.1\ s$ interval; by the end of the simulated interval, $O(10^1)$ bubbles have grown, detached and risen away from the pipe tip. Beyond the growth of the first bubbles (start–up), the data within the envelope of the bubble plume is representative of statistically steady flow, and time–averaged data in this envelope is representative of ergodic data. One feature of the flow within the initial $1.1\ s$ interval that is not sustained into the long–term statistically steady flow is the presence of a low–concentration dispersion of entrained bubbles well below the bubble plume envelope of steady–state venting. Due to the surge of the first jet into an initially quiescent bath, this dispersion has little effect on the flow associated with the bubble plume above it, and the region deep below pipe tip level is of little interest in the current study.

The transitional nature of the bubbling in the $10\ l/s$ air flow–rate case is shown in Figure 4.1. The first visible transition shown in the experimental frames is that between symmetric rise of the growing bubble and lop–sided rise. The second visible transition relates to interface wrinkle scales covering the majority of the bubble surface, with transition between smooth interface dominance and chopped–up interface dominance. The frames in Figure 4.1 show that transitioning of both types is captured in the simulation. Compared to experiment, a larger pipe–thickness–to–diameter ratio is used in the simulation, and is accompanied by a more substantial intrusion effect that promotes lop–sidedness in bubble growth. The simulation correctly reproduces this. Transitioning from small length–scale wrinkles to large length–scale smooth surfaces is also faithfully captured in the simulation. Increased resolution would promote the capturing of even more interface wrinkle scales, at both ends of the spectrum, such that the current difficulty in regaining the full smoothness of bubble surfaces would be ameliorated.

In the case of constant volumetric flow rate venting and away from the high–flow–rate end of the spectrum, Meier (1999*b*) found bubble growth to exhibit less distinguishable growth/detach patterns, and more a near–continuous escape of gas to the side. This lop–sidedness, faithfully captured in the simulation, was noted in the experimental work to be a factor that seriously complicates measurement of bubbling frequency. In such cases, pressure signal analysis was considered to be useless; bubble counting exclusively was used in experiment to determine the bubbling frequency in constant flow rate venting, and is therefore also used here. Table 1 shows the bubbling frequency extracted from the simulation matches the frequency captured in experiment for air–water systems (Meier, 1999*b*).

Given the nature of the video image database for the $10\ l/s$ case (Meier, 1999*b*), quantitative comparison for validation in the current study between simulation and experiment is best done using start–up data. Level measurements of the bubble's upper surface, and the maximal spreading of the growing bubble away from the outer pipe wall at tip level, were compared. The match of the upper–surface level was excellent over the entire time–history of start–up, while the maximal spreading of the bubble plume was overestimated by 7 percent. The

agreement shown here between simulation and experiment using three different measures for quantifying bubbling, even at the current mesh resolution, is a strong validation of our numerical method applied to the bubbling problem under investigation. The level of the lower bubble surface is not appropriate for use in quantitative comparison here, because the extreme fragmentation from the lower bubble surface, due to the surge of the initial jet, is poorly resolved

Another event observed but not documented here is the vigorous break–up of bubbles well above pipe tip level. This level is often at $\approx 5D_i$ above, where our characteristic length scale is the internal pipe diameter D_i. This break–up takes the form of a "mushroom cloud" – an abrupt inversion and radial expansion of the bubble plume, and resembles bubble swarming, i.e. massive fragmentation into smaller bubbles. This bubble swarming is captured in simulation, but we ignore this aspect of the flow here because of the close proximity of the outflow boundaries.

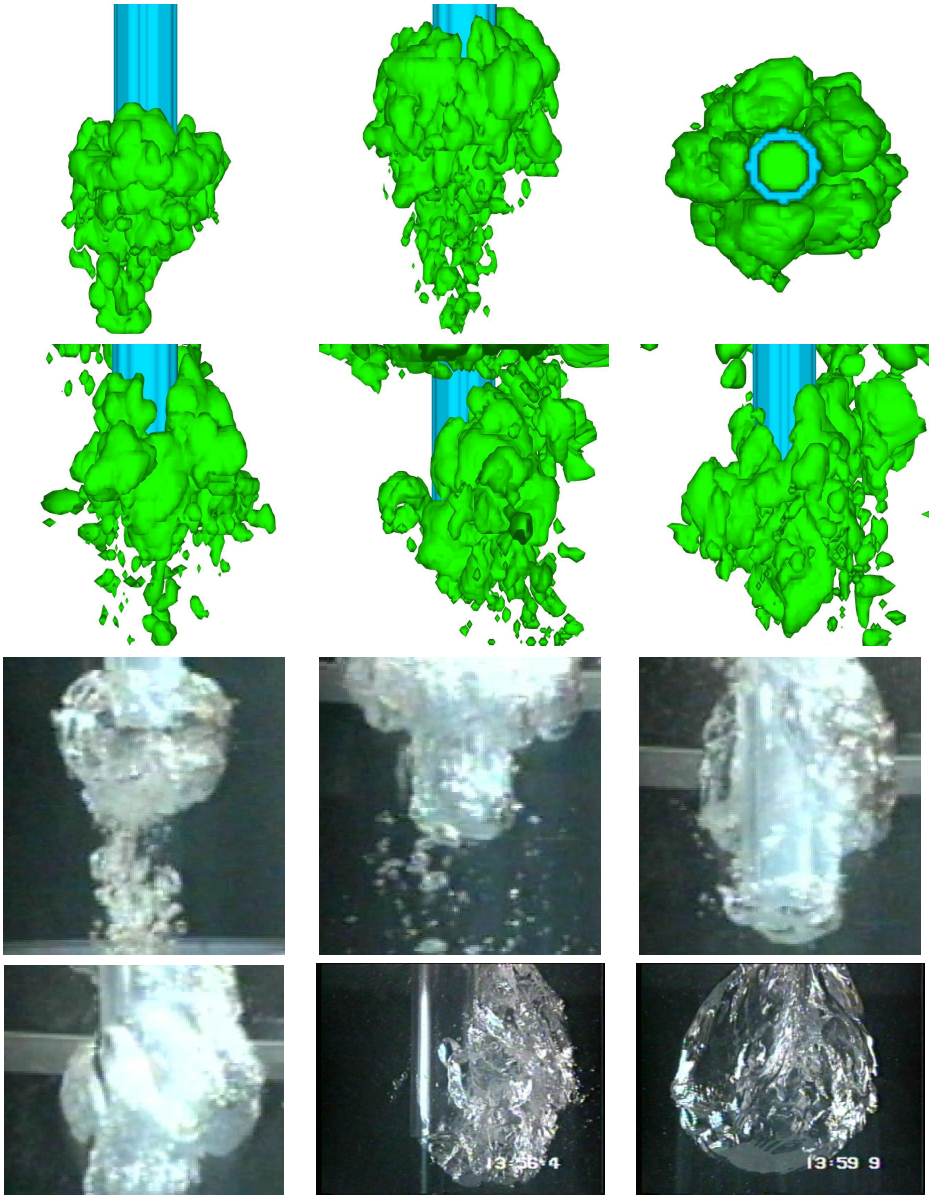

Figure 4.1 Frames of the bubbling resulting from air venting through a downcomer, for air flowing at 10 l/s into a water bath. First and second rows: simulation; third and fourth rows: experiment (from the work of Meier (1999*b*); Meier *et al.* (2000)). The first two experimental frames are captured within the simulated time frame simulated, while the other four frames are representative of steady–state operation. Experimental and LES animations of the flow can be found under: http://www.lkt.mavt.ethz.ch/cfmg/JET

4.4.3 Interfacial area evolution

The interfacial area and bubble volume were computed in a sub–domain excluding flow zones located above $z = 0.35\ m$, in order to avoid using unreliable sampling results in proximity to the outflow. Figure 4.3 shows (a) the bubble interfacial area, (b) the bubble plume gas volume, and (c) the plume surface–area/volume ratio, for the duration of the simulation. After the growth of the initial bubbles, the surface area exhibits a cyclic variation about a mean value, followed by a second surge near the end of the time interval. Large bubble volumes are seen to result from the more symmetric bubble growth events seen in Figure 4.1, while the other peaks coincide with more lop–sided bubble growth scenarios. Resemblance between the interfacial area signal and the bubble volume signal is apparent, with maxima, minima and inflections shown to be in phase and of similar magnitude relative to

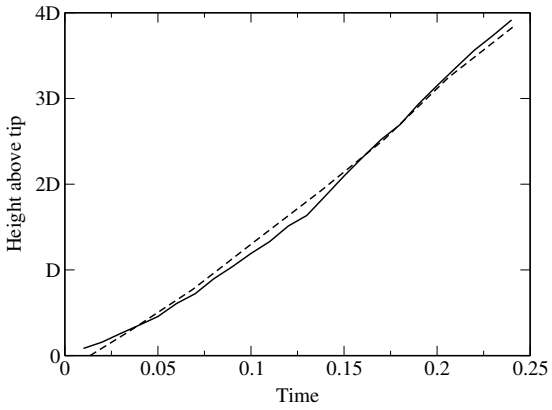

Figure 4.2 Transient behaviour of the level of upper bubble surface during start–up bubble formation and detachment for 10 l/s air venting: – – – – – refers to levels relative to the pipe tip obtained from the experiment, while ——— refers to results from the simulation.

the maxima of the first bubble. The interfacial area signal shows significant low–amplitude noise, as compared to the bubble volume signal.

The surface–area/volume ratio is at its lowest level in the early stages featuring a smooth–surfaced single growing bubble. Upon the establishment of steady–state conditions, the ratio converges to an average value of $\approx$ 200:1, with a relatively low standard deviation. Normalizing with the surface–area/volume ratio for a spherical bubble of constant diameter, this average value corresponds to a dispersion of spheres of diameter $\approx 6\overline{\Delta}$. Length $\overline{\Delta} = (\delta x \delta y \delta z)^{1/3}$ can be interpreted as the average resolvable length scale of the gas phase.

4.4.4 Interface/turbulence interactions

Figure 4.4(a) shows a profile through the axis of symmetry of the velocity vector map and interface location at a particular instant during the $10\ l/s$ simulation. The interaction between the interface and the large–scale structures formed in the gas phase is seen here. One form of such interaction is the formation of distinct lobes. Another feature shown by Figure 4.4(a), and even more clearly by Figure 4.4(b) (taken from a $16\ l/s$ simulation on a 96^3 mesh), is the existence of high–shear flow zones, that we have deduced to lay between the structures of the distinct lobes. High vorticities shown in Figure 4.5(a) are concentrated in the gas–side flow in the vicinity of the pipe tip, and some of the highest regions of vorticity indeed coincide with high–shear flow zones.

From comparing the 2D centre–plane plot of vorticity in Figure 4.5(a) to the corresponding interface profile of Figure 4.4(a), a damping of vorticity can be seen as the interface is approached from the gas side. This observation is consistent with conclusions drawn from DNS of counter–current stratified flow (Fulgosi, 2004). The contribution of the eddy viscosity from the SGS model, μ_T, to the total viscosity distribution, reveals that higher values coincide with high–vorticity gas–side flow regions. Locally higher values of μ_T in Figure 4.5(b) suggests that a considerable portion of the spectra has been washed out as a consequence of under–resolution of turbulence. The Smagorinsky SGS model used in the present work is also known to be overly dissipative and not to accommodate backscatter of energy, and is one contribution to the possibly high magnitudes of μ_T.

Figure 4.5(c)–(f) presents average and root–mean–square (rms) results of downward velocity and void fraction in the yz–plane through the centre of the pipe. The degree of asymmetry in these time–averaged results indicates that the actual simulation interval of $1.1\ s$ does not provide a satisfactory approximation to a long–time average (compared to single–phase channel flow), and suggests the need for even more computations to completely average out the asymmetries. The most intense velocity fluctuations are in the bubbling–jet area under the pipe tip, while a second area at $\approx 5D_i$ above the pipe tip coincides with the mushroom–cloud region.

More generally, areas of more intense velocity fluctuations coincide with the bubble plume, with gas–side turbulence intensity substantially greater than in the liquid. Away from the bubble plume, both in the pipe flow and the liquid–side flow, turbulence is low. Velocity fluctuations are an order of magnitude smaller in the liquid–side flow as compared to the gas–side flow, and μ_T/μ are $O(10) - O(10^2)$ smaller.

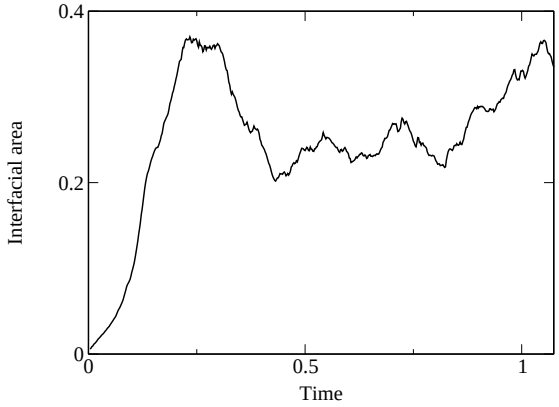

Fig. 2(a)

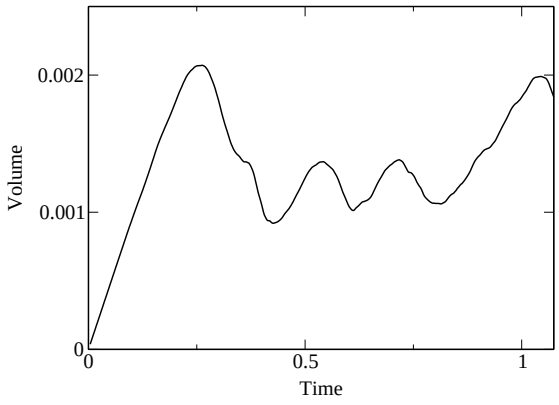

Fig. 2(b)

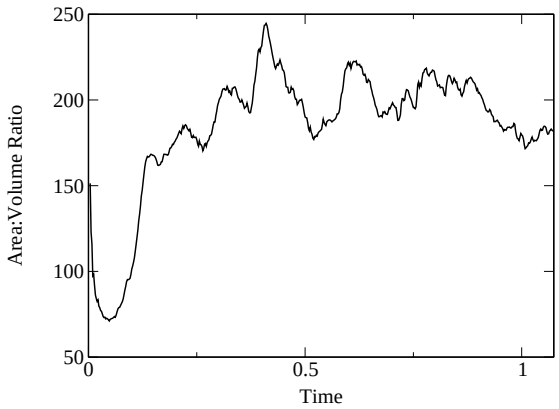

Fig. 2(c)

Figure 4.3 Time signals of bubble plume interfacial area, bubble plume volume, and the interfacial–area/volume ratio. The domain over which the volume and surface integrals are included is restricted, with the top 20 percent of the domain neglected to avoid contamination of results with near–outflow–boundary interface data.

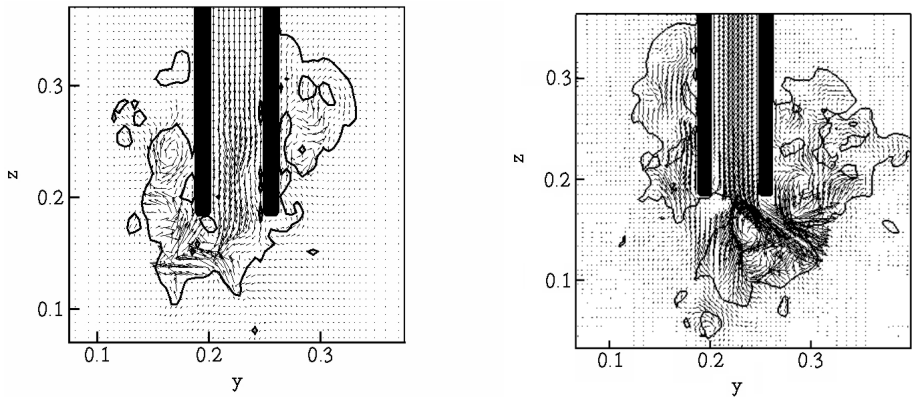

Figure 4.4 Plane interface locations and velocity vector maps at different instants: (upper panel) yz–plane for 64^3 resolution; (lower panel) for 96^3 resolution at a different flow rate ($16\ l/s$).

4.4.5 Coherent structures

The presence of the pipe and the gas–liquid interfaces seen from the gas–side as rigid walls contribute significantly to vorticity generation in the flow. Vorticity may therefore not be useful for *coherent structure* (CS) identification in this flow, because CS–specific contributions to the vorticity may be obscured by the near–wall/interface flow (Jeong & Hussain, 1995). In Fulgosi (2004), a range of different measures were used in an attempt to extract CS from flows featuring a well–defined deformable interface. The definition introduced by Jeong & Hussain (1995) based on the negative eigenvalue of second–largest magnitude from the tensor $s_{ij}s_{jk} + r_{ij}r_{jk}$, referred to as the $-\lambda_2$ approach, was found to provide the most accurate and thorough identification of CS even in near–interface turbulent flow, and is used here.

Figure 4.6(a) shows iso–surface visualizations of CS using the $-\lambda_2$ approach at three instants in time that are consecutive. The opaque iso–surfaces correspond to $\lambda_2 = -25000$, which was found to optimally filter out non–CS vorticity. The bubble surfaces, indicated by the $\overline{C} = 0.5$ iso–surfaces, are made translucent so as not to obscure CS. The alignment of CS shape with lobes in the surface of the large bubble in rise about the pipe is obvious. Impressively, despite lobes being resolved by no more than 10 mesh cells, the use of $-\lambda_2$ allows specific CS such as hairpin vortices to be recognizable.

Within the bubble plume rising about the pipe, CS is more concentrated in the lower half – which is not surprising in view of the high intensity of vorticity in the inertial jetting area near the pipe tip. At a height of $2D_i - 3D_i$ above the pipe tip, the second frame shows substantial CS within the uppermost surface of the rising bubble plume. By the last frame however, the bubble swarm is seen to rise further away from the pipe tip, and the CS dissipate gradually. The mushroom–cloud is clearly visible by the time of the last frame; the accompanying fragmentation results in smaller lobes in gas volumes trapped within large bubbles, as well as many bubbles of smaller size. More notably, however, small lobe/bubble formation has the effect of locally laminarizing the gas flow. Even if more nodes were available for better resolution, the proportion of void occupied by CS would be seen to dissipate through the bubble plume in any case.

For comparison with the results of the $-\lambda_2$ approach, Figure 4.6(b) shows the vorticity iso–surfaces of $\omega_z = -500$ and $\omega_z = 500$ at the same times as in Figure 4.6(a). The ω_z–pair clearly displays counter–rotating vortical structures – providing virtually the same insight as from the neighbouring panel (a). Note that the choice of $|\omega_z| = 500$ is qualitative: larger values filtered out too much structure, while lower values did not adequately decouple flow structures. Visualization with the enveloping bubble iso–surface shows the structures associated with the $|\omega_z| = 500$ cut–off, for the most part, to fully coincide with the lobes. In the inertial jetting area the coherent structures should have been seen within the large–scale lobes in the bubble surface, but vorticity iso–surfaces seem incapable of resolving these structures there. The use of vorticity iso–contours is seen here to be somewhat inferior to the $-\lambda_2$ approach for CS identification in this category of flow.

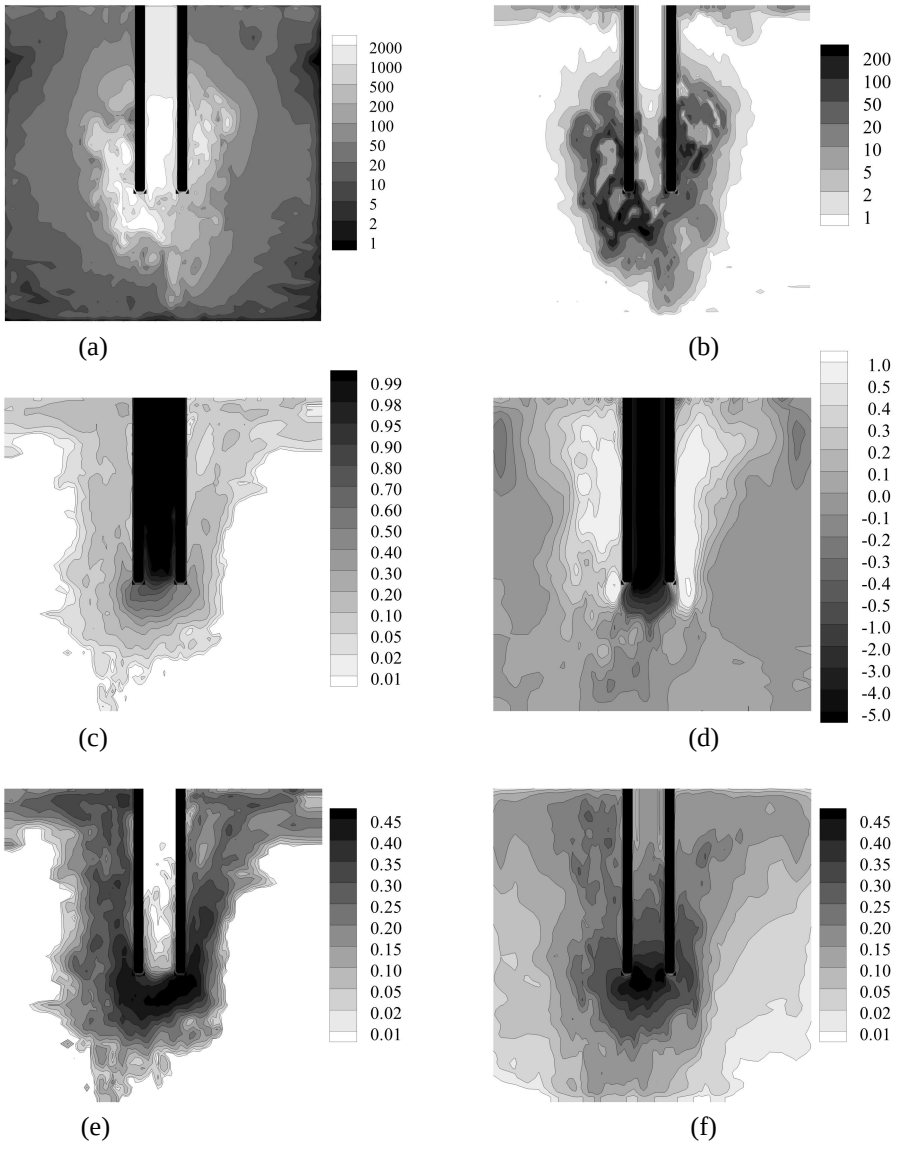

Figure 4.5 Instantaneous and time–averaged yz–plane distributions: (a) vorticity magnitude, and (b) μ_T/μ, at $t = 0.23\ s$; (c) average void fraction, (d) average w–velocity, (e) root–mean–square void fraction, and (f) root–mean–square w–velocity.

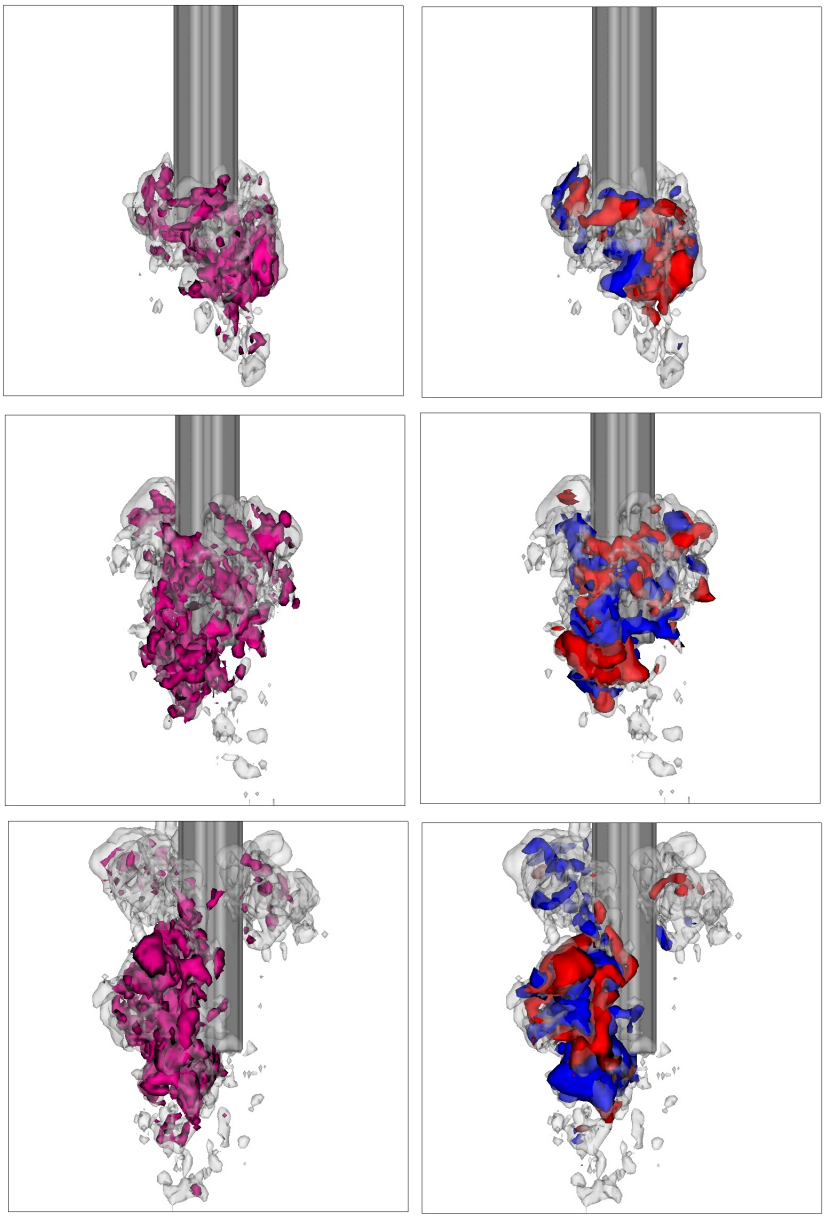

Fig. 5(a) Fig.5(b)

Figure 4.6 Coherent structures within the gas–side flow at $t = 0.15\ s$ (top row), $t = 0.25\ s$ (middle row), and $t = 0.35\ s$ (bottom row), after the commencement of the bubbling simulation: (a) the iso–surface of $\lambda_2 = -25000$, and (b) the iso–surfaces of the $-500/500\ \omega_z$ vorticity pair.

4.4.6 Azimuthally–averaged results

To characterize the plume boundaries about the downcomer as a function of distance from the pipe axis, the time–averaged results in 3D Cartesian space are averaged azimuthally in the xy–plane about the axis. A list of radial distances is created, and a minimum one–mesh–cell thick support of cells is flagged about each radial distance. Once the support of cells about any target radius, δ, is identified, an inverse distance–based interpolation is used to

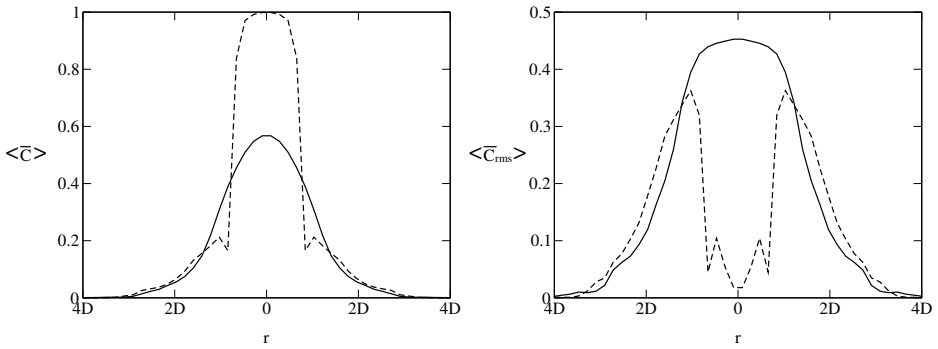

Figure 4.7 Azimuthally–averaged radial profiles of $\overline{C}$ and $\overline{C}_{rms}$: ——— refers to the xy–plane at a distance of $0.45D_i$ below the downcomer tip, and - - - - - refers to the xy–plane at a distance of $0.9D_i$ above the downcomer tip.

generate an azimuthally–averaged value. As an example, an azimuthally–averaged value of the void fraction, $\overline{\langle C \rangle}$, is determined by

$$\langle C \rangle = \frac{\sum_{(i,j,k)\epsilon\delta} w_{i,j,k} C_{i,j,k}}{\sum_{i,j,k\epsilon\delta} w_{i,j,k}}, \tag{4.22}$$

where

$$w_{i,j,k} = \frac{1}{|\mathbf{x}_{i,j,k} - \mathbf{x}_{r,\theta}|^p}, \tag{4.23}$$

with $p = 1/2$ being used for smoothness of the profiles. In the present study, two xy–slices are analyzed – one slice at a distance of $0.45D_i$ below the pipe tip, and the other slice at a distance of $0.9D_i$ above the downcomer tip.

Figure 4.7 shows the radial profiles of the average and rms of the void fraction, $\overline{\langle C \rangle}$ and $\langle C \rangle_{rms}$. For the curves corresponding to the plane below the tip, the pipe does not intersect the plane, such that both the average and rms distributions are continuous and smooth. The major difference between the average and rms curves of $\overline{C}$ is that the average curve features a bell–shaped distribution, while the rms profile exhibits a much broader peak. The curves corresponding to the plane above the tip show clear delineations between the flow in the bubble plume and the downward pipe flow. It can be seen that the bubble plume is slightly broader in the plane above the gas tip, and the rms fluctuations in void fraction are more intense – consistent with bubble rise through the plane. There is also a reduction in bubble plume void fraction adjacent to the outer pipe wall, and a more pronounced reduction in rms.

Figure 4.8 shows the radial profiles of the average and rms of the w–velocity, $\overline{\langle w \rangle}$ and $\langle w \rangle_{rms}$, scaled by the mean gas inflow velocity. For both planes considered, the mean vertical velocity is upwards in the region beyond the pipe radius; the profiles look similar, albeit with higher velocities for the plane above the tip, which was to be expected from the bubble acceleration up the plume. The downward velocity profile in the plane above the tip corresponds to the pipe flow. The profile in the plane below the pipe tip is dilated in the region beyond the outer pipe diameter by lateral spread of the jet, and the w–velocity fluctuations are high in the jetting region. Finally, Figure 4.9 shows the turbulent kinetic energy profile in the same planes, confirming that the turbulence is concentrated in the gas–side flow with particularly high–intensity in the jetting region below the pipe tip.

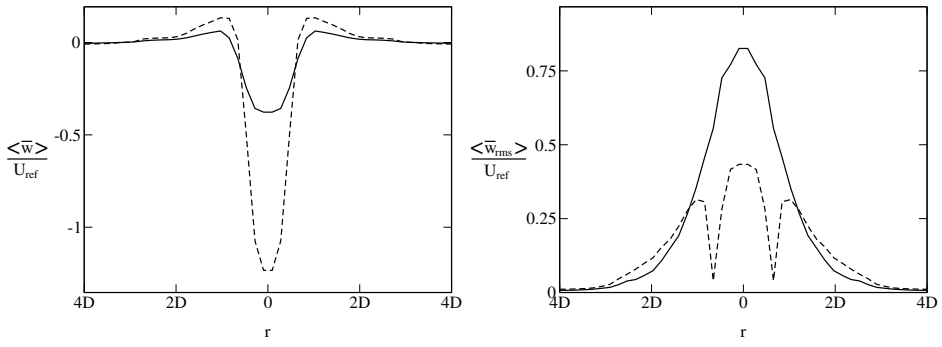

Figure 4.8 Azimuthally–averaged radial profiles of $\overline{w}$ and $\overline{w}_{rms}$: ——— refers to the xy–plane at a distance of $0.45D_i$ below the downcomer tip, and - - - - - refers to the xy–plane at a distance of $0.9D_i$ above the downcomer tip.

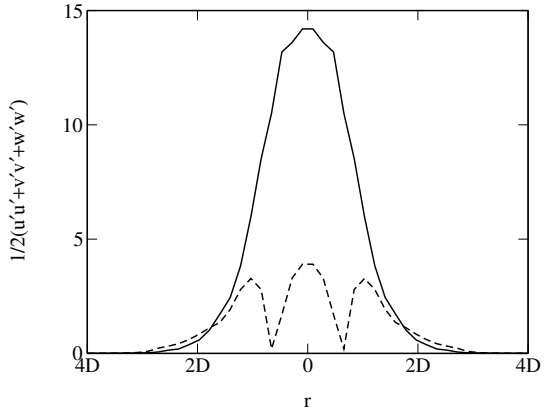

Figure 4.9 Azimuthally–averaged radial profiles of turbulent kinetic energy: ——— refers to the xy–plane at a distance of $0.45D_i$ below the downcomer tip, and - - - - - refers to the xy–plane at a distance of $0.9D_i$ above the downcomer tip.

4.4.7 Energy spectra and dissipation

The spectra shown in Figure 4.10 were obtained by velocity signal recording for sample points in selected azimuths about the pipe axis. Azimuth (a) corresponds to a ring $0.9D_i$ below the pipe tip and $0.4D_i$ off–axis, azimuth (b) corresponds to $0.9D_i$ below the tip and $1.3D_i$ off–axis, and azimuth (c) corresponds to $0.9D_i$ above the tip and $0.9D_i$ off–axis. Signals at 16 equally–spaced points were recorded in each azimuth, as well as the spatial average. The columns identify spectra of signals that are: (i) phase–independent, (ii) gas–specific, and (iii) liquid–specific. The energy spectra of the azimuthally–averaged phase–independent signals (results not included here) reveal the existence of an inertial sub–range characterized by a $-5/3$ decay law that prevails in all selected azimuths. The phase averaging might have embodied information that could be made evident only by the examination of individual sample signals.

The spectra of the phase–specific signals shown in columns (ii) and (iii) were introduced because, during the course of a simulation, the phase occupying that point may switch between gas and liquid. It is therefore possible that there is not only one type of turbulence that prevails at that point; different forms of turbulence with different energy decay behaviours can be conjectured to prevail during the simulation. Specifically, based on the assertion that turbulence cannot cross interfaces, one could conjecture that the less apparent turbulence in the liquid phase makes interpretation of the energy cascade based on a continuous single–fluid velocity signal meaningless.

Comparing the phase–independent spectra and the gas–specific spectra (top row, columns i and ii), the magnitudes of the energy profiles are virtually the same, since the jetting area is essentially occupied by the gas; the magnitudes of the liquid–specific spectra (top row, column iii) are one order smaller. The prevailing $-5/3$ decay law of spectra from all signals in that azimuth confirms that in the region immediately underneath the pipe tip, turbulence is shear–dominated. In the second row, the scatter between energy amplitudes at high wave numbers is significant, and suggests that the intermittency of the phase prevailing in any azimuth is highest for azimuth (b). This is in

line with the progressive tendency towards the $-8/3$ power law appearing in the second row. More importantly in the current problem, the $-8/3$ power law – a finding confirmed experimentally by Lance & Bataille (1991) for the liquid–side turbulence – does not seem to be specific to any phase. The $-8/3$ power law slope is seen even more clearly in azimuth (c), and implies a faster energy decay is induced by the presence of fragmented satellite bubbles. The first conclusion to be drawn from the above discussion is that turbulence in the jetting area is dominated by shear, whereas above and to the side of the pipe tip, it is controlled by buoyancy. The second conclusion is that, albeit different in magnitude, continuous phase–independent energy spectra and phase–specific energy spectra provide the same picture of the energy cascade in different portions of the flow. Gas–phase and liquid–phase turbulence are inseparable.

Tables 2(a)–(c) show dissipation rates, and Kolmogorov length and velocity scales, generated from the rms flow field upon which Figure 4.5 is based. The dissipation rate, and Kolmogorov length and velocity scales, are determined by

$$\epsilon = \frac{1}{\Omega}\int_{\Omega}\left(\overline{\mu+\mu_T}\right)\left(\frac{\partial u_i}{\partial x_j}+\frac{\partial u_j}{\partial x_i}\right)^2 dV, \tag{4.24}$$

$$l_k = \left(\frac{\overline{<\nu>}^3\,\overline{<\rho>}}{\epsilon}\right)^{1/4}, \tag{4.25}$$

$$U_k = \left(\frac{\epsilon\,\overline{<\nu>}}{\overline{<\rho>}}\right)^{1/4}, \tag{4.26}$$

where the overline represents time–averaging (and the operator $< ... >$ space–averaging in equations 4.25–4.26) of bulk property distributions, and Ω the selected integration domain. Three different sub–domains were used for integration: the entire flow domain minus the regions in the vicinity of the outflow and the outer vertical boundaries, the jetting region underneath the downcomer tip, and the buoyant flow region above it and in a tighter annulus about the pipe. Gas–specific and liquid–specific results were obtained for each region. Local data of $\overline{C} < 0.02$ and $\overline{C} > 0.5$ were used to identify the liquid– and gas–specific dissipation rates, respectively; the upper bound was set because the majority of the domain is essentially liquid. The jetting and buoyant regions feature higher dissipation, and the gas–side turbulence is more pronounced. Given a minimum top–hat filter width of 4.7×10^{-3}, the Kolmogorov length scales are $O(10^2)$ smaller, thus justifying the need for a higher grid resolution to perform adequate LES of this type of flow. The Smagorinsky kernel for SGS modeling in LES is known to be overly dissipative and to not accommodate backscatter, but in any case the ratio of the filter width to the Kolmogorov scale shows us to be far from a DNS of this bubbling process.

4.4.8 Interface–turbulence structure correlation

Although Figures 4.4 and 4.6 provide visual evidence of correlation between gas–side turbulence and the interface, they represent only snapshots in time, and are inadequate for any parametric assessment of interface–turbulence coupling. As a first step towards extending the fundamental knowledge of these interaction mechanisms to flows featuring significant topology changes and massive fragmentation and coalescence, we attempt to correlate filtered flow variables that separately quantify the interface and the turbulence.

For that purpose, we first adopt the second invariants of the fluctuating strain rate and vorticity tensors s_{ij} and r_{ij} as potential indicators of turbulence structures, i.e. $|S| = \sqrt{s_{ij}s_{ij}}$ and $|\omega| = \sqrt{r_{ij}r_{ij}}$, where

$$s_{ij} = \frac{1}{2}\left(\frac{\partial u_i'}{\partial x_j}+\frac{\partial u_j'}{\partial x_i}\right), \quad \text{and} \quad r_{ij} = \frac{1}{2}\left(\frac{\partial u_i'}{\partial x_j}-\frac{\partial u_j'}{\partial x_i}\right) \tag{4.27}$$

denote the fluctuating rates of strain and vorticity. Options for describing the interface deformations include its distance function and its local curvature. Surface curvature computation involves only small storage overhead since it is already determined in the surface force modeling. In contrast, constructing the distance function from 3D VOF data is currently difficult and costly for flows featuring massive stretching, fragmentation and coalescence. Therefore, we consider correlations between strain rate and curvature, and between vorticity and curvature. We actually correlate using the magnitude of the curvature, $|\kappa|$, to best make use of interpolated curvature estimates from CSF–based surface force modeling schemes.

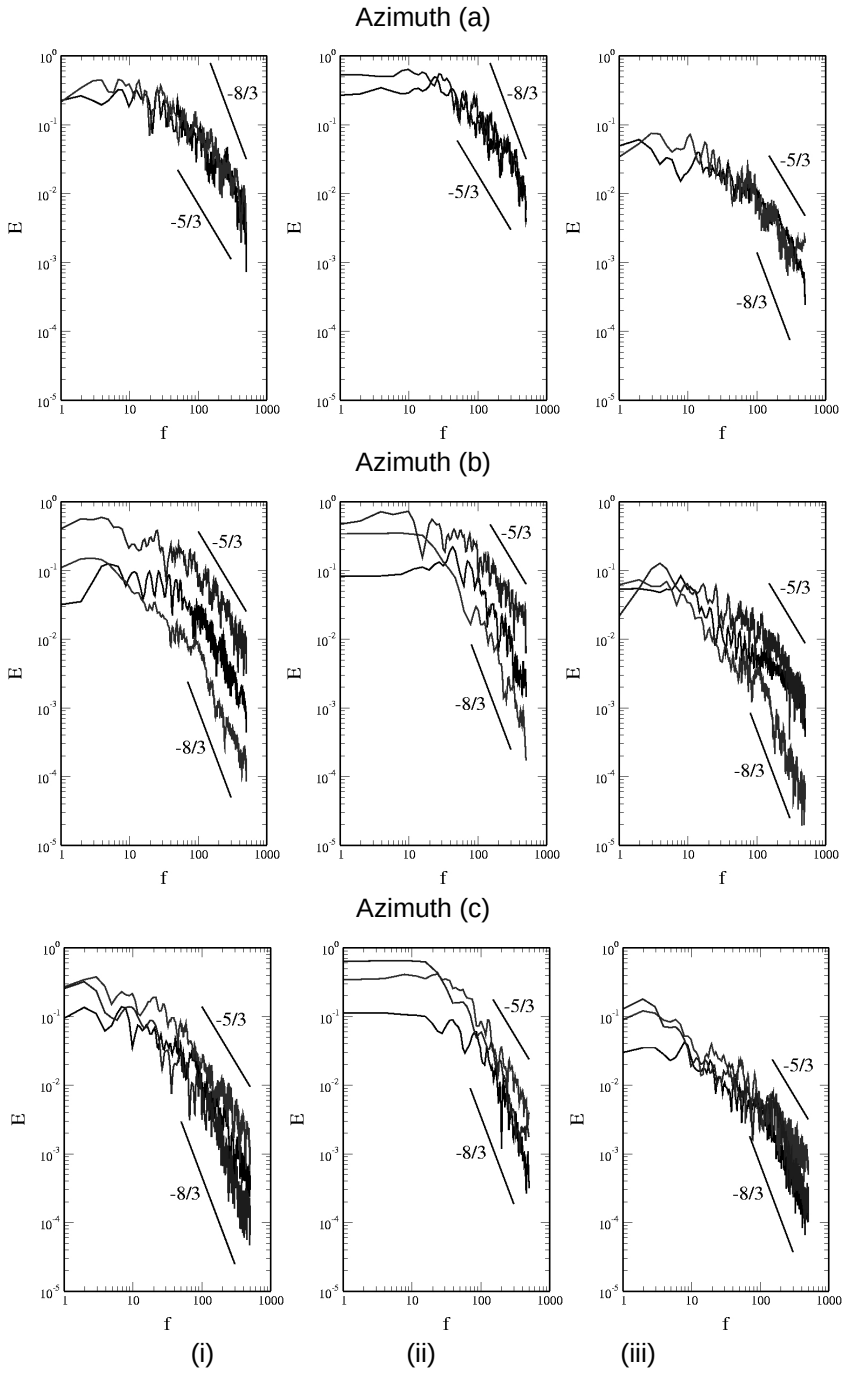

Figure 4.10 Energy spectra for azimuth (a) – top row – $0.9D_i$ below tip, $0.4D_i$ off–axis, azimuth (b) – second row – $0.9D_i$ below tip, $1.3D_i$ off–axis, and azimuth (c) – third row – $0.9D_i$ above tip, $0.9D_i$ off–axis. Columns show representative point spectra of phase–independent signals (i), gas–specific signals (ii), and liquid specific–signals (iii), respectively. Use was made of the color function C to distinguish gas flow events from liquid flow events.

	ϵ	ϵ/ρ	l_k	U_k
Large sub–domain	37.6	9.1×10^{-2}	5.8×10^{-5}	1.7×10^{-2}
Jetting region	1435.4	2.0	2.7×10^{-5}	3.8×10^{-2}
Buoyant rise region	76.7	8.0×10^{-2}	6.0×10^{-5}	1.7×10^{-2}

(a)

	ϵ	ϵ/ρ	l_k	U_k
Large sub–domain	1.6	1.6×10^{-3}	1.6×10^{-4}	6.3×10^{-3}
Jetting region	26.7	2.7×10^{-2}	7.9×10^{-5}	1.3×10^{-2}
Buoyant rise region	2.0	2.0×10^{-3}	1.5×10^{-4}	6.7×10^{-3}

(b)

	ϵ	ϵ/ρ	l_k	U_k
Large sub–domain	5371.5	13.9	1.7×10^{-5}	6.2×10^{-2}
Jetting region	5331.0	14.0	1.7×10^{-5}	6.2×10^{-2}
Buoyant rise region	5961.8	12.8	1.7×10^{-5}	6.0×10^{-2}

(c)

Table 4.2 Properties of the turbulence in the flow, in different regions of the domain. Statistics include the dissipation rate ϵ, the rate normalized by an average void fraction ($\overline{C}$) weighted density ρ, the Kolmogorov length scale l_k, and the Kolmogorov velocity scale U_k. Different sets of statistics have been obtained, in which point data in the integral computation for ϵ is (a) phase–independent (all data points included), (b) liquid phase–specific (all points of where $\overline{C} < 0.02$) included, and (c) gas phase–specific (all points of where $\overline{C} > 0.50$)

.

The first correlations considered are space–based measures of interface deformations and turbulence interactions, $< Corr_1\big(|S|, |\kappa|\big) >$ and $< Corr_2\big(|\omega|, |\kappa|\big) >$, defined by

$$< Corr_1\big(|S|, |\kappa|\big) >= \frac{< |S|'|\kappa|' >}{\sqrt{< |S|'|S|' >}\sqrt{< |\kappa|'|\kappa|' >}} \tag{4.28}$$

($< Corr_2\big(|\omega|, |\kappa|\big) >$ is similarly defined). The $< ... >$ operation represents space–averaging over the support of the interfaces at any instant in time. We then consider the same correlations but over time, denoted by $\overline{Corr_3\big(|S|, |\kappa|\big)}$ and $\overline{Corr_4\big(|\omega|, |\kappa|\big)}$, and defined as

$$\overline{Corr_3\big(|S|, |\kappa|\big)} = \frac{\overline{|S|'|\kappa|'}}{\sqrt{\overline{|S|'|S|'}}\sqrt{\overline{|\overline{\kappa}|'|\overline{\kappa}|'}}} \tag{4.29}$$

($\overline{Corr_4\big(|\omega|, |\kappa|\big)}$ is similarly defined). The overbar represents time–averaging at any point in space. To distinguish, $< Corr_1 >$ and $< Corr_2 >$ are functions of time, while $\overline{Corr_3}$ and $\overline{Corr_4}$ are functions of space.

Figure 4.11 shows the spatial correlations of $|S|$ and $|\omega|$ with $|\kappa|$ within the interface support, $Corr_1$ and $Corr_2$, at each point in time. The strain and the vorticity correlate with the interface curvature identically. Given that the

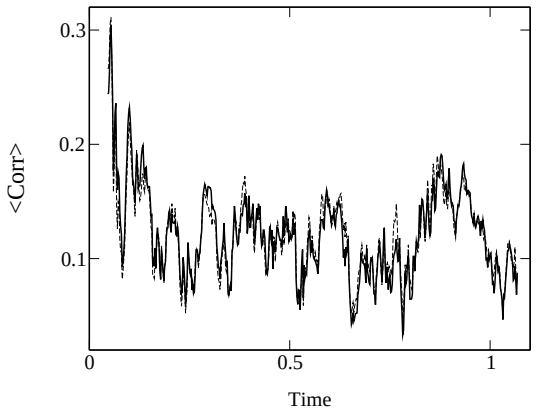

Figure 4.11 Time signals of the spatial correlations $< Corr_1\big(|S|, |\kappa|\big) >$ ——— and $< Corr_2\big(|\omega|, |\kappa|\big) >$ - - - - - .

interface is seen from the gas side like a rigid wall (Fulgosi, 2004), it is not surprising that bubble movement – be it bubble growth or bubble rise – is accompanied by an internal flow aligning itself with the interface.

Figure 4.12 shows the time correlations $Corr_3$ and $Corr_4$ at each point within various xy–plane slices, as well as in the xz– and yz–planes through the axis of symmetry in the pipe. The flood contours are used for the correlation distributions themselves, whereas thick line contours show the locations of 0.01, 0.5 and 0.99 time–averaged void–fraction contours; the 0.01 contour is always the outermost void fraction contour. High correlation regions align with the 0.01 void–fraction contour the best, coinciding with areas where the bubble has expanded out. The results of these two correlations in particular confirm that high–strain, high–vorticity flow regions do indeed coincide with more wrinkled high–curvature surface areas. In general, the vorticity is seen to correlate with curvature slightly better than the strain rate.

Having identified the difference between strain and vorticity magnitudes as bulk distributions and curvature as a property of the interfaces, it is worth noting that the curvature scales inversely with the local interface length scale, and that high–curvature sections of any interface correspond to relative fine wrinkles in the interface.

4.4.9 Enstrophy/Interface Interactions

As an alternative way to separate the contributions of small–scale and large–scale vortical structures on the kinetic energy concentrated at the interface, we introduce the concept of filtered interface–specific enstrophy (ω_I^2) and filtered gas–side enstrophy (ω_G^2). The first measure is defined as

$$\omega_I^2 = \frac{\sum_{ijk} C_{i,j,k}(1 - C_{i,j,k})(\omega_x^2 + \omega_y^2 + \omega_z^2)}{\sum_{ijk} C_{i,j,k}(1 - C_{i,j,k})}, \tag{4.30}$$

where the filter $C(1 - C)$ has been introduced to weight contributions such that the function peaks at the interface and reduces to zero in homogeneous regions of the domain. Using this filter helps determine the energy contained by small–scale eddies that directly contact the interface. The gas–side enstrophy is similarly defined by

$$\omega_G^2 = \frac{\sum_{ijk} C_{i,j,k}(\omega_x^2 + \omega_y^2 + \omega_z^2)}{\sum_{ijk} C_{i,j,k}}, \tag{4.31}$$

where use was made of the color function C to filter out the liquid–side vorticity. The summation is actually performed over a $(4D_i)^3$ sub–domain centered around the downcomer tip, in which the probability of the presence of the interface is high. The areas in proximity to the upper boundary are also ignored.

Figure 4.13 shows the evolution of ω_I^2 and ω_G^2 over time. The first feature to note is the temporal alignment of the peaks and troughs in the signals. Gas–side enstrophy ω_G^2 is larger than ω_I^2 by a factor of about five, suggesting that the majority of the kinetic energy is contained in the large–scale gas–side vortical structures, and less is associated with the surface deformations and fragmentation. The results also suggest that there is a clear out–scatter of vorticity–induced energy, from large scale motions in the core gas flow, to small scales concentrated at the interface, revealing a strong dependence of the interface topology on the vorticity in the core flow. Having said that

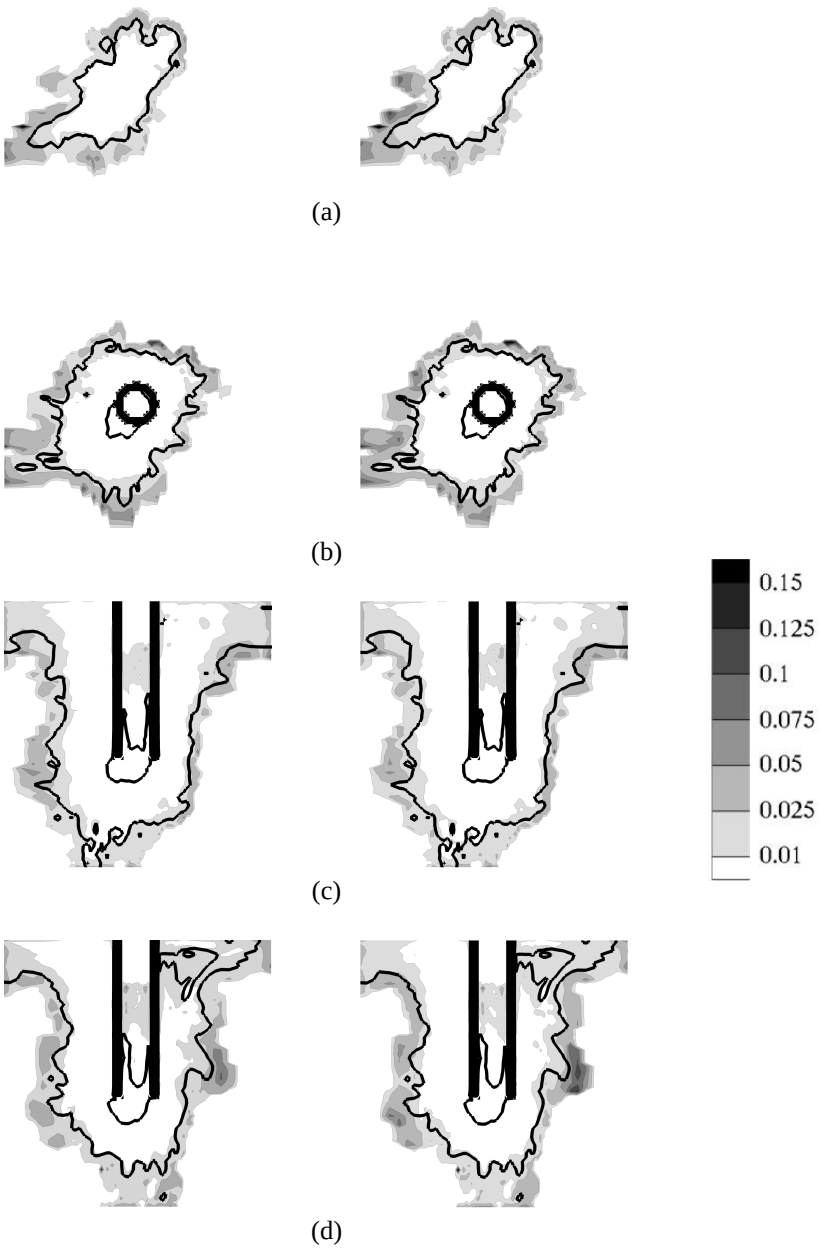

Figure 4.12 2D slices of time–averaged correlations $\overline{Corr_3(|S|', |\kappa|')}$ (left column) and $\overline{Corr_4(|\omega|', |\kappa|')}$ (right column): (a) xy–plane $1.8D$ below downcomer tip (b) xy–plane at tip level, (c) xz–plane through geometric centre, (d) yz–plane through geometric centre.

though, a non–negligible amount of kinetic energy resides in the small–scale structures associated with the interface wrinkling. FFT of the enstrophy signals yield a few low–frequency peaks – the dominant mode peaks at 6 Hz, while sub–harmonics are visible in the $10 - 20$ Hz range. The similarity of the main mode to the bubbling frequency is notable, but no specific correlation of peaks or troughs with structures in the flow can be clearly established.

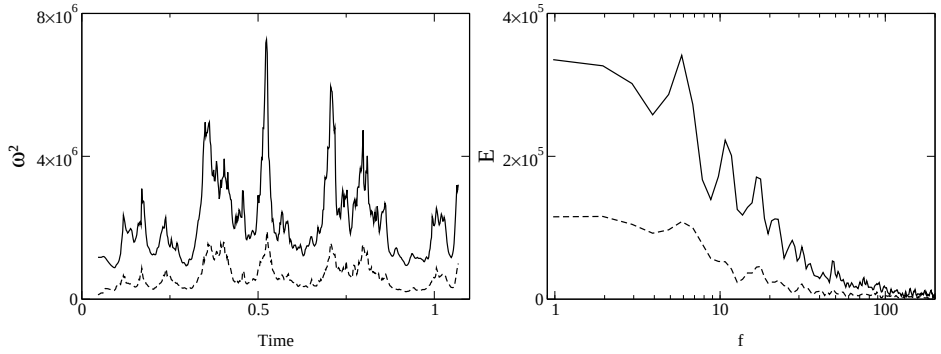

Figure 4.13 Time signals and spectra of the square of the enstrophy (ω^2): - - - - - refers to space–averaged enstrophy in the large bubble region isolated to the interface using the $C(1-C)$ filter, ——— refers to space–averaged gas–side enstrophy (C filter) in the large bubble region.

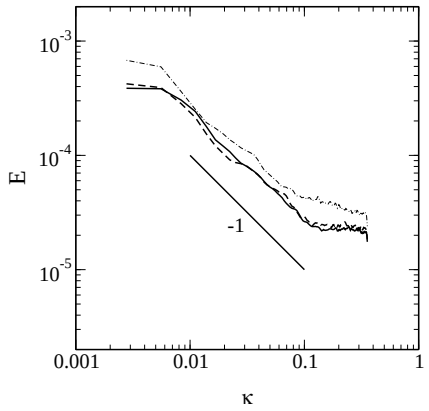

Figure 4.14 FFT of bubble–plume displacement $r_{C=0.5}$, where $r_{C=0.5}(\theta)$ are distances along rays emanating from the axis of symmetry to the outermost bubble surface. This distance is an approximation of the outer gas envelope at any point in time. —·—·refers to the xy–plane $0.45D_i$ below the downcomer tip, ——— refers to the xy–plane at tip level, and - - - - - refers to the xy–plane $0.9D_i$ above the downcomer tip.

4.4.10 Interface wrinkling

Turbulence in the vicinity of the interfaces is one potential cause for small–scale wrinkles in chopped–up bubble surfaces. It may also be a mechanism purely driven by interface instability: after the most dominant mode (i.e. the initially spherical–toroidal bubble shape) saturates, it drains energy to its sub–harmonics. To gain insight into the interface wrinkling in this process, we define a bubble–plume (surface) displacement from the axis of symmetry as $r_{C=0.5}(x,y,t)$, which outlines the location of the plume outer surface. The plume outer–surface location is determined by sweeping inwards along rays from the axis of symmetry at constant intervals $\Delta\theta$, then identifying it as the first location along the ray intersected by the interface. The result represents therefore an outermost extent of the bubble plume, whether it's the surface of the large bubble around the downcomer, or of satellite bubbles. This is the most sensible measure to define, and given that any region of satellite bubbles around the plume is relatively thin compared to the plume, the measure is accurate for the most part. The spectrum of this displacement was extracted for three xy–planes: $0.45D_i$ below the pipe tip, at tip level, and at $0.9D_i$ above pipe level.

The bubble–plume displacements spectra are shown in Figure 4.14. In all cases, the spectra of the surface displacements cascade according to a -1 power–law, and then give way to levelling out at high wave numbers. The spectra do not exhibit distinct peaks, but rather suggest that interface wrinkling is the ultimate end point of a progressive energy cascading mechanism between surface deformation scales. Energy accumulation at high wave numbers reflects the under–resolution of the interface; the average resolved interfacial scales were already discussed in Section C.

4.5 CONCLUSIONS

A novel LES formulation for incompressible multi–fluid flows involving resolvable evolving interfaces has been introduced. The component–weighted filtered single–fluid equations have been presented, and the resulting sub–grid related terms discussed. The method has been applied for a turbulent bubbling process driven by constant volume downward injection of air through a pipe into a water pool. Using a FD/FV–based projection algorithm and robust interface tracking as the core of the method, the LES has delivered turbulence statistics that would be difficult to obtain using other methods. For more modeling–intensive approaches such as the two–fluid approach, the effort required for reliable, scalable modeling is much too daunting.

Interfacial profile comparisons validate the LES as being able to capture the majority of fully 3D effects in bubble growth. The transition from symmetric bubbling featuring smooth surfaces to lop–sided bubbling with chopped up interfaces is well captured, and so is the generation of fragmentation–induced satellite bubbles. The transition from lop–sided bubble growth back to growth of symmetric bubbles is also captured. Transitions between different modes of bubble growth are not regular in reality, and this is reproduced in the simulations, too. The bubbling frequency is captured correctly to be $\sim 7 - 8$ Hz. The qualitative and quantitative macro–scale comparisons of the simulation with experiment validate the simulation as realistically capturing the important transient flow events.

The analysis of the turbulence characteristics of the flow draws the specific conclusions listed below:

- Turbulence is most intense in the gas side; although the liquid–side turbulence is not as obvious, statistical analysis yields energy decay there, too. Turbulence in the shear–dominated jetting region obeys the Kolmogorov K41 slope. Away from the downcomer tip, buoyancy–driven bubble rise coincide with faster energy decay rate, tending occasionally towards the -8/3 power law. A less intense turbulence is also generated in the region where vigorous bubble break–up into a swarm of smaller bubbles takes place.

- The decomposition of the interface into azimuthal modes shows an almost linear decay according to a -1 power law, describing a cascade of interfacial radius–of–curvature length scales.

- The cascade of interfacial length scales is accompanied by the out–scattering of vorticity from the large scale gas–side core flow to the small–scale structures aligning with the interface wrinkling.

5

Temporal instabilities of mixing layers with particles

Le contenu de ce Chapitre est extrait du papier "*Temporal instabilities of a mixing layer with uniform and nonuniform particle loadings*", paru dans *Phys. Fluids* [1]. **13**, 1150–1175, 2002.
Chidambaram Narayanan and Djamel Lakehal

Abstract

Temporal stability analysis of particle-laden mixing layers with uniform and nonuniform particle loadings is presented. New analytical results have been derived in the limit of small and large Stokes numbers using small-parameter expansions. A dichotomy in the behavior of the fluid–particle system, based on whether the particle diameter or density is increased to achieve large Stokes numbers, is clarified. Good agreement between the limiting analytical expressions and numerical results is obtained. Additional unstable modes are observed for nonuniform particle loadings for large Stokes numbers and high mass loadings conditions. The effect of the steepness of the non–uniformity is presented for the first time. The primary effect of non–uniformity, is an increase in the range of unstable wave numbers for small to intermediate Stokes numbers, and a change in the nature of the dominant Kelvin–Helmholtz instability from stationary to dispersive. The value of the most unstable wave number is shown to remain unaffected by the non–uniformity.

5.1 INTRODUCTION

Particle-laden turbulent flows are a common occurrence in nature and in many industrial applications. Although a field of intense research, the interaction of fluid turbulence with the dispersed particle-phase is not well understood yet. The accurate prediction of the concentration distribution of the particles, together with the modification of the fluid turbulence by the particles, is crucial in many situations. The mixing layer is well suited for a detailed analysis of the mechanisms of fluid–particle interaction; having both organized vortical structures and broad-band turbulence in the absence of complicating wall boundary effects. In spite of being a prototypical flow, the prediction of the growth rate of a mixing layer (reflecting the mixing efficiency of two flow streams coming together) under different circumstances is of great practical importance. The rate of mixing controls, for example, the rate of reaction in non–premixed combustion systems. Similarly, the dispersion of particles/droplets is important in situations such as liquid fuel spray combustion applications and industrial particle separation systems. Potentially, particles can also be added to mixing layers to control their growth rate.

[1] Reprinted with the permission of the publisher, *American Institute of Physics*

The linear stability analysis of mixing layers is a classical subject (Michalke, 1964, 1965; Ho & Huerre, 1984). The purpose of the analysis is to reveal the shape of the unstable modes and their associated wave numbers and frequencies. The most unstable mode and its interaction with the sub-harmonic mode dominates the initial evolution of a mixing layer and addition of particles is bound to have an impact on the flow evolution. Also, apart from the usual Kelvin–Helmholtz instability, there could be additional unstable modes inherent to the fluid–particle system. Therefore, a clear understanding of the modification of the flow stability by dispersed particles is necessary before attempting detailed studies to quantify turbulence modification by particles.

Classical hydrodynamic stability theory usually addresses the stability problem from either the spatial or temporal point of view. In the temporal analysis, it is assumed that small perturbations evolve in time from some initial spatial distribution, whereas, in the spatial analysis, the interest is in the spatial evolution of a time periodic signal at a fixed location in the flow. The choice between spatial and temporal analysis depends on the nature of the instability of the flow configuration under consideration. In this regard, the concept of absolute versus convective instability has been introduced (Huerre & Monkewitz, 1985). A flow is convectively unstable if the disturbances are convected away by the mean flow as they amplify and therefore leave the basic flow undisturbed at large times. This contrasts with absolutely unstable flows where a small disturbance at any location leads, in the linear regime, to exponential growth everywhere in the system. Spatial analysis is more apt for convectively unstable flows, whereas, the temporal theory is useful for analyzing absolutely unstable flows (Huerre & Monkewitz, 1985).

In experimental studies of free-shear flows, the instability is usually controlled by periodically forcing the flow at a given frequency at a particular location. Therefore, most experimental results seem to correlate closely with the predictions of spatial theory. Huerre & Monkewitz (1985) analyzed the absolute versus convective character of inviscid instabilities in parallel mixing layers. They show that the flow is convectively unstable only if the velocity difference parameter (defined later) is smaller than 1.315. When this parameter is greater, the instability develops temporally.

In the present study, a temporal stability analysis has been carried out. The reason for this choice is two-fold. Firstly, the analysis will provide accurate initial conditions for direct numerical simulations of particle-laden, temporally evolving mixing layers, so that the unstable modes can be appropriately excited. Secondly, since the main features and mechanisms of fluid–particle interactions are not dependent on the nature of the stability analysis, the goal of gaining insight into fluid–particle interactions in general, would not be compromised.

The stability of laminar, particle-laden flows was first analyzed by Saffman (1962) (he referred to this type of flows as a dusty gas). He showed through scaling analyses that fine particles will have a destabilizing influence on the flow whereas coarse particles will stabilize the flow. He also showed that, for a fixed mass loading, there is a particular particle size that maximizes the stabilizing influence. In this paper we present new analytical results in the limit of small and large particle Stokes numbers through a formal application of small-parameter expansions. In this process, some of the results from Saffman's work are also reproduced.

Numerical results on the spatial stability of particle-laden, inviscid mixing layers were first presented by Yang *et al.* (1990). However, their analysis was limited to particles with response times much larger than the fluid time scales. The particle-phase perturbation velocities, therefore, were assumed to be zero. They found that the maximum growth rate decreases linearly with increasing particle loading, with no significant change in the value of the most unstable frequency. The situation analyzed by Yang *et al.* (1990), under the constraint of dilute suspensions, implies real particles of very high density and would, therefore, not be a practically interesting regime.

(Wen & Evans, 1994, 1996) extended the work of Yang *et al.* (1990) to include nonuniform particle loading and arbitrary particle response times (dynamic particle phase) in two separate studies. They analyzed the temporal stability of piecewise linear velocity profiles and step-function particle loadings. They report the presence of a second instability due to the non–uniformity in particle loading which appears only in the regime of large Stokes numbers and high mass loadings. Although broken-line and discontinuous mean velocity profiles have been used widely for stability analysis, Maslowe (Maslowe, 1985) has cautioned against the sole use of such flow profiles in arriving at major conclusions. The use of discontinuous profiles can, in some cases, fail to reveal unstable modes. Keeping this aspect in mind, continuous profiles for both the mean velocity and the mean particle loading were chosen in this work. Our results reveal a more complicated behavior of the fluid–particle system under nonuniform particle loading.

Dimas & Kiger (1998) presented a detailed spatial stability analysis of an inviscid mixing layer uniformly loaded with a dynamic particle phase. Looking at the particle concentration perturbation, they have shown that the particle concentration field is organized into alternating bands of increased and decreased concentration corresponding to the braid and core regions in the mixing layer. The maximum non–uniformity in the particle concentration occurred at values of the particle Stokes number around unity. From their analysis of vorticity dynamics, particles were found to amplify the vorticity in the braid region and attenuate the vorticity in the core region. This mechanism acts

in opposition to the Kelvin–Helmholtz instability mechanism and explains the stabilizing influence of the particles. Our work differs from the work of Dimas & Kiger (1998) by the presence of viscosity, non–uniformity in particle loading, and the temporal nature of the analysis.

In this study, we have through the application of small parameter expansions, derived new analytical results in the limit of small and large Stokes numbers. In reality, mixing of fluid streams with differential particle loadings is the most commonly observed case in nature and in industrial processes. This paper also addresses the effect of non–uniformity in particle loading on the instability growth rates, an aspect that has not been addressed hitherto. Thus, our work extends previous studies on the stability of particle-laden mixing layers. The influence of the particle Stokes number and mass loading on the growth rates of the temporal instabilities is analyzed under both uniform and nonuniform particle loadings.

Details of the theoretical formulation along with the numerical method are given in Sec. 5.2; the section also contains a discussion about the validity bounds of the present study. Analytical and numerical results for a mixing layer uniformly loaded with particles are presented in Sec. 5.3, followed by numerical results for non–uniformly loaded mixing layers in Sec. 5.4. Conclusions are drawn in Sec. 5.5.

5.2 MATHEMATICAL FORMULATION

5.2.1 Mean profiles and reference quantities

The dimensional mean streamwise velocity profile for a mixing layer can be approximated by

$$\widetilde{U}(y) = \bar{U} + \frac{\Delta U}{2}\tanh(\frac{\tilde{y}}{\delta_{\omega h}}), \tag{5.1}$$

where $\bar{U} = (U_1 + U_2)/2$, $\Delta U = U_1 - U_2$, U_1 and U_2 are the edge velocities, and $\delta_{\omega h}$ is the vorticity half-thickness defined as, $\delta_{\omega h} = \Delta U/2(dU/dy)_{max}$. Choosing the reference velocity (U_{ref}) to be $\bar{U}$ and the reference length (L_{ref}) to be $\delta_{\omega h}$, the non–dimensional velocity profile can be written as

$$U(y) = 1 + \lambda\tanh(y), \tag{5.2}$$

where $\lambda = \Delta U/2\bar{U}$ is called the velocity difference parameter. The mean vertical velocity is assumed to be zero. The characteristic fluid time scale used to define the particle Stokes number (St) is given as $\tau_f = 2\,\delta_{\omega h}/\Delta U$. The particle inertial response time is defined as $\tau_p = \rho_p d_p^2/18\mu$, and the particle Stokes number is defined as the ratio of the particle to the flow characteristic time scale, $St = \tau_p/\tau_f$, μ being the fluid viscosity and ρ_p and d_p the particle density and diameter, respectively.

The mean profile for the particle volume fraction is assumed to have a form similar to that of the mean velocity profile

$$\Lambda(y) = \bar{\alpha}[\,1 + \lambda_p\tanh(\ell_p y)\,], \tag{5.3}$$

where $\lambda_p = 0$ yields a uniform loading of particles and $\lambda_p = \pm 1$ yield flows loaded with particles only in one of the two streams, and ℓ_p controls the steepness of the non–uniformity.

5.2.2 Governing equations

The governing equations for the fluid are the incompressible Navier–Stokes equations with added source terms in the momentum equation accounting for the fluid–particle interaction through the drag force. For the particles, an Eulerian description representing the case of a dilute, mono-disperse suspension of particles is used. In the equations presented below, it has been assumed that the particle volume fraction is very small, the particle Reynolds number remains much less than unity, the particle density is much larger than the fluid density, and that the particle size is much smaller than the smallest significant fluid length scale. The equations used are similar to those of Dimas & Kiger (1998) with the addition of the viscous terms. The governing equations nondimensionalized by U_{ref} and L_{ref} are given as

$$\frac{\partial u_j}{\partial x_j} = 0, \tag{5.4}$$

$$\frac{\partial u_i}{\partial t} + u_j\frac{\partial u_i}{\partial x_j} = -\frac{\partial p}{\partial x_i} + \frac{1}{Re}\frac{\partial^2 u_i}{\partial x_j^2} + \frac{1}{Fr} + \frac{\lambda}{St}\gamma\alpha_p(u_{p_i} - u_i), \tag{5.5}$$

$$\frac{\partial \alpha_p}{\partial t} + \frac{\partial u_{p_j} \alpha_p}{\partial x_j} = 0, \tag{5.6}$$

$$\frac{\partial u_{p_i}}{\partial t} + u_{p_j} \frac{\partial u_{p_i}}{\partial x_j} = -\frac{\lambda}{St}(u_{p_i} - u_i) + \frac{(\gamma - 1)}{\gamma Fr}, \tag{5.7}$$

where u_i and u_{p_i} are the fluid and particle velocities, respectively, α_p the particle volume fraction, γ the particle-to-fluid density ratio, and Fr the Froude number, defined by $U_{ref}^2/(L_{ref} g_i)$, with g_i being the acceleration due to gravity. The validity of the above set of Eulerian equations is an important issue. One of the key points that needs clarification concerns the neglect of closure terms arising out of the averaging procedure used to derive these equations which has been discussed by Dimas & Kiger (1998).

5.2.3 Perturbation equations

The governing equations are linearized by decomposing the unknowns into mean and perturbation components

$$\begin{aligned} u &= U + \varepsilon\, u'; & v &= V + \varepsilon\, v', \\ p &= \bar{p} + \varepsilon\, p'; & \alpha_p &= \Lambda + \varepsilon\, \alpha', \\ u_p &= U_p + \varepsilon\, u'_p; & v_p &= V_p + \varepsilon\, v'_p, \end{aligned} \tag{5.8}$$

where ε is the perturbation amplitude. Collecting terms that are first order in ε, we obtain the system of perturbation equations as

$$\frac{\partial u'}{\partial x} + \frac{\partial v'}{\partial y} = 0, \tag{5.9}$$

$$\begin{aligned} \frac{\partial u'}{\partial t} + U\frac{\partial u'}{\partial x} + v'\frac{dU}{dy} &= -\frac{\partial p'}{\partial x} + \frac{1}{Re}\left(\frac{\partial^2 u'}{\partial x^2} + \frac{\partial^2 u'}{\partial y^2}\right) \\ &\quad + \frac{\lambda}{St}\gamma\left[\Lambda(u'_p - u') + \alpha'(U_p - U)\right], \end{aligned} \tag{5.10}$$

$$\frac{\partial v'}{\partial t} + U\frac{\partial v'}{\partial x} = -\frac{\partial p'}{\partial y} + \frac{1}{Re}\left(\frac{\partial^2 v'}{\partial x^2} + \frac{\partial^2 v'}{\partial y^2}\right) + \frac{\lambda}{St}\gamma\Lambda(v'_p - v'), \tag{5.11}$$

$$\frac{\partial \alpha'}{\partial t} + \Lambda\frac{\partial u'_p}{\partial x} + U_p\frac{\partial \alpha'}{\partial x} + \Lambda\frac{\partial v'_p}{\partial y} + v'_p\frac{d\Lambda}{dy} = 0, \tag{5.12}$$

$$\frac{\partial u'_p}{\partial t} + U_p\frac{\partial u'_p}{\partial x} + v'_p\frac{dU_p}{dy} = -\frac{\lambda}{St}(u'_p - u'), \tag{5.13}$$

$$\frac{\partial v'_p}{\partial t} + U_p\frac{\partial v'_p}{\partial x} = -\frac{\lambda}{St}(v'_p - v'). \tag{5.14}$$

Under the parallel-flow assumption, the mean quantities are expressed only in terms of the vertical coordinate as given in Sec. 5.2.1. The perturbation continuity equation is eliminated by choosing a flow stream-function, ψ', such that $u' = \partial\psi'/\partial y$ and $v' = -\partial\psi'/\partial x$. Solution to the above set of equations is sought for perturbations given by normal mode traveling waves of the form

$$\begin{aligned} \psi' &= \phi(y)\, \exp\left[i(kx - wt)\right]; & \alpha' &= \alpha(y)\, \exp\left[i(kx - wt)\right] \\ u'_p &= u_p(y)\, \exp\left[i(kx - wt)\right]; & v'_p &= v_p(y)\, \exp\left[i(kx - wt)\right] \end{aligned} \tag{5.15}$$

where, k and ω are the complex wave number and frequency of the imposed perturbations, respectively. Substituting Eqs. (5.15) into the perturbation equations and eliminating the pressure term from the momentum equations by taking cross-derivatives and subtracting, we get

$$\begin{aligned} &(kU - iC_2)\left[\frac{d^2\phi}{dy^2} - k^2\phi\right] - k\frac{d^2U}{dy^2}\phi + \frac{i}{Re}\left[\frac{d^4\phi}{dy^4} - 2k^2\frac{d^2\phi}{dy^2} + k^4\phi\right] \\ &+ iC_2\left[\frac{du_p}{dy} - ikv_p\right] + iC_3\left[u_p - \frac{d\phi}{dy}\right] + iC_4\alpha + iC_5\frac{d\alpha}{dy} \\ &= \omega\left[\frac{d^2\phi}{dy^2} - k^2\phi\right], \end{aligned} \tag{5.16}$$

$$kU_p\alpha + k\Lambda u_p - i\Lambda\frac{dv_p}{dy} - i\frac{d\Lambda}{dy}v_p = \omega\alpha, \tag{5.17}$$

$$iC_1\frac{d\phi}{dy} + (kU_p - iC_1)u_p - i\frac{dU_p}{dy}v_p = \omega u_p, \tag{5.18}$$

$$kC_1\phi + (kU_p - iC_1)v_p = \omega v_p, \tag{5.19}$$

where

$$\begin{aligned} C_1 = \lambda/St; \quad C_2 = C_1\gamma\Lambda; \qquad & C_3 = C_1\gamma(d\Lambda/dy), \\ C_4 = C_1\gamma\,(dU_p/dy - dU/dy); \qquad & C_5 = C_1\gamma(U_p - U). \end{aligned} \tag{5.20}$$

Equation (5.16) without the particle related terms is the standard Orr–Sommerfeld stability equation. The mean particle velocity is set equal to the mean fluid velocity ($U_p = U; V_p = 0$); as a result the quantities C_4 and C_5 become identically zero and α is now decoupled from the set of equations. Gravity terms do not enter the perturbation equations and the assumption of identical fluid and particle mean velocities implies a large Froude number. Using finite-difference approximations, the equations can be written in matrix form to yield a generalized eigenvalue problem

$$\mathcal{A}\,\vec{e} = \omega\,\mathcal{B}\,\vec{e}, \tag{5.21}$$

where $\mathcal{A}$ and $\mathcal{B}$ are complex coefficient matrices and $\vec{e}$ is the eigenvector. A standard Q-Z matrix eigenvalue algorithm (Moler & Stewart, 1973) was used to directly obtain all the discrete eigenvalues and eigenvectors.

5.2.4 Validity of the parametric study

Before presenting results for particle-laden mixing layers we first analyze the constraints on the governing equations presented in the previous section; these are valid only under the following conditions:

1. The diameter of the particles is much smaller than the smallest significant length scale of the flow, so that a uniform-flow assumption in the vicinity of the particles is valid;

2. the particle Reynolds number is much less than one so as to conform to the Stokes flow regime;

3. the volume fraction of the particles is much smaller than one so that particle-particle interactions can be neglected;

4. the density of the particles is much larger than the density of the fluid. This allows the neglect of forces other than the drag force such as the added-mass, Basset, and fluid forces (Maxey & Riley, 1983*a*).

Conditions 3 and 4 are directly satisfied by choosing the two relevant parameters as required and, as such, requires no further clarification. In the present calculations, the mean volume fraction of the particles is always set to be 10^{-3} or less, and the particle to fluid density ratio is chosen to be at least 1000.

5.2.4.1 Particle diameter Condition 1 means that $d_p/\delta_{\omega h} \ll 1$. Using the definition of the particle Stokes number we get

$$\frac{d_p}{\delta_{\omega h}} = \left[\frac{18St}{\lambda\gamma Re}\right]^{1/2} \ll 1. \tag{5.22}$$

Substituting values for the worst-case scenario in our calculations of small $Re(=250)$ and large $St(=100)$, we get $d_p/\delta_{\omega h} = 0.085$, which is acceptable. Further implications of Eq. (5.22) with regard to analyzing very large Stokes numbers are discussed in Sec. 5.3.2.

5.2.4.2 Particle Reynolds number Condition 2 implies that $Re_p = d_p\tilde{u}_{slip}/\nu \ll 1$, where $\tilde{u}_{slip}$, the slip velocity, is the difference between local fluid and particle velocities. Substituting from Eq. (5.22) we get

$$Re_p = \left(\frac{18StRe}{\lambda\gamma}\right)^{1/2} u_{slip}, \tag{5.23}$$

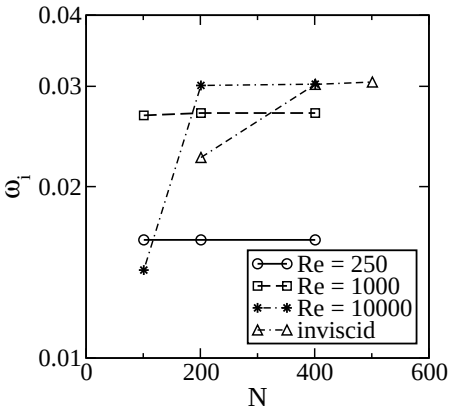

Figure 5.1 Grid convergence of instability growth rates at $k_r = 0.95$; N = no. of nodes.

where u_{slip} is the non–dimensional slip velocity. The particle Reynolds number cannot be calculated *a priori* as the slip velocity is obtained as part of the solution. However, it is clear that the above limitation becomes more restrictive at large particle Stokes numbers. Since the mean fluid and particle velocities are assumed to be identical, the slip velocity arises only due to the imposed perturbations. As the perturbations grow exponentially in time in the linear regime, the slip velocity also increases with time. Since the stability analysis measures the inherent response of the system to perturbations, an arbitrarily small value for ε can be chosen to give an acceptable particle Reynolds number for a significant period of time.

5.2.5 Numerical method

For a temporal stability analysis, the wave number k is specified as the input and the frequency ω is obtained as the eigenvalue. The imaginary part of k is set to zero. A positive imaginary part of ω implies an unstable perturbation that grows exponentially in time. To numerically solve the above eigenvalue problem, the derivatives were calculated using a tenth-order finite difference approximation (Fornberg, 1998). Careful studies were performed to examine the effect of the domain size and spatial resolution requirements. Figure 5.1 shows the grid convergence results at various Reynolds numbers and for the inviscid case for a particle-free mixing layer at $k_r = 0.95$. At smaller wave numbers the resolution constraints are less acute. For Reynolds numbers up to 1000, converged results are obtained with 201 grid points, whereas for higher values more grid points are required. The uniform particle loading calculations were performed with 201 uniformly distributed nodes. For the nonuniform loading cases the number of grid points was increased to 401.

The domain of a mixing layer extends to infinity. The exact boundary conditions for the viscous mixing layer are $\phi,\ \partial\phi/\partial y \rightarrow 0$ as $y \rightarrow \pm\infty$. This homogeneous boundary condition applied to finite domains will yield correct eigenvalues only for very large values of the domain size, H. However, it can be shown that for large y, where $\partial U/\partial y$ and $\partial^2 U/\partial y^2$ are small, the solution takes the form $\phi \approx \exp(\pm ky)$. This behavior was explicitly enforced at a finite domain size as an alternative to using a very large domain size. The appropriateness of the boundary condition incorporating the above asymptotic exponential behavior was verified by comparison with a domain-size converged solution with the homogeneous boundary condition. For all the calculations a domain size of H $= \pm 8$ was found appropriate.

Calculations were performed for Reynolds numbers of 250 and 1000, and a velocity difference parameter $\lambda = 1$. The effect of the Reynolds number was restricted to minor quantitative differences with no new qualitative features and hence only the $Re = 250$ results are mostly presented. A Stokes number range of 0.01 – 100 and a mass loading variation from 0.1 to 1.0 were analyzed.

5.3 UNIFORM PARTICLE LOADING

In this section, both analytical and numerical results are presented for mixing layers uniformly loaded with particles. The presentation is split into three regimes of small, large, and intermediate Stokes numbers. A small-parameter expansion was performed for uniform particle loading wherein the function $\Lambda(y)$ becomes a constant. The mass

loading is then defined as $M = \gamma\Lambda$. For small Stokes numbers, the Stokes number itself is considered as the small parameter, whereas, for large Stokes numbers, the quantity $C_1 = \lambda/St$ is chosen as the small parameter.

5.3.1 Small Stokes numbers

At small Stokes numbers, the particles are expected to further destabilize the mixing layer at finite Reynolds numbers (Saffman, 1962). This is due to the increased inertia of the pseudo-fluid coupled with an insignificant change in its viscosity (due to very small volume fraction of the suspension). This results in an increased effective Reynolds number (or reduced effective kinematic viscosity) and hence higher growth rates since the dissipative effect induced by small-Stokes-number particles is negligible.

The effect can be analytically shown through a small-parameter expansion, with the particle Stokes number taken as the small parameter ϵ. The unknowns ϕ, u_p, v_p in Eqs. (5.16), (5.18), and (5.19) and the eigenvalue ω are expanded based on the small parameter, for example,

$$\begin{aligned} \phi &= \phi_0 + \epsilon\,\phi_1 + \epsilon^2\,\phi_2 + \cdots, \\ \omega &= \omega_0 + \epsilon\,\omega_1 + \epsilon^2\,\omega_2 + \cdots. \end{aligned} \tag{5.24}$$

Substituting the expansions into the perturbation equations, Eqs. (5.16)–(5.19), and collecting terms of the order ϵ^0, we get the zeroth-order system of equations as

$$\phi_0'' - k^2\phi_0 = u_{p_0}' - ikv_{p_0}, \tag{5.25}$$

$$u_{p_0} = \phi_0', \tag{5.26}$$

$$v_{p_0} = -ik\phi_0, \tag{5.27}$$

where the prime stands for differentiation with respect to "y." Equations (5.26) and (5.27) show that, for zero-Stokes-number particles, the particle perturbation velocities are exactly the same as those of the fluid. Equation (5.25) is a redundant equality. The governing equation for ϕ_0 will be available only at the next order. Note that the zeroth-order growth rate ω_0 and the viscous terms do not enter into the zeroth-order system of equations.

The first-order system of equations is obtained as

$$\begin{aligned} -i\lambda\gamma\Lambda(\phi_1'' - k^2\phi_1 &- u_{p_1}' + ikv_{p_1}) = -(kU-\omega_0)(\phi_0'' - k^2\phi_0) \\ &+ kU''\phi_0 \\ &- \frac{i}{Re}(\phi_0'''' - 2k^2\phi_0'' + k^4\phi_0), \end{aligned} \tag{5.28}$$

$$i\lambda(\phi_1' - u_{p_1}) = (\omega_0 - kU)u_{p_0} + iU'v_{p_0}, \tag{5.29}$$

$$\lambda(k\phi_1 - iv_{p_1}) = (\omega_0 - kU)v_{p_0}. \tag{5.30}$$

Substituting from Eqs. (5.29) and (5.30) into Eq. (5.28) yields the equation for ϕ_0

$$(kU-\omega_0)(\phi_0'' - k^2\phi_0) - kU''\phi_0 + \frac{i}{Re(1+\gamma\Lambda)}(\phi_0'''' - 2k^2\phi_0'' + k^4\phi_0) = 0. \tag{5.31}$$

It is clear from Eq. (5.31) that zero-Stokes-number particles have the effect of increasing the effective Reynolds number $(Re\,(1+M))$ proportional to the mass loading, thus, further destabilizing the flow. This effect vanishes in the inviscid limit as the governing equation for ϕ_0 becomes the same for both the particle-free and particle-laden cases.

Numerical results for small Stokes numbers at $Re = 250$ and 1000 are presented in Figs. 5.2(a) and 5.2(b) where a slight increase in the growth rate compared to the particle-free case is observed. The destabilizing effect increases with the mass loading and reduces with increasing Reynolds number. It is seen that for $Re = 1000$ the destabilizing influence has almost vanished. This result has wider implications than in relation to flow stability. As shown by Druzhinin & Elghobashi (1999) in their study about the effect of micro-particles on the rate of decay of isotropic turbulence, micro-particles were shown to have a net effect of reducing the decay rate of the turbulence kinetic energy. This effect has exactly the same cause as above, where the particle-laden flow has the same basic velocity distribution as the particle-free fluid, but a reduced *effective* kinematic viscosity. The lower kinematic viscosity causes a reduction in the decay rate of turbulence.

This concludes the discussion on the effect of zero-Stokes-number particles. Since it is known that particles at small Stokes numbers can have a net stabilizing influence, it appears necessary to quantify the Stokes number at

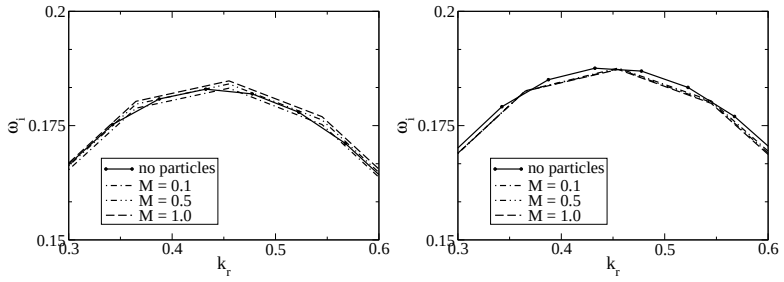

Figure 5.2 Growth rate vs wave number for $St = 0.01$ with different mass loadings: (a) $Re = 250$, (b) $Re = 1000$.

which the influence of the particles switches from destabilizing to stabilizing. If, in fact, this transition takes place in the small-Stokes-number regime ($\epsilon = St \ll 1$), then analyzing the eigenvalue problem for ϕ_1 and ω_1 would be useful. We obtain the following equation for ϕ_1 and ω_1 from the second-order set of equations:

$$\begin{aligned}(kU-\omega_0)(\phi_1''-k^2\phi_1) - kU''\phi_1 + \frac{i}{Re(1+\gamma\Lambda)}(\phi_1''''-2k^2\phi_1''+k^4\phi_1)\\ +\frac{i\gamma\Lambda}{\lambda(1+\gamma\Lambda)}[-(kU-\omega_0)^2(\phi_0''-k^2\phi_0)+2kU''(kU-\omega_0)\phi_0+2k^2U'^2\phi_0]\\ = \omega_1(\phi_0''-k^2\phi_0) \qquad .\end{aligned} \tag{5.32}$$

To obtain an expression for ω_1, Eq. (5.32) is multiplied by a function ϕ_0^*, which is a nontrivial solution of the *adjoint equation* of Eq. (5.31), and integrated along "y." To clarify this, we write Eq. (5.31) in short as $OS[\omega_0, Re, \gamma\Lambda, k]\phi_0 = 0$, where OS stands for the Orr–Sommerfeld operator and the quantities inside the square brackets are the parameters of the operator. The *adjoint* F^* of an operator F is defined by the relation

$$\int F(\phi)\psi = \int \phi F^*(\psi).$$

The operator F is called *self-adjoint* if $F^* = F$. The OS operator is not self-adjoint and its adjoint OS^* is given as

$$\begin{aligned}OS^*[\omega_0, Re, \gamma\Lambda, k]\phi &= (kU-\omega_0)(\phi''-k^2\phi)+2kU'\phi'\\ &+ \frac{i}{Re(1+\gamma\Lambda)}(\phi''''-2k^2\phi''+k^4\phi),\end{aligned} \tag{5.33}$$

the second term in the equation being the differing term in comparison to the OS operator.

For given values of the various parameters, let us call the solution to the adjoint equation as ϕ_0^*. Multiplying Eq. (5.32) by ϕ_0^* and integrating we get

$$\begin{aligned}\int OS[\omega_0, Re, \gamma\Lambda, k]\phi_1\,\phi_0^*\,dy \quad \left(\equiv \int \phi_1 OS^*[\omega_0, Re, \gamma\Lambda, k]\phi_0^*\,dy = 0\right)\\ +\frac{i\gamma\Lambda}{\lambda(1+\gamma\Lambda)}\int[-(kU-\omega_0)^2(\phi_0''-k^2\phi_0)+2kU''(kU-\omega_0)\phi_0+2k^2U'^2\phi_0]\,\phi_0^*\,dy\\ = \omega_1\int(\phi_0''-k^2\phi_0)\phi_0^*\,dy.\end{aligned} \tag{5.34}$$

Denoting the integrals on the left-hand and right-hand side as I_1 and I_2, respectively, we get

$$\omega_1 = \frac{i\gamma\Lambda}{\lambda(1+\gamma\Lambda)}\left.\frac{I_1}{I_2}\right|_{[k,\gamma\Lambda,Re,\omega_0]}. \tag{5.35}$$

The integrals remain functions of the parameters as a closed form solution for ϕ_0^* is unavailable; the three independent parameters being k, Re, and $\gamma\Lambda$. Evaluating the integrals numerically, it is observed that I_1/I_2 is independent of

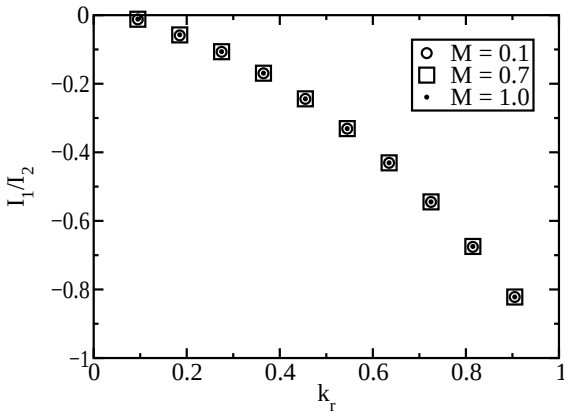

Figure 5.3 Variation of I_1/I_2 vs the wave number, k_r for different mass loadings; $Re = 250$.

the mass loading. Figure 5.3 shows the variation of the quantity I_1/I_2 versus the wave number for different values of mass loading at $Re = 250$. The fact that this ratio is negative implies that the first-order correction to the growth rate is a stabilizing one. Thus, for small Stokes numbers there is a competition between the destabilizing influence due to the increase in the effective Reynolds number of the flow and the stabilizing influence due to the drag-force related viscous dissipation.

Figure 5.3 shows that particles with small Stokes numbers have a stronger effect in the high wave number range. In order to understand this, it must be noted that the particle Stokes number is defined based on the mean velocity and length scales. This definition only accounts for the interaction between the particles and the mean flow and not between the particles and the imposed perturbations. Alternate Stokes numbers defined based on the wave number of the imposed perturbations can shed some light on the overall dynamics of the fluid–particle interaction. For small values of k, the perturbation based Stokes number would be even smaller than the mean based Stokes number, since the length scales associated with small wave numbers are much larger than the mean length scale. Therefore, the particles would have a smaller stabilizing influence at small wave numbers. Regarding the influence of mass loading, both the stabilizing and the destabilizing influences increase with mass loading in an asymptotic manner. From Eq. (5.35), a new scaling is obtained for the stabilizing effect of small-Stokes-number particles with respect to mass loading, represented by $M/(1+M)$.

The growth rate ω for small Stokes numbers can then be written as

$$\omega = \omega_0[k, Re, \gamma\Lambda] + \frac{iSt}{\lambda}\left(\frac{M}{1+M}\right) f(k)|_{[k,Re,\gamma\Lambda]} + \mathcal{O}(St^2), \tag{5.36}$$

where $f(k)$ is a polynomial curve fit for I_1/I_2 given by, $f(k) = -0.81k^2 - 0.18\,k + 0.0065$. In the above relations, we have expressed the instability growth rate of a particle-laden mixing layer in terms of the growth rate for a particle-free mixing layer accounting for variations in both the Stokes number and mass loading. However, due to the semi–analytic nature of the derivation, it is valid only for $Re = 250$.

Using the curve-fits for $\omega_0[k, Re, \gamma\Lambda]$ and the particle-free growth rate $\omega_{pf}[k, Re]$ we can calculate the particle Stokes numbers at which the destabilizing influence is exactly counterbalanced by the stabilizing effect of small Stokes number particles ($St_{neutral}$). Figure 5.4 shows the variation of $St_{neutral}$ with k_r for $Re = 250$. The neutral Stokes number is found to have very little dependency on the mass loading and, therefore, is a function of k and Re only. This was to be expected, since for a dilute suspension particle-particle interactions are negligible and a change in mass loading does not effect the qualitative behavior of the system. Further, since the stabilizing influence of particles is weak for small wave numbers, the neutral Stokes number is higher for small wave numbers. For the most unstable wave number (which for the particle-free case is $k_r = 0.443$), Stokes numbers above approximately 0.025 would have a net stabilizing influence.

5.3.2 Large Stokes numbers

The effect of large-Stokes-number particles can be analyzed by a similar small-parameter expansion, with the factor C_1 ($= \lambda/St$) being taken as the small parameter. However, at large Stokes numbers it becomes important to first assess the validity of the governing equations because the particles can now violate either the size or the small particle Reynolds number criteria (see Sec. 5.2.4). The Stokes number can approach a large value without violating

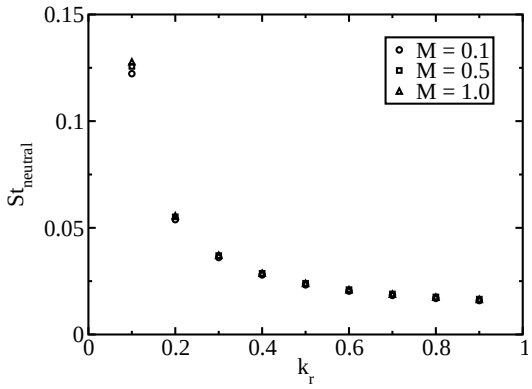

Figure 5.4 Variation of $St_{neutral}$ vs κ for different mass loadings; $Re = 250$.

the size criterion [Eq. (5.22)] in two ways. If the mean fluid flow is assumed to be inviscid (in the sense of having a large length scale), then the particle size and hence the Stokes number can be arbitrarily large. In this case, for a fixed volume-fraction, the mass loading remains fixed, but the number of particles or the particle number density decreases with increasing Stokes number. We refer to this situation as the "increasing size path."

On the other hand, for finite flow Reynolds numbers, the Stokes number can increase due to increasing particle density. In this case γ increases with Stokes number and for a fixed volume-fraction, the mass loading increases with increasing Stokes number. This situation is referred to as the "increasing density path." In both situations, the volume-fraction is held constant. Cases with both the diameter and density being varied can be considered as a combination of these two cases. This dichotomy has not been well emphasized in previous studies which have chosen either one of the two cases. The small parameter expansion for these two cases is presented next.

5.3.2.1 Increasing size path

Expanding the unknowns ϕ, u_p, v_p, and the eigenvalue ω in terms of the small parameter ($\epsilon = C_1$) and collecting terms of the order ϵ^0, we obtain

$$(kU - \omega_0)(\phi_0'' - k^2\phi_0) - kU''\phi_0 = 0, \tag{5.37}$$

$$(kU - \omega_0)u_{p_0} - iU'v_{p_0} = 0, \tag{5.38}$$

$$(kU - \omega_0)v_{p_0} = 0. \tag{5.39}$$

Equation (5.37) is the same as the stability equation for an inviscid fluid with no particles, known as the Rayleigh equation, and therefore, $\omega_0 = \omega_{pf,i}$ (the growth rate of an inviscid, particle-free mixing layer). This means that at the zeroth-order the fluid remains unaffected by particles of large Stokes numbers (increasing size). This was to be expected since for large Stokes numbers at a fixed volume-fraction, the number density would be small. The decrease in the number of particles more than outweighs the effect of an increase in the size of individual particles (Saffman, 1962). Equations (5.38) and (5.39) yield $v_{p_0} = u_{p_0} = 0$.

The first-order equations are obtained as follows:

$$(kU - \omega_0)(\phi_1'' - k^2\phi_1) - kU''\phi_1 = (\omega_1 + i\gamma\Lambda)(\phi_0'' - k^2\phi_0), \tag{5.40}$$

$$i\phi_0' + (kU - \omega_0)u_{p_1} - iU'v_{p_1} = (\omega_1 + i)u_{p_0}\ (= 0), \tag{5.41}$$

$$k\phi_0 + (kU - \omega_0)v_{p_1} = (\omega_1 + i)v_{p_0}\ (= 0). \tag{5.42}$$

Equations (5.41) and (5.42) can be solved to yield

$$v_{p_1} = \frac{k\phi_0}{(\omega_0 - kU)} \quad \text{and} \quad u_{p_1} = i\left[\frac{\phi_0'}{(\omega_0 - kU)} - \frac{kU'\phi_0}{(\omega_0 - kU)^2}\right].$$

To derive an expression for ω_1 we proceed as in the small-Stokes-number analysis, and evaluate the solution to the adjoint equation of Eq. (5.37) and call it ϕ_0^*. In this case, Eq. (5.40) yields

$$(\omega_1 + i\gamma\Lambda)\int(\phi_0'' - k^2\phi_0)\,\phi_0^*\,dy = 0. \tag{5.43}$$

Verifying numerically that the above integral is nonzero, we obtain $\omega_1 = -i\gamma\Lambda$. Thus, the growth rate for large Stokes numbers (increasing size) becomes

$$\omega = \omega_0 + \epsilon\,\omega_1 + \mathcal{O}(\epsilon^2) = \omega_{pf,i} - i\frac{\lambda}{St}\gamma\Lambda + \mathcal{O}(St^{-2}). \tag{5.44}$$

The above relation shows that for large Stokes numbers, it is the combination of parameters $\gamma\Lambda/St$ that is important. For the increasing size path, this quantity goes to zero with increasing Stokes number and hence, in the limit of large Stokes numbers, particles have a vanishing influence.

5.3.2.2 Increasing density path

For the increasing density path, when the particle density is increased while keeping the diameter and volume fraction fixed, the parameter $C_2 = \lambda\gamma\Lambda/St$ becomes constant. Both γ and St increase at the same rate. Thus, the mass loading increases with increasing Stokes number. In such a scenario, the following zeroth-order set of equations are obtained:

$$\begin{aligned}(kU - \omega_0 - iC_2)(\phi_0'' - k^2\phi_0) &= kU''\phi_0 \\ &= -\frac{i}{Re}(\phi_0'''' - 2k^2\phi_0'' + k^4\phi_0), \qquad (5.45)\\ (kU - \omega_0)u_{p_0} - iU'v_{p_0} &= 0, \qquad (5.46)\\ (kU - \omega_0)v_{p_0} &= 0, \qquad (5.47)\end{aligned}$$

where the fact that $u_{p_0} = v_{p_0} = 0$ has already been used to obtain Eq. (5.45). Noting that $(\omega_0 + iC_2)$ in the first term of Eq. (5.45) is the same as the particle-free growth rate (ω_{pf}), we can write $\omega_0 = \omega_{pf} - iC_2$. Thus, the growth rate for the increasing density path can be written as

$$\omega = \omega_0 + \mathcal{O}(\epsilon) = \omega_{pf} - i\frac{\lambda}{St}\gamma\Lambda + \mathcal{O}(St^{-1}). \qquad (5.48)$$

It is clear that this result is different from that of the increasing size case, Eq. (5.44), by the fact that the effect of the particles is felt even at the zeroth order. Previous studies (Yang *et al.*, 1990; Wen & Evans, 1994) dealing with large-Stokes-number particles have only analyzed the increasing density path. The motivation for this choice in those cases is clear, as the increasing size path leaves the flow stability unaffected. In other studies (Dimas & Kiger, 1998; Tong & Wang, 1999), either one of two paths has been chosen.

To summarize, in this section we have clarified this dichotomy and have presented a consolidated analysis. Our analysis shows that for both the increasing size and increasing density paths, the quantity $C_2 = \lambda\gamma\Lambda/St$ is the only relevant parameter. In the increasing size path, C_2 tends to zero as the Stokes number becomes large; as a result the particles have a vanishing influence. For the increasing density path, C_2 remains constant with increasing Stokes number and the particles have a very strong stabilizing influence on the flow.

5.3.3 Intermediate Stokes numbers

The effect of particles with different Stokes numbers at mass loadings of 0.1, 0.5, and 1.0 is presented in Figs. 5.5(a)-5.5(d). The main observation is the significant attenuation of the instability growth rates by intermediate-Stokes-number particles. Low and high-Stokes-number particles have negligible influence on the growth rates for the range of mass loadings computed. An increase in mass loading simply results in a monotonic decrease in the growth rates for all wave numbers (except in the case of very small Stokes numbers, as discussed before).

Particles with $St = 0.1$ and 1.0 have a stronger stabilizing effect on the mid-range and particularly the high wave numbers. On the other hand, $St = 10$ and 100 particles have a significant stabilizing influence over the whole wave number range. The calculation with $St = 100$ conforms to the increasing size path, and therefore, shows a very small influence. This wave number-specific effect on the flow instability can be attributed to the combined response of the particles to the fixed mean flow length scale ($\delta_{\omega h}$) and the length scale of the perturbations which is inversely proportional to the imposed wave number. The exact scaling of this phenomenon with respect to the different length scales could not be obtained for intermediate-Stokes-number particles.

The range of unstable wave numbers is greatly reduced, especially for particles with Stokes numbers close to unity [Fig. 5.5(b)]. This would significantly alter, for example, the response of a mixing layer to broadband excitation. The intermediate Stokes number particles also significantly change (reduce) the most unstable wave number, as discussed in the following section. A particle-laden mixing layer, therefore, would give rise to larger sized vortical structures that grow much slower as compared to a particle-free mixing layer. This would, in turn, strongly influence the overall time evolution of the flow including the onset of three-dimensionalization and transition to turbulence.

A comparison of the limiting analytical expressions derived in previous sections with numerical results is presented in Fig. 5.6 for a single wave number $k_r = 0.455$ and mass loadings of 0.5 and 1.0. From the numerical results it is evident that the Stokes number with the highest stabilizing influence, though wave number dependent, lies between 1 and 10. The analytical expansions are seen to provide a good match to the numerical results in

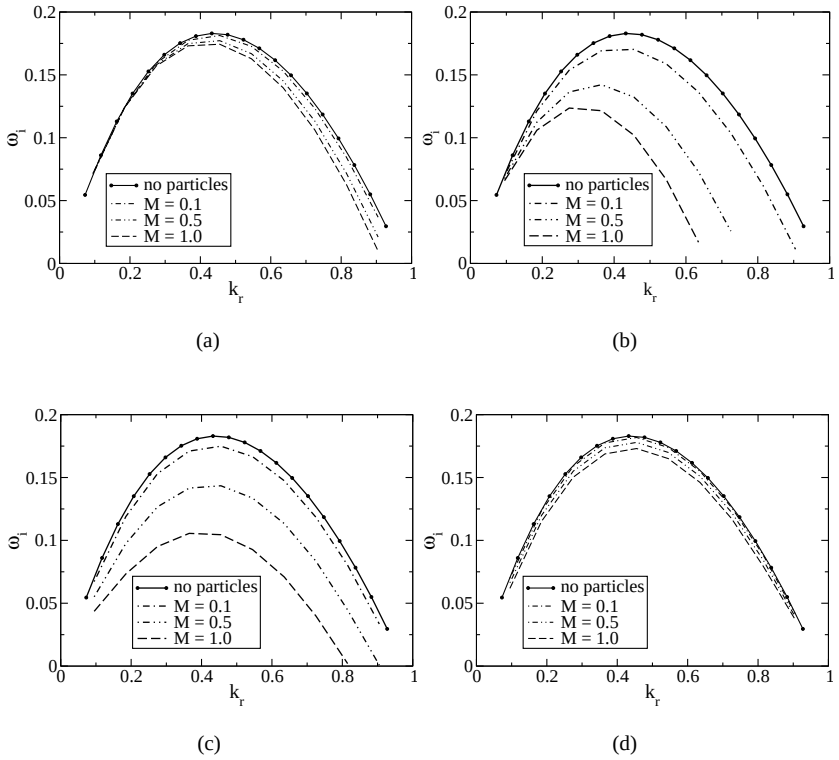

Figure 5.5 Effect of mass loading on the instability growth rate for different particle Stokes numbers, (a) St = 0.1, (b) St = 1, (c) St = 10, (d) St = 100.

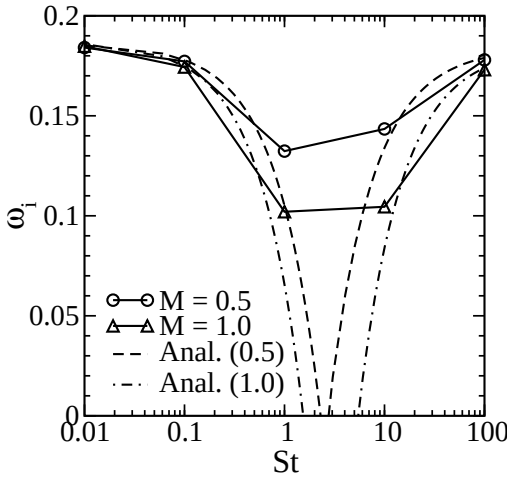

Figure 5.6 Comparison of numerical growth rates with analytically obtained limiting behavior; $k_r = 0.455$, $Re = 250$.

their regions of validity. The small-Stokes-number expansion is accurate up to a Stokes number of 0.5 and the large-Stokes-number expansion down to Stokes numbers around 10. As mentioned before, the scaling in the crucial intermediate range of $0.5 - 10$ could not be derived.

As shown in the analytical study, for small Stokes numbers the particle perturbation velocities coincide with the fluid velocities and for large Stokes numbers the particle perturbations tend to zero. For intermediate Stokes numbers of 1 and 10 the fluid and particles velocities differ dramatically. To interpret the behavior of the perturbation velocities, we generate the fluid and particle velocity fields by summing up the mean and the perturbation components for a particular time instant. Figure 5.7 shows the instantaneous "particle" trajectories for the fluid and particle velocity fields for a frame moving with the reference velocity. As expected, the fluid velocity perturbations give

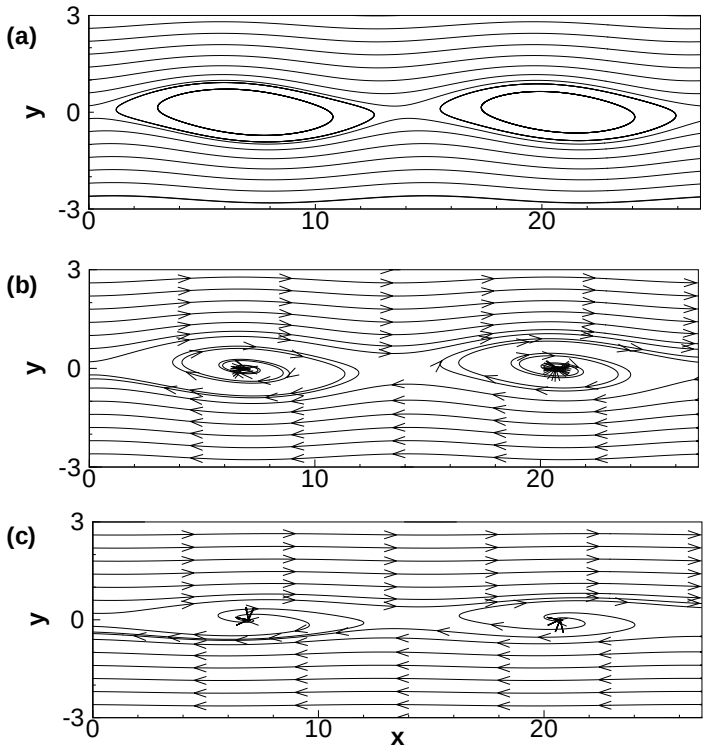

Figure 5.7 Particle trajectories for fluid and particle velocities for $k_r = 0.455$ (a) fluid streamlines, (b) particle-phase trajectories for $St = 1$, (c) for $St = 10$.

rise to the Kelvin–Helmholtz vortex cores signified by the closed particle trajectories. The particle velocity field, on the other hand, does not have closed particle paths. The particle-phase particle paths show that the vortex cores act as unstable foci, implying a migration of the particles out of the vortex cores. The difference between the $St = 1$ and $St = 10$ manifests in the path or time taken by the particles to migrate out of the vortex cores. The $St = 1$ particles move out slower than the $St = 10$ particles, which are quickly ejected from the vortex core.

5.3.4 Most unstable wave number

The most unstable wave number represents the mode dominating the initial evolution of a mixing layer and is, therefore, of practical interest. The effect of particles with different Stokes numbers on the most amplified wave number (k_{max}) and the corresponding growth rate (ω_{max}) with increasing mass loading is shown in Figs. 5.8(a) and 5.8(b). The quantities presented in the figure have been normalized by the corresponding values for a particle-free mixing layer.

Particles of all Stokes numbers tend to reduce the most amplified wave number except the very small Stokes number particles which show a small contrary tendency, due to the increased "effective" Reynolds number effect. Due to their approximately even influence over the whole wave number range [see Fig. 5.5(c)], $St = 10$ particles do not reduce k_{max} as much as the $St = 1$ particles which have a strong influence in the mid and high wave number ranges. The same conclusion can be drawn with regard to the comparison between the $St = 100$ and 0.1 particles. In essence, only particles with Stokes number close to one change the most unstable wave number significantly.

At higher mass loadings (> 0.5) it is the $St = 10$ particles that cause a higher reduction in the growth rate of the most unstable wave number than the $St = 1$ particles. This is due to the fact that in the case of $St = 1$ particles, k_{max} reduces to such an extent that the particles then have a reduced effect at that lower wave number. The strong influence of high density particles, even at low concentrations, is evident by the reduction in the growth rate of up to 50 percent.

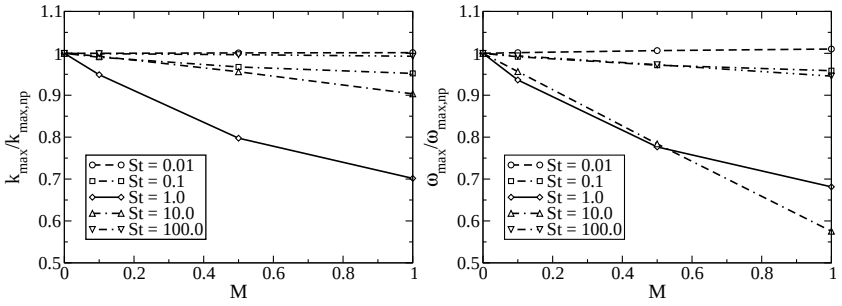

Figure 5.8 Effect of Stokes number and mass loading on (a) the most unstable wave number (b) the corresponding growth rate.

5.4 NONUNIFORM PARTICLE LOADING

For particle-free and uniformly-laden mixing layers only one instability mode exists which is known as the Kelvin–Helmholtz instability. This is an inviscid phenomenon due to the presence of an inflection point in the mean velocity profile. For nonuniform loadings, additional unstable modes within certain parameter regimes exist.

Wen & Evans (1994) presented results on the stability of non–uniformly loaded mixing layers. They analyzed the influence of large-Stokes-number particles on piecewise linear velocity profiles and step-function particle concentration distributions. In a subsequent paper (Wen & Evans, 1996), they extended their analysis to a range of particle Stokes numbers. They showed the existence of a second instability which owes its presence to mechanisms similar to the Holmboe instability in density-stratified mixing layers (Lawrence *et al.*, 1991). This mode has its maximum growth rate at a higher wave number as compared to the Kelvin–Helmholtz instability, and is unstable for a smaller range of wave numbers.

In the present study, we have chosen continuous and more realistic mean profiles. In addition, the effect of the steepness of the non–uniformity of the particle loading (effect of changing ℓ_p) is also investigated. The calculations were carried out in two separate parts with regards to the path chosen in approaching high Stokes numbers, similar to the analysis of the constant particle loading case. Given the large parameter space, the parameters λ_p, Re, and $\bar{\alpha}$ were not varied and set to 0.5, 250, and 5×10^{-4}, respectively. The effect of the non–uniformity was examined by setting $\ell_p = 1$ and 10. At $\ell_p = 10$ the particle loading changes very steeply at the center of the shear layer and is closer to the step function used by Wen & Evans (1994). The density ratio, whenever not specified explicitly, was chosen to be 1000. For a given mean volume-fraction both the uniform and the nonuniform distributions have the same total volume-fraction, thus allowing a direct comparison between the two scenarios.

5.4.1 Small and intermediate Stokes numbers

In this section the effect of the non–uniformity for range of Stokes numbers with the increasing size path taken for large Stokes numbers. We have, therefore, a fixed mean mass loading of 0.5 for these cases. In this case the effect of the particles is known to vanish at high Stokes numbers and hence, results for only small and intermediate Stokes numbers are presented. Figure 5.9 shows the effect of the non–uniformity on the Kelvin–Helmholtz instability growth rates for different Stokes numbers. For the $\ell_p = 1$ case the non–uniformity does not have any significant effect on the growth rates as compared to the constant particle loading case as seen in Fig. 5.9(a). For $\ell_p = 10$ [Fig. 5.9(b)] there is, however, a significant effect on both the magnitude of the growth rates and the range of unstable wave numbers as compared to the uniform loading case. The growth rates for nonuniform particle loading are slightly higher and the range of unstable wave numbers is significantly larger. This can be attributed to the introduction of an additional smaller length scale into the problem which affects the dynamics of the fluid–particle interaction.

The other important effect of the non–uniformity is the departure of the phase speed, ω_r/k_r, from its value of one for the particle-free and the uniformly loaded cases. This means that the modes no longer remain stationary with respect to a frame moving with the reference velocity. Figures 5.10(a) and 5.10(b) illustrate this effect for $\ell_p = 1$ and 10, respectively. We observe that the non–uniformity makes the basic Kelvin–Helmholtz instability

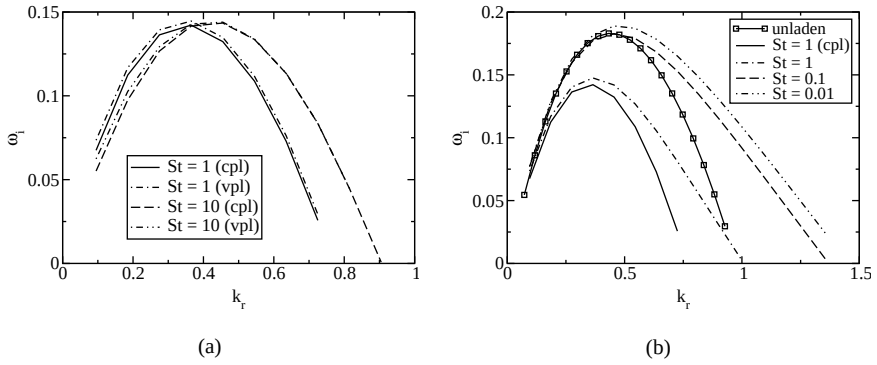

Figure 5.9 Effect of nonuniform loading on the growth rate, (a) $\ell_p = 1$ (b) $\ell_p = 10$ ($M = 0.5$; cpl - constant particle loading; vpl - variable particle loading).

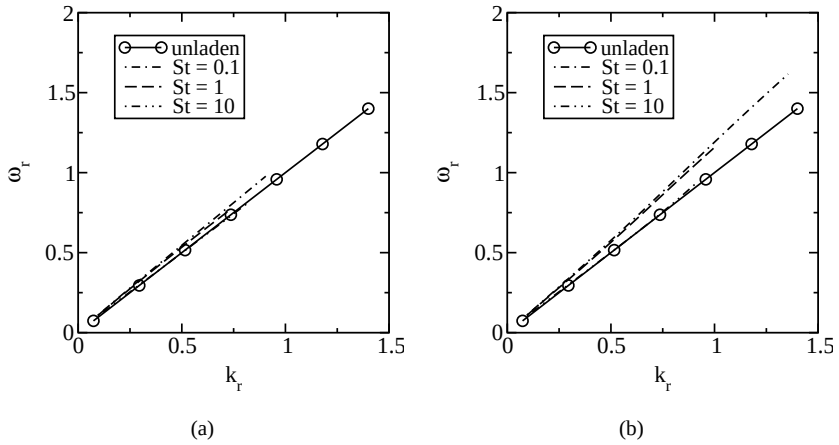

Figure 5.10 Effect of nonuniform loading on the phase speed, (a) $\ell_p = 1$ (b) $\ell_p = 10$ ($M = 0.5$).

dispersive. The dispersive effect depends on the extent of non–uniformity as seen from the figures. The steeper the non–uniformity the higher the dispersive effect. The dispersive influence is maximum for small-Stokes-number particles and progressively vanishes for large Stokes numbers, as could be expected from previous discussions on the effect of large-Stokes-number particles. To clarify this aspect, we look at the fluid streamwise velocity in a frame moving with the reference velocity

$$\begin{aligned} u &= U(y) + \varepsilon\, \Re(u') \\ &= \lambda \tanh(y) + \varepsilon\, [u_r \cos(k_r x - (k_r - \omega_r)t) \\ &\quad -u_i \sin(k_r x - (k_r - \omega_r)t)]\, \exp(\omega_i t), \end{aligned} \tag{5.49}$$

where u_r and u_i denote the real and complex components of the perturbation eigenfunction, respectively. For the particle-free and the constant loading cases we always obtain $\omega_r = k_r$ which yields

$$u = \lambda \tanh(y) + \varepsilon\, [u_r \cos(k_r x) - u_i \sin(k_r x)]\, \exp(\omega_i t). \tag{5.50}$$

The above equation represents a standing wave which grows exponentially in time. On the other hand, with the introduction of non–uniformity in the particle loading, $\omega_r \neq k_r$ and the wave moves relative to the frame moving with the reference velocity as in Eq. (5.49). This concludes the discussion on the effect of the non–uniformity in particle loading on the Kelvin–Helmholtz instability at various Stokes numbers for a fixed mass loading of 0.5.

An additional pair of unstable modes is found at $St = 100$, but both are very weak and restricted to a small wave number range around $k_r = 1$. As observed by Wen & Evans (1996), their second instability is significant only at much higher mass loadings. This new pair of unstable modes have almost the same growth rates but have higher

and lower phase speeds with respect to the reference velocity, thus, representing right and left moving waves. At this Stokes number the primary Kelvin–Helmholtz mode is non–dispersive or stationary. This situation is similar to the Holmboe instability for density stratified mixing layers which consists of a pair of interfacial waves growing at the same rate but traveling in opposite directions. This pair of unstable modes is further analyzed below. For convenience this pair of unstable modes is referred to as the Holmboe instability, although the particle-laden scenario is quite different from the density stratified mixing layer case (Lawrence *et al.*, 1991).

At this stage, important differences between our analysis and that presented by Wen & Evans (1996) must be clarified. Due to the simplifications resulting from the use of broken-line and discontinuous profiles, Wen and Evans obtained an eighth-order polynomial expression for the perturbation frequency, which can be solved using a symbolic computing software. They obtained two unstable modes independent of the Stokes number. This is in contrast to our results where an additional *pair* of unstable modes are observed, but only at a high Stokes number. This difference can be explained by their choice of a step profile for the particle loading which introduces a vanishingly small length scale that even small Stokes number particles interact with, giving rise to the second instability at all Stokes numbers. This is similar to the case of the classical Kelvin–Helmholtz instability for a discontinuous velocity profile, wherein all the wave numbers are found to be unstable (Drazin & Reid, 1981). Whereas, for a real mixing layer of finite thickness, we find that large wave numbers are stable.

Another difference lies in the fact that in the work of Wen & Evans (1996), the second unstable mode is excited at all wave numbers as compared to the current analysis where additional unstable modes appear only at higher wave numbers. This is due to their choice of the maximum nonuniform loading case ($\lambda_p = 1$), where even the large length-scales perceive the non–uniformity, whereas, for smaller values of λ_p the distribution would appear nearly as a uniform loading for large length scales. In their previous study (Wen & Evans, 1994), where they have analyzed the case of $\lambda_p = 0.5$, the second instability was indeed found to be stable at small wave numbers.

5.4.2 Large Stokes number and high mass loading

Since the Holmboe instability is expected to be strong only for large Stokes numbers and high mass loadings, we now focus on this regime. Calculations were performed for Stokes number of 100, $\ell_p = 1$ and 10, and $\gamma = 5000$ and 10000. This implies mean mass loadings of 2.5 and 5, respectively. In this regime, the stability properties of the mixing layer become considerably more complicated. The main departure observed is the appearance of a large number of unstable modes at high wave numbers ($k_r > 1$). To understand this behavior, the eigenvalue spectrum for a few typical cases is examined at a particular wave number. It must be pointed out that we are interested only at the top end of the eigenvalue spectrum.

Firstly, in Fig. 5.11(a) we compare the eigenvalue spectra at $k_r = 0.635$ for the particle-free and the uniformly laden ($St = 100$, $\gamma = 1000$) cases. The important observation is the appearance of two horizontal lines of weakly stable modes for the uniformly laden case which are absent in the particle-free case, as detailed in Fig. 5.11(b). For the non–uniformly laden case, spectra at two wave numbers are presented for the case of $\ell_p = 1$ and $\gamma = 10000$ in Figs. 5.11(c) and 5.11(e). At $k_r = 0.635$, the two horizontal lines move apart a little, making some modes unstable. At this wave number the most unstable mode (the Kelvin–Helmholtz mode) still has a significantly higher growth rate compared to the new unstable modes [see Fig. 5.11(d)]. At $k_r = 1.175$, the horizontal lines of modes move further apart introducing many more unstable modes as shown in Fig. 5.11(f). The most unstable mode no longer has a significantly higher growth rate. At this wave number there are many unstable modes that have almost the same growth rates. It can also be noted that the new unstable modes become progressively more dispersive and almost equal numbers of right and left moving modes are excited. This behavior of the current system is quite different from the simplified system of Wen and Evans.

Directing our attention now only on the Kelvin–Helmholtz and the pair of Holmboe instabilities, we observe that their growth rates become comparable at high wave numbers as, shown in Figs. 5.12(a) and 5.12(b). The figures compare the growth rates of the two instabilities at a Stokes number of 100, for density ratios of 5000 and 10000 at $\ell_p = 10$. The attenuation in the Kelvin–Helmholtz growth rate is seen to be very close to the uniformly loaded case given by

$$\omega \approx \omega_{pf} - i\lambda\gamma\bar{\alpha}/St, \tag{5.51}$$

where the *mean* mass loading has been used here. The main difference is observed at high wave numbers. These remain weakly unstable even up to $k_r = 1.5$, in contrast to the uniformly loaded cases where wave numbers greater than one are stable. The steepness of the non–uniformity has negligible influence in this regime and therefore, $\ell_p = 1$ results are not presented here. Similar to the uniformly loaded cases, the effect on the most unstable wave number is not significant at high Stokes numbers. Also, at these high mass loadings the stationarity of the

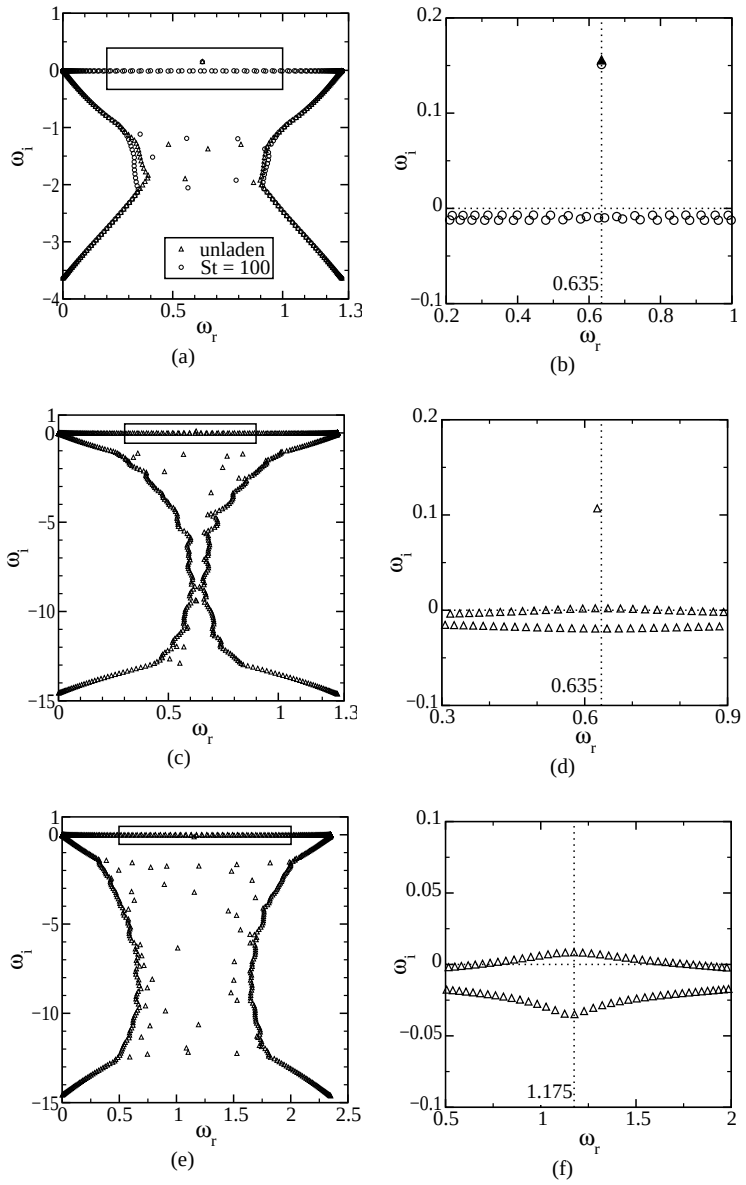

Figure 5.11 Eigenvalue spectra for (a) particle-free and uniformly loaded cases ($k_r = 0.635$, $\gamma = 1000$), (b) detailed view. Non–uniformly loaded, $\ell_p = 1$, $\gamma = 10000$, (c) $k_r = 0.635$, (d) detailed view, (e) $k_r = 1.175$, (f) detailed view.

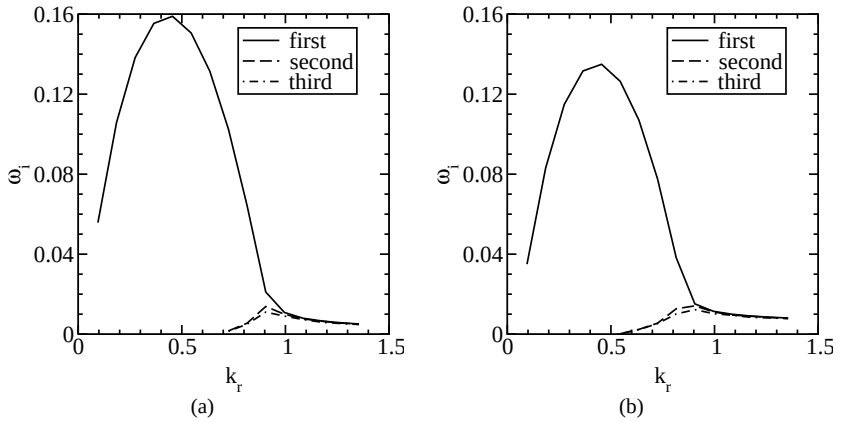

Figure 5.12 Effect of nonuniform loading; $St = 100$, $\ell_p = 10$, and high mass loadings; (a) $\gamma = 5000$, (b) $\gamma = 10000$.

Kelvin–Helmholtz instability is lost which can be observed in Fig. 5.11(d). The primary mode becomes slightly right or left moving depending on the wave number. The pair of Holmboe modes retain the feature of being right and left moving waves with respect to the primary mode, as observed in the low mass loading situation presented before.

In brief, additional instabilities appear only under conditions of large Stokes numbers and high mass loading. This implies that for dilute suspension, only heavy particles can produce this effect. The eigenvalue spectra show the complex behavior of the system in this regime. At high wave numbers a large number of slightly unstable modes are excited with almost equal numbers of right and left moving modes. The primary effect of nonuniform loading is the extension of the unstable wave number range for small and intermediate Stokes numbers, and a change in the nature of the Kelvin–Helmholtz instability from stationary to dispersive. Importantly, the most unstable wave number that would dominate the initial evolution of a mixing layer is not significantly affected by the non–uniformity in the loading.

5.5 CONCLUSIONS

A thorough analysis of the temporal stability of a particle-laden mixing layer was carried out. The mean streamwise velocity was approximated by a hyperbolic-tangent profile and the governing equations were linearized about the mean to obtain the system of perturbation equations. The resulting eigenvalue problem was discretized using finite differences and solved using a QZ matrix eigenvalue algorithm.

New analytical results for the effect of particles on the instability growth rates were obtained in the limit of small and large particle Stokes numbers through the application of formal small-parameter expansions. The destabilizing influence of particles with small Stokes numbers at finite Reynolds numbers was presented; the effect was shown to increase with mass loading. A new expression was derived for the instability growth rate for small Stokes number particles and arbitrary mass loadings. Since larger Stokes number particles have a stabilizing influence, there exists a finite Stokes number where the destabilizing influence is exactly counterbalanced. The variation of this neutral Stokes number with the perturbation wave number was examined using the analytical expressions derived. The neutral Stokes number has been found to be small at high wave numbers and increases as the wave number becomes smaller. It was also found to be independent of the mass loading.

For large Stokes numbers the analysis was performed in two parts, the increasing diameter and the increasing density paths. The volume-fraction was always maintained small to adhere to the constraint of dilute suspensions. The study revealed the following features. If the size of the particles is progressively increased to yield high Stokes numbers, the particles have a vanishing influence on the growth rates. This is due to the decrease in the number density of the particles with increasing Stokes number, which outweighs the effect of an increase in the particle size. In such a scenario, the mass loading remains fixed. Independently, if the density of the particles is increased to yield high Stokes numbers, the particles have a strong stabilizing influence in the limit of large Stokes numbers. This is due to an increase in the mass loading with increasing Stokes number. However, in both the above cases the only relevant quantity turns out to be $\gamma\Lambda/St$ which goes to zero in the former case and remains a fixed value in the latter, in the limit of large Stokes numbers.

For intermediate-Stokes-number particles, the combined response of the particles to the mean flow length scale and the dynamic perturbation length scales results in a wave number-specific attenuation of the growth rate. An increase in mass loading results in a monotonic reduction of the growth rate. The effect of particles of different Stokes numbers on the most unstable wave number and the corresponding maximum growth rate was also presented. The limiting analytical expressions derived were compared to numerical results for a range of Stokes numbers spanning from 0.01 to 100. Good agreement was observed for Stokes numbers up to 0.5 with the small Stokes number expansion and down to a Stokes number of 10 with the large Stokes number expansion. Reconstructing the fluid and particle velocity fields by summing up the mean and perturbation profiles showed that the particle velocity perturbations are such that the particles migrate out of the vortex cores. For higher Stokes numbers the migration takes place faster.

The final part of the contribution dealing with nonuniform particle loadings showed the presence of additional instabilities only for large Stokes numbers and high mass loading. For small and intermediate Stokes numbers an increase in the range of unstable wave numbers was observed whenever the particle loading length scale is much smaller than the mean flow length scale. The non–uniformity also results in the unstable modes no longer being stationary with respect to a frame moving with the reference velocity. The analysis of this stability problem still remains incomplete. From a practical standpoint, the effect of a poly-disperse suspension of particles on the flow is very important. It is not clear if a straightforward extrapolation from current knowledge would be sufficient. The possible lack of equilibrium between the fluid and particle mean velocities should also be considered. The presence of a lag in the streamwise mean particle velocity and a finite settling velocity could have a significant impact on the influence of the particles on the flow stability and are fruitful paths for future research.

6

Mechanisms of particle deposition in channel flow

Le contenu de ce Chapitre est extrait du papier "*On the Mechanisms of particle deposition in a turbulent open channel flow*", paru dans *Phys. Fluids* [1]. **15**/3, 763–775, 2003.
Chidambaram Narayanan, Djamel Lakehal, Lorenzo Botto and Alfredo Soldati

abstract

Particle dispersion and deposition in the region near the wall of a turbulent open channel is studied using direct numerical simulation of the flow, combined with Lagrangian particle tracking under conditions of one–way coupling. Particles with response times of 5 and 15, normalized using the wall friction velocity and the fluid kinematic viscosity, are considered. The simulations were performed until the particle phase reached a statistically stationary state before calculating relevant statistics. For both response times, particles are seen to accumulate strongly very close to the wall in the form of streamwise oriented streaks. Deposited particles were divided into two distinct populations; those with large wall–normal deposition velocities and small near–wall residence times referred to as the *free–flight* population, and particles depositing with negligible wall–normal velocities and large near–wall residence times (more than 1000 wall time units), referred to as the *diffusional deposition* population. Diffusional deposition (deposition induced by the small residual turbulent fluctuations near the wall) is found to be the dominant mechanism of deposition for both particle response times. The free–flight mechanism is shown to gain in importance only for $\tau_p^+ = 15$ particles. For $\tau_p^+ = 5$ particles only 10% deposit because of free flight, whereas the fraction is around 40% for $\tau_p^+ = 15$ particles. This result runs counter to the widely held opinion that free flight is the dominant mechanism of deposition in wall–bounded flows and clearly quantifies the relative importance of the two mechanisms. A simple relationship between the particle wall–normal velocity on deposition and the residence time for free–flight particles is presented. Particle deposition locations over the period of the entire simulation reveal that, while diffusional deposition occurs mostly along streamwise oriented lines below the near–wall particle accumulation patterns, free–flight particles deposit more evenly over the wall.

6.1 INTRODUCTION

Particle deposition in wall–bounded flows has received considerable attention for more than four decades due to its practical relevance to many industrial applications. One of the earliest models of deposition is the one by Friedlander & Johnstone (1957), who proposed the so–called free–flight theory. The essence of this model is that particles are transported by turbulent motions to within one *stop–distance* of the wall, where they acquire sufficient inertia to

[1] Reprinted with the permission of the publisher, *American Institute of Physics*

coast through the viscous sublayer and deposit. This pioneering model was further improved by the work of many researchers. Cleaver & Yates (1975) suggested that the free–flight theory ignores the structure of the near–wall turbulence, and developed a sublayer model for the turbulent deposition process which considered the effect of 'sweep' events in carrying particles to the wall.

Direct numerical simulation (DNS) of a channel flow with Lagrangian particle tracking carried out by McLaughlin (1989) showed that particles tend to gradually accumulate in the viscous sublayer and conjectured that this process of accumulation would continue for times much longer than their simulation interval. Some evidence was also provided on the enhancement of particle accumulation due to the addition of the Saffman lift force in the particle equation. However, the time interval of their simulation was too short to obtain reliable results on deposition rates and other Eulerian statistics, as will be clarified later.

Rashidi *et al.* (1992), describing an experiment in which particles were released in an open–channel flow, underlined the importance of sweep–ejection events in depositing and reentraining particles. They too report an accumulation of particles near the wall and observe that particles with radii less than 0.5 wall units, approaching very close to the wall without depositing, are rarely lifted up by wall ejections. The above observations have been confirmed in another experiment conducted by Kaftori *et al.* (1995*a*), where the motion of particles was found to be intimately related to the action of the quasi–streamwise vortices populating the near–wall region. In a recent DNS study, Marchioli & Soldati (2002) have helped identify the turbulent mechanisms which promote particle accumulation near the wall. They report particle transfer mechanisms due to strong, coherent sweep and ejection events, and specifically point out the effect of small streamwise vortices very close to the wall in promoting particle accumulation under the low–speed streaks. Recently, some attempts to develop empirical models accounting for the near–wall phenomena have been presented Shams *et al.* (2000).

Brooke *et al.* (1992) employed DNS to study particle deposition in a channel flow with the view of evaluating the free–flight theory of Friedlander & Johnstone (1957). By looking at the probability density function (PDF) of the near–wall particle wall–normal velocities, they point out that at any instant only a small fraction of particles have a high enough velocity to execute a free flight to the wall and to deposit. This fact is at odds with the assumption of the original free–flight model, where, at the stop–distance, all particles are supposed to move on a free flight path to the wall Friedlander & Johnstone (1957).In a subsequent paper, Brooke *et al.* (1994) make an interesting subdivision of the particle flux into three components: the free–flight flux, the turbophoretic flux, and the diffusive flux. The turbophoretic flux Reeks (1983) accounts for the particle flux due to gradients in turbulence intensity, whereas the diffusive flux accounts for the particle flux due to concentration gradients. They found that deposition was dominated by particles starting free flights to the wall at large distances from the wall. However, noting the accumulation of particles near the wall, they mention the possibility of particle deposition due to diffusive processes, even though in their simulation the diffusive deposition flux was reported to be insignificant.

An important point to be noted with regard to the above studies (McLaughlin (1989); Brooke *et al.* (1992, 1994)) is the fact that in all simulations the mean particle concentration remained in a state of continuous evolution due to the short simulation times. The wall–normal deposition velocities for most particles was found to be quite high, implying that deposition was predominantly caused by free flight. However, since only a small fraction of the total particle flux directed towards the wall was seen to deposit by free flight Brooke *et al.* (1992), it is natural to expect continued particle accumulation near the wall. In order to reach a steady state under such conditions, some additional mechanism of deposition has to arise to balance the accumulation. Hence, although the diffusive deposition flux was found to be negligible in the above studies, it could become important at later times when a large number of particles have accumulated very close to the wall.

A statement by Brooke *et al.* (1994) in this regard acts as the main motivation for the present work. They state that diffusion is not likely to control the deposition flux *at any time* since most of the particles near the wall are trapped in a region of very small wall–normal velocity fluctuations. Very close to the wall, the distance required by a particle to deposit is very small, but the probability of having large enough momentum to carry the particle across that distance is also extremely small. Brooke *et al.* (1994) hypothesize that particles residing in the near–wall region would need to move away from the wall in order to acquire a high enough velocity to deposit. Present results for similar particle response times show, to the contrary, that the diffusive flux is the dominant deposition flux.

The present study aims at investigating the mechanisms of particle deposition in the wall region of an open channel flow, using DNS for simulating the flow and Lagrangian particle tracking under the conditions of one–way coupling. The focus is on dilute suspensions of particles for which Brownian effects can be ignored, but which interact strongly with the turbulent structures. The study uses the same simulation methodology as van Haarlem *et al.* (1998), who focus in detail on the preferential accumulation phenomenon near the free–slip surface of an open channel, apart from presenting deposition rate coefficients and near–wall variation of particle fluxes. Their method differs from previous numerical work in that it allows the particle field to reach a statistically stationary state

by reintroducing deposited particles at the inflow plane. Although the present study follows their work closely, it provides new insight into the mechanisms of particle deposition onto a flat wall for a fully developed particle field. Various conflicting viewpoints exist in the current understanding of deposition mechanisms as pointed out in the previous paragraph. In this work, we clearly show the two dominant mechanisms of deposition and quantify their relative importance.

The outline of the paper is as follows: in the next section we present the governing equations for the fluid and the particle phases, followed by a section describing the numerical methods used and the particle parameters chosen. In the section on results , we present instantaneous particle concentration patterns both near the wall and near the free–slip surface, deposition coefficients, and particle–phase mean and RMS velocity profiles, in order to put the present study in perspective with respect to previous ones. The last part of this section is devoted to studying deposition velocity statistics in different ways to bring out the dominant mechanisms of deposition. Conclusions are presented at the end.

6.2 GOVERNING EQUATIONS

6.2.1 Fluid equations

The fluid flow in an open channel is described by the Navier–Stokes equations under the assumptions that the fluid is incompressible, isothermal, and Newtonian. The equations are,

$$\frac{\partial u_j}{\partial x_j} = 0 \tag{6.1}$$

$$\frac{\partial u_i}{\partial t} = S_i - \frac{\partial p}{\partial x_i} + \frac{1}{Re}\nabla^2 u_i \tag{6.2}$$

where u_i are the velocity components, $\partial p/\partial x_i$ are the kinematic pressure gradients minus the mean part, and S_i are the nonlinear convective terms minus the mean kinematic pressure gradient. All the variables are normalized by the wall friction velocity $u_\star$ and the half height of the domain h. The friction velocity is defined by $u_\star = \sqrt{< \tau > /\rho}$, where $< \tau >$ is the mean shear stress at the wall. No–slip boundary conditions are imposed at the wall and at the free–slip boundary free–slip conditions are imposed in order to represent an open channel flow Lam & Banerjee (1992).

6.2.2 Particle equations

The motion of particles is described by solving a set of ordinary differential equations for the particle velocity and position at every time instant. Most calculations found in the literature are based on the Maxey & Riley (1983*b*) formulation for the force acting on a rigid sphere in a nonuniform flow under the following conditions: the diameter of the sphere is smaller than the Kolmogorov length scale and the sphere is isolated and far from the boundaries (in this manner particle–particle interaction and particle–boundary interaction are excluded). Moreover, the Reynolds number for the relative motion between the particle and the fluid has to be small. The equation for the particle acceleration thus includes the well–known forces such as buoyancy, fluid (due to the pressure gradient and viscous stresses), added–mass, Stokes drag, and Basset forces.

For the case of particles much heavier than the fluid ($\rho_p/\rho \gg 1$), Elghobashi (1994*b*) have shown that the only significant forces are the Stokes drag, the buoyancy, and the Basset forces. Moreover, they found that the Basset force was always an order of magnitude smaller than the drag and buoyancy forces. In the present work the effect of gravity is not accounted for either. With the above simplifications the following Lagrangian equation for the particle velocity is obtained,

$$\frac{d\mathbf{u}_p}{dt} = -\frac{3}{4}\frac{C_D}{d_p}\left(\frac{\rho}{\rho_p}\right)|\mathbf{u}_p - \mathbf{u}|\,(\mathbf{u}_p - \mathbf{u}) \tag{6.3}$$

where C_D is the drag coefficient given by,

$$C_D = \frac{24}{Re_p}(1 + 0.15Re_p^{0.687}) \tag{6.4}$$

in which Re_p is the particle Reynolds number ($Re_p = d_p|\mathbf{u}_p - \mathbf{u}|/\mu$). The empirical correlation Clift *et al.* (1978) for C_D is necessary because Re_p does not necessarily remain small, in particular for depositing particles McLaughlin (1989). For particles strictly in the Stokes regime ($Re_p \ll 1$), Eq. (6.3) simplifies to,

$$\frac{d\mathbf{u}_p}{dt} = -\frac{(\mathbf{u}_p - \mathbf{u})}{\tau_p} \tag{6.5}$$

where τ_p $(= \rho_p d_p^2/18\mu)$ is the particle response time, which is a measure of the time required by a particle released at rest to reach velocity equilibrium with the surrounding fluid.

Other authors McLaughlin (1989); Wang *et al.* (1998) have also considered the Saffman lift force that could be important near the boundaries. This force acts in the wall–normal direction and is proportional to the wall–normal gradient of the streamwise fluid velocity. Therefore, its contribution might be important near the wall and could influence the particle deposition rate McLaughlin (1989). However, Wang *et al.* (1998) in their study of the role of the lift force in particle deposition have found that neglecting the lift force altogether results in only a slight reduction in the deposition rate. Moreover, since many of the previous studies do not account for this term, it has not been included in the present study to facilitate direct comparison.

6.3 NUMERICAL PROCEDURE

6.3.1 Direct numerical simulation of the open channel flow

The fluid equations are solved using a pseudo–spectral method based on Fourier representations in the streamwise and spanwise directions and a Chebychev representation in the wall–normal (nonhomogeneous) direction. For time marching, a two–level explicit Adams–Bashforth scheme was employed for the nonlinear terms and an implicit Crank–Nicholson scheme for the viscous terms. Further details of the numerical procedure can be found in Lam and Banerjee Lam & Banerjee (1992).

The dimensions of the computational domain are chosen to be $l_x = 4\pi h$, $l_y = 2\pi h$, $l_z = 2h$, in the streamwise, spanwise, and normal directions, respectively. In wall units (i.e. normalized using the kinematic viscosity and the friction velocity) the dimensions are $(l_x^+, l_y^+, l_z^+) = (1074, 537, 171)$. A grid consisting of $64 \times 64 \times 65$ nodes was used to perform the computations. A nonuniform distribution of collocation points is used in the normal direction for the Chebychev polynomials, with the grid spacing varying from $\Delta z^+ = 0.10$ near the wall to $\Delta z^+ = 4.19$ in the domain center. The shear Reynolds number of the flow defined as $Re_* = u_* h/\nu$ was chosen to be 85.5. Periodic boundary conditions were imposed in the streamwise and spanwise directions.

6.3.2 Lagrangian particle tracking

A Lagrangian particle tracking code Narayanan *et al.* (2002) has been used to track particles in the flow field. The code interpolates fluid velocities at discrete grid nodes onto the particle position, and with this velocity the equations of motion of the particle are integrated in time.

The code incorporates linear, cubic and fifth–order Lagrangian polynomials for interpolation yielding second, fourth, and sixth–order accuracy, respectively. For the time integration the module has the choice between second and fourth–order Runge–Kutta, and second–order Adams–Bashforth schemes. A parametric study Botto (2002) was conducted to choose the appropriate numerical methods for interpolation, integration, and the number of particles needed to obtain accurate statistics. For the simulations presented here, 100000 particles were tracked using fourth–order Runge–Kutta time integration and fourth–order Lagrangian polynomial interpolation for an interval of 5436 wall time units.

At the start of the simulation, particles were distributed homogeneously over the computational domain. The positions of the particles were chosen randomly and their initial velocity was set equal to the fluid velocity.

6.3.2.1 Particle–phase boundary conditions When a particle leaves the domain across the outflow plane or in the spanwise direction periodic boundary conditions are applied for both the position and the velocity of the particle. The wall and free–slip boundaries are considered to be completely absorbing; a particle at a distance less than one particle radius from these boundaries is assumed to have deposited and is removed.

Since the total number of particles has to be maintained constant in time to reach statistically stationary conditions, a particle is reintroduced in the domain at the inflow plane (at $x^+ = 0$), whenever a particle deposits at the wall or the free–slip boundary. The spanwise and normal coordinates of the reintroduced particle are chosen randomly

and their velocity is set equal to the fluid velocity at that position. This procedure introduces a constraint wherein the velocities of the reintroduced particles are necessarily affected by the imposed initial conditions for a certain amount of time.

According to the arguments presented by van Haarlem *et al.* (1998) the distance covered by a $\tau_p^+ = 15$ particle before its velocity becomes independent of the inflow conditions is approximately ten times the height of the channel (which is equivalent to 1700 wall units in the present work). As this length is greater than the streamwise extent of the fluid domain, a longer domain has to be adopted for tracking the particles. The streamwise extent of this domain was set to $5 \times l_x$, whereas the spanwise and normal dimensions were kept unchanged. The dimensions of the computational domain in which the particles were tracked were thus, $L_x = 5370$, $L_y = 537$ and $L_z = 171$ in the streamwise, spanwise, and normal directions, respectively. The fluid velocity at every grid point was obtained simply by a periodic extension of the original flow in the streamwise direction. Moreover, only particles located more than 1700 wall units away from the inflow plane were considered for analysis. This method is the same as that used by van Haarlem *et al.* (1998).

This procedure offers a twofold advantage: firstly, it allows the particle–phase to reach a statistically stationary state due to the reintroduction process, and secondly, particle statistics can be computed as a function of both the wall–normal and the streamwise directions without any effect of the imposed inflow conditions.

6.3.3 Particle parameters

Studies on particle deposition suggest that based on the nondimensional particle response times three different regimes of deposition can be defined Young & Leeming (1997). For very small particles with $\tau_p^+ < 0.2$ the deposition rate decreases as τ_p^+ increases. In this regime, particle transport is well represented by a gradient diffusion model accounting for turbulent diffusion in the bulk flow and Brownian diffusion in a thin region adjacent to the wall.

For $0.2 < \tau_p^+ < 20$ a dramatic increase of several orders of magnitude in the deposition rate is observed as the particle time constant increases. This regime is referred to as the *diffusion–impaction* regime, and the observed increase in deposition is mainly due to the strong interaction between particles and the turbulent eddies. In this regime transport of particles due to turbulence plays an important role. In the third regime, known as the *inertia–moderated* regime, particles having very high inertia acquire sufficient momentum from eddies in the turbulent core to reach the wall. Here diffusion plays a very small role and deposition tends to decrease with an increase in the particle time constant, as the response of the particles to the turbulence becomes weaker Young & Leeming (1997).

Two sets of particles with $\tau_p^+ = 5$ and 15 belonging to the diffusion–impaction regime have been chosen in this study, since the aim is to understand the contribution of turbulence to particle deposition. The values are the same as those studied by van Haarlem *et al.* (1998) and have been chosen to facilitate comparison.

6.4 RESULTS AND ANALYSIS

6.4.1 Preferential concentration

The phenomenon of preferential concentration of particles is one of the most important aspects of this problem. Several animations and snapshots of the particle field clearly reveal varied concentration patterns both in the bulk and near the boundaries.

Starting with a uniform distribution, particles quickly assume a inhomogeneous distribution as they start moving towards both boundaries, due to the phenomenon of turbophoresis. This results in the accumulation of particles, particularly in the near–wall region. The accumulation process continues for a long time until a sharp peak in the concentration is formed in the near–wall region, as shown in the following section. Also, the distribution of particles near the wall is far from being homogeneous in the spanwise direction. The particles, in fact, accumulate in streamwise–oriented streaks. Instantaneous correlation between particle streaks near the wall and the low–speed streaks in a turbulent boundary layer has been established previously (Rashidi *et al.* (1992); Kaftori *et al.* (1995*a*); Marchioli & Soldati (2002); van Haarlem *et al.* (1998)). Instantaneous near–wall particle concentration patterns are shown in Fig. 6.1 for both particle response times, for $z^+ < 3$. Both sets of particles strongly accumulate in streamwise streaks.

Once the particles reach the region near the free–slip boundary, they are subjected to the large–scale structures characteristic of free–surface turbulence such as upwellings, down–drafts, and attached vortices van Haarlem *et al.* (1998). Typical particle concentration snapshots near the free surface ($z^+ > 150$) are shown in Fig. 6.2. Particles

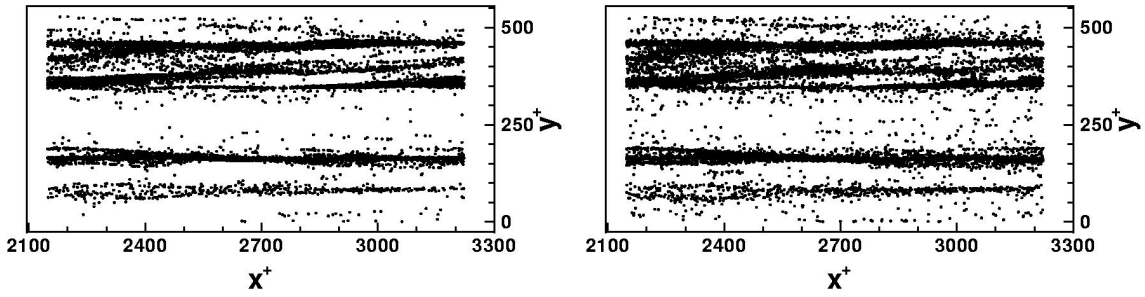

(a)

Figure 6.1 Particle accumulation patterns near the wall (a) $\tau_p^+ = 5$, (b) $\tau_p^+ = 15$.

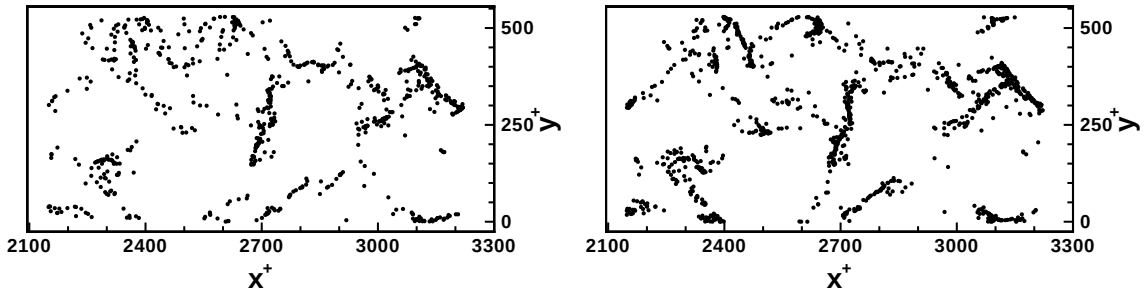

(a)

Figure 6.2 Particle accumulation patterns near the free surface (a) $\tau_p^+ = 5$, (b) $\tau_p^+ = 15$.

are distributed in the form of roughly circular and elongated voids surrounded by thin regions of high concentration, very similar to those obtained by van Haarlem *et al.* (1998) The behaviour of particles near the free surface will not be discussed further, as the study primarily focuses on near–wall deposition mechanisms.

6.4.2 Particle concentration profiles

Figure 6.3 presents the development of particle number concentration along the streamwise direction. Statistics were obtained by dividing the domain into cross–stream bins of 200 wall units each. The mean concentration in each bin is normalized by the concentration in the case of uniform particle distribution over the entire domain. As expected, the concentration shows an overall decreasing trend which accounts for particle deposition at both boundaries. A discrepancy can be observed at the beginning of the domain, which may be ignored, since the particles there are still affected by the imposed conditions on reintroduction at the inflow plane. The periodic undulations in the concentration, though, require further clarification.

The periodic undulations seen in Fig. 6.3(a) are an obvious artifact of the periodic extension of the flow domain. Periodic patterns are formed immediately at the start of the simulation and the particles accumulated very close to the wall retain a memory of this fact for a long time due to the quiescent nature of the region and because of their small streamwise velocity. Thus, the actual flow–through time required to wipe out these undulations would be much higher than the current simulation period making it computationally prohibitive. Indeed, in Fig. 6.3(b), showing the streamwise concentration profile obtained with the procedure described previously, but accounting only for particles located in the region $3 < z^+ < 171$, the profile is almost linear, confirming the observation that the periodic features are mainly due to particle accumulation patterns in the region very close to the wall ($z^+ < 3$). Figure 6.3(b) now clearly reveals the difference in the rate of change of bulk concentration between $\tau_p^+ = 5$ and $\tau_p^+ = 15$ particles. It points to the fact that $\tau_p^+ = 15$ particles have a higher overall deposition rate and a higher concentration in the bulk.

The variation of particle concentration along the wall–normal direction at equilibrium (i.e. when the statistically stationary state is achieved; $t^+ > 1000$) is shown in Fig. 6.4. In this case, the bin height was kept constant

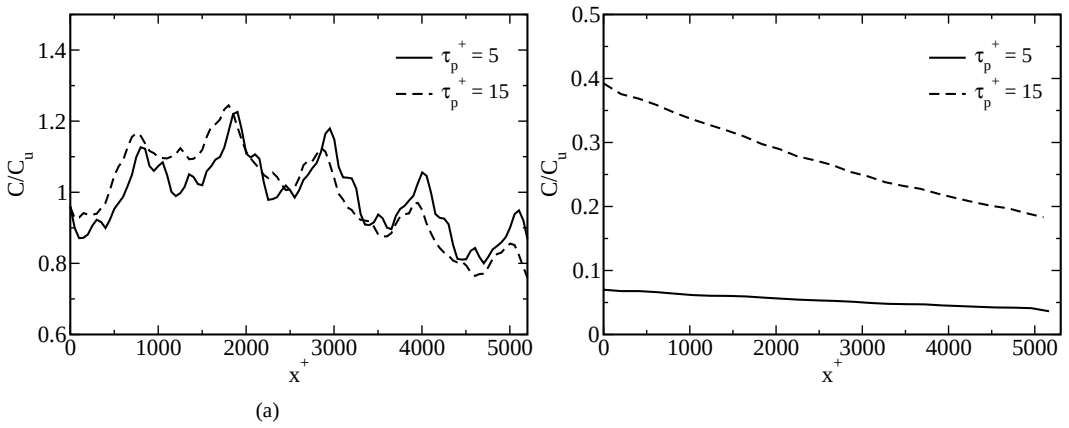

Figure 6.3 (a) Streamwise variation of the cross-section averaged concentration, (b) not accounting for particles accumulated very close to the wall ($z^+ < 3$).

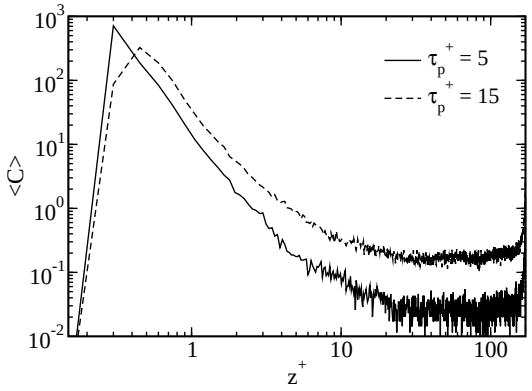

Figure 6.4 Average particle concentration profile in the wall-normal direction.

at $\Delta z^+ = 0.15$. The distribution shown refers to a region located in the center of the computational domain ($x^+ = 2400 - -2600$), and the time–averaged concentration in every slab has been normalized by the average concentration of particles in the region considered (i.e. setting the integral across the channel height and width equal to unity). A large increase in particle concentration very close to the wall is observed. Peak values occur at $z^+ = 0.3$ for $\tau_p^+ = 5$ particles and at $z^+ = 0.4$ for $\tau_p^+ = 15$ particles. Particle concentration is higher for $\tau_p^+ = 5$ particles very close to the wall ($z^+ < 0.4$), whereas the opposite is true for $z^+ > 0.4$. This behaviour very close to the wall has not been reported in any of the previous studies.

Particle accumulation near the wall has also been observed by other authors (McLaughlin (1989); Rashidi *et al.* (1992); Marchioli & Soldati (2002); van Haarlem *et al.* (1998)) in both numerical simulations and experiments. However, a great deal of ambiguity exists between the values and the way the statistics were obtained. In particular, van Haarlem *et al.* (1998), who studied conditions similar to those considered here, do not report such high peaks near the wall for the same particle response times. Their values are of the order of 10, normalized by the initial uniform concentration. This is due to the larger bin size they have used to calculate the average quantities. In fact, their first bin was ten times larger than the one used in the present study. Also, they could not have captured the variation at distances less than one wall unit mentioned in the previous paragraph. In van Haarlem's work, accumulation of particles near the wall is higher for the higher–response–time particles. This trend is confirmed only up to a distance of $z^+ > 0.4$ in the present calculations. Very close to the wall the trend is inverted. A possible scenario to explain this observation is presented below.

Time evolution of the particle concentration (not shown here) indicates clearly that turbophoresis plays an important role in particle dispersion. Since the initial particle distribution is homogeneous, the only mechanism at the beginning capable of inducing a net drift towards the wall is turbophoresis. Referring to the region of maximum particle concentration as the accumulation zone (AZ) and looking at the fluxes towards and away from it at steady state, one can discern a balance between four main contributions: (i) turbophoresis, where particles migrate from

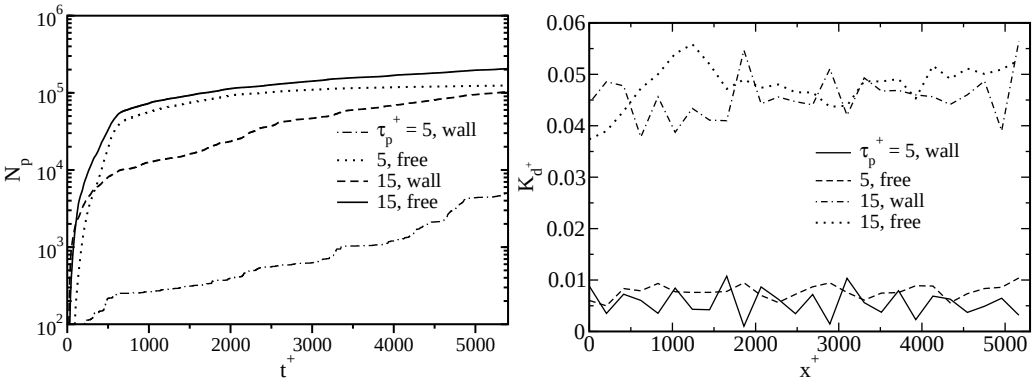

(a)

Figure 6.5 (a) Cumulative number of particles deposited at the lower and upper boundaries, (b) Deposition coefficient at the lower and upper boundaries

the bulk flow towards the AZ, (ii) free–flight deposition flux, which represents a fraction of the turbophoretic flux passing directly through the AZ and leading to deposition, (iii) *turbulent diffusion* flux acting to smooth the concentration build up in the AZ, and (iv) diffusional deposition flux which again acts to remove particles from the AZ by deposition due to the residual turbulent fluctuations at the AZ. Note that, although in standard parlance the term *turbulent diffusion* accounts for all the above transport mechanisms, here it is specifically meant to signify only the effect of turbulence to smooth out concentration gradients.

Since the deposition of $\tau_p^+ = 5$ particles is mainly due to diffusional deposition (as will be shown later), one would expect the concentration build up required to balance the turbophoretic flux to be higher. Also, the diffusional deposition for $\tau_p^+ = 5$ is less efficient as compared to $\tau_p^+ = 15$ because of the lower level of particle normal–velocity fluctuations at the AZ (refer to Fig. 6.9). This would strengthen the case for a higher near–wall concentration of $\tau_p^+ = 5$ particles. According to the above scenario, it would be logical to expect a higher concentration very close to the wall for $\tau_p^+ = 5$ particles. However, the situation is quite complicated and a detailed study of the near–wall flux balance would be required to resolve this issue.

It is interesting to note that there is also a slight accumulation of particles at the upper boundary for the cases considered, with values two to three times larger than the bulk concentration. This phenomenon has also been reported by van Haarlem *et al.* (1998) and is again attributed to turbophoresis since the free–slip boundary condition generates a gradient in the wall–normal turbulence intensity in the normal direction.

6.4.3 Deposition rate

Figure 6.5(a) shows the cumulative number of particles impinging on the boundaries as a function of time. The slope of the curve reaches an asymptotic value after approximately $t^+ > 1000$. This reflects the fact that after a transient period in which particles redistribute in the domain, the number of particles depositing every instant of time is almost constant. The deposition rate is a strong function of particle inertia, being larger for $\tau_p^+ = 15$ than for $\tau_p^+ = 5$.

The deposition of smaller particles on the wall is remarkably low. The underlying reason is that a large number of these particles reside very close to the wall without depositing and keep continuously accumulating. These particles neither deposit for long times nor are they significantly reentrained in the core flow on reaching the near wall region. This phenomenon was observed by Kaftori *et al.* (1995*a*), and it mainly characterizes experiments with small particles and low shear rate.

The deposition coefficient is defined by

$$K_d^+ = \frac{J_w}{C_m u_\star} \tag{6.6}$$

where J_w is the mass of particles reaching the surface per unit area per unit time, C_m is the mean bulk concentration of particles, and $u_\star$ is the friction velocity. Note that the concentration can alternatively be expressed in terms of number or mass density, as the suspension is mono–disperse.

The nondimensional deposition coefficient is presented in Fig. 6.5(b) as a function of the streamwise coordinate. Here slabs of $\Delta x^+ = 200$ were used. Tests performed showed that the calculated quantities were actually insensitive

EXP/DNS	St=5	St=15
(Exp. McCoy & Hanratty (1975))	0.0081	0.073
(Exp. Liu & Agarwal (1974))	0.015	0.135
(DNS van Haarlem *et al.* (1998))	0.0064	0.051
Present (DNS)	0.0056	0.045

Table 6.1 Comparison of deposition coefficients from the present study and from previous works.

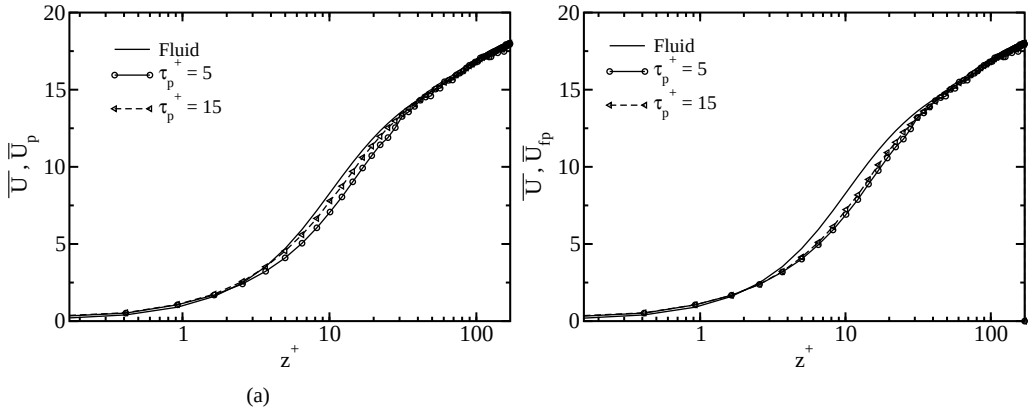

(a)

Figure 6.6 (a) Mean particle streamwise velocity, (b) Mean streamwise fluid velocity at particle positions.

to the exact slab thickness. The deposition rate is observed to be rather uniform along the streamwise direction. The deposition rates on the wall are reported in Table 6.1 compared to the values found in the literature. The values of the present simulations are in general smaller than those reported in experiments; the comparison shows, for instance, the deposition rate to be three times lower than the data of Liu & Agarwal (1974) and 40–60% lower than those of McCoy & Hanratty (1975). It can be argued that there is no general agreement among authors on the exact values of the deposition rate. Reportedly, experiments show a wide range of different deposition rates for a given particle response time. For example, one of the key differences could be due to the mean concentration profile existing when the deposition rate was measured. Brooke *et al.* (1994) report that in the experiment of Liu & Agarwal (1974) droplets were distributed uniformly in a vertical pipe flow. In the present case, the mean profile shows a sharp peak very close to the wall.

Other reasons for the differences could be as follows: The inclusion of the Saffman lift force would enhance deposition as discussed in Section 6.2.2. Moreover, the near–wall accumulation of particles being very high, other effects, not easily reproducible by numerical simulation, could become important in reality (e.g. particle–fluid interaction or two–way coupling, particle–particle interaction, etc.). Differences in the turbulence properties can also bring about significant changes. In fact, experimental databases are obtained in physical situations significantly different from those simulated here (e.g. pipe flow at higher Reynolds number).

6.4.4 Velocity statistics

6.4.4.1 Mean velocity Particles having finite inertia accumulate preferentially in the flow both in the bulk and in the near–wall region as discussed in previous sections. Evidently, the particle–phase velocity statistics would not be the same as those of the fluid. Figure 6.6(a) shows the particle–phase mean streamwise velocity as compared to the fluid. Particle velocity on average is seen to lag behind the fluid. This is surprising for a particle field in equilibrium with the flow, unless one accounts for the preferential concentration of particles in specific regions of the flow which could be characterized by lower average velocities (in this case, the low–speed streaks). A lower particle–phase streamwise velocity was also obtained by Rouson & Eaton (2001) in their channel flow simulations for a similar particle response time.

Figure 6.6(b) shows the mean streamwise velocity obtained by considering the fluid velocity at the particle positions (FVPP) rather than the particle velocities themselves. If the particles were not preferentially distributed in the domain, the profiles for the fluid and FVPP should coincide (to within statistical uncertainty). Therefore, the extent of deviation between these two quantities can be taken as a quantitative estimate of the magnitude of

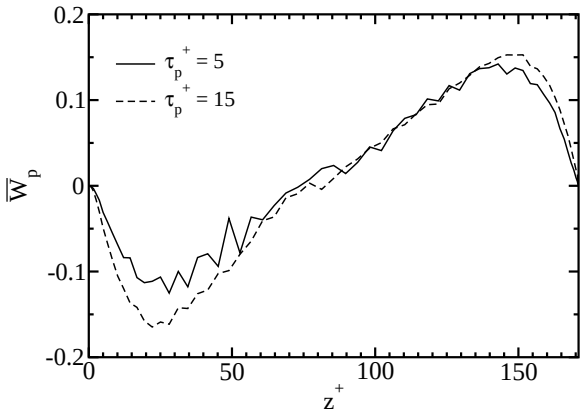

Figure 6.7 Mean particle wall-normal velocity.

preferential concentration. Figure 6.6(b) shows that the region with the largest deviation between the particle streamwise velocity and the fluid velocity corresponds to the region with higher preferential concentration. One should also note that particles with $\tau_p^+ = 5$ are slightly more preferentially concentrated than $\tau_p^+ = 15$ particles.

As can be observed in Fig. 6.6(a), $\tau_p^+ = 15$ particles exhibit a slightly larger mean velocity than $\tau_p^+ = 5$ particles, especially in the region $5 < z^+ < 30$. This behaviour has not been noticed in the work of van Haarlem *et al.* (1998). In their work, no difference in the mean streamwise velocity was found between the two sets of particles. In reality, since both sets of particles accumulate in the low–speed streaks, a quantitatively lower accumulation would imply a higher mean velocity for the $\tau_p^+ = 15$ particles.

It is interesting to note that in the experiments of Kaftori *et al.* (1995*b*) for smaller response times than in the current study ($\tau_p^+ = 0.065, 0.51, 4.41$) the streamwise velocity defect increases with increasing particle response time. Rouson & Eaton (2001) obtain similar results as the present study for $\tau_p^+ = 8.6$ but for larger response times ($\tau_p^+ = 117$ and 810) the particle streamwise velocity is greater than the fluid velocity (in this case, the gravitational acceleration along the streamwise direction was also considered). The reason for this varied behaviour is the dependence of the extent of preferential concentration on the particle response time.

Studies conducted for homogeneous isotropic turbulence Wang & Maxey (1993) show that there exists a critical particle response time which results in maximum preferential accumulation (the value for homogeneous turbulence being of the order of the Kolmogorov time scale). For response times higher and lower than this critical value preferential accumulation is quantitatively lower, which in this particular case would translate into a higher mean velocity. Thus, for increasing particle response times the mean streamwise velocity will first see an increase in the lag up to the critical response time, and from then on a trend in the opposite direction. Therefore, the observed trend in the streamwise velocity would depend on the position of particle response times relative to the critical particle response time. Although it has been shown Rouson & Eaton (2001); Fessler *et al.* (1994) that the Kolmogorov scale remains an appropriate time scale for characterizing preferential concentration for channel flows, a more accurate quantitative estimate for this critical particle response time is not available. As the Kolmogorov scale for inhomogeneous turbulent flows also varies with position, the exact behaviour is difficult to quantify without further detailed study.

Figure 6.7 presents the particle–phase mean wall–normal velocity. Even if the fluid has a zero wall–normal velocity, the particles do have a nonzero wall–normal velocity on average. This is consistent with the fact that for deposition to occur, particles must have a mean drift velocity towards the boundaries. The velocity towards the wall is higher for $\tau_p^+ = 15$ particles signifying a higher deposition rate. Qualitatively similar results have been presented previously for a pipe flow problem Young & Leeming (1997); Cerbelli *et al.* (2001). However, since these studies use a Reynolds–averaged approach involving modelling the complex turbulent transport mechanisms in both phases, the results presented here are more reliable and can be looked upon as a validation of previous results. Most of the other studies have not reported the Eulerian particle–phase mean wall–normal velocity which would be very useful for model validation.

6.4.4.2 Turbulence intensity

Turbulence intensity profiles in the streamwise, spanwise, and normal directions are shown in Fig. 6.8. As can be observed in all cases, particles have a lower fluctuation intensity than the fluid except very close to the wall. The near–wall behaviour will be discussed later. A comparison of the results with the data of Brooke *et al.* (1994) is satisfactory, whereas the comparison with those of van Haarlem *et al.*

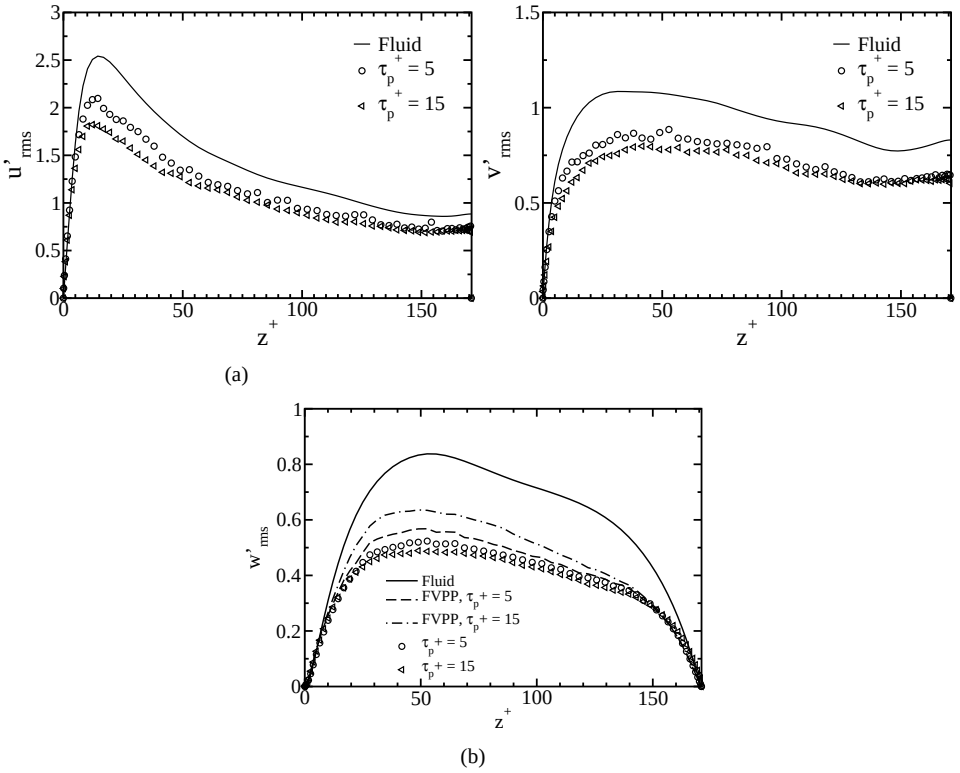

Figure 6.8 Particle-phase turbulence intensity, (a) streamwise, (b) spanwise, and (c) wall-normal directions.

(1998) is not. However, the fact that the latter authors report RMS values for $\tau_p^+ = 5$ particles higher than the fluid is difficult to reconcile.

The particle phase turbulence intensity is lower than the fluid due to two mechanisms acting in tandem. The first mechanism is preferential concentration of particles in regions with lower turbulence intensity (for example, low speed streaks) and the second one is the unresponsiveness of a particle to high frequency or wave number fluid fluctuations due to its inertia. For Stokesian particles in homogeneous turbulence, an expression relating the power spectrum of the particle velocities to that of the fluid velocities can be derived **?**:

$$E_p(\omega) = \frac{1}{1 + \tau_p^{+2}\omega^2} E_f(\omega) \tag{6.7}$$

where ω is an angular frequency and E_p and E_f are the particle and the fluid velocity spectra along the particle path, respectively. This expression shows that even in the absence of preferential concentration, the particle fluctuating intensity is suppressed[†]. For ease of further discussion, we refer to this effect as *inertial filtering* **?** due to fact that the particle energy spectrum can be obtained from the fluid spectrum through the action of a filtering function. Inertial filtering is the incomplete response of a single particle to its fluctuating fluid environment whereas preferential concentration is related to pattern formation and loses meaning for an isolated particle. Another difference between the two mechanisms is that while the inertial filtering effect increases monotonically with particle inertia, preferential concentration has a more complex dependence on particle inertia. It must be noted that both the above effects are due to the inertia of the particles.

To quantify the contributions of these mechanisms, the fluctuation intensity of the *fluid velocities at the particle positions* (FVPP) is also presented in Fig. 6.8(c) along with the particle velocity fluctuation intensity. The fluctuation intensity of FVPP represents the average turbulence intensity felt by the particles and captures the effect of preferential concentration on the particle velocity fluctuation intensity. The figure shows that preferential concentration does cause a large decrease in the particle velocity fluctuation intensity. It shows that $\tau_p^+ = 5$ particles have a higher chance of being in regions of lower turbulence intensity as compared to $\tau_p^+ = 15$ particles. This is

[†]We thank one of the reviewers for bringing this point to our attention.

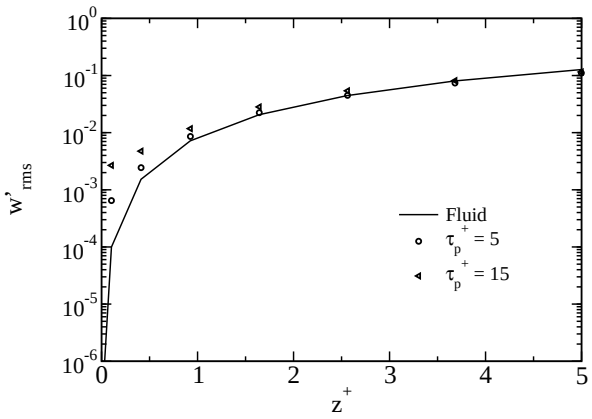

Figure 6.9 Near-wall variation of particle wall-normal turbulence intensity.

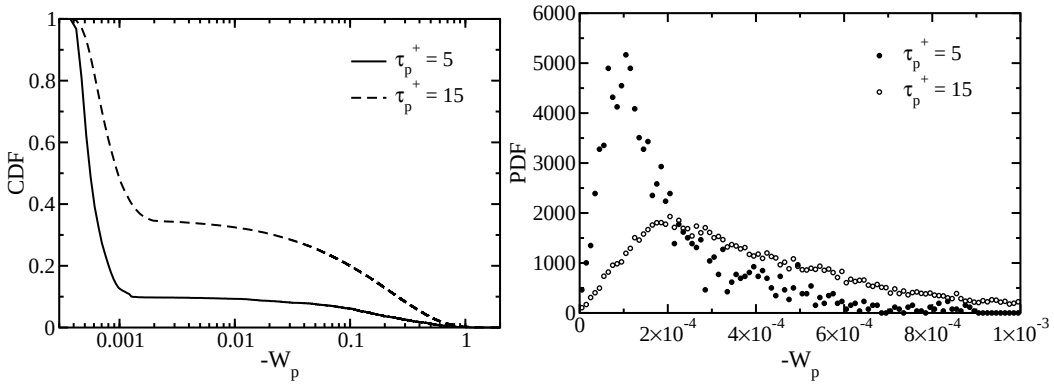

(a)

Figure 6.10 (a) Cumulative distribution function, (b) Probability density function of wall-normal velocity of depositing particles

consistent with the previous observation that $\tau_p^+ = 5$ particles are more preferentially concentrated than $\tau_p^+ = 15$ particles. Inertial filtering results in a further reduction in the particle velocity fluctuation intensity with respect to the fluctuation intensity of FVPP because of the inability of the particles to respond to the small–scale fluid fluctuations in the surrounding fluid.

The departure of the particle turbulence intensity from the fluctuation intensity of FVPP is again a function of the particle response time. Particles with $\tau_p^+ = 5$ can follow the local fluid turbulent motion better than $\tau_p^+ = 15$ particles. Their turbulence intensity, therefore, is very close to the fluctuation intensity of FVPP, whereas a significant difference between the two quantities exists for $\tau_p^+ = 15$. For large particle response times the reduction in particle turbulence intensity can be attributed mainly to inertial filtering as preferential concentration effects will be small. However, for the response times studied in this work, both the mechanisms play a significant part in reducing the particle turbulence intensity.

Very close to the wall, it can be observed from Fig. 6.9 that the RMS of particle normal–velocity fluctuations remain nonzero, with $\tau_p^+ = 15$ particles having a significantly higher RMS value as compared to $\tau_p^+ = 5$ particles. This implies that the diffusional deposition process for $\tau_p^+ = 15$ particles would be more efficient.

6.4.5 Mechanisms of particle deposition

In this section we first present the cumulative distribution function of particle deposition velocities in Fig. 6.10(a). Here W_p denotes the wall–normal velocity of a depositing particle oriented towards the wall. Reading from right to left, it indicates the probability that a particle deposits with a velocity higher than the value on the abscissa. A large increase in probability around $W_p \approx 0.001$ can be observed for both particle response times. The figure suggests the possibility of dividing the population of sampled velocities into two groups: population A with low

deposition velocities, and population B with high velocities. The division is necessarily arbitrary, but the existence of a significant intermediate range of velocities where no deposition occurs (the flat portion of the curves) clearly implies such a separation.

For $\tau_p^+ = 5$ particles almost 90% deposit with velocities smaller than 0.001, and the remaining 10 % deposit with velocities greater than 0.1. For $\tau_p^+ = 15$ particles, the corresponding fractions are 60% and 40%, respectively. As mentioned by Brooke *et al.* (1994), particles depositing with a velocity roughly equal to the fluid velocity fluctuations very close to the wall may be said to undergo *diffusional deposition*. On the other hand, particles depositing with velocities much larger than the near–wall velocity fluctuations may be referred to as *free–flight particles*. Using this definition, the present study suggests that once the particle field has reached a statistically steady state, the dominant mechanism of deposition is diffusional. The free–flight population, however, constitutes a significant fraction for $\tau_p^+ = 15$ particles. Figure 6.10(b) shows the PDF for normal velocities of the deposited particles. The peaks correspond to velocity values of around 1×10^{-4} for $\tau_p^+ = 5$ particles and of 2×10^{-4} for $\tau_p^+ = 15$ particles, confirming the above fact.

At this point, an interesting comparison can be made between the present study and some of the previous work (McLaughlin (1989); Brooke *et al.* (1992, 1994)) mentioned earlier. Brooke *et al.* (1994) found that most of the depositing particles have a velocity much higher than the RMS wall–normal velocity near the wall. This led them to conclude that deposition occurs predominantly because of the free–flight process similar to the model proposed by Friedlander & Johnstone (1957). They also found that the number of particles depositing by diffusion is small and that the diffusion flux is negligible. Thus, their conclusions run exactly counter to the results obtained in the present study. This fact is also observed in the probability density function (Fig. 6.10(b)), where, in the case of Brooke *et al.* (1994), the value of the most probable deposition velocity is around 1000 times larger for similar particle response times. This is understandable because, in their simulation, free flight was the only observed mechanism of deposition.

The reason for this drastic discrepancy lies in the differences between the simulation procedures. In their work, approximately 16000 particles were released from a plane at $z^+ = 40$ and were tracked for 700 wall time units. The deposited particles were removed and not reintroduced into the flow, thus precluding the possibility of achieving a statistically stationary state. Also, given the short simulation time, they report that the mean concentration profile continues to evolve throughout the simulation. In the present study, the simulation was carried out for more than 5000 wall time units, so that an acceptable steady state was reached for the calculation of the deposition coefficient (refer to Fig. 6.5(a)). At steady state, the concentration near the wall becomes high enough for diffusional deposition to be dominant. Since only a small fraction of the particles arriving near the wall have large enough velocities to deposit by free flight Brooke *et al.* (1992), a steady state can be reached only by an increase in diffusional deposition. Although this process of deposition is not very efficient because of the quiescent environment close to the wall, it is aided by the large accumulation of particles very close to the wall. Moreover, a lower concentration away from the wall results in a reduction in the number of possible free–flight particles.

To analyze this claim further, a particle residence time analysis has been conducted. The time spent by a particle before deposition in a slab 3 wall units from the wall has been recorded. An algorithm was implemented such that, if a particle escapes from the slab before depositing (due to reentrainment), the time counter for this particle was reinitialized to zero. Figure 6.11 shows a scatter plot of the particle residence time versus the particle wall–normal velocity on deposition. The two populations of diffusional and free–flight particles can now be distinguished more clearly in combination with the residence time. The free–flight population can now be defined as particles having both a high deposition velocity and a short residence time, and the diffusional deposition particles are those with very small deposition velocities and very large residence times. Logarithmic scales have been deliberately adopted to clearly show the separation between the two different populations.

6.4.5.1 Free–flight mechanism

The behaviour of the deposition velocity versus residence time shown for the free–flight particles in Fig. 6.11 can be explained using a very simple analysis. Assuming that the particle wall–normal velocity is much larger than the wall–normal fluid velocity fluctuations in the near–wall region ($z^+ < 3$ for the residence time analysis), then the equation for the particle wall–normal velocity can be approximated by,

$$\frac{dW_p}{dt} = -\frac{W_p}{\tau_p^+} \tag{6.8}$$

the solution of which is obtained as,

$$W_p = W_{p,[z^+=3]}\ \exp(\frac{-t}{\tau_p^+}) \tag{6.9}$$

.27ure[]

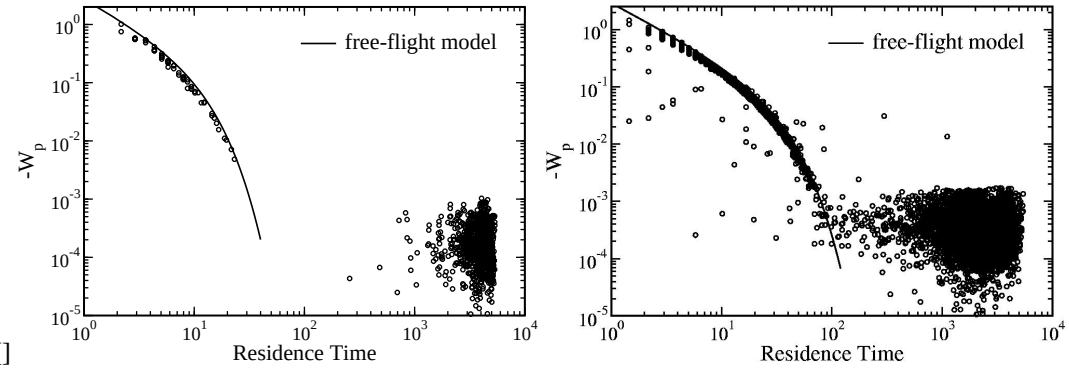

Figure 6.11 Residence time of particles in the slab $z^+ < 3$ versus deposition velocity for (a) $\tau_p^+ = 5$, (b) $\tau_p^+ = 15$.

The wall–normal velocity at deposition, W_{dep}, therefore is,

$$W_{dep} = W_{p,[z^+=3]}\ \exp(\frac{-t_{res}}{\tau_p^+}) \tag{6.10}$$

where t_{res} is the residence time of the particle. Solving for the position of the particle such that $z^+ = 3$ at $t^+ = 0$ and $z^+ = 0$ at $t^+ = t_{res}$, the following condition is obtained,

$$3 = W_{p,[z^+=3]}\ \tau_p^+\ [\exp(\frac{-t_{res}}{\tau_p^+}) - 1] \tag{6.11}$$

Eliminating $W_{p,[z^+=3]}$ from Eqs. (6.10) and (6.11), a relationship between t_{res} and W_{dep} is obtained,

$$\tau_p^+\ W_{dep}\ [\,1 - \exp(\frac{t_{res}}{\tau_p^+})\,] = 3 \tag{6.12}$$

where the number 3 on the right–hand side is the slab height chosen for the residence time analysis.

This expression matches very well the actual behaviour obtained by the DNS for particles with $\tau_p^+ = 5$ as well as 15, as shown in Fig. 6.11. As the velocity of the particles entering the slab becomes smaller and comparable to the RMS fluid velocity in the region (< 0.01), it is no longer appropriate to neglect the effect of the fluid velocity fluctuations on the particle path, and the assumption of free flight breaks down. Particles now do not have sufficient momentum to deposit directly and remain in the slab for longer periods of time until they deposit by a random process due to the residual fluctuations near the wall.

6.4.5.2 Preferential deposition Another interesting statistic is the location where particles tend to deposit on the wall. At every time step, only a few particles deposit, hence no preferential zones can be discerned when taking instantaneous snapshots of deposition locations. Figure 6.12 shows the locations where particles have deposited on the wall over the whole simulation interval. This can be considered as the probability that a particle deposits at a certain position on the wall. In the figure, the diffusional deposition population is shown in grey.

An examination of the distribution leads to the conclusion that the diffusional deposition population deposits preferentially in streamwise oriented streaks, while the free–flight ones are more evenly distributed over the whole plane. This is not surprising, since diffusional deposition particles come from locations very close to the wall, where particles have already accumulated in such streaks. These near–wall streamwise particle streaks have a long lifetime because they exist very close to the wall in a particularly quiescent region, and move with very small streamwise velocity. Consequently, particle distribution at the deposition position clearly reflect the near wall particle distribution. On the other hand, free–flight particles arrive from regions further away from the wall, where larger scale fluid motions project particles more evenly towards the wall. This result has not been presented in previous studies.

6.5 SUMMARY AND CONCLUSIONS

Direct numerical simulation of a turbulent open channel flow was combined with Lagrangian particle tracking to study the mechanisms of particle deposition onto the wall. Particles with inertial response times of 5 and 15 were

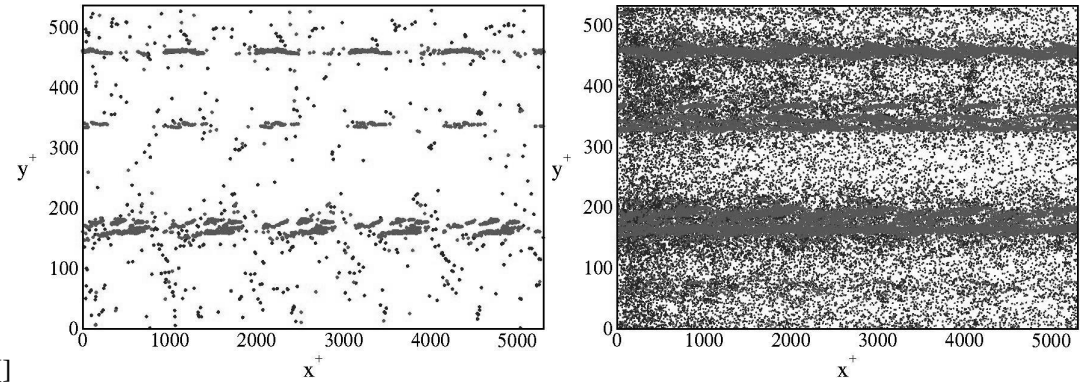

.27ure[]

Figure 6.12 Particle deposition patterns, (a) $\tau_p^+ = 5$, (b) $\tau_p^+ = 15$.

tracked under the assumptions of one–way coupling. The Stokes drag force, corrected for higher particle Reynolds numbers, was assumed to be the only force acting on the particle. Particles were removed on coming within one radius of the boundaries and reintroduced at the inflow plane at a random location. This procedure allowed the eventual development of a statistically stationary particle field.

Particle concentration patterns were found to reflect the flow characteristics in the different regions of the flow. Near the wall, particles accumulate in streamwise oriented streaks correlated with the so–called low–speed streaks in wall turbulence. Near the free–slip boundary they form large circular and elongated voids surrounded by thin regions of high concentration, consistent with the large–scale structure of turbulence near a free surface. A large increase in particle concentration very close to the wall is observed. The peak value is located around $z^+ \approx 0.3-0.4$. This flux of particles towards the wall is driven by the process of turbophoresis. Very close to the wall, particle concentration is higher for $\tau_p^+ = 5$ particles than for $\tau_p^+ = 15$ particles.

The deposition rates presented in the paper compare reasonably well with nominal experimental and numerical results presented previously. The deposition rate for $\tau_p^+ = 15$ particles was found to be significantly higher than for $\tau_p^+ = 5$ particles. The particle–phase mean streamwise velocity is shown to be smaller than that of the fluid for both sets of particle response times. This is attributed to the accumulation of particles in the low–speed regions of the flow. Preferential concentration was quantified by examining the mean streamwise velocity of the fluid at the particle positions. The results show that $\tau_p^+ = 15$ particles are slightly less preferentially concentrated in the region $5 < z^+ < 30$. The particle–phase mean wall–normal velocity is nonzero, even though the fluid has zero mean wall–normal velocity. The velocity towards the wall was found to be higher for $\tau_p^+ = 15$ particles, consistent with their higher deposition rate. The particle phase turbulence intensity was found to be significantly lower than the fluid phase due to two mechanisms working in conjunction with each other. The first mechanism is the preferential concentration of particles in regions with lower turbulence intensity and the second one is the lack of response of a particle to small–scale turbulent fluctuations due to its inertia.

Studies on particle deposition had so far indicated that free flight is the dominant mechanism for particle deposition in wall–bounded flows. One of the main findings of this study is the fact that diffusional deposition (deposition induced by the small residual turbulent fluctuations near the wall) of particles strongly concentrated near the wall is the dominant mechanism for particle deposition. This is clearly suggested by the cumulative distribution functions of the wall–normal velocities of depositing particles. Almost $90\,\%$ of the $\tau_p^+ = 5$ particles deposit due to this mechanism. The free–flight mechanism is shown to gain in importance for $\tau_p^+ = 15$, where it accounts for $40\,\%$ of the deposited particles. This fact is further clarified by looking at the deposition velocity vis–a–vis the residence time of the particles in a thin slab adjacent to the wall before deposition. A clear distinction between diffusional and free–flight particles was revealed. It was also shown that free–flight particles deposit more uniformly over the wall as compared to the diffusional particles that deposit in streamwise oriented streaks coinciding with the near–wall accumulation patterns.

7

DNS of turbulence in a sheared air–water flow

Le contenu de ce Chapitre est extrait du papier "*DNS of turbulence in a sheared air–water flow with a deformable interface*", paru dans *Journal of Fluid Mechanics*[*]. **482**, 319–345, 2003 by Marco Fulgosi, Djamel Lakehal, Sanjoy Banerjee and Valerio De Angelis.

7.1 INTRODUCTION

The fundamental mechanisms controlling heat and mass transfer across gas–liquid interfaces play a central role in the modelling of contacting multi–component systems. Whether the process is purely diffusive, such as soluble gas absorption, or involving condensation–induced suction, the exchange process is generally dominated by interfacial shear and/or turbulence. From a practical viewpoint, the subject is equally important to nuclear and chemical engineering, and to environmental problems. For example, a good understanding of interfacial exchange processes is essential for the thermal hydraulics of the class of nuclear power plants resorting to passive emergency cooling systems. Of primary importance in this case is to understand the behaviour of the steam–air mixtures vented into the containment pools. On a much larger scale, more specifically in marine climatology, quantifying the rate of mass transfer through absorption of carbon dioxide by the oceans is important, as well as the impact of aerosol production and transport from surface wave breaking (Melville, 1996). The interest in this field is to properly relate the transfer mechanisms to the imposed interfacial shear, and the way this shear scales with the turbulence structure.

Progress towards a sufficient understanding of the various types of gas–liquid exchanges has been hindered by obvious difficulties with measurements and computer simulations. Turbulence near deformable interfaces separating immiscible phases has received less attention than for wall–bounded flows. Recent developments in measuring technology contributed to advancing knowledge in this field (Jaehne *et al.*, 1987; Rashidi & Banerjee, 1990*a*; Komori *et al.*, 1993*a*; Kumar *et al.*, 1998), but there are still many non–clarified issues regarding the way molecular and turbulent transport processes interact with the transfer mechanisms. This is particularly crucial in the non–wall–bounded flow context, where deformable interfaces are synonymous with surface velocity fluctuations and surface wave generation.

Relating the mass transfer process to the interfacial turbulence structure has been approached mainly via two classes of model, *i.e.* the *surface renewal theory* (Higbie, 1935), and the *eddy diffusivity concept*. For instance, experimental evidence for correlations between the mass transfer rate and the surface renewal motion was demonstrated in most of the experiments dealing with wind–driven turbulence at air–water wavy interfaces (Jaehne *et al.*, 1984; Coantic, 1986; Komori *et al.*, 1993*a*). The presence of interfacial waves was also found to further enhance

[*]Reprinted with the permission of the publisher, *Cambridge University Press*

the exchange processes (Jaehne *et al.*, 1987), because part of the energy gained by the waves through the action of the wind is transferred to near–interface turbulence.

The advancement in computer technology and numerical methods has made it possible to investigate flows involving non–flat boundaries using Direct Numerical Simulation (DNS) and Large–Eddy Simulation (LES). For example, Maass & Schumann (1994) resorted to finite difference DNS to investigate the flow structure over stationary, high amplitude-to-wavelength ratio ($a/\lambda = 0.05$) sinusoidal waves, and observed large separation regions downstream of the wave crests. DeAngelis *et al.* (1997) employed pseudo–spectral DNS for the flow over a wavy wall with $a/\lambda = 0.025$ and 0.05, and reported significant effects of the wavy boundary on the turbulence statistics and the mean flow. Cherukat *et al.* (1998), performing spectral–element DNS of the flow over stationary sinusoidal waves with $a/\lambda = 0.05$ confirmed the modification of the mean flow only; the local turbulence appeared to be less influenced when rescaled with the increased (effective) friction velocity. With their LES study of flow over a wavy wall up to $a/\lambda = 0.1$, Henn & Sykes (1999) were able to reproduce most of the flow features observed in moderate high–Re experiments. DNS studies dealing with non–stationary sinusoidal waves are very rare, except for the work of Sullivan *et al.* (2000). Their high amplitude waves ($ak = 0.1$) were found to significantly influence the mean flow and turbulence characteristics. Moreover, they observed that in comparison to stationary waves, slow moving waves increase the form drag, whereas fast moving waves decrease it.

DNS studies devoted to the analysis of turbulence at interfaces, involving two–phase flows, have been relatively few. Some early important work was presented with regard to the turbulence structure near free surfaces with and without shear (Lam & Banerjee, 1992; Komori *et al.*, 1993*b*; Lombardi *et al.*, 1996). Because of its relative simplicity, *stratified* gas–liquid flow has been the best suited configuration to investigate the underlying physics at the interface. The DNS–based study of Lombardi *et al.* (1996) centered around a flat interface configuration, where gas and liquid were coupled through continuity of velocity and stress jump conditions at the interface. The authors found that turbulence characteristics on the gas side are quite similar to those at the wall. This led them to conclude that in some two–phase flow problems, depending on the density ratio between the phases, the lighter phase might look at the interface like a solid surface. DeAngelis (1998*a*) extended the research of Lombardi *et al.* (1996) to non–flat interfaces by considering stratified flow with a freely deformable interface in the capillary wave regime.

Following the work of Lombardi *et al.* (1996) and DeAngelis (1998*a*), the present investigation aims at analyzing in great detail the interfacial sublayer, with emphasis on the gas side because of the presumed analogy between near–wall and near–interface turbulence. The issue is approached by means of a global analysis of the energy budgets and the interfacial turbulence structure obtained from a rigorous DNS of a sheared air–water flow with a freely deformable interface, within the capillary wave regime. One objective here is to analyze turbulent flow on the gas side and discuss the wave–induced mechanisms influencing the flow. In fact, the major effect expected from interface deformation in the presence of shear is the extra transverse motion superimposed on the mean flow, and its associated energy, in the direction normal to the interface. The final objective is to exploit the outcoming data to develop suitable *near–interface turbulence models* useful for practical applications, for example by incorporating them into *interface tracking methods*, where the topology and dynamics of the interface are directly computed. In contrast to the *two–fluid* formalism, direct interface tracking algorithms may lead to situations where the interface is perceived like a solid surface to one of the phases, a conjecture to which the employed eddy diffusivity type of models need to conform.

The paper is structured as follows: the problem under consideration and the numerical procedure are described in Section 7.2. The characteristics of the waves are discussed in Section 7.3. The flow statistics are presented in Section 7.4, together with the data obtained by repeating the open–channel flow numerical experiment of Lam & Banerjee (1992). In Section 7.5, the budgets for the turbulent kinetic energy and for the Reynolds stresses are discussed, and the main differences relative to open–channel flow data are highlighted. The mechanisms behind turbulence interaction with the deformable interface are treated in Section 7.6. The flow structure is qualitatively analyzed in Section 7.7 by use of three different eduction techniques. Finally, conclusions are drawn in Section 7.8.

7.2 NUMERICAL METHOD

In this section, since the governing equations and the numerical procedure have been extensively described in chapter **??***, part of the original text is omitted.*

The shear-based Reynolds number, defined by $Re_\star = u_\star 2h/\nu$, with $u_\star$ taken at the initial stage of the simulation, is 171 in both phases. Moreover, the nondimensional time is defined by $t^+ = t\,\nu/u_\star^2$ in wall units, or by $t_{ls} = t\,U_0/h$ in large-scale units, where U_0 is the mean streamwise velocity. On the basis of scaling arguments, the Weber and

Froude numbers were set equal to $We = 4.8 \times 10^{-3}$ and $Fr = 8.7 \times 10^{-5}$ in order to limit the elevation amplitude and steepness to the range of capillary waves.

The dimensions of the computational domain are $4\pi h \times 2\pi h \times 2h$, with $h = 0.02$ m. The computational domain for each phase was $1074 \times 537 \times 171$ wall units in the streamwise, spanwise and normal directions respectively, with a resolution of $64 \times 64 \times 65$, which had been proven satisfactory in the work of Fulgosi *et al.* (2001).

The density ratio between the two phases was such that $\mathcal{R} = 29.9$, corresponding to air–water flows at atmospheric pressure and at roughly 320 K.

7.3 CHARACTERISTICS OF THE WAVES

The topology of the waves developing over a deformable free surface manifests itself in various forms depending on the intensity of the interfacial shear stress caused by the nature of the underlying turbulence. The action of this shear is balanced by two stabilizing factors: one due to gravity and one caused by surface tension (Brocchini & Peregrine, 2001).

In the air–water wave literature, it is customary to characterize the wave motion using the second moments of the joint probability density of the surface displacement $P(f(\overrightarrow{x_1}), f(\overrightarrow{x_2}))$. In particular, the covariance of the instantaneous nondimensional surface displacement

$$Z(\overrightarrow{r}) = \overline{f(\overrightarrow{x}, t_0) f(\overrightarrow{x} + \overrightarrow{r}, t_0)}\,, \tag{7.1}$$

and the covariance of the nondimensional surface displacement at a fixed location as a function of time

$$Z(t) = \overline{f(\overrightarrow{x}, t_0) f(\overrightarrow{x}, t_0 + t)} \tag{7.2}$$

The other useful wave–characterizing quantity, defined in terms of the covariance of the surface displacement (7.1), is the two-dimensional wave spectrum

$$\Psi(\overrightarrow{k}) = (2\pi)^{-2} \int Z(\overrightarrow{r}) e^{-i\overrightarrow{k}\cdot\overrightarrow{r}}\, d\overrightarrow{r} \tag{7.3}$$

It is important to note that, since the wave number k is here defined in the dimensional space, Ψ has the dimension of $[L^2]$, leading to the following definition of the saturation spectrum of the wave displacement

$$B(\overrightarrow{k}) = |\overrightarrow{k}|^2\, \Psi(\overrightarrow{k}) \tag{7.4}$$

The reader is referred to the book of Phillips (1977) and to Phillips (1985) for further exhaustive theoretical details.

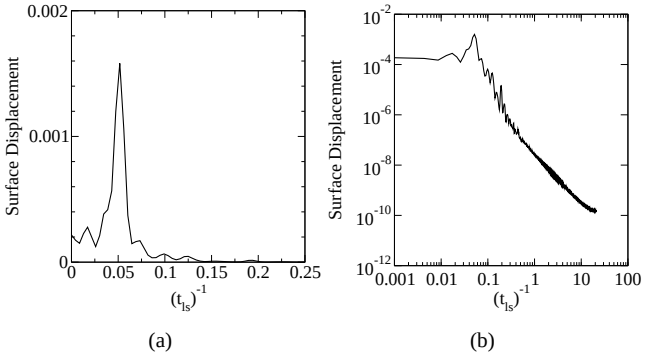

Figure 7.1 Time spectra of the wave amplitude. (a) Linear scale, (b) Log-Log scale.

The maximum wave amplitude observed in the present simulation was about 0.25 mm, and the maximum waveslope ak (amplitude a times wavenumber k) never exceeded $ak = 0.01$. The time spectra of the nondimensional wave elevation delivered by the DNS is shown in figure 7.1. The left panel is presented in linear scale whereas the right one is in a log-log scale. The spectrum was obtained over a time interval of $\Delta t_{ls} = 350$ large-scale nondimensional time units. The peak value is reached at $t_{ls} = 20$, in agreement with the measurements of

McCready & Hanratty (1985*a*), and indicates the frequency of the dominating wave. The equilibrium range is well represented in the time spectrum, covering a range of events larger than that of the peak. At the high frequencies, the straight line portion in figure 7.1(b) indicates that the small–scale dynamical effects induced by the waves cannot be expected to become important since they cannot grow in time. The estimation of the peak frequency has direct implications in modelling the mass transfer coefficient, as postulated by McCready & Hanratty (1985*a*).

The covariance of the surface displacement as a function of time and the saturation spectra of the wave displacement are shown in figures 7.2(a) and 7.2(b), respectively. The covariance shows the waves to reach a steady state

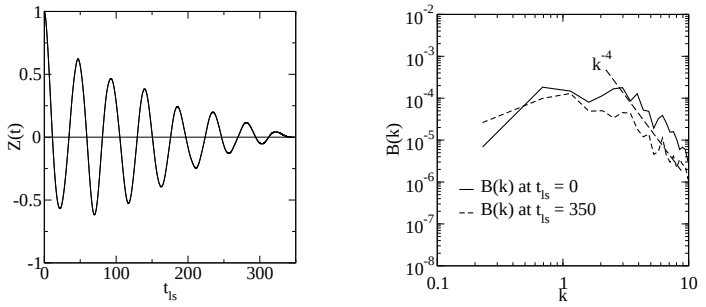

Figure 7.2 (a) Covariance at a fixed point on the interface (auto–correlation) as a function of the nondimensional time. (b) Saturation spectra at the beginning and the end of the simulation.

over the time interval considered in the simulation. In fact, the growth of the waves under the influence of the wind shear cannot continue indefinitely because it is limited by several dissipation effects. In spectral terms, this means that in the wave spectrum there is an upper limit of the spectral density imposed by these dissipation phenomena. The range of wave numbers over which this occurs is called the saturation range (Phillips, 1977). The saturation spectra are plotted in figure 7.2(b) at two different times during the computation: at the beginning ($t_{ls} = 0$) and at the end ($t_{ls} = 350$) of the time interval over which the statistics were performed. The results clearly show that the waves have not changed their properties in the course of the 350 large-scale time units.

7.4 ANALYSIS OF THE TURBULENT FIELD

As it is customary in DNS, statistical analysis of the data was performed by averaging the collected flow database over the two homogeneous directions (*i.e.* x–y plane average) and in time. For the type of flow considered here, this procedure can be reliable only if the collected database covers a sufficiently large time interval over which the wave field does not change its properties. In this case, the impact of the interfacial motion can be inferred in an average sense. This applies to the flow over the freely deformable interface since the characteristics of the waves have been shown in Section 7.3 to remain invariant in time. After statistically stationary conditions were reached, the flow database was collected over 350 large-scale time units (19500 time steps) with a frequency of sampling of $\Delta t_{ls} = 0.04$, which corresponds roughly to twice the large–eddy turnover time of the flow. The stratified flow data have then been compared to the open–channel flow results obtained by repeating the numerical experiment of Lam & Banerjee (1992). The flow database in this case was collected over 240 large-scale time units (13500 time steps).

Because the wave dynamics induces extra motion in the vertical direction of the flow, the velocity field may be thought of as superposition of mean, coherent and non–coherent (turbulent) contributions, *i.e.*

$$\tilde{u}_i = U_i + u_i^w + u_i \tag{7.5}$$

where U_i is the mean velocity (*i.e.* averaged over time and the two horizontal directions), u_i^w is the flow component induced by the orbital motion, and u_i is the superimposed turbulent fluctuation. This suggests that, in order to analyze the non–coherent turbulent fluctuating field in stratified flow, it is necessary to separate it from the coherent field, u_i^w. Also, the wave component is removed in the vertical direction only because the other two components (in the plane tangential to the interface) are negligible, *i.e.* of the order 10^{-4}. This has been achieved by removing the grid velocity u_3^g from the vertical velocity component, *i.e.* $u_3^w = u_3^g$, leading to a zero value of $\tilde{u}_3$ at the interface.

Most of the following results are presented using a logarithmic scale for the abscissa $z^+ = u_\star z/\nu$ in order to better appreciate the changes very close to the interface.

7.4.1 Velocity field

Figure 7.3 shows the profiles of the mean streamwise velocity for flow over the deformable interface (referred to as FDI) and for the open channel (OCH). DNS results obtained by Hu *et al.* (2002) for closed–channel flow at

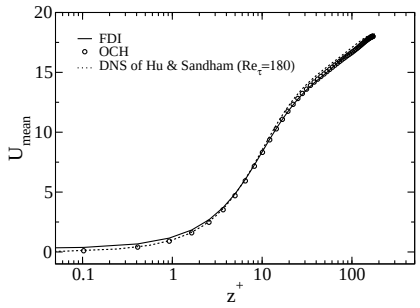

Figure 7.3 Profiles of the mean streamwise velocity.

$Re_\tau = 180$ are also included for comparison. The profiles are practically the same starting from $z^+ = 10$, but below, while both the wall–bounded flows converge towards zero at the wall, the velocity in the FDI case has a finite value at the interface, corresponding to 2% of the maximum velocity. The root–mean–square (RMS) profiles of the velocity fluctuations are presented in figure 7.4. The behaviour is almost identical, but again, because of different boundary conditions, the RMS values of u and v in the FDI case do not start from the same value at the interface/wall. At this stage, the results presented in this section suggest that there is an "apparent similarity" between wall–turbulence and near–interfacial turbulence. In reality, although small in magnitude, differences do exist and manifest themselves in very subtle ways.

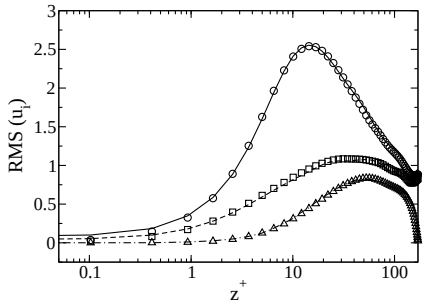

Figure 7.4 RMS profiles of the three velocity components. Lines and symbols are used to identify FDI and OCH, respectively. (—) and (○), streamwise velocity; (− − −) and (□), spanwise component; (− · −) and (△), normal component.

The effect of filtering the wave-induced motion from the vertical velocity component has also been investigated, and the results are reported in figure 7.5, comparing the RMS of $\tilde{w} - w^w$ (filtered) to the RMS of $\tilde{w}$ (unfiltered), referred to as FDI–1 and FDI–2, respectively. The comparison highlights the influence of the wave dynamics on the velocity fluctuating field, although, compared to the maximum value, the RMS of $\tilde{w}$ is small.

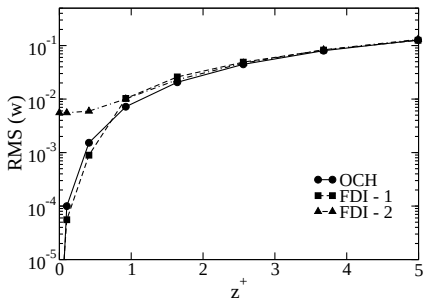

Figure 7.5 Profiles of the RMS of fluctuating vertical velocity near the interface/wall. FDI-1: filtered data ($\tilde{w} - w^w$); FDI-2: unfiltered data ($\tilde{w}$).

Another persuasive indication that the interfacial deformation acts on the velocity field can be provided by examining the variation of the components of the fluctuating rate-of-strain tensor

$$s_{ij} = \frac{1}{2}\left(\frac{\partial u_i}{\partial x_j} + \frac{\partial u_j}{\partial x_i}\right) \tag{7.6}$$

The analysis, discussed in the context of figure 7.6, indicates that the most affected components are the off-diagonal ones, *i.e.* $s_{12},\ s_{13}$ and s_{23}. The lower values of s_{13} and s_{23} in the FDI case provide evidence that the impact of

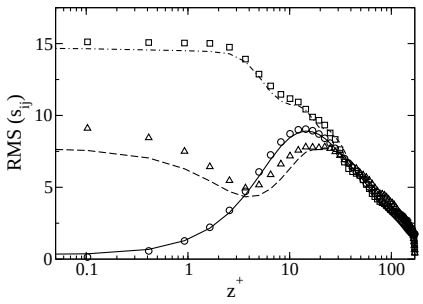

Figure 7.6 Profiles of the RMS of the fluctuating strain tensor s_{ij}. Lines and symbols are used to identify FDI and OCH, respectively. (—) and ($\circ$), s_{12}; ($-\cdot-$) and ($\square$), s_{13}; ($---$) and ($\triangle$), s_{23}.

the interface dynamics on the turbulence at the interface is to reduce the rate-of-deformation of the fluid in the near–interface region $z^+ < 12$. The implications of this result are better measured by looking at the off-diagonal components of the viscous dissipation tensor

$$\varepsilon_{ij} = 2\nu\ s_{ik}s_{kj} \tag{7.7}$$

plotted in figure 7.7, together with $\varepsilon = 1/2\ \varepsilon_{ii}$, the dissipation of the turbulent kinetic energy. The analysis shows that the off-diagonal components of ε_{ij} are weakened in the FDI case, in particular ε_{12} (because of the significant difference in s_{23}); this applies also to ε. Thus, it can be concluded that the effect of the interfacial deformations on the near–interfacial turbulence leads to *general dampening* of the turbulent fluctuating field.

7.4.2 Vorticity field

The aim of this section is to evaluate the influence of the interfacial deformations on the flow field away from the interface. Emphasis will be placed upon the modification of the *quasi–streamwise vortices*. Although the current knowledge on wall–flow structures prompted by DNS is richer than ever, questions regarding certain aspects of the energy transfer and regeneration mechanisms near the wall are still open. The lack of consensus is even more acute as to which of the streamwise velocity streaks or quasi–streamwise vortices are directly implicated in the turbulence self-sustaining mechanisms (Jimenez & Pinelli, 1999; Schoppa & Hussain, 2002). This latter mechanism, in particular, has long been associated with the dynamics of the quasi–streamwise vortices oriented in the flow direction (Rashidi & Banerjee, 1990*b*). Pairs of these quasi–streamwise vortices neighboring the wall

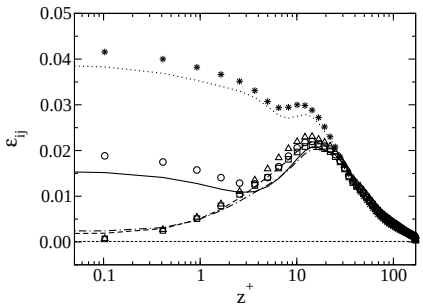

Figure 7.7 Profiles of the off-diagonal components of the dissipation tensor. Lines and symbols are used to identify FDI and OCH, respectively. (—) and ($\circ$), ε_{12}; ($-\cdot-$) and ($\square$), ε_{13}; ($---$) and ($\triangle$), ε_{23}; ($\cdot\cdot$) and ($*$), ε.

are known to be directly linked to the formation of the *streaky structure* of the velocity field through two types of events: ejections and sweeps. These two flow events are also known to result from the interaction between the quasi–streamwise vortices (see figure 7.8). The streaky structure pattern consists in the alternation between regions of low and high speed fluid; high–speed regions are associated with low–shear stress regions, and vice versa.

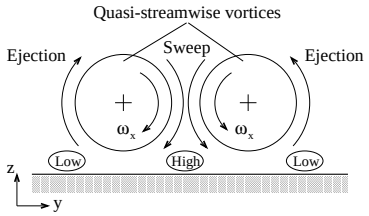

Figure 7.8 Schematic of the interaction between streamwise vorticity ω_x and streaky structure.

Some preliminary information about the phenomenon of generation of quasi–streamwise vortices have been inferred from the analysis of the fluctuating vorticity field. For instance, it is known that the main contributor to changes of ω_x is $\omega_z \frac{dU}{dz}$, which can be interpreted as the tilting of a vortex with component ω_z in the streamwise direction. Figure 7.9 shows the variation of the RMS of the three components of the vorticity vector for the FDI

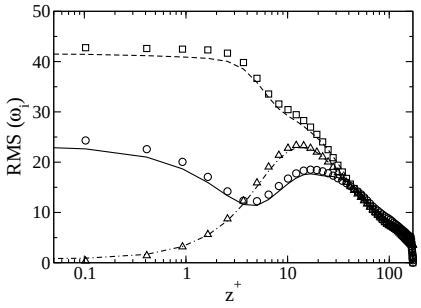

Figure 7.9 RMS profiles of components of the vorticity vector $\overrightarrow{\omega}$. Lines and symbols are used to identify FDI and OCH, respectively. (—) and (○), ω_x; (− − −) and (□), ω_y; (−·−) and (△), ω_z.

and OCH cases. Since dU/dz is almost equal in both configurations, and no substantial differences occur in the variation of ω_z, it can be argued that the orientation of the quasi–streamwise vortices is not affected by the interfacial motion, at least in an average sense. Further, the influence of the interfacial deformation on the core flow can also be discussed by examining the behaviour of the fluctuating velocity gradient tensor, decomposed as

$$\frac{\partial u_i}{\partial x_j} = s_{ij} + r_{ij} \tag{7.8}$$

where s_{ij} is the fluctuating rate-of-strain tensor (symmetric) defined in (7.6), and r_{ij} is the fluctuating rate-of-rotation tensor (skew-symmetric), defined as

$$r_{ij} = \frac{1}{2}\left(\frac{\partial u_i}{\partial x_j} - \frac{\partial u_j}{\partial x_i}\right) \tag{7.9}$$

Of particular interest in evaluating the rate-of-deformation/rotation of the fluid, is the second invariant (Q) of the velocity gradient tensor, defined as

$$Q = -\frac{1}{2}\left[tr(\underline{\underline{r}}^2) + tr(\underline{\underline{s}}^2)\right] = \frac{1}{2}\left(r_{ij}r_{ij} - s_{ij}s_{ij}\right) \tag{7.10}$$

Since Q vanishes at the wall, it cannot be directly used in the present context to estimate the influence on the fluid deformation/strain of the interfacial dynamics. However, useful information can be inferred by analyzing separate contributions of $r_{ij}r_{ij}$ and $s_{ij}s_{ij}$ in terms of auto–correlation functions between their values at the interface/wall and in the bulk region. The auto–correlation functions have been defined as

$$Corr(r_{ij}) = \frac{\overline{< r_{ij}r_{ij} > (0) \; < r_{ij}r_{ij} > (z)}}{< r_{ij}r_{ij} >^{rms} (0) \; < r_{ij}r_{ij} >^{rms} (z)} \tag{7.11}$$

and

$$Corr(s_{ij}) = \frac{\overline{< s_{ij}s_{ij} > (0) \ < s_{ij}s_{ij} > (z)}}{< s_{ij}s_{ij} >^{rms} (0) \ < s_{ij}s_{ij} >^{rms} (z)} \tag{7.12}$$

where $< r_{ij}r_{ij} > (0)$ stands for the value of the space-averaged (x–y) component at the interface/wall, and $< r_{ij}r_{ij} > (z)$ for the values along the direction normal to the interface/wall; the same applies to $< s_{ij}s_{ij} >$. Figure 7.10, comparing the auto–correlation functions $Corr(r_{ij})$ and $Corr(s_{ij})$, shows that these are both stronger

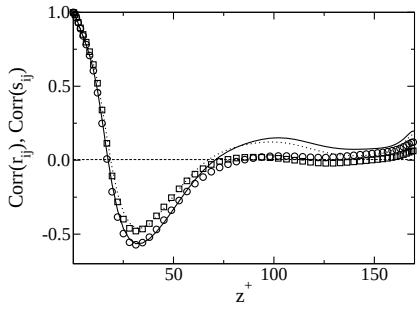

Figure 7.10 Profiles of the auto–correlation function between the $< r_{ij}r_{ij} >$ and $< s_{ij}s_{ij} >$ at the interface/wall and that in the bulk flow. Lines and symbols are used to identify FDI and OCH, respectively. (—) and (○), $Corr(r_{ij})$; (·····) and (□), $Corr(s_{ij})$.

in the FDI flow configuration than in OCH. A close inspection of the plot reveals that, for the FDI case, the location where the rotation overcomes the strain is 10 wall units earlier than for OCH. This result reflects the fact that the interface affects the evolution of the flow field throughout the entire boundary layer, in contrast to a rigid wall.

7.4.3 Pressure field

In the vicinity of the wall, pressure fluctuations, p, are a direct measure of the surface excitation force, and are closely linked to flow unsteadiness. The generation of pressure fluctuations in a turbulent boundary layer is coupled to the dynamics of the instantaneous velocity field throughout the entire layer. This coupling is expressed in terms of the following Poisson equation

$$\frac{1}{\rho}\nabla^2 p = -2\,\frac{\partial U_i}{\partial x_j}\frac{\partial u_j}{\partial x_i} - \frac{\partial^2}{\partial x_i \partial x_j}\left(u_i u_j - \overline{u_i u_j}\right) \tag{7.13}$$

which embodies a dependency on the interaction between the fluctuating velocity field and the mean shear as well as on the non–linear interaction of the velocity fluctuations with themselves. Moreover, since the instantaneous gradients of the pressure fluctuations are equal to the flux of vorticity from the wall, the wall–pressure fluctuations are intimately related to the vorticity fluctuations and the organization of the turbulent structures within the boundary layer (Robinson, 1991). Figure 7.11 shows the variations in the fluctuating pressure in the direction normal to

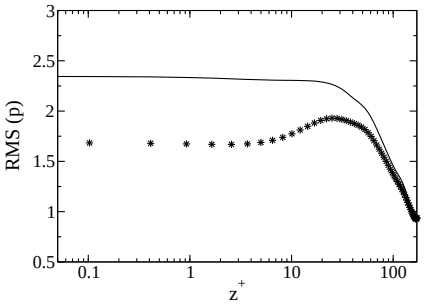

Figure 7.11 Profiles of the RMS pressure fluctuation, p. Lines and symbols are used to identify FDI and OCH, respectively.

the interface/wall. It is readily apparent that the freely deformable interface is associated with a higher level of near–interface pressure fluctuations, which is maintained across the entire viscous sublayer and above ($z^+ \approx 20$). In the OCH case, the RMS of the pressure at the wall is around 1.7, which agrees fairly well with the channel

flow data of Kim *et al.* (1987). In the FDI case, the interfacial RMS pressure value is around 2.3, which can be interpreted as resulting from the formation of local pressure gradients promoted by the alternation of "hills" and "valleys" developing over the deformable interface. In Section 7.4.1, it has been shown that the impact of the interfacial motion on the velocity field results in a reduction in the near–interfacial dissipation, via a reduction in the deformations induced by the fluctuating strain, s_{ij}; *i.e.* the fluctuating velocity gradients in the direction normal to the interface are reduced compared to those at the wall. The larger values of the RMS of pressure in the near–interface region are then in accord with the observed dampening of the turbulent fluctuating field; in fact this is required by conservation of the pressure–rate-of-strain term in equation (7.16).

7.5 ENERGY BUDGET EQUATIONS

7.5.1 Turbulent Kinetic Energy budget

The transport equations for the turbulent kinetic energy (TKE), $k = 1/2\ (\overline{u^2} + \overline{v^2} + \overline{w^2})$, can be derived from the Navier–Stokes equations. For incompressible turbulent flow the transport equation is given by

$$\frac{Dk}{Dt} = \underbrace{-\overline{u_i u_j}\frac{\partial U_i}{\partial x_j}}_{Production} \underbrace{-\frac{1}{\rho}\frac{\partial}{\partial x_i}\overline{pu_i}}_{Press.\ Diff.} \underbrace{-\frac{1}{2}\frac{\partial}{\partial x_j}\overline{u_i u_i u_j}}_{Turb.\ Transp.} + \underbrace{\frac{1}{2}\nu\frac{\partial^2}{\partial x_j^2}\overline{u_i u_i}}_{Visc.\ Diff.} \underbrace{-\nu\overline{\frac{\partial u_i}{\partial x_j}\frac{\partial u_i}{\partial x_j}}}_{Dissipation} \tag{7.14}$$

where D/Dt is the substantial derivative. The analysis below follows the approach used by Mansour *et al.* (1988). Figure 7.12 compares the terms on the right-hand-side of equation (7.14) for FDI and OCH cases. The only

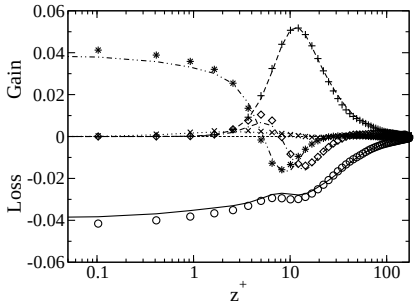

Figure 7.12 Terms in the budget for the TKE in wall units. Lines and symbols are used to identify FDI and OCH, respectively. (—) and (○), dissipation; (− − −) and (+), production; (· · · · ·) and (×), pressure diffusion; (− · −) and (⋄), turbulent diffusion; (− · · −) and (∗), viscous diffusion.

significant difference can be observed close to the interface, where both viscous diffusion and dissipation rates are smaller in the FDI case. This is due to the previously observed dampening effect of the turbulent field caused by interfacial motion. It is interesting to note that even in the presence of a deformable interface the dissipation rate close to the interface is balanced entirely by the viscous diffusion, exactly as in the case of a rigid wall.

7.5.2 Reynolds stress budget

The transport equations for the Reynolds stresses are also derived from the Navier–Stokes equations. For incompressible turbulent flow the generic transport equation is given by

$$\begin{aligned}\frac{D}{Dt}\overline{u_i u_j} \;=\; & \underbrace{-\left(\overline{u_i u_k}\frac{\partial U_j}{\partial x_k} + \overline{u_j u_k}\frac{\partial U_i}{\partial x_k}\right)}_{Production} \underbrace{-\frac{1}{\rho}\overline{\left(u_i\frac{\partial p}{\partial x_j} + u_j\frac{\partial p}{\partial x_i}\right)}}_{Press.\ Diff.} \\ & \underbrace{-\frac{\partial}{\partial x_k}\overline{u_i u_j u_k}}_{Turb.\ Transp.} \underbrace{+\nu\frac{\partial^2}{\partial x_k^2}\overline{u_i u_j}}_{Visc.\ Diff.} \underbrace{-2\nu\overline{\frac{\partial u_i}{\partial x_k}\frac{\partial u_j}{\partial x_k}}}_{Dissipation}\end{aligned} \tag{7.15}$$

It is important to note that the pressure diffusion term provides both a source of energy and a mechanism to redistribute it. This term, also called velocity–pressure–gradient tensor and denoted by Π_{ij}, can be decomposed

into a redistributive part and a transport part as follows

$$\Pi_{ij} = \overline{\frac{p}{\rho}\left(\frac{\partial u_i}{\partial x_j} + \frac{\partial u_j}{\partial x_i}\right)} - \frac{\partial}{\partial x_k}\overline{\left[\frac{p}{\rho}\left(u_i\,\delta_{jk} + u_j\,\delta_{ik}\right)\right]} = \mathcal{R}_{ij} - \frac{\partial}{\partial x_k}\,\mathcal{T}_{ijk}\,, \tag{7.16}$$

where δ_{ij} indicates the Kronecker delta. $\mathcal{R}_{ij}$, the pressure–rate-of-strain tensor, serves to redistribute energy among the Reynolds stresses promoting isotropy of turbulence. $\mathcal{T}_{ijk}$, the pressure–transport term, constitutes the source of kinetic energy due to pressure transport. As discussed in Section 7.4.3, due to the homogeneity of the flow in the streamwise and spanwise directions, the transport equation for $\overline{uv}$ reduces to $\Pi_{12} - \varepsilon_{12} = 0$. The reduction of ε_{12} near the interface (see figure 7.7) is therefore counterbalanced by an increase in Π_{12} through the pressure.

By virtue of continuity, the trace of $\mathcal{R}_{ij}$ is zero, and consequently this term vanishes in the transport equation of the turbulent kinetic energy (7.14). Each term of the trace of $\mathcal{R}_{ij}$ is used to define the pressure–strain correlation

$$PS_i = \frac{1}{\rho}\,\overline{p\,\frac{\partial u_i}{\partial x_i}}\,,\quad i = 1,2,3 \tag{7.17}$$

A positive value of PS_i implies a transfer of energy into component i from the other components, and vice versa.

Figure 7.13 shows the profiles of the pressure–strain correlation. In both OCH and FDI cases, the streamwise component, PS_1, transfers energy into the spanwise (PS_2) and the normal (PS_3) components. What is remarkable

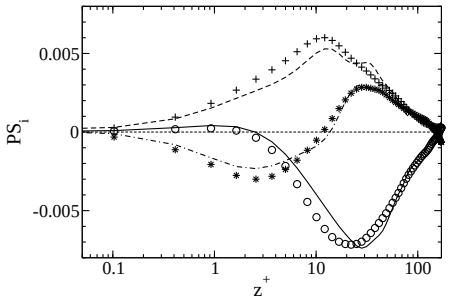

Figure 7.13 Profiles of the pressure–strain correlation. Lines and symbols are used to identify FDI and OCH, respectively. (—) and (○), streamwise direction; (− − −) and (+), spanwise direction; (− · −) and (∗), vertical direction.

is that this effect is less pronounced for FDI, meaning that the streamwise component loses less energy than in the channel flow. Hence, the deformable boundary reduces the interface-normal component less than the solid boundary does. The reduced values of PS_2 and PS_3 occur as $\mathcal{R}_{22}$ and $\mathcal{R}_{33}$ are smaller in the flow over a deformable interface than near the wall. This leads to the conclusion that near–interface turbulence is more isotropic than near–wall turbulence.

The intercomponent energy transfer near a boundary (described by the pressure–strain correlation) can be further explained by considering the presence of two types of effect when the surface is approached: a viscous effect that reduces the turbulence intensities, and a wall–blocking effect that amplifies the tangential turbulence intensities. The latter event is referred to as *splat*; a local region of stagnation flow resulting from impingement on a solid boundary (Perot & Moin, 1995). As it cannot penetrate the boundary the fluid turns and moves parallel to it, yielding a transfer of energy from the normal velocity component to the tangential components and an enhancement of tangential turbulence. The proximity of a vortical structure close to the boundary produces vorticity of opposite sign, which can be ejected away by the primary vortex. This scenario, known as *antisplats*, can be regarded as the counterpart of the splat event which explains the energy redistribution between PS_i components. This clearly shows that interfacial motion weakens the role of splats.

A comparison between the budgets of the normal stress component, $\overline{uu}$, is presented in figure 7.14(a). In the vicinity of the interface ($z^+ < 10$), turbulent transport, viscous diffusion, and dissipation are smaller in absolute value in FDI than in OCH, while production and pressure diffusion remain unchanged. Close to the interface the dissipation is entirely balanced by the viscous diffusion. The budgets for $\overline{vv}$ are presented in figure 7.14(b). Again, viscous diffusion, pressure diffusion, and dissipation are smaller in absolute value in FDI than in OCH, whereas turbulent transport remains unchanged. In the spanwise direction there is no production, and close to the interface the dissipation is balanced by viscous diffusion, whereas up to $z^+ > 10$ the dissipation is entirely balanced by the pressure diffusion term. Figure 7.14(c) compares the budgets for the interface/wall normal component $\overline{ww}$. In the viscous sublayer no substantial differences can be seen, indicating that the interfacial motion very close to the

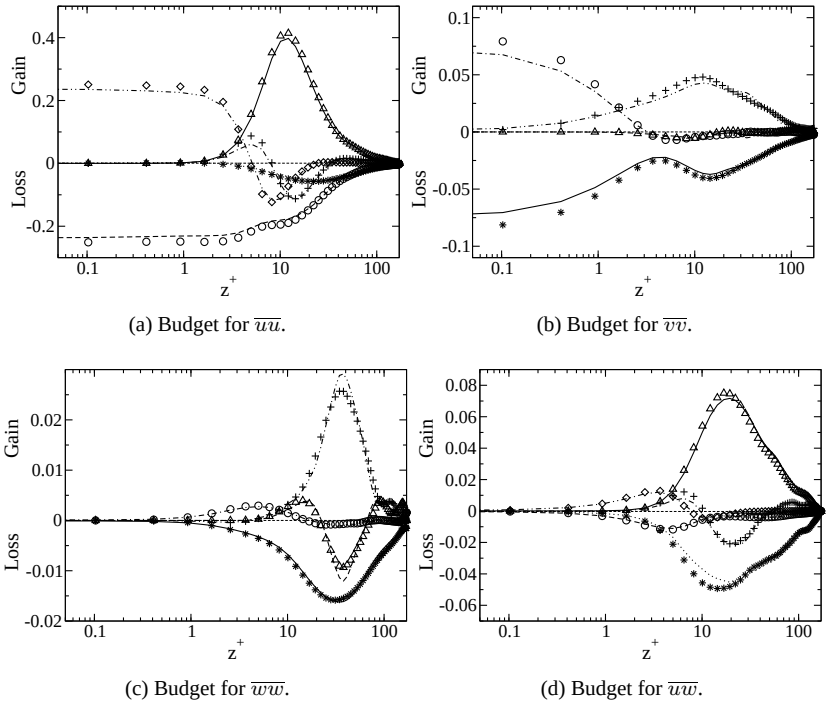

(a) Budget for $\overline{uu}$.

(b) Budget for $\overline{vv}$.

(c) Budget for $\overline{ww}$.

(d) Budget for $\overline{uw}$.

Figure 7.14 Reynolds stress budgets. Lines and symbols are used to identify FDI and OCH, respectively. (—) and (∗), dissipation; $(-\cdots-)$ and (+), pressure diffusion; $(---)$ and (△), turbulent diffusion; $(-\cdot-)$ and (○), viscous diffusion.

interface does not affect the balance. However, in the buffer region, $20 < z^+ < 40$, pressure diffusion, turbulent transport, and dissipation (the former is not very evident in a logarithmic plot) are more pronounced in FDI than in the OCH case. In the normal direction there is no production either, and the only important source of energy is the pressure diffusion term, which is balanced by turbulent transport and dissipation. A comparison of budgets for the shear stress $\overline{uw}$, plotted in figure 7.14(d), indicates that in both cases the production is balanced by the pressure diffusion term. Viscous diffusion, dissipation, and production remain unchanged in the viscous sublayer, whereas pressure diffusion and turbulent transport are slightly smaller at the deformable interface.

In summary, it can be concluded that the interfacial motion affects the flow in the viscous layer through a reduction of the viscous mechanisms (*i.e.* dissipation and viscous diffusion) and a reduction of the flux of Reynolds stresses (*i.e.* turbulent transport). The production mechanisms including pressure diffusion, however, remain unchanged. This confirms the role of the interface deformation in reducing most of the gradients of turbulent correlations (*i.e.* the terms requiring modelling in equation (7.15)) as the interface is approached.

7.6 TURBULENCE/INTERFACE INTERACTION MECHANISMS

7.6.1 Drag at the sheared deformable interface

Of fundamental interest in turbulent two–phase flow research is a better understanding of the interaction between turbulence and the neighboring deformable interface. More precisely, identifying the various mechanisms through which interfaces affect turbulence is the key to understanding the subsequent processes of inter–phase heat and mass transfer, which is the ultimate goal of this work. The turbulence/interface interaction mechanisms induced by the interfacial shear and their relationship to interfacial drag are examined first. The near–interface/wall distributions of the shear stress, $-\overline{uw}$, are compared in figure 7.15. The comparison shows that the peak value is smaller in the two–phase flow, indicating that there is a small drag reduction due to interfacial dynamics. This is due to the fact that the form drag, even if very small, $u_\tau/u_\star = 0.986$, takes energy away from the flow and thus the shear decreases. This result is consistent with the observation that drag reduction can be obtained over adaptive and flexible walls (*e.g.* compliant coating) rather than rigid walls (Choi, 2001). This also suggests that statistically stationary capillary waves may similarly lead to drag reduction, even if by a smaller amount.

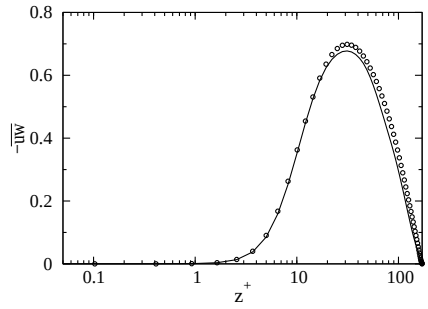

Figure 7.15 Profiles of the shear stress $-\overline{uw}$. Lines and symbols are used to identify FDI and OCH, respectively.

A more detailed view of the mechanisms by which the shear stress can be lowered in intensity by interfacial dynamics is provided by the quadrant analysis (Kim *et al.*, 1987; Soldati & Banerjee, 1998). This analysis quantifies the possible combinations of u and w in terms of physical flow events. Figure 7.16 displays the fractional contribution of each event to the shear stress $-\overline{uw}$ for both FDI and OCH cases studied. Although first and third quadrant events are favorable to drag reduction, their contribution is actually smaller than the other quadrant events. Sweep events in channel flow are dominant close to the wall, whereas away from the wall ejection events dominate. The crossover point is located at $z^+ = 12$. For the FDI case the variation of quadrant events is small. All the events seem to be enhanced at the interface but the crossover point between the second and fourth quadrant events is still located around $z^+ = 12$. Above the crossover point, first and third quadrant events are larger in the FDI case (not clearly noticeable), which explains why the drag reduction is not significant.

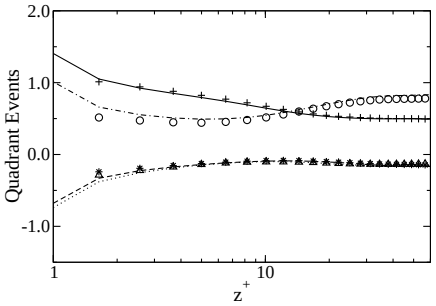

Figure 7.16 Quadrant analysis terms. Lines and symbols are used to identify FDI and OCH, respectively. ($---$) and ($*$), first quadrant events; (—) and ($+$), second quadrant events; ($\cdots\cdots$) and ($\triangle$), third quadrant events; ($-\cdot-$) and ($\circ$), fourth quadrant events.

7.6.2 Turbulence characteristics

In order to study the flow structure without explicitly employing an identification criterion other than the shear stress, the nondimensional shear rate parameter $\tilde{S}$ introduced by Lam & Banerjee (1992) was employed. It is defined by

$$\tilde{S} = \frac{dU}{dz}\,\frac{|\overline{uw}|}{\varepsilon} = \frac{\mathcal{P}}{\varepsilon} \tag{7.18}$$

and represents the ratio of the rate of production of turbulent kinetic energy $\mathcal{P}$ to its rate of dissipation ε. This parameter is therefore intimately related to the streaky structure of the velocity field, as discussed in Section 7.4.2. If $\tilde{S} > 1$ the shear is high enough for streaks to form, indicating that the generation of turbulence is more dominant than dissipation. Figure 7.17 shows a comparison of the time-averaged nondimensional shear rate parameter, $\tilde{S}$, obtained from the DNS of both FDI and OCH flows. In both flow configurations, the formation of the streaks is seen to take place at the same distance from the interface/wall, at $z^+ \approx 8$. Figures 7.18(a) and (b) compare two snapshots of the streaky structure (note that, for sake of clarity, the amplitude of the surface elevation has been amplified by a factor of 5). It can be observed that the streaky structure in the channel flow appears to be more regular than on top of the deformable interface. The clear alternation between high and low speed regions is also more visible, while overall the streaky pattern looks less organized. However, the streamwise elongation of the streaks does not seem to be affected by the deformation of the interface.

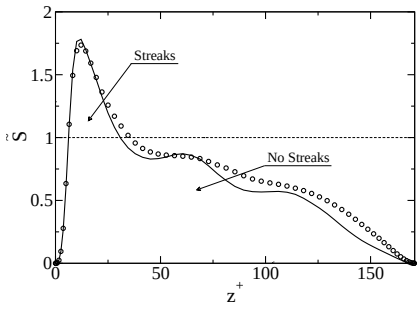

Figure 7.17 Profiles of the nondimensional shear–rate parameter. Lines and symbols are used to identify FDI and OCH, respectively.

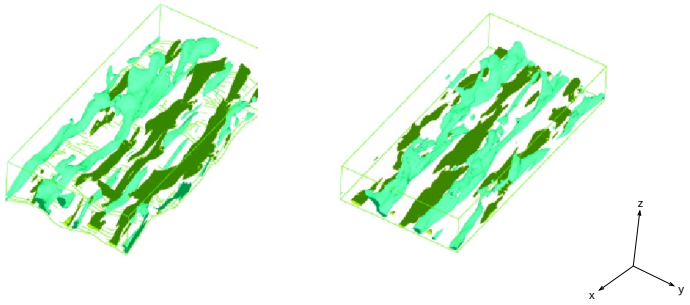

(a) (b)

Figure 7.18 Three–dimensional view of the streaky structure in (a) FDI and (b) OCH cases. Light green and dark green colors indicate low and high speed streaks respectively.

The analysis of the ratio $\mathcal{P}/\varepsilon$ via local conditions rather than global parameters characterizing the boundary layer, can be further detailed in terms of the same shear rate parameter,

$$\tilde{S} = \frac{\mathcal{P}}{\varepsilon} = S\,\frac{|\overline{uw}|}{\varepsilon} = \frac{S\,q^2}{\varepsilon}\,\frac{|\overline{uw}|}{q^2} = S^*\,\frac{|\overline{uw}|}{q^2} \tag{7.19}$$

where $S = dU/dz$ and $q^2 = 2k$. With this definition the two contributions to $\mathcal{P}/\varepsilon$, namely the structure parameter $|\overline{uw}|/q^2$ and $S^* = \tau_T/\tau_S$, the ratio of the turbulent time scale $\tau_T = l_T/u_T$, to the time scale characterizing the mechanical deformation, $\tau_S = (dU/dz)^{-1}$, can be separated. In the latter definition, $l_T = q^3/\varepsilon$ stands for the turbulent length scale, and $u_T = q$ for the corresponding velocity scale. The structure parameter is the ratio of shear to the trace of the turbulent stress tensor, representing the degree of turbulence anisotropy. The previous discussion of the Reynolds stress budget has revealed that the main role of interface motion is to act on the viscous and transport mechanisms, in particular on the pressure–rate-of-strain tensor, promoting the isotropy of near–interface turbulence. Further evidence of this result is provided in the context of figure 7.19(a), where the peak value of the anisotropy parameter in FDI appears to be lower than in the OCH case. The two time scales defining S^* are plotted against z^+ in figure 7.19(b) both for the FDI and the OCH cases. It can be observed that while τ_S is overall of the same magnitude, τ_T does not vanish near the interface as it does near the wall, implying that the smallest scales of turbulence remain active approaching the interface whereas they vanish as the wall is approached. Therefore, the role of the interfacial motion also consists in accelerating the turbulent transfer processes.

The degree of turbulence anisotropy can best be obtained by an analysis of the anisotropy tensor, defined as

$$b_{ij} = \frac{\overline{u_i u_j}}{q^2} - \frac{1}{3}\delta_{ij} \tag{7.20}$$

In contrast to equation (7.19) that compares the magnitude of the shear stress to that of the turbulent kinetic energy, the above relation indicates the magnitude of each stress component to the turbulent kinetic energy. The distribution of the non–zero b_{ij} components are compared in figure 7.20. Deviations in the profiles near the interface/wall are visible only for b_{11} and b_{33}; the other two components show no such deviations. In fact, the absolute values of

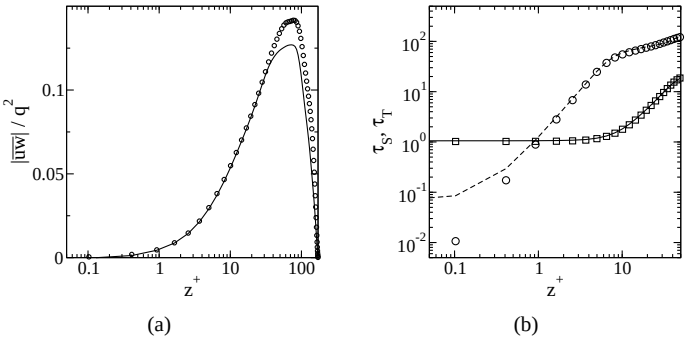

Figure 7.19 (a) Profiles of the structure parameter $|\overline{uw}|/q^2$. Lines and symbols are used to identify FDI and OCH, respectively. (b) Time scales. (—) and (□), τ_S; (− − −) and (○), τ_T.

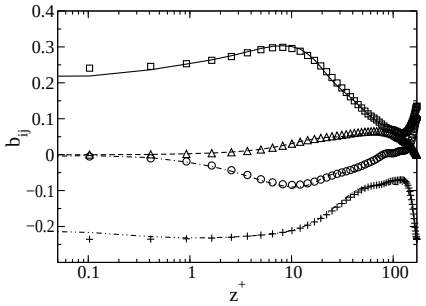

Figure 7.20 Profiles of the components of the anisotropy tensor. Lines and symbols are used to identify FDI and OCH, respectively. (—) and (□), b_{11}; (− − −) and (△), b_{13}; (−·−) and (○), b_{22}; (−· · −) and (+), b_{33}.

b_{11} and b_{33} at the wall are greater than at the deformable interface, which, as discussed above, is expected due to the imposed near–interface/wall boundary conditions. This, again, confirms that the interfacial motion yields a global dampening of the turbulent fluctuating field in the vicinity of the interface which, in turn, explains why the near–interface turbulence appears less anisotropic than the near–wall one.

7.7 COHERENT STRUCTURE IDENTIFICATION

Hussain (1983) defines a *coherent structure* as a connected, large–scale turbulent fluid mass with a phase–correlated vorticity throughout its spatial extent. The separation between coherent and non–coherent motion is of crucial importance to obtain a better understanding of the transfer processes. In fact, in a turbulent boundary layer, streamwise coherent structures have been linked to ejections and sweeps, which are responsible for draining slow–moving fluid into the outer region and high momentum fluid into the wall region, respectively. These events generate the major part of the drag and are well correlated with heat and mass transfer fluxes (Rashidi & Banerjee, 1990*b*). The key issue is to define a suitable criterion that identifies boundaries, topology, and dynamics in the spatial and temporal extent of these vortices.

According to Hussain's definition the high vorticity modulus $|\omega|$ is a possible candidate for vortex identification in free–shear flow. However, in the presence of a boundary (interface/wall) this criterion fails because the mean–shear creates a residual vorticity, which is uncorrelated with the vorticity caused by the coherent motion. Three different vortex identification criteria have therefore been employed here. The first criterion used is the so–called Q–factor proposed by Hunt *et al.* (1988), which has already been introduced in Section 7.4.2. Q can be thought of as the balance between the rate-of-rotation and the rate-of-strain within the superimposed non–coherent field. Positive values of Q indicate regions where the strength of rotation overcomes the strain. The second criterion employed is the second largest eigenvalue (λ_2) of the tensor $s_{ik}s_{kj} + r_{ik}r_{kj}$, defined by Jeong *et al.* (1997). With this criterion coherent vortices are well represented by connected regions where the local value of λ_2 becomes negative. The $\lambda_2 < 0$ and $Q > 0$ criteria should present very similar types of behaviour, unless the vortices are subjected to high stretching and/or compression. The last identifier used is the streamline rotation vector, proposed

by Perry & Chong (1987). The definition of this identifier is based on the classification of complex flow fields by the identification of their three–dimensional critical points. It is defined by

$$\overrightarrow{\Omega} = -\lambda_i \frac{\overrightarrow{e_a}}{|\overrightarrow{e_a}|} \frac{\overrightarrow{e_a} \cdot (\overrightarrow{r} \times \overrightarrow{c})}{|\overrightarrow{e_a} \cdot (\overrightarrow{r} \times \overrightarrow{c})|} \tag{7.21}$$

where λ_i is the imaginary part of the pair of complex eigenvalues of the velocity gradient tensor, $\overrightarrow{r}$ is the real part of the conjugate complex eigenvectors corresponding to the complex eigenvalues, $\overrightarrow{c}$ is the imaginary part of the conjugate complex eigenvectors and $\overrightarrow{e_a}$ is the eigenvector corresponding to the real eigenvalue.

The purpose of this section is to employ the above mentioned eduction techniques to qualitatively characterize the quasi–streamwise vortices in the turbulent flow over the freely deformable interface, and test their sensitivity to the change in boundary conditions. To compare the results of the different identifiers, isosurface values high enough to capture the strong vortices were selected. For this purpose, the probability density functions (PDF) of the three identifiers were determined and, to make the comparison consistent, isosurface values of $PDF = 0.1$ were selected, meaning that each identifier carries the same amount of information. The selected isosurface values are identified in figure 7.21 with A for the Q-factor, B for the $-\lambda_2$ criterion and C for the streamline rotation vector, respectively. Figures 7.22(a), 7.22(b), and 7.22(c) display one realization of the instantaneous distributions of the

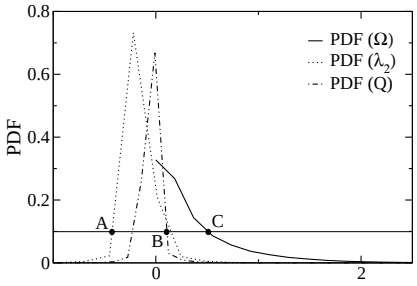

Figure 7.21 PDF distribution of the three different identification criteria.

vortical structures in the FDI case by using isosurfaces of Q, $-\lambda_2$, and the streamline rotation vector, respectively. As it can be seen, the three different criteria provide virtually the same details of the quasi–streamwise vortices developing over the interface. The comparison between several flow snapshots of OCH and FDI, using isosurfaces of the streamline rotation vector (result not included here), has not revealed perceptible differences between the wall–bounded and the air–water flow. This leads to the conclusion that the turbulence structure is not sensitive to small waveslope ripples. However, a detailed quantitative description of the structures could be better inferred from the data using the method of conditional averaging described in Jeong *et al.* (1997).

7.8 CONCLUSIONS

Direct numerical simulation of turbulence in a counter-current air–water flow configuration separated by a deformable interface has been performed. Attention has been focused on the gas side of the interface because of its similarity to wall–bounded flows. A systematic analysis of the near–interface turbulence has been provided. Turbulence intensities for the flow over an interface free to deform were found to be similar to those of wall–turbulence. The RMS values of the off-diagonal components of the fluctuating rate-of-strain tensor are found to be reduced by the interfacial motion, implying a general dampening of the turbulent fluctuating field near the interface. This effect is manifested by a significant reduction in the magnitude of the off-diagonal components in the dissipation tensor. This result was further corroborated by the increased value of the RMS of the fluctuating pressure. Analysis of the auto–correlation function of the trace of the fluctuating rate-of-strain and rate-of-rotation tensors has shown that the interfacial deformation determines the cross-over point where the rotation overcomes the strain and affects the flow field more deeply into the boundary layer. The differences in the turbulent kinetic energy and Reynolds stress budgets are localized in the dissipation, viscous diffusion and turbulent transport terms in the direction normal to the interface. These terms are seen to be slightly smaller than in wall turbulence, whereas the production contributions remain unchanged. A study of the pressure–strain correlation reveals that although the streamwise component remains the only source of energy, the spanwise and normal components are smaller in absolute value, suggesting that the near–interface turbulence is less anisotropic than that near the wall. This conclusion is further

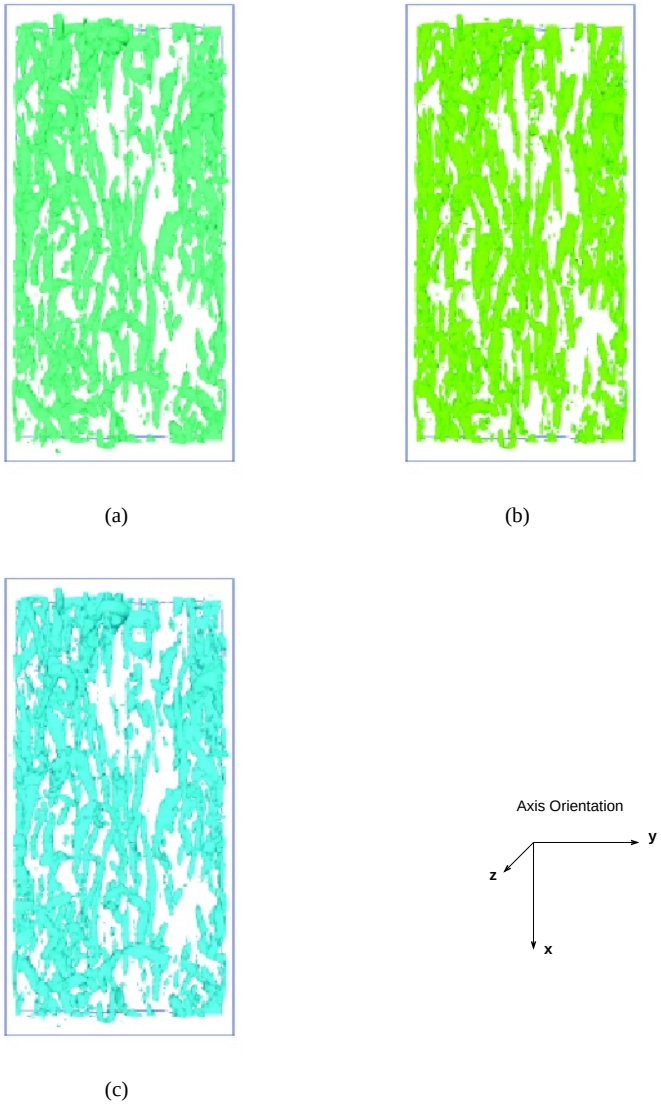

Figure 7.22 Three–dimensional distribution of vortical structures in the FDI case identified by using isosurfaces of (a) Q, (b) $-\lambda_2$, and (c) streamline rotation vector. Values of the isosurfaces were selected with the criterion that $PDF = 0.1$.

confirmed by examining the anisotropy parameter and anisotropy tensor. However, quadrant analysis applied to the shear stress does not reveal important differences in the fractional contributions of individual events compared to wall–turbulence. A detailed study of the nondimensional shear rate parameter shows that the turbulent kinetic energy at the interface does not vanish, suggesting that the turbulent transfer mechanisms are enhanced by the interfacial motion. The streaky structure of the flow over the deformable interface was seen to be somewhat less organized than at the wall. Three well–known eduction techniques, namely isosurfaces of Q, $-\lambda_2$, and the streamline rotation vector, are used to identify the structure of the turbulent flow. A simple qualitative comparison leads to the conclusion that the quasi–streamwise vortices are not significantly modified by the presence of the freely deformable boundary. The small differences found between near–wall and near–interface turbulence might be due to the relatively small value of the Reynolds number, and to the fact that the numerical algorithm is not able to handle strong deformation of the interface. However, these findings provide the starting point for further investigations that use Large Eddy Simulation coupled with Level Set methods, which are capable of exploring large Reynolds number situations featuring wave breaking.

8

DNS of turbulent heat transfer in stratified flow

Le contenu de ce Chapitre est extrait du papier "*DNS of turbulent heat transfer across a mobile, sheared gas–liquid interface*", paru dans *ASME Journal of Heat Transfer*[*] **125**(6), 1129–1139, 2003 by Djamel Lakehal, Marco Fulgosi, George Yadigaroglu and Sanjoy Banerjee.

Here, some inconsistencies in the notation that appeared in the published version have been corrected.

8.1 INTRODUCTION

Most investigations dealing with turbulent heat and mass transfer have traditionally focused on simple configurations involving rigid or flat surfaces. In practice, however, single-phase or two-phase flows may take place in the presence of boundaries which are neither flat nor rigid. In multi-phase flow systems involving immiscible fluids, the interface separating the fluids plays a role similar to that of an impermeable boundary. An example is the exchanges between the atmosphere and the oceans that take place across a continuously deforming interface. On a much smaller scale, gas–liquid exchange mechanisms across deformable interfaces may be encountered in annular flows, falling liquid films, *etc.*

Environmental studies on CO_2 absorption by the oceans (Komori *et al.*, 1982; Rashidi & Banerjee, 1990*a*) have focused on the proper scaling of the averaged mass transfer coefficient with the Reynolds and Prandtl/Schmidt numbers. The principle consists in relating local mass transfer rates and scalar fluxes to the properties of the fluctuating velocity field. The classical approach uses the analogy between diffusion of momentum and of a scalar quantity (heat or mass), extending Fick's gradient laws up to the turbulent regime, *i.e.* the scalar turbulent diffusivity, α_t, is made proportional to the turbulent viscosity, ν_t. The *surface renewal theory* (Danckwerts, 1951*a*) has also been widely employed to parameterize gas–liquid mass transfer rates. Its principle consists in relating the mass transfer rate to the time between sweeps and bursts (τ_{ren}) impinging on the interface, assumed to be responsible for surface renewal, *i.e.* $K \equiv (\mathcal{D}/\tau_{ren})^{1/2}$, where $\mathcal{D} = \nu/Pr$ refers to molecular diffusivity of heat (or mass by simply replacing Pr with Sc, the Schmidt number).

Heat and mass transfer at interfaces depends on the resistance of diffusive layers with thickness $\delta_L \sim O(0.01mm)$ on the liquid side and $\delta_G \sim O(1mm)$ on the gas side. Accordingly the transport across both layers is controlled by fine-scale turbulence, so that the transport mechanisms can be faithfully simulated only by the use of DNS. The complexity of the problems increases if the interface is further sheared and free to deform, in which case an extra

[*]Reprinted with the permission of the publisher, *American Society of Mechanical Engineers.*

transverse motion superimposed on the mean flow is expected to occur in the direction normal to the interface. The continuously deformable interface could then affect the heat/mass transport indirectly by modifying the turbulence in the vicinity of the interface, or more precisely by increasing the portion of frictional drag transferred into form drag. The exact conditions for frictional drag transferred into form drag. The importance of such phenomenon is not yet clear, but a higher impact is expected an order of magnitude larger than δ_G. For longer waves, the time scale over which the surface renews its structure becomes too large compared to the turbulence time scale, and the movement of the interface does not affect the transport phenomena. In summary, momentum and heat/mass transfer across deformable, sheared interfaces depends on the nature of the waves, and hence on the interfacial shear inducing them. An important question that arises then is whether the interfacial heat transfer scales with the friction velocity based on frictional drag and kinematic viscosity.

Although confined to simple configurations involving flat and non-deformable interfaces, early DNS studies proved particularly efficient in providing insight into the scalar exchanges all the way down to the diffusive sublayer. The contributions have generally concentrated on two aspects: a first group essentially focused on modelling turbulent convection mechanisms (Kasagi *et al.*, 1992; Kawamura *et al.*, 1998; Lyons *et al.*, 1991; Na *et al.*, 1999), while a second dealt with mass transfer (Campbell & Hanratty, 1983; McCready & Hanratty, 1984). Wall flow simulations at similar Reynolds numbers, but for different thermal boundary conditions, produced DNS data for the development and calibration of turbulent convection models. The studies involving heat and mass transfer are the most relevant ones for the present contribution. Campbell & Hanratty (1983), who pioneered this class of DNS, were interested in identifying the frequency fluctuations controlling most of the transfer at the wall. McCready & Hanratty (1984) re-investigated the problem considering a flat, mobile gas–liquid interface. Lyons *et al.* (1991) simulated the case of differential heating between channel walls. Calmet & Magnaudet (1997) showed that similar results can be obtained for $Sc = 200$ by use of LES, supporting the fact that the effect of high-frequency turbulence near the wall is filtered out by increasing Pr or Sc (McCready & Hanratty, 1984). Na *et al.* (1999) studied the effect of the Prandtl number on turbulent statistics characterizing transport and the spatial variation of the variance of the fluctuating temperature. The very recent contribution of Piller *et al.* (2002) examines the influence of low Prandtl numbers ($0.025 - 1.0$) on turbulent transport in channel flow. Their study has shown the molecular conductivity to act as a filter for high-frequency velocity fluctuations as Pr decreases, rendering them ineffective in the heat exchange processes.

Paralleling these studies, new steps have been taken in this area with the appearance of DNS of turbulent flow over wavy walls and sheared, gas–liquid interfaces (Lombardi *et al.*, 1996; DeAngelis *et al.*, 1997; DeAngelis, 1998*b*). Lombardi *et al.* (1996) performed a DNS of coupled gas–liquid flows over a flat interface, which revealed that the interface appears to the gas phase almost like a rigid wall, whereas the liquid perceives the interface like a slip surface. DeAngelis *et al.* (1997) studied flows over rigid, sinusoidal wave trains. Their results show that fixed, high-amplitude waves exert significant effects on the mean flow and turbulence characteristics. DeAngelis (1998*b*) employed the same tools to study turbulent mass transfer at the sheared and deformable gas–liquid interface in the limit of capillary waves. A detailed comparison of the turbulence structure at the two different types of interface has later been provided by Fulgosi *et al.* (2003).

The objective of the present study is to complement the aforementioned contributions by exploring the heat transfer processes at a deformable interface, separating counter-flowing gas and liquid. The emphasis is on wave–induced mechanisms influencing the flow and the associated heat transfer in the context of low–to–moderate Pr numbers. The analysis is limited to the gas side, due to the presumed similarity between near–wall and near–interface turbulence. The effect of Prandtl number ($Pr = 1, 5$ and 10) on the thermal field is investigated by means of a global analysis of the averaged heat fluxes, $\overline{u_i\theta}$, the temperature variance, $\overline{\theta^2}$, and the eddy diffusivity. Moreover, a scaling law for the heat transfer coefficient based on the effective viscous friction velocity is presented.

8.2 MATHEMATICAL MODEL AND NUMERICAL STRATEGY

In this section, since the governing equations and the numerical procedure have been extensively described in chapter **??***, part of the original text is omitted.*

The reference quantities employed for normalization in each domain are the effective shear velocity $u_\star = \sqrt{2h\Pi/\rho}$, where Π is the the mean pressure gradient driving the flow, the half-depth of each computational domain h, and the kinematic viscosity ν.

The reference temperature $T_\star$ is defined as

$$T_\star = \frac{q_{int}}{\rho c_p u_\star} \; ; \quad q_{int} = -\lambda \left(\frac{d\overline{T}}{dz} \right)_{int} \tag{8.1}$$

where q_{int} represents the interfacial heat flux. The time is made nondimensional using $\nu/u_\star^2$, and the length scales are normalized using $u_\star/\nu$. In each computational domain, the shear Reynolds number, defined as $Re_\star = u_\star 2h/\nu$, is 171.

The size of each computational domain is $4\pi h \times 2\pi h \times 2h$ in streamwise, spanwise and interface–normal directions, corresponding to $1074 \times 537 \times 171$ wall units. As capillary waves do not produce significant domain distortion, a grid resolution (for each domain) of $64 \times 64 \times 65$ in the streamwise, spanwise and interface–normal directions was found to be appropriate for the solution of the velocity field. This is proved in figure 8.1, displaying the energy spectra against wave numbers k_x and k_y for the three velocity components, evaluated at five wall units distance from the interface in the gas side. The result shows no energy accumulation at high wave numbers,

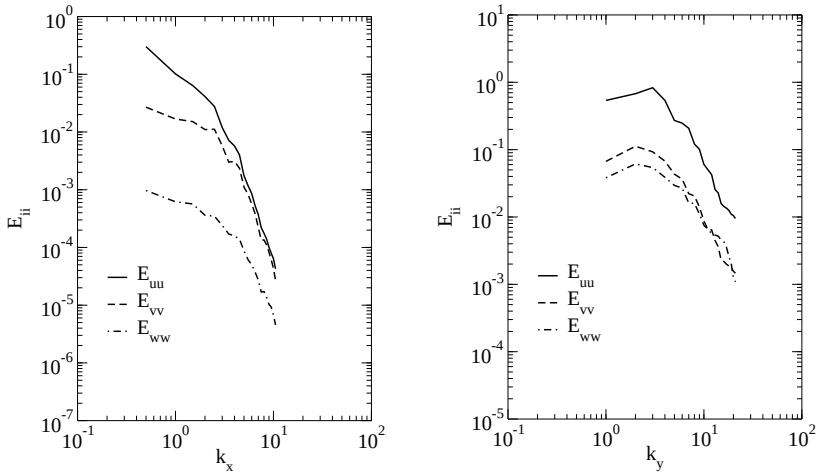

(a) Streamwise direction. (b) Spanwise direction.

Figure 8.1 Energy spectra at $z^+ = 5$ for the velocity components, in the gas phase.

confirming that this resolution is sufficiently accurate for the solution of the velocity field. The extension of the spectrum to higher wave numbers, obtained by doubling the grid resolution in the interface–normal direction, did not show energy accumulation either (result not presented here). In their review of past DNS of heat transfer in channel flow, Piller *et al.* (2002) note that the differences observed between some of the published results were chiefly due to insufficient statistical convergence, rather than to lower space resolution in the wall–normal direction.

8.2.1 Simulations

The shear Reynolds number $Re_\star$ is in each phase equal to 171. The inter-phase heat transfer does not include phase change. To limit the wave amplitude and steepness to the range of capillary waves, the Weber and Froude numbers were set equal to $We = 4.8 \times 10^{-3}$ and $Fr = 8.7 \times 10^{-5}$. The gas and liquid phases considered are such that $\mathcal{R} = 29.9$. Three different thermal conditions have been investigated, namely $Pr = 1$, 5 and 10. For $Pr = 1$, the spatial resolution employed in each domain is $64 \times 64 \times 65$ (hereinafter referred to as G1), whereas for $Pr = 5$ and 10, it was doubled in the direction normal to the interface, *i.e.* $64 \times 64 \times 129$ (referred to as G2). The grid resolutions in G1 ($\Delta x^+ = 16.77$, $\Delta y^+ = 8.38$, $\Delta z^+ = 0.102 - 4.191$) and G2 ($\Delta x^+ = 16.77$, $\Delta y^+ = 8.38$, $\Delta z^+ = 0.026 - 2.096$) are comparable to those employed by Tiselj *et al.* (2001*a*). The time increments are $0.024\ \nu/u_\star^2$ for the G1 grid, and $0.012\ \nu/u_\star^2$ for G2.

After statistically stationary conditions were achieved in each run, the velocity and thermal fields were collected over $4000\ \nu/u_\star^2$ nondimensional time units. The criterion used to establish steady state conditions was that the turbulent shear stress, $\overline{u^+w^+}$, and the turbulent heat flux, $\overline{w^+\theta^+}$, were no longer varying over a time interval of 1000 nondimensional time units. The simulation parameters are summarized in table 8.1.

Table 8.1 Computational Parameters.

	Pr = 1	***Pr = 5***	***Pr = 10***
$Re_\star$	171	171	171
We	4.8×10^{-3}	4.8×10^{-3}	4.8×10^{-3}
Fr	8.7×10^{-5}	8.7×10^{-5}	8.7×10^{-5}
$\mathcal{R} = \sqrt{\rho_L/\rho_G}$	29.9	29.9	29.9
Grid points in each domain	$64 \times 64 \times 65$	$64 \times 64 \times 129$	$64 \times 64 \times 129$
Δx^+	16.77	16.77	16.77
Δy^+	8.38	8.38	8.38
Δz^+	0.102 - 4.191	0.026 - 2.096	0.026 - 2.096
Time Increment	$0.024\ \nu/u_\star^2$	$0.012\ \nu/u_\star^2$	$0.012\ \nu/u_\star^2$

8.3 INTERPRETATION OF RESULTS

Motivated by the uncertainties as to the existence of a similarity between near–wall and near–interfacial turbulence, Fulgosi *et al.* (2003) studied the turbulent gas flow over the deformable interface, and compared the results to wall–bounded flow data at the same shear Reynolds number. In a time–averaged sense, the interfacial motion was seen to affect some features of the turbulence field in the near–interface region; the most pertinent effect is a general dampening of the turbulent fluctuating field which, in turn, leads to a reduction in the interfacial dissipation. Furthermore, the turbulence was found to be less anisotropic at the interface than at the wall. The analysis of the turbulent kinetic energy and Reynolds stress budgets revealed that the interface deformations mainly affect the so-called boundary term involving the redistribution of energy, and the dissipation terms, leaving the production terms almost unchanged. Away from the interface, the decomposition of the fluctuating velocity gradient tensor demonstrated that the fluctuating rate-of-strain and rate-of-rotation at the interface influence the flow throughout the boundary layer more vigorously.

Following this comparative strategy, in the present work, the interfacial turbulent heat transfer in the gas is investigated, and the results compared to wall–bounded flow data to reveal the effect of the interfacial deformation on heat transfer mechanisms for a range of low Prandtl numbers. As it is customary in DNS, the statistical analysis of the data is performed by averaging the collected velocity and thermal database over the two homogeneous directions (*i.e.* x–y plane average) and in time. For the flow under consideration here, this averaging procedure can be reliable only if the collected data cover a sufficiently large time interval over which the wave properties do not change. The statistical stationarity of the wave field is discussed below.

8.3.1 Characteristics of the waves

In this section part of the original text is omitted, because the theoretical part on the wave characterization has been introduced already in section 7.3.

The wave saturation spectra, obtained using grid G1, are plotted in figure 8.2 at two different times during the simulation: at the early stage (referred to as B_{in} in figure 8.2) and at the end (referred to as B_{out}) of the time interval over which the statistical analysis has been performed. The graph clearly indicates that the wave properties did not change significantly within this time interval, confirming the existence of the saturation or equilibrium range, which is synonymous to convergence in this context. The impact of the interfacial motion can then be inferred in an average sense.

8.3.2 Statistics of the thermal field

The mean temperature profiles plotted against the distance to the interface are shown in figure 8.3(a) for all Prandtl numbers. The results obtained by Kawamura *et al.* (1998) at $Re_\tau = 180$ for $Pr = 1$ and $Pr = 5$, and by Tiselj *et al.* (2001*b*) at $Re_\tau = 171$ for $Pr = 1$ and $Pr = 5.4$ (for an isothermal wall boundary condition) have been included for comparison. For $Pr = 10$ the present DNS has been compared to that of Na *et al.* (1999) at $Re_\tau = 150$. For $Pr = 1$ the present results agree fairly well with both data bases (Kawamura *et al.*, 1998; Tiselj *et al.*, 2001*b*), whereas for $Pr = 5$ the agreement is better with that of Kawamura *et al.* (1998) than with those

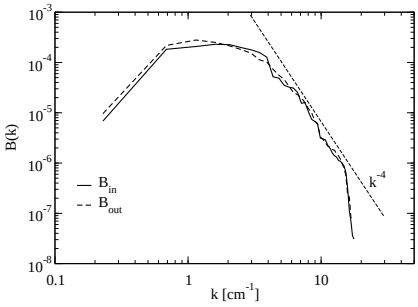

Figure 8.2 Saturation spectra of the wave fields at the beginning (B_{in}) and at the end (B_{out}) of the sampling period.

of Tiselj *et al.* (2001*b*). For $Pr = 10$ the comparison with the data of Na *et al.* (1999) is overall satisfactory. Figure 8.3(b) shows that inside the diffusive sublayer, the mean temperature profiles are in agreement with the linear relation $\Theta^+ = Pr\, z^+$. Further analysis of the data also permits to identify the extent of the logarithmic layer,

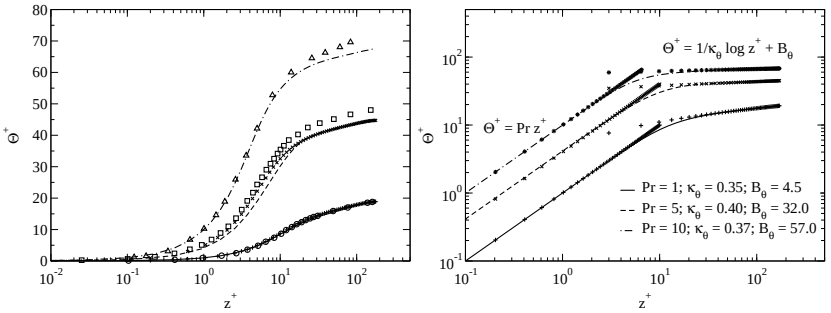

Figure 8.3 Mean temperature profiles. (a) Comparison with other DNS databases. Lines are used to identify the present DNS result: —, $Pr = 1$; − − −, $Pr = 5$; −·−, $Pr = 10$. Symbols identify respectively: $+$, $Pr = 1$ and $\times$, $Pr = 5$: DNS of Kawamura *et al.* (1998); $\circ$, $Pr = 1$ and $\square$, $Pr = 5$: DNS of Tiselj *et al.* (2001*b*); $\triangle$, $Pr = 10$: DNS of Na *et al.* (1999). (b) Present DNS extrapolated data; lines are used to identify present DNS results and symbols to identify the fitting equations.

where $\Theta^+ = 1/\kappa_\theta\ ln\ z^+ + B_\theta$. Both the slope, κ_θ^{-1}, and the shift, B_θ, are found to vary with Prandtl number, though without leading to the establishment of a clear relationship. The diffusive sublayer exists in all three flows, with thicknesses Δ_θ^+ decreasing with increasing Prandtl number, *i.e.* $\Delta_\theta^+ \approx 6$, 4 and 2 wall units, respectively, for $Pr = 1$, 5 and 10. While the results for Δ_θ^+ agree with those of Na *et al.* (1999) and Kawamura *et al.* (1998), those for the slope $1/\kappa_\theta$ and the shift B_θ deviate appreciably from Na *et al.* (1999) data. These deviations are perhaps due to the lower Reynolds number used by Na *et al.* (1999) rather than the wall boundary conditions employed in their simulation. The difference in the slopes, in particular, suggests that the intensity of turbulence in Na *et al.* (1999) is simply weaker.

The behaviour of the fluctuating temperature field near the wall/interface is generally accepted as a good indicator of the way scalar turbulent transport operates. An important feature requiring understanding is the effect of the Prandtl number on the interplay between molecular and turbulent transport near the wall. The r.m.s. values of the temperature fluctuations are presented in figure 8.4, where the results of Kawamura *et al.* (1998) and Tiselj *et al.* (2001*b*) for $Pr = 1$ and $Pr = 5$, and those of Na *et al.* (1999) for $Pr = 10$, are again included for comparison. As can be observed, in both wall–bounded and interfacial flows, the increase in Prandtl number corresponds to a shift of the maximum of the temperature fluctuations towards the boundary. Both in the present results and in the simulation of Kawamura *et al.* (1998) for $Pr = 1$, the maximum of the temperature fluctuations is located around $z^+ = 17$. Increasing the Prandtl number to 5 shifts the peak location to about $z^+ = 7$ in the wall–bounded flow, and to around $z^+ = 9$ in the flow over the deformable interface. The wall flow data of Na *et al.* (1999) show the maximum of the temperature fluctuations located around $z^+ = 3$, whereas the present study shows that location to be around $z^+ = 5$. It is interesting to note that the exact location of the maximum r.m.s. value is not correlated with the position of the edge of the diffusive sublayer Δ_θ^+: the two locations tend to coincide with increasing Prandtl number.

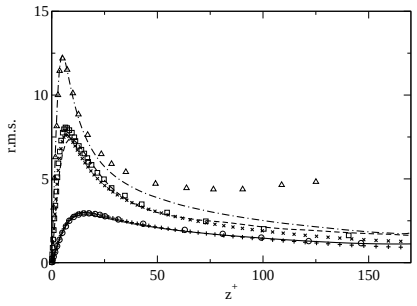

Figure 8.4 Root mean square value of temperature fluctuations. Lines are used to identify the present DNS result: —, $Pr = 1$; − − −, $Pr = 5$; −·−, $Pr = 10$. Symbols identify respectively: $+$, $Pr = 1$ and $\times$, $Pr = 5$: DNS of Kawamura *et al.* (1998); $\circ$, $Pr = 1$ and $\square$, $Pr = 5$: DNS of Tiselj *et al.* (2001*b*); $\triangle$, $Pr = 10$: DNS of Na *et al.* (1999).

The first important conclusion to be drawn from the above comparisons is that, as in wall flows, the most relevant statistical quantities scale with the friction velocity, based on frictional drag. The ratio of frictional drag to total drag (including form drag) was found to be around 0.98. The second important finding is the appreciable effect of Pr on $\overline{\theta^{+2}}$, indicating that the range of wave numbers in the thermal fluctuating field increases with Pr, for which the spectral functions of the velocity field are negligible.

8.3.3 Turbulent fluxes and inter-phase heat exchange

Figure 8.5 shows the nondimensional averaged turbulent heat flux (THF), $\overline{u^+\theta^+}$, in the streamwise direction versus the dimensionless distance to the interface/wall. The data are compared to the channel-flow DNS of Kawamura *et al.* (1998). For $Pr = 1$ the streamwise THF over the deformable interface compares very well with the wall data;

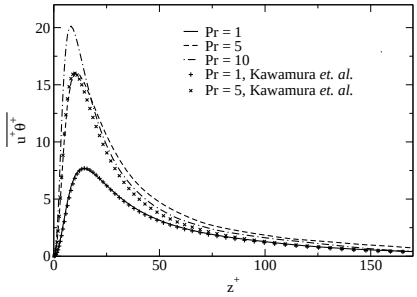

Figure 8.5 Streamwise turbulent heat flux and comparison with Kawamura *et al.* (1998).

the behaviour is similar and the peak value in both cases is located at the same distance from the interface/wall, $z^+ \approx 18$, which corresponds to the location of the maximum r.m.s. value of the temperature fluctuations. For $Pr = 5$, the streamwise THF near the interface exhibits some differences compared to that near the wall, but peak values are almost identical and are furthermore reached almost at the same location from the interface/wall ($z^+ \approx 11$). Beyond the peak location, however, the THF for the flow over the deformable interface remains slightly higher than for the wall flow. For $Pr = 10$ the streamwise THF peak location occurs at $z^+ \approx 8$. This analysis confirms that increasing the molecular Prandtl number substantially increases the intensity of the heat flux when approaching the wall/interface, depending on the thickness of the thermal boundary layer. Away from the diffusive thermal sublayer, the value of the THF drops faster for higher Prandtl numbers. Deeper in the bulk flow, heat transfer by turbulent transport does not depend much on the Prandtl number.

Figure 8.6(a) presents the distribution of the nondimensional averaged THF in the direction normal to the interface, $\overline{w^+\theta^+}$. We note that as the molecular Prandtl number increases the peak location moves closer to the interface, and so does the intensity of the flux. The deviation between the near–interface and near–wall values (at $z^+ < 10$) of the normal THF is analyzed in detail in figure 8.6(b). For both $Pr = 1$ and $Pr = 5$ the flux intensity near the deformable interface is higher than at the wall. This implies that the interfacial dynamics leads to an increase in the vertical THF as compared to the situation near the rigid wall. The only plausible explanation for this difference is that the waves promote the velocity fluctuating field normal to the interface. Fulgosi *et al.*

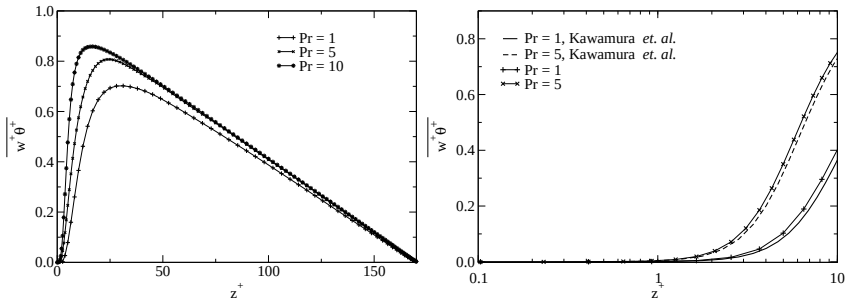

Figure 8.6 Interface–normal turbulent heat flux. (a) Boundary layer. (b) Near interface/wall region and comparison with Kawamura *et al.* (1998).

(2003) indeed report that the turbulent kinetic energy decays faster at the wall than at the mobile interface. The differences between the streamwise and vertical THFs will be explained more fully in Section 8.3.5, where the budget equations for the heat fluxes are compared term by term.

The nondimensional heat transfer coefficient (HTC) is defined by

$$K_\tau^+ = \frac{q_{int}}{\rho \Delta \overline{T} c_p u_\tau} = \frac{1}{Pr} \frac{1}{\left(\overline{T}_{top} - \overline{T}_{int}\right)} \left.\frac{d\overline{T}}{dz^+}\right|_{int}, \tag{8.2}$$

where $\overline{T}_{top}$ represents the mean temperature at the upper boundary of the gas domain (in Papavassiliou & Hanratty (1997), $\overline{T}_{top}$ was taken at the center of the closed channel). Note, too, that K^+ is normalized by the friction velocity, *i.e.* associated with a frictional drag $u_\tau = 0.98 u_\star$. The scaling of the heat transfer coefficient with the frictional velocity u_τ has so far shown that it scales with $Pr^{-1/2}$ at mobile interfaces, and with $Pr^{-2/3}$ at immobile interfaces. DeAngelis (1998*b*) have shown the $Pr^{-2/3}$ scaling to also hold on the gas side of wavy gas–liquid interfaces, but for high–Sc numbers only.

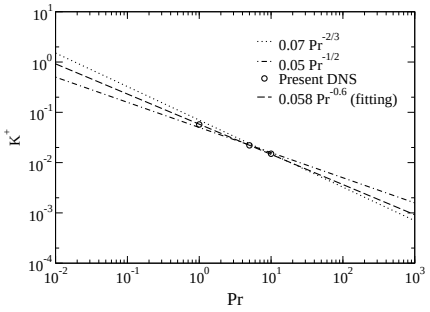

Figure 8.7 Heat transfer coefficient.

Figure 8.7 presents the values of the nondimensional HTC obtained for the gas side in the present DNS as a function of Prandtl number. For the range of Pr investigated here, the present DNS provides the following variation of the HTC

$$K_\tau^+ = 0.058\, Pr^{-3/5}, \tag{8.3}$$

which can be seen to vary between $\propto Pr^{-1/2}$ for free surfaces and $\propto Pr^{-2/3}$ for immobile interfaces and much higher Prandtl numbers. For instance, the DNS of Na *et al.* (1999) delivered smaller values for both the coefficient of proportionality and the exponent, *i.e.* 0.0509 and 0.546, respectively. A parameterization of the scalar transfer rate by reference to the *surface renewal theory*, using the above result, yields

$$K_\tau^+ = 0.41\, \tau_{ren}^{+-0.5}\, Pr^{-0.6}, \tag{8.4}$$

where the normalized (by ν/u_τ^2) mean time between sweeps, τ_{ren}^+, given by the DNS is approximately equal to $f_{sweep}^{-1} = 50$, where f_{sweep} denotes the frequency of sweeps/ejections. Banerjee (1971) obtained a similar

relationship for high–Sc mass transfer at solid walls based on the Leveque boundary layer solution, reading

$$K_\tau^+ = 0.68\, \tau_{ren}^{+^{-0.5}}\, Sc^{-0.66}, \tag{8.5}$$

in which both the constant and the Sc power are actually functions of the Schmidt number. A close inspection of the Polhausen's boundary layer solution reveals on the other hand that the best fit for Sc in the range of Pr =5 to 15 is obtained with the constant fixed to 0.6 and the Sc exponent to -0.6.

Contours of the instantaneous HTC at the interface are shown in figures 8.8(d), 8.8(f) and 8.8(h), for Pr= 1, 5 and 10, respectively, and are compared with the thermal streaks represented by contours of θ^+ at $z^+ = 12$, shown in the neighbouring left panels (figures 8.8(c), 8.8(e), 8.8(g)). The comparison also includes contours of instantaneous velocity streaks, marked by contours of u^+ at $z^+ = 12$ (figure 8.8(a)), and the instantaneous shear stress at the interface (figure 8.8(b)). The three-dimensional interfacial waves can be seen to develop and propagate in the direction of the gas-flow (in the pictures the wave amplitude has been magnified by a factor 10). Regions of high shear-high heat transfer rates at the crests can be clearly distinguished from regions of low shear-low heat transfer rates at the troughs. The streaky structure of the velocity field is well represented by contours of u^+, similar to what is observed in wall flow (Lam & Banerjee, 1992), and is shown to conform to the thermal streaks for $Pr = 1$. This result indeed confirms the Reynolds analogy between diffusion of momentum and diffusion of heat; the deviations become evident with increasing Prandtl number.

Observing the HTC contours also reveals that heat transfer rates correlate with the interfacial shear; the largest values, occurring at the bulges imposed by turbulent motions, correspond to strongly positive shear values and positive u^+ levels, presented in figure 8.8(a). According to the quadrant analysis of near–wall/interface turbulence structure (Lombardi *et al.*, 1996), this scenario is the signature of sweep events through which the surface renews its structure, leading to high scalar transfer rates. By controlling surface renewal throughout the migration of high momentum fluid towards the interface, sweep motions create regions of high interfacial shear stress, leading in turn to high heat transfer rates. The scalar transfer rate reaches its peak value when the sweep impinges on the surface; during the decay time the diffusive layer saturates by the actions of molecular diffusion. On the other hand, increasing the Pr number produces a much finer thermal streaky structure and a decrease in heat transfer rate (note that the scale of the plots changes with Pr).

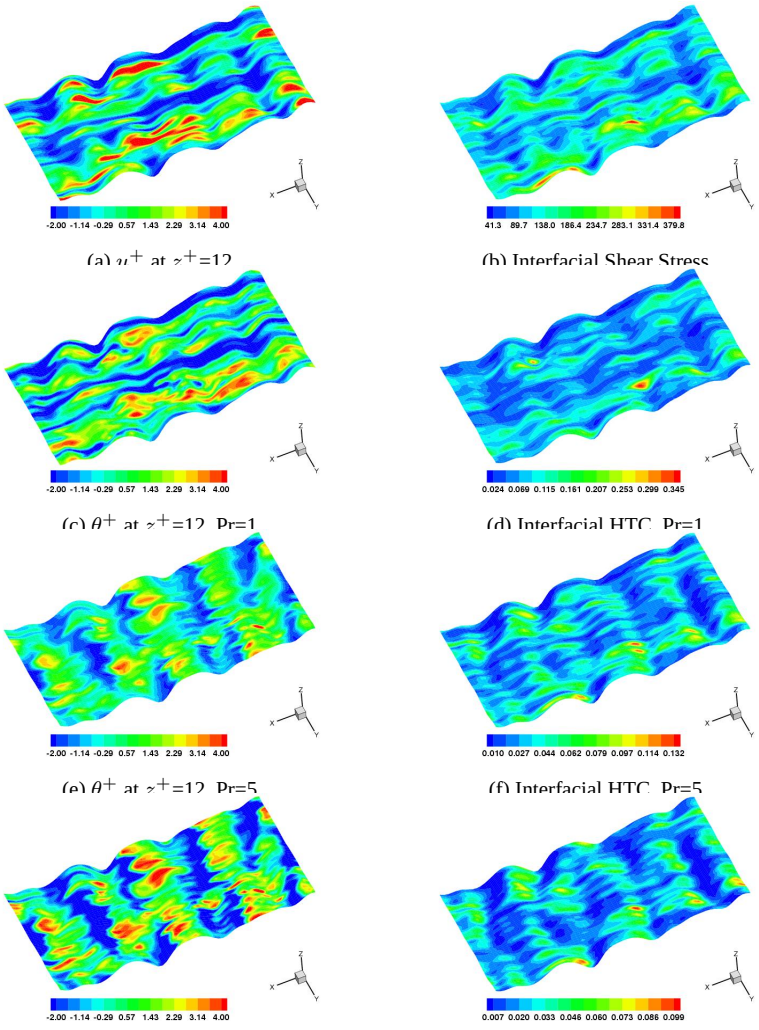

(a) u^+ at z^+=12 (b) Interfacial Shear Stress

(c) θ^+ at z^+=12, Pr=1 (d) Interfacial HTC, Pr=1

(e) θ^+ at z^+=12, Pr=5 (f) Interfacial HTC, Pr=5

(g) θ^+ at z^+=12, Pr=10 (h) Interfacial HTC, Pr=10

Figure 8.8 The elevation of the waves is amplified by factor 10.

8.3.4 Temperature variance

As the turbulent kinetic energy represents an integral measure of the energy associated with the fluctuating velocity field, the variance of the fluctuating temperature $\overline{\theta^2}$ may be regarded as the energy carried by the fluctuating temperature field. The equation for the evolution of the temperature variance can be written in compact form (see, for example, Nagano (2002)) as

$$\frac{D\overline{\theta^2}}{Dt} = \mathcal{D}_\theta + \mathcal{T}_\theta + \mathcal{P}_\theta - \varepsilon_\theta \tag{8.6}$$

where D/Dt is the substantial derivative. The first and second terms on the right-hand side of this equation represent the diffusion by molecular actions and the diffusion due to turbulent transport, respectively. The third term is the production of $\overline{\theta^2}$ by the interactions between heat fluxes and mean temperature gradients. The last contribution represents the dissipation of the variance.

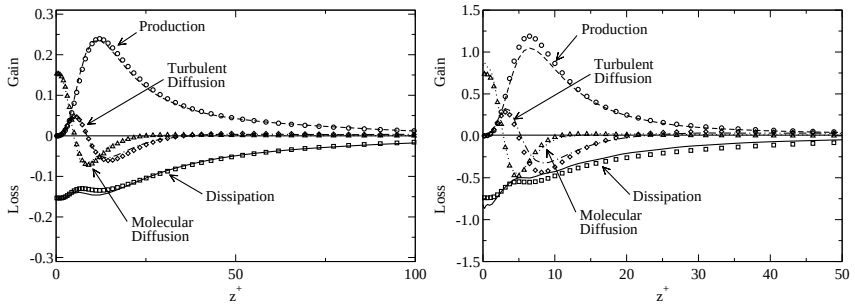

(a) Temperature variance budget – Pr = 1 (b) Temperature variance budget – Pr = 5

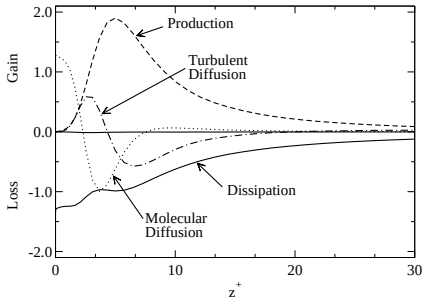

(c) Temperature variance budget – Pr = 10

Figure 8.9 Budget for the temperature variance in the near interface/wall region. Lines are used to identify the results of the present DNS and symbols to identify the wall–bounded DNS results of Kawamura *et al.* (1998).

Figure 8.9 presents the budget terms obtained, for the gas side, from the present DNS. For the smaller Prandtl numbers, $Pr = 1$ and 5, results are again compared to the data of Kawamura *et al.* (1998). For $Pr = 1$, there are only small differences in the contributions to the balance (figure 8.9(a)), which conforms with previous results regarding the thickness of the thermal and momentum boundary layers and averaged heat fluxes. The effects of interfacial motion on the fluctuating thermal field are negligible at this Prandtl number. As the molecular Prandtl number increases (figure 8.9(b)), minor deviations from the wall–bounded data begin to appear, in particular concerning the production and turbulent diffusion terms. A comparison of the averaged normal heat flux in figure 8.6(b) explains why the production in wall flow is stronger than in the flow over the deformable interface.

The budget for $Pr = 10$, presented in figure 8.9(c), indicates that the contribution of the production term becomes important with increasing Prandtl number, which is also true of the dissipation. In particular, these two contributions can be compared to the results of Na *et al.* (1999) (their figures 7 and 13), which also show the values of $\mathcal{P}_\theta$ and ε_θ at the wall to increase drastically for $Pr = 10$. The behaviour of the dissipation in the diffusive thermal sublayer appears to be much more flat than for the case of the wall flow, and the starting value is also smaller.

8.3.5 Turbulent heat fluxes

In turbulence modeling, the most sophisticated approach accounting for the effects of turbulence-induced stresses in the heat transport consists in solving the transport equation for the turbulent heat fluxes, $\overline{u_i\theta}$, rather than resorting to the eddy diffusivity concept. In compact form, this transport equation can be written as

$$\frac{D\overline{u_i\theta}}{Dt} = \mathcal{P}_i^\theta + \Pi_i^\theta + \mathcal{D}_i^\theta - \varepsilon_i^\theta \tag{8.7}$$

where the first term, $\mathcal{P}_i^\theta$, represents the mean flow production due to the combined actions of mean temperature gradients and mean velocity gradients. The second term is the pressure-temperature correlation, $\Pi_i^\theta \equiv -\overline{\theta\,\nabla p}$. The third contribution, $\mathcal{D}_i^\theta$, designates the diffusive transport comprising molecular, $\mathcal{D}_i^{m\theta}$, and turbulent counterparts, $\mathcal{D}_i^{t\theta}$. The last term, ε_i^θ, refers to the dissipation of turbulent heat flux (see, for example, Kasagi *et al.* (1992) or Nagano (2002) for the exact definition of each contribution).

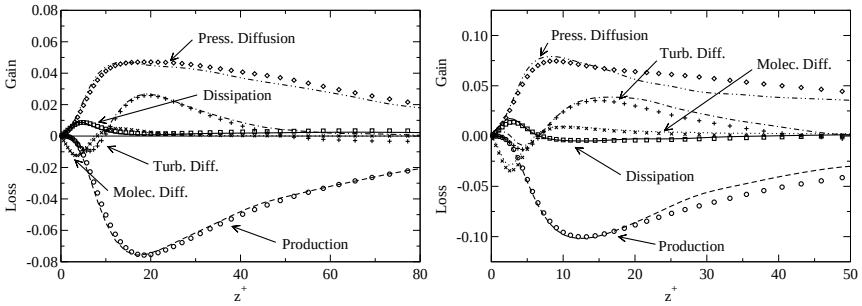

(a) Vertical turbulent heat flux budget – Pr = 1

(b) Vertical turbulent heat flux budget – Pr = 5

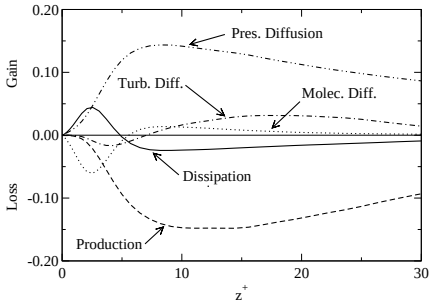

(c) Vertical turbulent heat flux budget – Pr = 10

Figure 8.10 Budget for the vertical turbulent heat flux in the near interface/wall region. Lines are used to identify the results of the present DNS and symbols to identify the wall–bounded DNS results of Kawamura *et al.* (1998).

Budgets of the streamwise heat flux, $\overline{u^+\theta^+}$, for the gas flow data obtained by the present DNS were compared (result not included here) to the channel-flow data of Kawamura *et al.* (1998), for Pr=1 and 5. The comparison revealed the same behaviour as observed before: the production becomes more important with increasing Pr, the molecular diffusion dominates as a positive contribution in the diffusive sublayer and is balanced by the dissipation, while away from the wall/interface the production is balanced by the dissipation. The behaviour of the dissipation, ε_i^θ, was particularly interesting: for $Pr = 1$ its level gradually decreases away from the wall/interface, whereas for $Pr = 5$ and 10 it marks a sharp drop at locations around the edge of the diffusive sublayer.

The effect of varying Prandtl number on the wall/interface-normal heat flux balance, $\overline{w^+\theta^+}$, is discussed in relation to figure 8.10, comparing the wall and the present deformable interface database. Again, the production, which is negative in this case, gains in importance with increasing Pr, with the peak location always moving closer to the wall. In contrast to the streamwise component, the production in the normal direction is balanced by the pressure-gradient correlation $\Pi_3^\theta \equiv -\overline{\theta\,\partial_z p}$, and to a small extent by the turbulent diffusion $\mathcal{D}_3^{t\theta}$. The dissipation again shows an interesting behaviour: the peak value of ε_3^θ in the diffusive sublayer increases with the Prandtl number. For $Pr = 1$ the dissipation converges asymptotically almost to zero at $z^+ \approx 20$. For higher Prandtl

numbers, the sign of ε_3^θ reverses exactly where the molecular and turbulent diffusion contributions change sign, too, indicating that in some flow regions the dissipation contributes positively as a gain. This was already revealed by Kasagi *et al.* (1992) and Kawamura *et al.* (1998), and was attributed to the fact that the dissipation takes place in the large-scale structures.

8.3.6 Turbulent thermal diffusivity

Turbulent thermal diffusivities were determined by averaging the thermal stress data and temperature gradients in the homogeneous directions and in time. The turbulent thermal diffusivity, α_t, was defined by applying the simplified Gradient Diffusion Hypothesis (GDH)

$$\overline{w^+\theta^+} = -\alpha_t \, \frac{d\Theta^+}{dz^+} \, . \tag{8.8}$$

The impact of varying Pr on the distribution of eddy diffusivity scaled by Pr is shown in figure 8.11(a), where the eddy viscosity – determined by use of GDH – is also included for comparison. For $Pr = 1$ the data show the natural increase of α_t with distance to the interface, converging towards 15.5 at $z^+ = 100$. An increasing Prandtl number has no effect on α_t in the region close to the interface ($z^+ < 40$), but a larger one away from it. The eddy diffusivity is shown to gain almost 30% in this flow region. An attempt to infer values of the turbulent Prandtl number from this plot would not be conclusive, owing to the ragged profiles of α_t in the core flow region. Again, there is no clear picture on the exact dependence of α_t on Pr away from the interface.

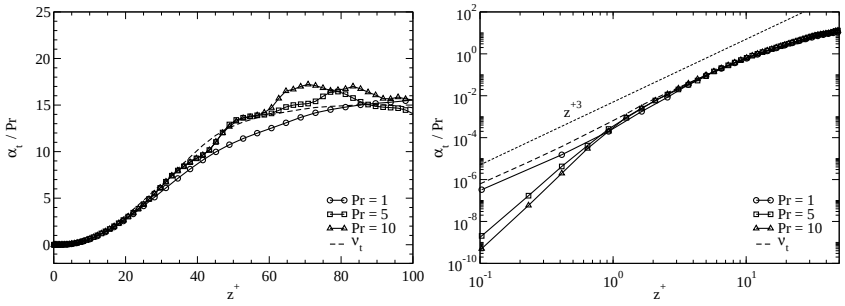

Figure 8.11 (a) Turbulent diffusivity. (b) Turbulent diffusivity in the vicinity of the deformable interface.

The limiting behaviour of the thermal diffusivity in the vicinity of the deformable interface is presented in figure 8.11(b), where the turbulent diffusivity for momentum is also included. For $Pr = 1$ both α_t and ν_t vary with z^{+3}, as in wall flows. This again lends support to the hypothesis that the interface appears to the lighter phase like a wall. On the other hand, the result confirms the analogy between the diffusivities of momentum and heat for $Pr = 1$. However, at the same time it is noted that the slope of α_t / z^{+n} ($n > 3$) increases with Pr as the interface is approached. This result suggests that $\alpha_t \sim z^{+3}$ cannot be justifiably generalized. The results of Na *et al.* (1999) reveal the existence of a conductive layer at the wall, where α_t / z^{+3} appears to be constant, although it is decreasing with increasing Pr.

In summary, deformable, sheared interfaces populated by capillary waves with small wavelength play a similar role in heat transfer as solid walls. In particular, the near–interface limiting behavior is such that the normal velocity varies quadratically with the distance to the interface, and therefore the shear stress $\overline{u^+w^+}$ and the heat flux $\overline{w^+\theta^+}$ vary with z^{+3}. The scaling for α_t is, however, strongly tied to the Prandtl number, in that the variation with z^{+3} holds only for $Pr = 1$. For $Pr = 5$ and 10, on the other hand, the variation is proportional to z^{+n}, where $n > 3$.

8.4 CONCLUDING REMARKS

Turbulent heat transfer across a mobile, sheared gas–liquid interface has been studied using direct numerical simulation. The purpose of the investigation was to examine the impact of the interfacial dynamics on turbulent heat transfer, and to investigate the influence of the Prandtl number on the transports by comparing the results to existing wall flow data. The motivation arose from the fact that investigations dealing with turbulent scalar transfer

have focused on simple configurations involving rigid, flat surfaces, while in multicomponent systems the flow necessarily involves interfaces that are neither flat nor rigid.

The flow system studied comprises counter-flowing gas and liquid phases, each at a shear-based Reynolds number of 171. The interface deformations were limited to capillary-wave ripples with waveslope $ak = 0.01$. Since, for high density ratios, interfaces play a role similar to that of a solid boundary, emphasis has been placed on the gas side. For both $Pr = 1$ and $Pr = 5$ the flux intensity near the deformable interface was found to be higher than at the wall. This implies that the interfacial dynamics leads to an increase in the vertical THF as compared to its value near the rigid wall. The explanation for this difference is that the waves enhance the velocity fluctuating field normal to the interface, as was revealed in Fulgosi *et al.* (2003). The effect of Prandtl number ($Pr = 1, 5,$ and 10) on the averaged heat flux, the temperature variance, the eddy diffusivity, and the heat transfer scaling laws has been examined.

The changes in Pr were indeed found to affect the average results, but in very much the same way as in available wall flow data. This was particularly true for the way the thickness of the diffusive sublayer reduces with increasing Pr, and in reference to the induced influence on the production of heat flux and variance. It was also noticed that the pressure diffusion and dissipation contributions to the normal heat flux balance change with varying Prandtl number. This is an important result, since the capillary waves are expected to modify the local rate of heat transfer only through a reduction of the frictional drag in favor of form drag. This tendency accentuates with increasing waveslope caused by increasing $u_\star$. In the present case, the imposed shear velocity at the beginning of the computations led to a ratio of frictional drag to total drag (including form drag) of 0.98. Another important result is the appreciable effect of Pr on $\overline{\theta^{+2}}$, and also on the thermal time scale $\tau_\theta \equiv \overline{\theta^{+2}}/\epsilon_\theta$ (results not included), indicating that the range of spectral functions for the thermal fluctuating field increases with Pr.

The scaling law for the nondimensional heat transfer velocity K_τ^+ on the gas side, normalized using the friction velocity u_τ, suggests an approximate $Pr^{-3/5}$ relationship, varying between $Pr^{-1/2}$ for free surfaces and $Pr^{-2/3}$ for immobile interfaces and much higher Prandtl numbers. The parameterization of the heat transfer rates based on the surface renewal theory delivers values for the constant of proportionality and the Pr–power that conform with both the Leveque and the Polhausen boundary layer solutions. A close inspection of the transfer rates reveals a strong and consistent relationship between the transfer rate, the frequency of sweeps impacting the interface, the interfacial velocity streaks, and the interfacial shear stress. Similarly to what is observed in wall flows, for $Pr = 1$ the turbulent viscosity/diffusivity was found to asymptote with z^{+3}. For higher Pr, however, the scaling was seen to change to z^{+n}, with $n > 3$. In the viscosity-affected layer the assumption that $\alpha_t \sim \nu_t$ was found to hold in this context, too, whereas in the outer core flow, α_t was greater than ν_t, and no clear picture emerged as to the distribution of the turbulent Prandtl number.

The present study has addressed only some of the many issues of this complex problem. It would be intriguing to see how statistical quantities scale with higher imposed shear velocities, *i.e.* in the presence of higher amplitude waves.

9

Surface Divergence Models Between Turbulent Streams

Le contenu de ce Chapitre est extrait du papier "*Surface Divergence Models Between Turbulent Streams*", paru dans *Int. J. Multiphase Flow*[*] **30**, 963-977, 2004 by Sanjoy Banerjee, Djamel Lakehal and Marco Fulgosi.

abstract

Surface divergence models for prediction of scalar exchange at fluid–fluid interfaces are investigated. The models, based on the Hunt-Graham blocking theory, are shown to predict experimental data at unsheared interfaces, and new results of direct numerical simulation for deformable, non-breaking sheared interfaces. The parametrization is in terms of the turbulent Reynolds number defined by the integral velocity and length scales in the bulk flow, which makes it useful for practical purposes.

9.1 INTRODUCTION

Scalar exchange between turbulent streams separated by a deformable fluid–fluid interface plays an important role in the performance of equipment like evaporators, condensers, gas–liquid and liquid–liquid contactors, and in environmental systems. There has been an intense and renewed interest in the subject due to its central role in the uptake of greenhouse gases and release of moisture by terrestrial water bodies. To put the greenhouse gas uptake problem in context, it should be noted that approximately 30-40 percent of man-made CO_2 (the most persistent greenhouse gas) is taken up by the oceans. However, the uncertainty in the correlations used to estimate CO_2 uptake is such that they range from 1.1 PgC /year ((Liss & Merlivat, 1986) correlation) to 3.3 PgC/year ((Wanninkhof & McGillis, 1999*a*) correlation) according to (Wanninkhof & McGillis, 1999*b*).

Clearly, there are considerable incentives to improve our understanding of scalar exchange phenomena and reduce such uncertainties, which have major impacts on policy, related, for example, to the utilization of fossil fuels. Gas exchange problems also occur in numerous other environmental settings, such as desorption of dissolved substances, like PCBs, from inland and coastal water bodies, that can be of significant air quality concern.

Be that as it may, a comprehensive review of turbulence and scalar exchange is available in (Banerjee & S.MacIntyre, 2004), hence-forward called BM, and should be referred to for a discussion of the published literature. The purpose of this paper is to focus on a particular scalar exchange model, viz. the surface divergence model of (Rashidi & Banerjee, 1988). This is also briefly discussed in the BM review, which considered its application to a limited set of laboratory and field data, but not the direct numerical simulations (DNS) discussed here.

[*]Reprinted with the permission of the publisher, *Elsevier*.

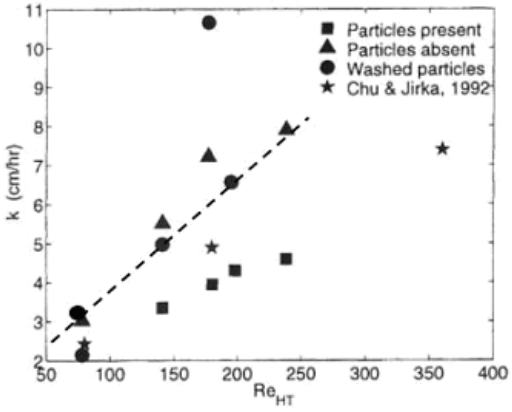

Figure 9.1 Mass transfer coefficients at the unsheared surface of a grid-stirred vessel. Data from (McKenna & McGillis, 1999). Particles evidently give rise to surfactant-like effects. The data with the particles absent is condered the most reliable. The line is from Eq. (9.9) with $C = 0.20$ (also called C_3 in Table 9.1). (Adapted from (Banerjee & S.MacIntyre, 2004))

We will proceed as follows. First, we will briefly review the so-called surface divergence models and their derivation from the (Hunt & Graham, 1978) "blocking" theory . Second, we will review applications of these models to laboratory data for scalar exchange across unsheared gas–liquid interfaces (also done in BM) to set the stage for what follows. Third, we will consider their application to recent DNS of coupled gas–liquid turbulence and scalar exchange across deformable surfaces (DeAngelis, 1998*a*; Fulgosi *et al.*, 2003; Lakehal *et al.*, 2003). New direct numerical simulations performed by the ETH Zurich group with variations in shear velocities have been used to validate the models.

The DNS allows direct calculation of the surface divergence field, which was predicted on the basis of the (Hunt & Graham, 1978) "blocking" theory by (Rashidi & Banerjee, 1988). The DNS data also allows calculation of the relationship between scalar exchange and the surface divergence field, and thus tests the exchange model directly. The direct simulation studies referred to here consider situations with a range of gas shear at the surface, with turbulence being generated at the interface itself, rather than elsewhere, e.g. at the bottom boundary of the flowing stream.

The flow configuration studied in these simulations have previously helped clarify the transfer mechanisms at deformable interfaces (DeAngelis, 1998*a*; Fulgosi *et al.*, 2003; Lakehal *et al.*, 2003). In these references the waves fall within the gravity-capillary range, with waveslope $ak = 0.01$ (wave amplitude a times wavenumber k), and very small phase-speed to friction-velocity ratio, $C/u_\star$. In the new simulations presented here, the friction velocities, $u_\star$, were considerably increased so as to generate surface deformations of higher waveslopes (up to $ak = 0.12$), but without leading to wave breaking.

9.2 SURFACE DIVERGENCE (SD) MODELS

9.2.1 The basic idea

The surface divergence model is now briefly discussed before making comparisons with experiments and DNS. Rashidi & Banerjee (1988) derived a general form of the expression for the mass transfer coefficient for the case where there is no gas shear at the interface and the far-field turbulence is homogeneous and isotropic, based on the blocking theory of Hunt & Graham (1978). Using a result from McCready & Hanratty (1985*b*), Rashidi & Banerjee (1988) showed that for unsheared interfaces at which high Sc gas transfer occurs, the gas transfer velocity, β, is given by

$$\frac{\beta\, Sc^{1/2}}{u} \approx Re_t^{-1/2} \left[\left(\frac{\partial u'}{\partial x} + \frac{\partial v'}{\partial y} \right)^2 \right]_{int}^{1/4} \tag{9.1}$$

where the subscript int denotes the interface, and all quantities on the RHS of (9.1) have been normalized by u and Λ, the integral velocity and length scales in the far field, and $Re_t = u\Lambda/\nu$ is the turbulent Reynolds number based on these scales.

The quantity in square brackets in (9.1) is the square of the surface divergence field, or the divergence of the 2D velocity vector tangential to the interface (u' and v' are the fluctuating velocities in the streamwise and spanwise directions, respectively), due to the fluctuating motions. Indeed, on a free water surface tangential velocity fluctuations are possible, meaning that the 2D continuity equation at the interface is not satisfied. Physically, this is the signature of surface convergence/divergence and renewal caused by turbulence events that bring bulk fluid to the interface, known as "sweeps". On the liquid side these are sometimes termed "upwellings" and on the gas side as "downdrafts".

Equation (9.1) arises in a straightforward way by noting that in contrast to rigid walls, at a free surface the velocity fluctuations normal to the interface are given by (where z being the distance from the interface)

$$w' \propto \frac{\partial w'}{\partial z}|_{int}\, z + HOT \tag{9.2}$$

as a result of the boundary conditions, whereas at rigid surfaces it scales as

$$w' \propto \frac{\partial^2 w'}{\partial z^2}|_{wall}\, z^2/2 + HOT \tag{9.3}$$

This has of course been pointed out by many authors, notably (McCready & Hanratty, 1985*b*). If the interface deforms then its curvature, $\kappa = -\nabla \cdot \mathbf{n}$, where $\mathbf{n}$ is the normal vector to the interface, should also enter the definition of (9.1), *i.e.*

$$\frac{\beta\, Sc^{1/2}}{u} \approx \frac{C}{Re_t^{1/2}} \left[\left(\frac{\partial u'}{\partial x} + \frac{\partial v'}{\partial y} - 2\, w'\, \nabla \cdot \mathbf{n} \right)^2 \right]_{int}^{1/4} \tag{9.4}$$

where we have now introduced a proportionality coefficient $C \sim O(1)$. While we will refer to the quantity between the parentheses on the RHS as the surface divergence, the last term is actually a surface dilation. If (9.1) and (9.4) are written in dimensional terms then

$$\beta \approx C\, (D\gamma)^{1/2} \tag{9.5}$$

where γ is the dimensional surface divergence, which has the dimensions of an inverse time scale (1/s), and D is the molecular diffusivity. In a sense γ takes the place of the renewal parameter – the mean time between surface renewals – $\overline{\tau}$ in (Danckwerts, 1951*b*), who extended the (Higbie, 1935) penetration theory to turbulence-dominated situations. Note that the Higbie-Danckwerts surface renewal model predicted the dependence of the liquid-side scalar transfer rate on D, as $D^{1/2}$, which was also found in lab experiments for high Schmidt numbers.

However, application of the Higbie-Danckwerts surface renewal models is difficult since the time between renewals $\overline{\tau}$ remains unspecified. This led a number of researchers to propose various models for this quantity, notably the "large-eddy model" (LE) of (Fortescue & Pearson, 1967) and the "small-eddy model" (SE) of (Banerjee *et al.*, 1968), viz. $\overline{\tau} \approx \Lambda/u$ and $\overline{\tau} \approx (\nu/\varepsilon)^{1/2}$, respectively. The main advantage of transfer models involving the surface divergence instead of the time between renewals is that γ is more easily measured than $\overline{\tau}$ – usually by scattering particles on the liquid surface and measuring their trajectories (see, for example, (Kumar *et al.*, 1998)).

As explained previously, expressions (9.1) and (9.4) apply strictly for far-field turbulence that is homogeneous and isotropic, and at unsheared interfaces. If gas shear is imposed, then the turbulence structure near the interface has characteristics somewhat similar to that of wall turbulence. The surface divergence scaling is still expected to apply for liquid-controlled transport processes, but the turbulence structure is now controlled by generation in the near-interface region. The appropriate scaling variables are now related to the gas stress imposed on the water surface and the fluid kinematic viscosity (the so-called inner variables), *i.e.* $\beta^+ = \beta/u_{\star,frict}$ and $u_i^{'+} = u_i'/u_{\star,frict}$), in which case expression (9.4) should be recast in the form

$$\beta^+\, Sc^{1/2} \approx C \left[\left(\frac{\partial u'^+}{\partial x^+} + \frac{\partial v'^+}{\partial y^+} - 2 w^{'+}\, \nabla^+ \cdot \mathbf{n} \right)^2 \right]_{int}^{1/4} \tag{9.6}$$

with the same proportionality coefficient $C \sim O(1)$ as in (9.4), and all quantities on the RHS of (9.6) are now normalized by $u_{\star,frict}$ and ν.

9.2.2 Blocking-theory based SD model

The surface divergence cannot be predicted without a theory, and therefore the (Hunt & Graham, 1978) blocking theory was used to relate it to the far-field turbulence characteristics when they are homogeneous and isotropic.

Model	$\beta\, Sc^{1/2} =$	Ref.
(LE)	$C_1\, u\, Re_t^{-1/2}$	(Fortescue & Pearson, 1967)
(SE)	$C_2\, u\, Re_t^{-1/4}$	(Banerjee *et al.*, 1968)
(SD)	$C_3\, Sc^{1/2}\, (D\gamma)^{1/2}$	(Banerjee, 1990)
SD no shear	Eq. 9.9	(Banerjee, 1990)
with shear	$0.108 - 0.158\, u_\star$	(Banerjee, 1990)
Eddy resolving	$C_4\, p_1\, u_\star$	(Csanady, 1963)
Surface proc.	$\frac{C_5\, p_2\, u_\star\, (1+Rf/Rf_{cr})^{1/4}}{(1+Ke/Ke_{cr})^{1/2}}$	(Soloviev & Schluessel, 1994)

Table 9.1 Various correlations for mass transfer velocity (β or k) for liquid side at high Schmidt number. $C_1,\ C_2,\ C_3,\ C_4$ are constants. p_1 is the fraction of the surface undergoing intense renewal. p_2 is the probability distribution of renewal events, Rf is the flux Richardson number, *i.e.* $gH\nu/\rho c_p u_\star^4$, and Rf_{cr} is the critical value $\approx 1.5 \times 10^{-4}$. Ke is the Keulegan number, *i.e.* $u_\star^3/g\nu$, and $Ke_{cr} \approx 0.18$. H is the surface heat flux obtained by summing latent, sensible and long wave radiation fluxes. (Adapted from (Banerjee & S.MacIntyre, 2004))

To proceed, for an unsheared interface with homogeneous isotropic far-field turbulence, (Rashidi & Banerjee, 1988) derived, reworking a result of (Brumley & Jirka, 1987), the spectrum for the surface divergence term $\gamma = [\partial u'/\partial x + \partial v'/\partial y]_{int}$ in the form

$$S(\Omega) = 0.3 \left[12\, \Omega^{1/2} - 7.2\, \Omega^{1/3}\right] \tag{9.7}$$

where Ω is the non-dimensional frequency $(\Lambda\omega/u)$, and the spectrum is valid for $\Omega > 5$. Banerjee then integrated the spectrum from the integral length scale Λ to the viscous cut-off $(\nu/\varepsilon)^{1/2}$ and used the relationship between the integral and Kolmogorov scales as

$$\Lambda/\eta \approx 0.5\, Re_t^{3/4} \tag{9.8}$$

with $\eta = (\nu^3/\varepsilon)^{1/4}$ to obtain the mass transfer coefficient for high Sc as

$$\frac{\beta\, Sc^{1/2}}{u} \approx \frac{C}{Re_t^{1/2}} \left[0.3 \left(2.83\, Re_t^{3/4} - 2.14\, Re_t^{2/3}\right)\right]^{1/4} \tag{9.9}$$

The proportionality constant $C \approx O(1)$ is as in (9.4) and (9.6). This is sometimes called the surface divergence (SD) model. The quantity within the first set of parentheses is the square of the nondimensional surface divergence. The expression was asymptotic to $Re_t^{-1/2}$ at small turbulent Reynolds numbers and to $Re_t^{-1/4}$ at large turbulent Reynolds numbers, which was in line with (Fortescue & Pearson, 1967) LE models, and (Banerjee *et al.*, 1968) SE model, respectively, and supported Theofanous' (1984) predictions for the asymptotic forms of the mass transfer rate with regard to Re_t. Note that this expression applies only to clean, unsheared rigid interfaces, with no effects due to surfactants or natural convection. Note, too, that the expression for surface divergence can be directly checked by DNS – a procedure we will follow when assessing the model.

The various expressions for the transfer rate of sparingly soluble gases are summarized in Table 9.1, which also includes expressions from (Csanady, 1963) and (Soloviev & Schluessel, 1994). Several other forms of parameterization were suggested, *e.g.* by (Caussade *et al.*, 1990) and (Coantic, 1986), so Table 9.1 does not list all the parameterizations proposed.

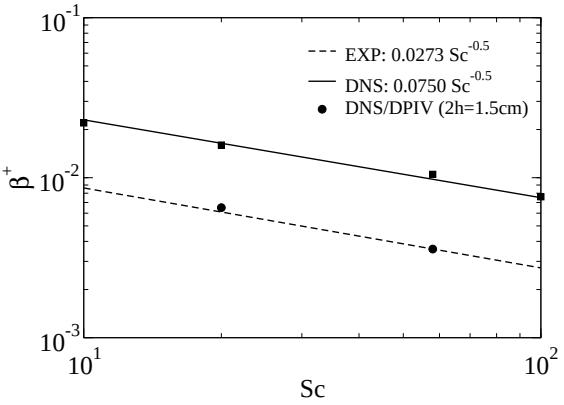

Figure 9.2 Comparison of DNS with rigid slip surface as the interface in channel flow with experiments ((Komori *et al.*, 1982)) and calculations based on experimentally determined surface divergence field. Note that the rigid surface gives higher values for the mass transfer velocity. (Adapted from (Knowlton *et al.*, 1999))

9.3 UNSHEARED INTERFACES: COMPARISONS

In this section we will consider turbulence phenomena and scalar exchange when gas shear at the interface is relatively small or nonexistent. We review here for a more complete picture of the SD model some results of comparisons with experiments, which also appear in BM. In laboratory studies, the unsheared interface situation is reproduced using either a stirred tank or open-channel flow, where turbulence is generated by the shear at the bottom. In most of these experiments, it is difficult to keep the liquid surface free of surfactants, and therefore the results should be treated with caution, unless precautions have been explicitly taken to keep the surface clean. This is especially true for stirred-vessel experiments, where the liquid surface is quite stagnant.

Turning now to gas transfer data, (Chu & Jirka, 1992) measured the gas flux at the air–water interface of a grid-stirred tank. There is some concern that their data may have been affected by accumulation of surfactants at the water surface. This is discussed in more detail by (McKenna & McGillis, 1999), who also made simultaneous mass transfer and surface divergence measurements using DPIV. They found that the particles used for DPIV gave rise to surface-active effects unless they were thoroughly cleaned. In fact, the mass transfer rate data with particles that had not been washed fell below data without particles or with washed particles. The data with and without particles are compared with Chu and Jirka's data, and the predictions of the parameterization in Eq. (9.9) as shown in Figure 9.1. As evident from the figure, the particles reduce the gas transfer velocity, and Chu and Jirka's data lies somewhere between the cases in (McKenna & McGillis, 1999), with and without particles.

The parameterization in Eq. (9.9) also gives a reasonable fit to the data, which is encouraging, since it was developed before the data were taken. The constant $C \approx 0.20$, might be expected since Eq. (9.9) is based on a "rigid lid" approximation for the free surface, and in reality there will be some give which would reduce the surface divergence. Note also that the turbulent Reynolds number, Re_t, in Eq. (9.9) is half the turbulent Reynolds number, Re_{HT}, used by (McKenna & McGillis, 1999). Also, the point in their data shown in Figure 9.1, where k (also called β) $\approx$ 11 cm/hr at $Re_{HT} \approx 180$, is out of line with all the other data and may be an outlier.

(Knowlton *et al.*, 1999) compared predictions to (Komori *et al.*, 1982) open channel mass transfer data and attempted to validate the surface divergence theory by calculating surface divergence directly from the velocity field measured by (Kumar *et al.*, 1998). They then used it to solve the 3D concentration field equation from which they calculated the mass transfer coefficient. The only case for which (Kumar *et al.*, 1998) data coincided with one of Komori's cases was for depth-based Re= 2800. (Knowlton *et al.*, 1999) found remarkable agreement with (Komori *et al.*, 1982) data for this case. However, when (Knowlton *et al.*, 1999) calculated the gas transfer data based on a "rigid lid" direct numerical simulation, they found gas transfer velocities that were about 2-3 times higher. These results are shown in Figure 9.2. In Table 9.2, we show the predictions of Eq. (9.9) with $C = 0.20$ (which was the value for C that agreed with the stirred vessel gas transfer data of (McKenna & McGillis, 1999)). It is evident that the agreement with these predictions is quite good. The velocity scale for Eq. (9.9) is taken to be the wall friction velocity, and the length scale was the depth. While these scales are reasonable, it is likely that the length scale is a weak function of the depth-based Reynolds number, *i.e.* $(\Lambda/depth)$ varies as $Re^{-1/8}$, which is what would be expected in the core region of pipe flow. Making such an assumption would improve the agreement

between Eq. (9.9) and the experimental data, which is rather over predicted at low Reynolds numbers and under predicted at high Reynolds numbers.

In any case, the SD model with $C = 0.20$ appears to predict gas transfer rates reasonably for unsheared interfaces. Note that experimental data are at high Schmidt numbers.

Run	δ [cm]	U_{av} [cm/s]	$u_\star$ [cm/s]	Exp. β' [m/s]	Eq. (9.9) $\beta'[m/s]$
I	1.1	23.5	1.48	1.65	1.97
II	2.9	9.7	0.61	0.75	0.81
III	3.1	18.3	1.06	1.60	1.22
IV	5.0	5.9	0.37	0.45	0.49
V	5.1	11.9	0.69	0.90	0.78
VI	6.4	19.9	1.01	1.20	1.01
VII	7.0	13.8	0.75	1.30	0.80
VIII	10.0	10.5	0.58	0.70	0.56
IX	11.2	10.9	0.59	0.80	0.55

Table 9.2 Comparison of Komori *et al.* (1989) experimental data with Eq. (9.9) with $C = 0.20$. Transfer coefficients β' stand for $\beta \times 10^5$ (Adapted from (Banerjee & S.MacIntyre, 2004))

9.4 SHEARED INTERFACES: COMPARISONS

9.4.1 Simulations

(DeAngelis & Banerjee, 1999) have reported DNS with a nonbreaking deformable interface between turbulent air and water streams. The details are available in (DeAngelis, 1998*a*). Their results show that waves exert significant effects on the mean flow and turbulence characteristics. The turbulence intensities and other qualitative features, *e.g.* streak spacing and burst frequency, on both gas and liquid sides of the interface, were found to scale with $u_{\star,frict}$ and ν, the kinematic viscosity.

More recently, (Fulgosi *et al.*, 2003) conducted a similar DNS with shear Reynolds number of 171, in which they were interested in the turbulence structure at the gas side of the interface as this deforms under the actions of the imposed shear. Figure 9.3 shows the wave spectra obtained after statistical steadiness was reached. The wave saturation spectrum is defined by

$$B(\mathbf{k}) = |\mathbf{k}|^2 \, (2\pi)^{-2} \int Z(\mathbf{r}) e^{-i\mathbf{k}\cdot\mathbf{r}} \, d\mathbf{r} \tag{9.10}$$

where $Z(\mathbf{r}) = \overline{f(\mathbf{x}+\mathbf{r}, t_0) \, f(\mathbf{x}, t_0)}$ is the covariance of the instantaneous nondimensional surface displacement $f(\mathbf{x}, t)$. The figure clearly indicates that the wave properties did not change significantly within this time interval, confirming the existence of the saturation or equilibrium range, which is synonymous to convergence in this context. The comparisons reported with the data are when these "equilibrium" conditions are reached.

The initial study of (Fulgosi *et al.*, 2003) has been extended for the present contribution by performing new simulations with higher liquid shear velocities $u_{\star_L}$, although at the same shear Reynolds number (by varying the domain size). The purpose is to study the effect of surface dilation on the transfer mechanism for variable waveslopes. These new simulations were performed for shear velocities $u_{\star_L}$ equal to 0.000685 m/s, 0.002013 m/s, and 0.004 m/s, respectively. For the smallest shear velocity, the gas-liquid interface was almost flat. Note that $u_{\star_L}$ was set to 0.001 m/s in (Fulgosi *et al.*, 2003).

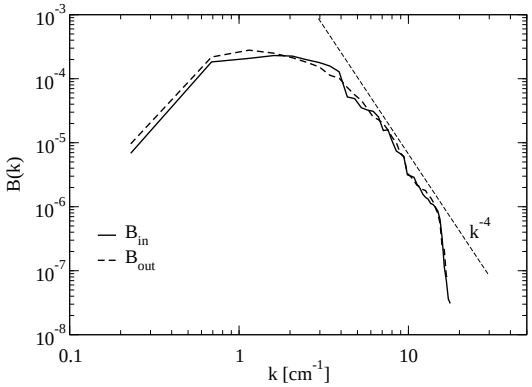

Figure 9.3 Saturation spectra of the wave fields at the beginning (B_{in}) and at the end (B_{out}) of the sampling period. (Adapted from (Lakehal *et al.*, 2003))

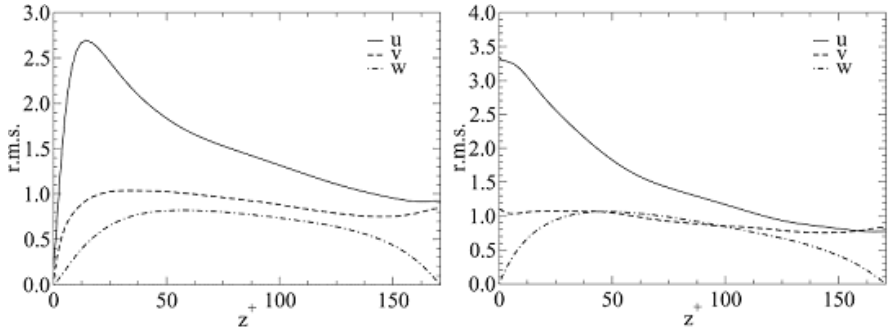

Figure 9.4 Turbulence intensities on the gas side (left panel) and liquid side (right panel) as a function of the nondimensional distance z^+ from the interface, in the wavy interface conditions ($u_{\star_L} = 0.002013m/s$). All quantities are nondimensionalized by the friction velocity.

For all shear velocities studied, the difference between the gas and the liquid phase turbulence intensities in the near-interface region followed the same trend, as shown in Figure 9.4. Gas-side turbulence displayed in the left panel behaves much like flow over a solid wall. If the distance is measured from the wavy interface, then there is little effect of wave deformations on intensity. The liquid, as evident from the neighboring panel, has the largest fluctuations in the streamwise and spanwise direction right at the interface itself. The interface is perceived as a free slip boundary, except for the mean shear. The wave effect is somewhat more pronounced, but still rather small in the nondimensionalized form shown.

The simulations of (DeAngelis & Banerjee, 1999) and (Fulgosi *et al.*, 2003) both proved useful in clarifying aspects of turbulence structure near deformable (nonbreaking) air–water interfaces, and they have been extended to studies of scalar exchange by (DeAngelis, 1998*a*) for high Sc numbers (up to Sc=200), and recently by (Lakehal *et al.*, 2003) for low-to-moderate Pr or Sc numbers, up to Sc=10. The calculations for $Sc \approx 0(1)$ are straightforward once the velocity field has been calculated. However, for higher Sc, (DeAngelis, 1998*a*), who did not solve explicitly the coupled momentum and scalar equations, reduced the interface-normal mesh spacing in order to resolve concentration fluctuations using interpolated velocity flow fields (on the refined grid). In contrast, (Lakehal *et al.*, 2003), who were interested in comparing the entire scalar flux and variance balance equations solved the coupled equations for $Pr(Sc)$ = 1, 5 and 10, using two grid resolutions.

The results presented below are new and differ from those presented in (Lakehal *et al.*, 2003), in that they concern the two shear velocities resulting in a flat interface ($u_{\star_L} = 0.000685m/s$) and a wavy interface ($u_{\star_L} = 0.002013m/s$). Contours of the instantaneous scalar fluxes at flat (left panels) and deformable (right panels) interfaces from these direct simulations are shown in Figures 9.5, for the gas (1st row) and the liquid side (2nd row), respectively. These results are compared in Figure 9.6 with the shear stress at the interface, for flat and deformable interfaces. It is immediately evident that the gas-side fluxes correlate well with the shear stress, which has been independently found by (DeAngelis, 1998*b*). This suggests that sweeps give rise to higher scalar exchange rates, as they also produce regions of high shear stress. On the other hand, the flux field on the liquid side shows a much

finer structure and no such correlation exists. (DeAngelis, 1998*b*) showed that this occurred because liquid-side sweeps did not give rise to the high shear stress regions at the surface, but they did give rise to regions of high mass transfer.

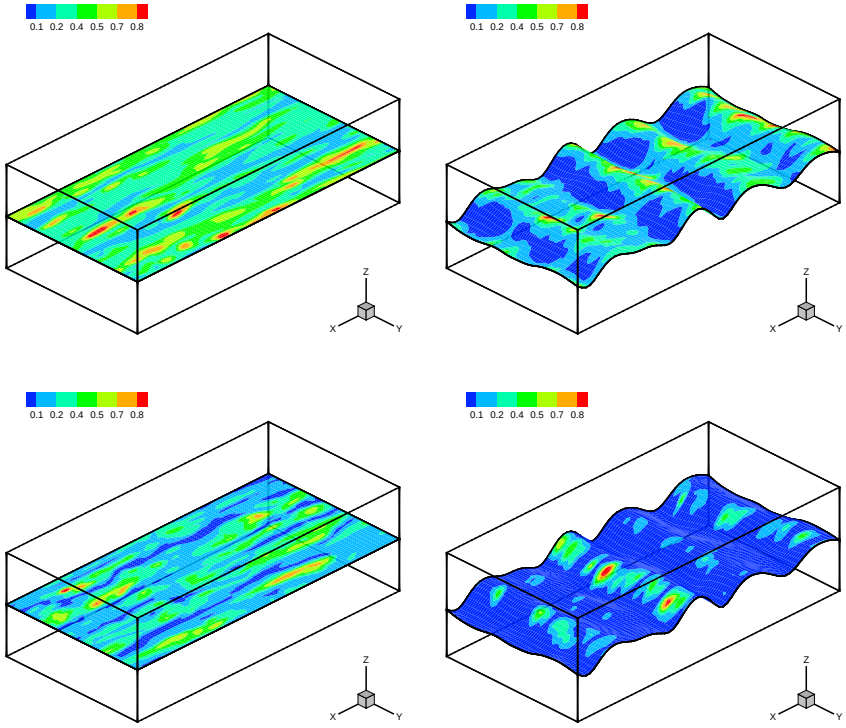

Figure 9.5 Instantaneous patterns of the interfacial heat transfer coefficient at the flat and wavy interface. (upper panels) gas side, (lower panels) liquid side.

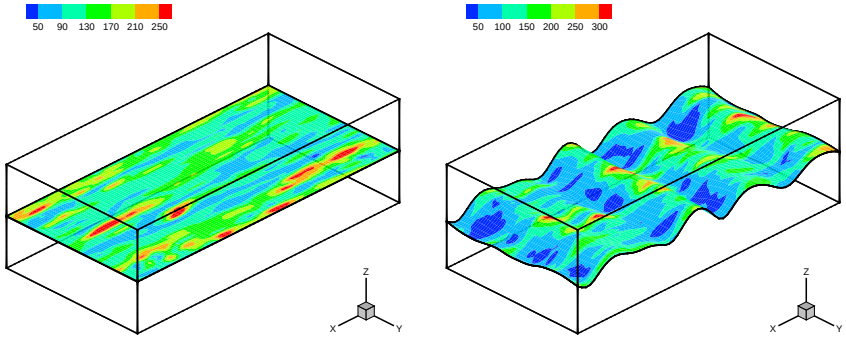

Figure 9.6 Instantaneous patterns of the nondimensional interfacial shear stress, at the flat and wavy interface.

9.4.2 Surface Divergence Model Comparisons

Présenté à l'Ecole Centrale de Lyon

Before comparing the results of the new simulations with the surface divergence models, we first examine the surface divergence term γ^+ with and without curvature contribution for $u_{\star_L}$=0.002013 m/s. The isocontours of the normalized (by inner variables) surface divergence is shown in Figure 9.7, with (panel c) and without (panel a) the surface dilation contribution (shown in panel b). The dilation term is clearly shown to play an important role in estimating γ^+; panel (b) highlights indeed the crests and the troughs marked by positive and negative isocontours of the nondimensionalized dilation term κ^+. The wavelengths are also clearly visible from the figure. The lower panel corresponding to the modified surface divergence term including the dilation term exhibits differences with panel (a), which excludes the dilation term from the surface divergence.

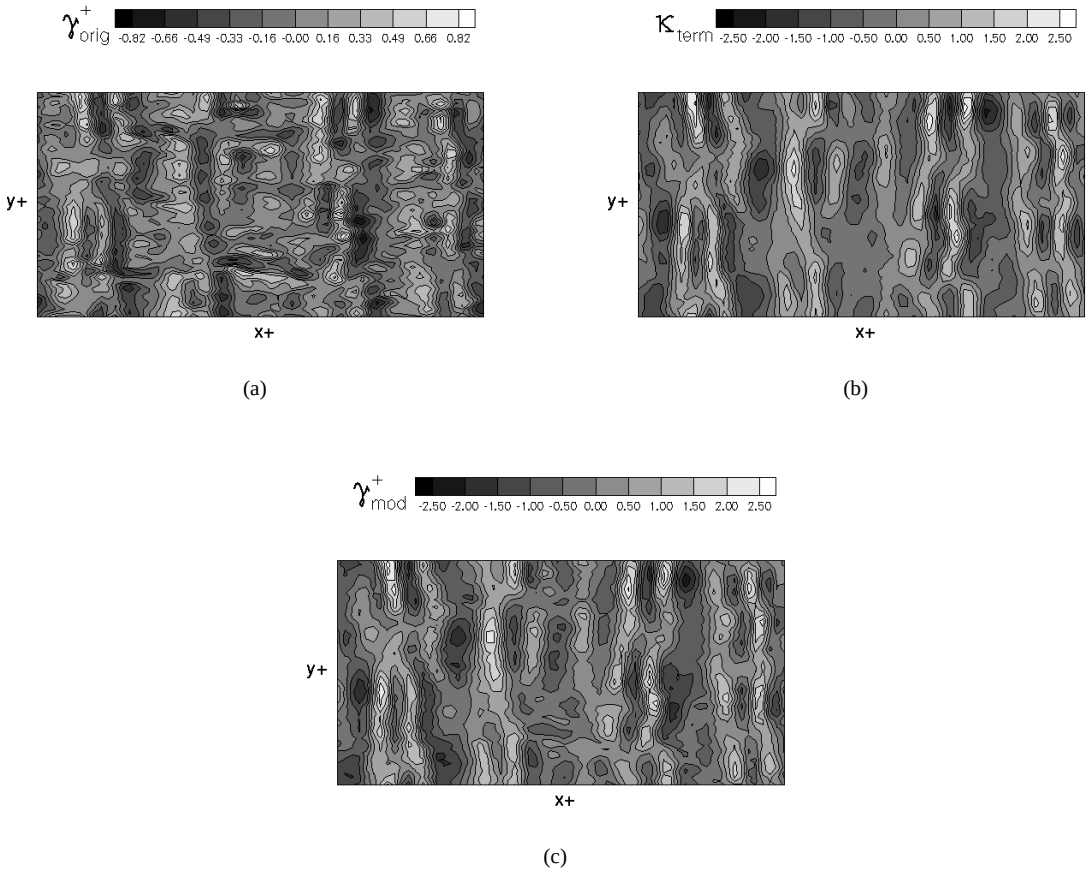

Figure 9.7 (a) Isocontours of the surface term without the dilation term for $u_{\star_L}$=0.002013 m/s. (b) Isocontours of the curvature or dilation term. (c) Isocontours of the surface term with the dilation term.

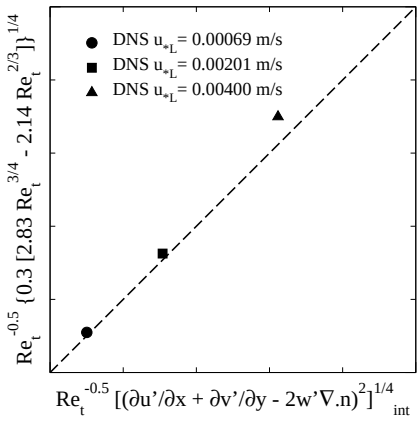

Figure 9.8 Comparison of the surface term with the dilation contribution to the Hunt-Graham blocking theory, using DNS data for various shear velocities.

Next, we assess the (Rashidi & Banerjee, 1988) derivation of the surface divergence field based on Hunt-Graham blocking theory (term in parenthesis in Eq. (9.9)) against the DNS data, before turning to the parameterization of the scalar exchange based on the SD transfer models. Note that in estimating the integral velocity scale Λ appearing in the definition of the turbulence Reynolds number, use was made of expression $\varepsilon \approx u^3/\Lambda$, where ε is the turbulent energy dissipation rate in the bulk flow. For the purpose of comparison, we have plotted in Figure 9.8 the DNS-calculated values of γ (term between parentheses in Eq. (9.4)) against the term between brackets in Eq. (9.9), for various shear velocities (note though that the figure compares the entire RHS terms of these two equations). The comparison shows very good agreement between the two quantities. This is a remarkable result, confirming the validity of the derivation proposed by (Rashidi & Banerjee, 1988) starting from blocking theory. Why it works for sheared interfaces is not clear, but the surface divergence expression derived from the blocking theory in (9.9) is certainly accurate.

Turning now to the scalar exchange parameterization, we consider the case where gas stress is imposed on the liquid interface, which is the context of the DNS studies discussed here. In these circumstances, the parameterization of the scalar exchange should be first examined with reference to Eq. (9.6). The Schmidt number dependencies in Eq. (9.6) are compared with simulation results for different values of Sc and for $u_{\star_L}$=0.002013 m/s in Figure 9.9 (a). The best fit to the DNS data is obtained with the proportionality constant $C \approx 0.45$. It is clear that the dependence is well predicted up to Sc=200, but there is some deviation at $Sc = 1.0$. In Figure 9.9 (b) the DNS results of the liquid-side mass transfer coefficient are compared with the SD model (Eq. (9.6)) for $Sc = 1.0 - 1.2$. The value of the constant $C \approx 0.35$ fits the SD model to the DNS results for various shear velocities quite well. Here the surface divergence is calculated from the DNS directly. This result is in conformity with what has been speculated before: for $Sc \approx 1$ the proportionality coefficient C in Eq. (9.6) should be somewhat lower. A similar trend has already been observed by (DeAngelis, 1998*b*) (and confirmed by the present DNS simulations) in their parametrization of the scalar transfer by reference to the (Banerjee *et al.*, 1968) SE model, i.e. $\beta^+ \approx 0.108 Sc^{-0.5}$, as also shown in Figure 9.9 (a). It is evident now that in sheared interface situations, both the SE and SD models (using inner-variables scalings) predict the gas transfer rate less accurately for $Sc \approx 1$ than for higher Schmidt numbers.

It is understandable that from an engineering point of view, the surface divergence term γ^+ with the dilation contribution cannot be easily determined; the alternative approximation to it is the Banerjee's expression (9.9) using the far-field turbulence quantities, i.e. Re_t. According to the results in Figure 9.8, the derivation is likely to hold for scalar transfer.

Let us then proceed to test whether even in gas-shear conditions, the SD model still applies for liquid-controlled transport processes. The question to which we seek an answer is as to whether the far-field turbulent Reynolds number could be employed for prediction, albeit the turbulence is actually generated in the near-interface region. It is therefore interesting to see how equations (9.4) and (9.9) compare with simulation results. The Schmidt number dependencies in both equations are compared with simulation results for Schmidt numbers up to 10 in Figure 9.10. The Sc dependence of the dimensional liquid-side mass transfer coefficient can be well predicted by both equations only with the proportionality coefficient set equal to $C = 0.35$. Figure 9.10 shows the SD model (Eqs. 9.4 and 9.9 with C = 0.35) to compare surprisingly well with simulation results for different values of the shear velocity.

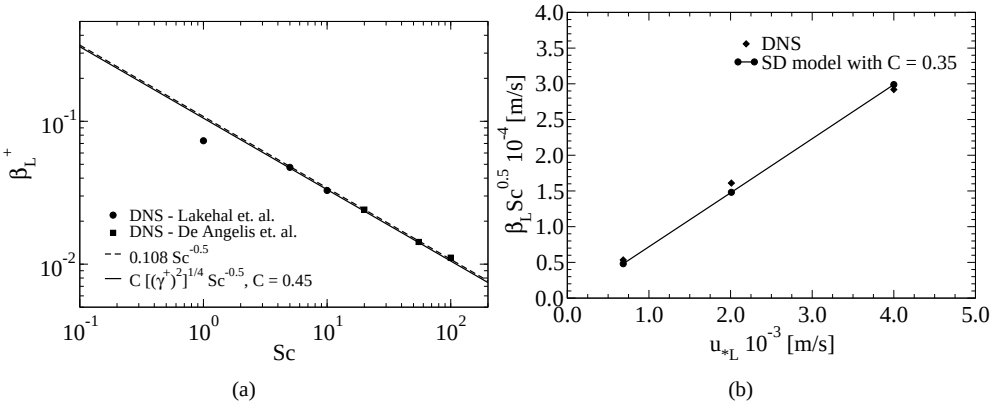

Figure 9.9 (a) The scaling of the liquid-side mass transfer velocity (nondimensionalize by inner variables) with the Sc number using the SE model parameterization ($\beta^+ \approx 0.108 Sc^{-0.5}$; c.f. (DeAngelis, 1998*b*)) and (9.6) with $C = 0.45$, for $u_{\star_L}$=0.002013 m/s. (b) Dimensional mass transfer velocity versus frictional velocity for $Sc = 1.0 - 1.2$. The SD model Eq. (9.6) is clearly seen to fit the DNS data with $C = 0.35$.

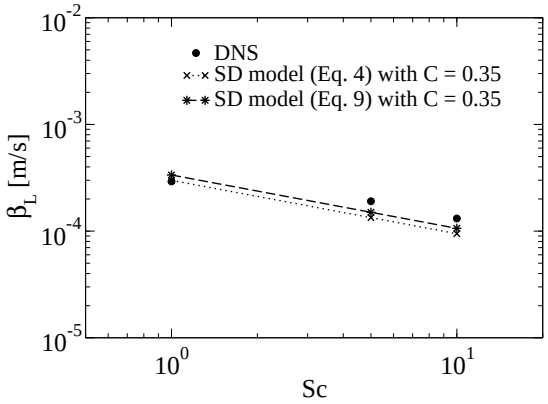

Figure 9.10 The scaling of the liquid-side mass transfer velocity versus the the Sc number using the SD models under Eqs. (9.4) and (9.9) forms, for $u_{\star_L}$=0.002013 m/s.

However, the value of the constant should not be taken outside the interval $1 < Sc < 10$, as for higher Sc it may be different, as suggested by the results in Figure 9.9 (a).

9.5 CONCLUSIONS

In the absence of shear, and when the far-field turbulence approximates the homogeneous isotropic case, it has been found that the Hunt-Graham blocking theory applies, and predictions of the near-interface damping of the normal component of turbulence, and enhancement of the tangential components, are well predicted ((Brumley & Jirka, 1987)). (Rashidi & Banerjee, 1988) has applied the Hunt-Graham theory to calculate the surface divergence and developed the so-called surface divergence model, which predicts gas transfer across unsheared interfaces. It has also been shown that this model predicts at low turbulent Reynolds number the same behavior as the (Fortescue & Pearson, 1967) large-eddy model, and the (Banerjee *et al.*, 1968) small-eddy model at high turbulent Reynolds numbers. The model also agrees with gas transfer experiments across unsheared interfaces.

In situations in which the shear rate imposed by the gas is high, turbulence is generated in the vicinity of the interface, much like near solid boundaries. Models for gas transfer based on scaling of active periods (such as sweeps and ejections) with interfacial frictional shear, have proved to be successful in predicting laboratory data, before microbreaking of waves in the capillary/gravity range commences, typically at 10m wind velocities (U_{10}) of 4-5 m/s ((DeAngelis, 1998*b*); (Lakehal *et al.*, 2003)).

We have also tested the surface divergence model against DNS for sheared interfaces. What is the most surprising finding is that the expression for the surface divergence derived by (Rashidi & Banerjee, 1988) and shown in Eq. (9.9) applies not only for predictions of gas transfer at unsheared interfaces, but also in cases with wind shear. In fact, the predictions of the surface divergence in terms of Re_t on the RHS of Eq. (9.9) appears to hold even at sheared interfaces. This is a remarkable, and difficult to explain, finding. The value of the constant in Eq. (9.9) apparently changes somewhat between the sheared and unsheared cases with regard to scalar exchange, but the surface divergence itself is directly and accurately predicted. As the SD model is widely used to predict field experiments with high wind shear (Banerjee & S.MacIntyre, 2004), this finding supports such usage.

10

Perspectives futures

Dans l'immédiat, il y a certainement beaucoup à faire avec nos travaux en suspend. Mais les recherches qui méritent plus d'égards à notre avis sont ceux mettant en jeu les techniques de suivi d'interface pour les écoulements multiphasiques turbulents. Notre choix pour la simulation de la turbulence dans ce contexte s'est porté sur la LES. Il reste à savoir comment peut-on bien combiner ces méthodes afin de généraliser leur utilisation. Plusieurs points restent en effet sans réponses, comme par exemple la modélisation des termes interfaciaux et des tensions de Reynolds sous-mailles, ou le traitement de la turbulence à l'interface.

L'approche multifluide nécéssite un travail de fonds, beaucoup plus au niveaux de sa formulation que sur la modélisation de la turbulence. À notre avis, il est impératif de se pencher sur les termes d'échanges interfaciaux. Peu importe la qualité ou le degré de sophistication des modèles de turbulence (RANS ou LES), si des efforts soutenus ne sont pas engagés sur le front des échanges interfaciaux. Et c'est prècisément en se basant sur les techniques de suivi d'interface que nous puissions un jour faire des d'avancées concrètes. Il suffit de constater qu'àvec notre approche LES/VOF, on a pu prédire l'évolution de l'aire interfaciale dans le problème d'injection de vapeur dans l'enceinte de confinement (c.f. Chap. 4).

Il faut aussi savoir (ou accepter de) changer de perspectives si les efforts passés n'ont pas abouti. Ceci est particulièrement vrai pour la modélisation RANS (stationnaire), qui ne fera pas de miracles pour des écoulements aussi non-homgènes et instationnaires que les panaches à bulles, etc.

Finalement, plusieurs éléments se situant au niveau mésoscopique de la cascade des phénomènes restent aujourd'hui sans modèles convaincants; de la ligne triple et des tensions interfaciales, au changement de phase par évaporation ou par condensation. Ce créneau occupera sans doute la scène de la recherche sur les écoulements multiphasiques pour le prochain quart de siècle, je l'espère du moins.

Bibliography

ACHARD, J. & DELHAYE, J. 1977 On the use of averaging two-phase flow modelling. *Thermal and Hydraulic Aspects of Reactor Safety* **Vol. 1: Light Water Reactors**, 289–332.

VAN DEN AKKER, H. 2003 Coherent structures in multiphase flows. *Powder Technology* **495**, 77–118.

AUTON, T., HUNT, J. & PRUD'HOMME, M. 1988 The force exterted on a body in inviscid unsteady non-uniform rotational flow. *J. Fluid Mechanics* **197**, 241–257.

BANERJEE, S. 1971 A note on turbulent mass transfer at high schmidt numbers. *Chem. Eng. Sci.* **26**, 989.

BANERJEE, S. 1990 Turbulence structure and transport mechanisms at interfaces. 9^{th} *Int. Heat Transfer Conference* p. 395.

BANERJEE, S. & CHAN, M. 1980 Separated flow models-i. *Multiphase Flow* **6**, 1–24.

BANERJEE, S., LAKEHAL, D. & FULGOSI, M. 2004 Surface divergence models between turbulent streams. *J. Multiphase Flow* **30/7-8**, 965–979.

BANERJEE, S., RHODES, E. & SCOTT, D. S. 1968 Mass transfer to falling wavy liquid films in turbulent flow. *Ind. Engng. Chem. Fundam.* **7**, 22.

BANERJEE, S. & S.MACINTYRE 2004 The air-water interface: turbulence and scalar exchange. *Ind. Eng. Chem. Fundamentals* **7**, 22.

BARDINA, J., FERZIGER, J. & REYNOLDS, W. 1980 Improved subgrid models for large eddy simulation. *AIAA paper* **80**, 1358.

BATAILLE, J. 1981 *AVERAGED FIELD EQUATIONS FOR MULTIPHASE FLOWS*. Brown University: DOE Report N0 GEOFLO/9.

BATAILLE, J., MARIE, J. & LANCE, M. 1999 Turbulence in bubbly blow: from experiments to numerical modelling. *Proc. 2nd Int. Symp. on Two-Phase Flow Modelling and Experimentation, Piza, Italy, May 23-26* .

DE BERTODANO, M. L., LAHEY, R. & JONES, O. 1994 Development of a $k-\varepsilon$ model for bubbly two-phase flows. *J. Fluids Engrg.* **116**, 128–134.

BESNARD, D. & HARLOW, F. 1988 Turbulence in multiphase flow. *Int. J. Multiphase Flow* **14 (6)**, 679–699.

BOTTO, L. 2002 Droplet deposition in turbulent air/water sheared flow. Master's thesis, Univeristy of Udine, Italy.

BRACKBILL, J., KOTHE, D. & ZEMACH, C. 1992 A continuum method for modelling surface tension. *J. Comp. Phys.* **100**, 335–354.

BROCCHINI, M. & PEREGRINE, D. H. 2001 The dynamics of strong turbulence at the free surface. part 1. description. *J. Fluid Mech.* **449**, 225.

BROOKE, J. W., HANRATTY, T. J. & MCLAUGHLIN, J. B. 1994 Free-flight mixing and deposition of aerosol. *Phys. Fluids* **6**, 3404.

BROOKE, J. W., KONTOMARIS, K., HANRATTY, T. J. & MCLAUGHLIN, J. B. 1992 Turbulent deposition and trapping of aerosol at the wall. *Phys. Fluids* **A 4**, 825.

BRUMLEY, B. H. & JIRKA, G. H. 1987 Near surface turbulence in a grid-stirred tank. *J. Fluid Mech.* **183**, 235.

BUNNER, B. & TRYGGVASON, G. 2003 Effect of bubble deformation on the properties of bubbly flows. *Journal of Fluid Mechanics* **495**, 77–118.

CALMET, I. & MAGNAUDET, J. 1997 Large–eddy simulation of high–schmidt number mass transfer in a turbulent channel flow. *Phys. Fluids* **9**, 438.

CAMPBELL, J. A. & HANRATTY, T. J. 1983 Mechanisms of turbulent mass transfer at solid boundaries. *AIChE Journal* **29**, 221.

CARRICA, P., DREW, D., BONETTO, F. & LAHEY, R. 1999 A polydisperse model for bubbly two-phase flow around surface ships. *Int. J. Multiphase Flow* **25 (2)**, 257–305.

CAUSSADE, B., GEORGE, J. & MASBEMAT, L. 1990 Experimental study and parametrization of interfacial gas absorption. *AIChE Journal* **36**, 265.

CERBELLI, S., GIUSTI, A. & SOLDATI, A. 2001 Ade approach to predicting dispersion of heavy particles in wall–bounded turbulence. *Int. J. Multiphase Flow* **27**, 1861.

CHAN, M. & BANERJEE, S. 1980 Separated flow models-i. *J. Multiphase Flow* **6**, 1–24.

CHERUKAT, P., NA, Y., HANRATTY, T. J. & MCLAUGHLIN, J. B. 1998 Direct numerical simulation of a fully developed turbulent flow over a wavy wall. *Theoret. Comput. Fluid Dynamics* **11**, 109.

CHOI, K. 2001 Turbulent drag–reduction mechanisms: Strategies for turbulent management. *Turbulence Structure and Modulation, (ed. A. Soldati & R. Monti), CISM Courses and Lectures, vol. 415* p. 161.

CHU, C. R. & JIRKA, G. H. 1992 Turbulent gas flux measurements below the air–water interface of a grid-stirred tank. *Int. J. Heat and Mass Transfer* **35**, 1957.

CLEAVER, J. W. & YATES, B. 1975 A sublayer model for the deposition of particles from a turbulent flow. *Chem. Eng. Sci.* **30**, 983.

CLIFT, R., GRACE, J. & WEBER, M. 1978 *BUBBLES, DROPS, AND PARTICULES*. New York: Academic Press.

COANTIC, M. 1986 A model of gas transfer across air–water interfaces with capillary waves. *J. Geophysical Research* **91**, 3925.

CSANADY, G. T. 1963 Turbulent diffusion of heavy particles in the atmosphere. *J. atmos. Scie.* **20**, 201–208.

DANCKWERTS, P. V. 1951*a* Significance of liquid–film coefficients in gas absorption. *Ind. Engng. Chem.* **43**, 1460.

DANCKWERTS, P. V. 1951*b* Significance of liquid–film coefficients in gas absorption. *Ind. Engng. Chem.* **43**, 1460.

DEANGELIS, V. 1998*a* Numerical investigation and modeling of mass transfer processes at sheared gas–liquid interface. *Ph.D. Thesis, UCSB* .

DEANGELIS, V. 1998*b* Numerical investigation and modeling of mass transfer processes at sheared gas–liquid interface. *Ph.D. Thesis, UCSB* .

DEANGELIS, V. & BANERJEE, S. 1999 Heat and mass transfer mechanisms at wavy gas–liquid interfaces. *in Proceedings of TSFP-1, S. Banerjee, J. K. Eaton (Eds.), Begell House, New York* .

DEANGELIS, V., LOMBARDI, P. & BANERJEE, S. 1997 Direct numerical simulation of turbulent flow over a wavy wall. *Phys. Fluids* **9(8)**, 2429.

DELHAYE, J. 1987 Fundamentals of time-varying two-phase flow formulation. *Proc. Int. Seminar Transient Phenomena in Multiphase Flow* .

DESPIRITO, J. & WANG, L.-P. 2001 Linear instability of two-way coupled particle-laden jet. *Int. J. Multiphase Flow* **27**, 1179–1198.

DIMAS, A. A. & KIGER, K. T. 1998 Linear instability of a particle-laden mixing layer with a dynamic dispersed phase. *Phys. Fluids* **10**, 2539.

DRAZIN, P. G. & REID, W. H. 1981 *Hydrodynamic Stability*. Cambridge, UK: Cambridge U. P.

DREW, D. & LAHEY, R. 1987 The virtual mass and lift force on a sphere in rotating and straining inviscid flow. *Int. J. Multiphase Flow* **13(1)**, 113–121.

DREW, D. & LAHEY, R. 1988*a* The three-dimensional time and volume averaged conservation equations of two-phase flow. *Adv. Nucl. Science and Technology* **20**, 1–69.

DREW, D. & LAHEY, R. 1988*b* The three-dimensional time and volume averaged conservation equations of two-phase flow. *Adv. Nucl. Science and Technology* **20**, 1–69.

DRUZHININ, O. A. & ELGHOBASHI, S. 1999 On the decay rate of isotropic turbulence laden with microparticles. *Phys. Fluids* **11**, 602.

ELGHOBASHI, S. 1994*a* On predicting particle-laden flows. *Appl. Scientific Res* **52**, 309–329.

ELGHOBASHI, S. 1994*b* On predicting particle-laden flows. *Appl. Scientific Res* **52**, 309–329.

ELGHOBASHI, S. & TRUESDELL, G. C. 1992 Direct simulation of particle dispersion in a decaying isotropic turbulence. *J. Fluid Mech.* **242**, 655–700.

FABRE, J., RIVERO, M. & MAGNAUDET, J. 1995 Accelerated flows past a rigid sphere or a spherical bubble .i. steady straining flow. *J. Fluid Mech.* **284**, 97–135.

FESSLER, J. R., KULICK, J. D. & EATON, J. K. 1994 Preferential concentration of particles in a turbulent channel flow. *Phys. Fluids* **6**, 3742.

FORNBERG, B. 1998 Calculation of weights in finite difference formulas. *SIAM Rev.* **40**, 685.

FORTESCUE, G. E. & PEARSON, J. R. 1967 On gas absorption into a turbulent liquid. *Chem. Engng. Sci.* **22**, 1163.

FRIEDLANDER, S. K. & JOHNSTONE, H. F. 1957 Deposition of suspended particles from turbulent gas streams. *Ind. Eng. Chem.* **49**, 1151.

FULGOSI, M. 2004 *DNS OF TURBULENT HEAT TRANSFER AND CONDENSATION IN STRATIFIED FLOW WITH A DEFORMABE INTERFACE*. Zurich: Doctoral Thesis, ETH.

FULGOSI, M., LAKEHAL, D., BANERJEE, S. & 0.34GAROGLU, G. 2001 Direct numerical simulation of turbulence and interfacial dynamics in counter–current air–water flows. *Proceedings of DLES-4, in Direct and Large-Eddy Simulation - IV, Kluwer Academic Publishers, B.J. Geurts, R. Friedrich, O. Metais (Eds.), ERCOFTAC Series Vol. 8* .

FULGOSI, M., LAKEHAL, D., BANERJEE, S. & DEANGELIS, V. 2003 Direct numerical simulation of turbulence in a sheared air–water flow with deformable interface. *J. Fluid Mech.* **482**, 319–345.

GERMANO, M., PIOMELLI, U., MOIN, P. & CABOT, W. 1991 A dynamic subgrid-scale eddy viscosity model. *Phys. Fluids* **3**, 1760–1765.

GRAHAM, D. 1998 Improved eddy interaction models with random length and time scales. *Int. J. Multiphase Flow* **24(2)**, 335–345.

VAN HAARLEM, B., BOERSMA, B. J. & NIEWSTADT, F. M. T. 1998 Direct numerical simulation of particle deposition onto a free–slip and no–slip surface. *Phys. Fluids* **10**, 2608.

HENN, D. S. & SYKES, R. I. 1999 Large-eddy simulation of flow over wavy surfaces. *J. Fluid Mech.* **383**, 75.

HIGBIE, R. 1935 The rate of absorption of a pure gas into a still liquid during short periods of exposure. *Trans. AIChE* **31**, 365.

HINZE, J. O. 1975 *TURBULENCE, 2nd edition*. New York, USA: McGraw Hill.

HIRT, C. & NICHOLS, B. 1980 Adding limited compressibility to incompressible hydrocodes. *Journal of Computational Physics* **34**, 390–400.

HO, C.-M. & HUERRE, P. 1984 Perturbed free shear layers. *Ann. Rev. Fluid Mechanics* **16**, 365.

HU, Z., LUO, X. & LUO, K. H. 2002 Numerical simulation of particle dispersion in a spatially developing mixing layer. *Theor. Comp. Fluid Dynamics* **15**, 403–420.

HUERRE, P. & MONKEWITZ, P. A. 1985 Absolute and convective instabilities in free shear layers. *J. Fluid Mech.* **159**, 151.

HUNT, J. & GRAHAM, J. 1978 Free stream turbulence near plane boundaries. *J. Fluid Mech.* **84**, 209.

HUNT, J. C. R., WRAY, A. A. & MOIN, P. 1988 Eddies, stream and convergence zones in turbulent flows. *Report CTR-S88, Center For Turbulence Research* .

HUSSAIN, A. 1983 Coherent structures - reality and myth. *PF* **26(10)**, 2816.

ISHII, M. 1975 *THERMO-FLUID DYNAMIC THEORY OF TWO-PHASE FLOW*. Paris, France: Eyrolles.

JAEHNE, B., HUBER, W., DUTZI, A., WAIS, T. & ILMBERGER, J. 1984 Wind–wave–tunnel experiments on the schmidt number and wave field dependence of air–water gas exchange. *Gas Transfer at Water Surfaces, (ed. W. Brutsaert & G. H. Jirka), Reidel/North–Holland, Amsterdam* .

JAEHNE, B., MUENNICH, O., BOESINGER, R., DUTZI, A., HUBER, W. & LIBNER, P. 1987 On the parameters influencing air–water gas exchange. *J. Geophysical Research* **92(C2)**, 1937.

JEONG, J. & HUSSAIN, F. 1995 On the identification of a vortex. *Journal of Fluid Mechanics* **285**, 69–94.

JEONG, J., HUSSAIN, F., SCHOPPA, W. & KIM, J. 1997 Coherent structures near the wall in a turbulent channel flow. *J. Fluid Mech.* **332**, 185.

JIMENEZ, J. & PINELLI, A. 1999 The autonomous cycle of near–wall turbulence. *J. Fluid Mech.* **389**, 335.

KAFTORI, D., HETSRONI, G. & BANERJEE, S. 1995*a* Particle behaviour in the turbulent boundary layer: motion, deposition and entrainment. *Phys. Fluids* **7**, 1095.

KAFTORI, D., HETSRONI, G. & BANERJEE, S. 1995*b* Particle behaviour in the turbulent boundary layer: velocity and distribution profiles. *Phys. Fluids* **7**, 1107.

KASAGI, N., TOMITA, Y. & KURODA, A. 1992 Direct numerical simulation of passive scalar field in a turbulent channel flow. *ASME J. Heat Transfer* **114**, 598.

KATAOKA, I. 1986 Local instant formulation of two-phase flow. *Int. J. Multiphase Flow* **12**, 745–758.

KAWAMURA, H., OHSAKE, K., ABE, H. & YAMAMOTO, K. 1998 Dns of turbulent heat transfer in channel flow with low to medium-high prandtl number. *Int. J. Heat and Fluid Flow* **19**, 482.

KIM, J., MOIN, P. & MOSER, R. 1987 Turbulence statistics in fully developed channel flow at low reynolds number. *J. Fluid Mech.* **177**, 133.

KNOWLTON, B., GUPTA, R. & BANERJEE, S. 1999 Estimation of free surface mass transfer coefficients using experimental dpiv velocity data. *in Proceedings of TSFP-1, S. Banerjee, J. K. Eaton (Eds.), Begell House, New York* .

KOLEV, N. 1993 Fragmentation and coalescence dynamics in multiphase flows. *Exp. Thermal and Fluid Science* **6**, 211–251.

KOLMOGOROV, A. 1949 On the disintegration of drops in a turbulent flow. *Doklady Akademii Nauk SSSR* **66**, 825–828.

KOMORI, S., NAGAOSA, R. & MURAKAMI, Y. 1993*a* Turbulence structure and mass transfer across a sheared air–water interface in wind–driven turbulence. *J. Fluid Mech.* **249**, 161.

KOMORI, S., NAGAOSA, R., MURAKAMI, Y., CHIBA, S., ISHII, K. & KUWAHARA, K. 1993*b* Direct numerical simulation of three–dimensional open–channel flow with zero–shear gas–liquid interface. *Phys. Fluids* **A 5(1)**, 115.

KOMORI, S., UEDA, H., OGINO, F. & MIZUSHINA, T. 1982 Turbulence structure and transport mechanisms at the free surface in an open channel flow. *Int. J. Heat and Mass Transfer* **25**, 513.

KOTHE, D. & RIDER, W. 1997 Reconstructing volume tracking. *Journal of Computational Physics* **141**, 112–152.

KUMAR, S., GUPTA, R. & BANERJEE, S. 1998 An experimental investigation of the characteristics of free–surface turbulence in channel flow. *Phys. Fluids* **10(2)**, 437.

LAKEHAL, D. 2004 Dns and les of turbulent multifluid flows. In *Keynote Lecture, 3rd Symp. of Two-Phase Flow Modelling and Experimentation, Pisa Sept. 22-24, (ISTP04), CD-ROM* , p. 12 p. G-P. Celata and P. Di Marco.

LAKEHAL, D., FULGOSI, M., YADIGAROGLU, G. & BANERJEE, S. 2003 Direct numerical simulation of heat transfer at different prandtl numbers in counter-current gas–liquid flows. *J. Heat Transfer, ASME* **125(6)**, 1129–1140.

LAKEHAL, D., LIOW, J.-L. & LIOVIC, P. 2004 Les of turbulent bubble formation and break-up based on interface tracking. *Direct and Large-Eddy Simulation V Amsterdam: Kluwer Academic* .

LAKEHAL, D., MEIER, M. & FULGOSI, M. 2002*a* Interface tracking for the prediction of interfacial dynamics and heat/mass transfer in multiphase flows. *Int. J. Heat and Fluid Flow* **23(3)**, 242–257.

LAKEHAL, D. & NARAYANAN, C. 2003 Numerical analysis of the continuum formulation for the initial evolution of mixing layers with particles. *Int. J. Multiphase Flow* **29**, 927–941.

LAKEHAL, D., SMITH, B. & MILELLI, M. 2002*b* Large-eddy simulation of bubbly turbulent shear flows. *J. Turbulence* **3(25)**, 1–21.

LAKEHAL, D., SMITH, B. & MILELLI, M. 2002*c* Large-eddy simulation of bubbly turbulent shear flows. *J. Turbulence* **3(25)**, 1–21.

LAM, K. & BANERJEE, S. 1992 On the condition of streak formation in a bounded turbulent flow **4**, 306.

LANCE, M. & BATAILLE, J. 1991 Turbulence in the liquid phase of a uniform bubbly air-water flow. *J. Fluids Mech.* **222**, 95–118.

LANCE, M., BATAILLE, J. & MARIE, J. 1999 Turbulence in bubbly blow: from experiments to numerical modelling. *Proc. 2nd Int. Symp. on Two-Phase Flow Modelling and Experimentation, Piza, Italy* .

LANDAU, L. & LIFSHITZ, E. 1987 *FLUID MECHANICS, 2nd Eds*. Pergamon Press.

LAWRENCE, G. A., BROWAND, F. K. & REDEKOPP, L. G. 1991 The stability of a sheared density interface **3**, 2360.

LEONARD, A. 1974 Energy cascade in large–eddy simulations of turbulent fluid flows. *Advances in Geophysics* **18A**, 237–248.

LEWIS, W. K. & WHITMAN, W. G. 1924 Principles of gas absorption. *Ind. Engng. Chem.* **16**, 1215.

LIOVIC, P. & LAKEHAL, D. 2004 Turbulence-interface interactions in large-scale bubbling processes. *Phys. Fluids, in review* .

LIOVIC, P., LAKEHAL, D. & LIOW, J.-L. 2003 *LES OF TURBULENT BUBBLE FORMATION AND BREAKUP BY USE OF INTERFACE TRACKING*. Dordrecht: Kluwer Academic Publishers.

LIOVIC, P., RUDMAN, M. & LIOW, J.-L. 2001 A volume-of-fluid (vof) method for the simulation of metallurgical flows. *ISIJ International* **41**, 225–233.

LIOVIC, P., RUDMAN, M. & LIOW, J.-L. 2002 Numerical modelling of free surface flows in metallurgical vessels. *Applied Mathematical Modelling* **26**, 113–140.

LISS, P. S. & MERLIVAT, L. 1986 Air-sea gas exchange rates: introduction and synthesis. *The role of air-sea exchange in geochemical cycling, (Ed. P. Buar-Menard, D. Reidel, Norwell, Mass)* pp. 113–129.

LIU, B. Y. H. & AGARWAL, J. K. 1974 Experimental observation of aerosol deposition in turbulent flow **5**, 145.

LOMBARDI, P., DEANGELIS, V. & BANERJEE, S. 1996 Direct numerical simulation of near-interface turbulence in coupled gas-liquid flow. *Phys. Fluids* **8**, 1643.

LYONS, S. L., HANRATTY, T. J. & MCLAUGHLIN, J. B. 1991 Large–scale computer simulation of fully developed turbulent channel flow with heat transfer. *Int. J. Numerical Methods in Fluids* **13**, 999.

MAASS, C. & SCHUMANN, U. 1994 Numerical simulation of turbulent flow over a wavy boundary. *Proceedings of DLES-1, in Direct and Large-Eddy Simulation - I, Kluwer Academic Publishers, P. R. Voke, L. Kleiser and J. P. Chollet (Eds.), ERCOFTAC Series Vol. 26* .

MANSOUR, N. N., KIM, J. & MOIN, P. 1988 Reynolds–stress and dissipation-rate budgets in a turbulent channel flow. *J. Fluid Mech.* **194**, 15.

MARCHIOLI, C. & SOLDATI, A. 2002 Mechanisms for particle transfer and segregation in turbulent boundary layer. *J. Fluid Mech.* **468**, 283.

MARTINEZ-BAZAN, C., MONTANES, J. & LASHERAS, J. 1999*a* On the breakup of an air bubble injected into a fully developed turbulent flow. part 1. breakup frequency. *Journal of Fluid Mechanics* **401**, 157–182.

MARTINEZ-BAZAN, C., MONTANES, J. & LASHERAS, J. 1999*b* On the breakup of an air bubble injected into a fully developed turbulent flow. part 2. size pdf of the resulting daughter bubbles. *Journal of Fluid Mechanics* **401**, 183–207.

MASBERNAT, L., SUZANNE, C. & ROIG, V. 1997 Experimental investigation of a turbulent bubbly mixing layer. *Int. J. Multiphase Flow* **24**, 35–54.

MASLOWE, S. A. 1985 Shear flow instabilities and transition. *in* Hydrodynamic Instabilities and the transition to turbulence*, edited by H. L. Swinney and J. P. Gollub, 2nd ed. Springer-Verlag, Berlin* .

MAXEY, M. R. & RILEY, J. K. 1983*a* Equation of motion for a small rigid sphere in a nonuniform flow. *Phys. Fluids* **26**, 883–889.

MAXEY, M. R. & RILEY, J. K. 1983*b* Equation of motion for a small rigid sphere in a nonuniform flow. *Phys. Fluids* **26**, 883.

MCCOY, D. D. & HANRATTY, T. J. 1975 Rate of deposition of droplets in annular two-phase flow. *Int. J. Multiphase Flow* **3**, 319.

MCCREADY, M. J. & HANRATTY, T. J. 1984 A comparison of turbulent mass transfer at gas–liquid and at solid–liquid interfaces. *in GAS TRANSFER AT WATER SURFACES* pp. 283–292, Edited by W. Brutsaert and G. H. Jirka.

McCready, M. J. & Hanratty, T. J. 1985*a* Effect of air shear on gas absorption by a liquid film. *AIChE Journal* **31(12)**, 2066.

McCready, M. J. & Hanratty, T. J. 1985*b* Effect of air shear on gas absorption by a liquid film. *AIChE J.* **31**, 2066.

McKenna, S. P. & McGillis, W. R. 1999 Free surface turbulence in air–water gas transfer. *in Proceedings of TSFP-1, S. Banerjee, J. K. Eaton (Eds.), Begell House, New York* .

McLaughlin, J. B. 1989 Aerosol particle deposition in numerically simulated channel flow. *Phys. Fluids* **1**, 1211.

Meier, M. 1999*a Numerical and Experimenta Study of Large Steam-Air Bubbles Injected in a Water Pool*. ETH Zurich, CH: Ph.D Thesis.

Meier, M. 1999*b Numerical and Experimenta Study of Large Steam-Air Bubbles Injected in a Water Pool*. ETH Zurich, CH: Ph.D Thesis.

Meier, M., Andreani, M. & Yadigaroglu, G. 2000 Numerical and experimental study of large steam-air bubbles injected in a water pool. *Nuclear Science and Engineering* **136**, 363–375.

Meier, M., Yadigaroglu, G. & Smith, B. 2002 A novel technique for including surface tension in plic-vof methods. *Eur. J. Mechanics B-fluids* **21**, 61.

Melville, W. K. 1996 The role of surface–wave breaking in air–sea interaction. *Annu. Rev. Fluid Mech.* **28**, 279.

Michalke, A. 1964 On the inviscid instability of the hyperbolic-tangent velocity profile. *J. Fluid Mech.* **19**, 543.

Michalke, A. 1965 On spatially growing disturbances in an inviscid shear layer. *J. Fluid Mech.* **23**, 521.

Milelli, M. & Smith, B. 1998 An investigation of confined bubble plumes. *3rd Int. Conf. on Multi-Phase Flow ICMF'98, Lyon* **Paper 641**.

Milelli, M., Smith, B. & Lakehal, D. 2001*a* Large-eddy simulation of turbulent shear flows laden with bubbles. *Direct and Large-Eddy Simulation IV* .

Milelli, M., Smith, B. & Lakehal, D. 2001*b* Subgrid scale modelling in les of turbulent bubbly flows. *Proc. of TSFP-2, KTH Stockholm, Sweden* .

Moler, C. B. & Stewart, G. W. 1973 An algorithm for generalized matrix eigenvalue problems. *SIAM J. Numer. Anal.* **10**, 241.

Na, Y., Papavassiliou, D. V. & Hanratty, T. J. 1999 Use of direct numerical simulation to study the effect of prandtl number on temperature fields. *Int. J. Heat and Fluid Flow* **20**, 187.

Nagano, Y. 2002 Modelling heat transfer in near-wall flows. *in Closure Strategies for Turbulent and Transitional Flows, edited by B. Launder and N. Sandham, Cambridge Univ. Press* .

Narayanan, C. 2004 Numerical analysis of particle transport and flow modification in temporally evolving mixing layers. PhD thesis, ETH Zurich, Switzerland.

Narayanan, C. & Lakehal, D. 2002 Temporal instabilities of a mixing layer with uniform and nonuniform particle loadings. *Phys. Fluids* **14**, 3775–3789.

Narayanan, C., Lakehal, D., Botto, L. & Soldati, A. 2003 Mechanisms of particle deposition in a fully–developed turbulent open channel flow. *Phys. Fluids* **15**, 763.

Narayanan, C., Lakehal, D. & Yadigaroglu, G. 2002 Linear stability analysis of particle–laden mixing layers using lagrangian particle tracking. *Powder Tech.* **125**, 122–130.

Papavassiliou, D. V. & Hanratty, T. J. 1997 Transport of a passive scalar in a turbulent channel flow. *Int. J. Heat and Mass Transfer* **40**, 1303.

PEROT, B. & MOIN, P. 1995 Shear–free turbulent boundary layers. part 1. physical insight into near–wall turbulence. *J. Fluid Mech.* **295**, 199.

PERRY, A. E. & CHONG, M. S. 1987 A description of eddying motions and flow patterns using critical point concepts. *Annu. Rev. Fluid Mech.* **19**, 125.

PHILLIPS, O. M. 1977 *THE DYNAMICS OF THE UPPER OCEAN*. Cambridge, UK: Cambridge University Press.

PHILLIPS, O. M. 1985 Spectral and statistical properties of the equilibrium range in wind-generated gravity waves. *J. Fluid Mech.* **156**, 505.

PILLER, M., NOBILE, E. & HANRATTY, T. J. 2002 Dns study of turbulent transport at low prandtl numbers in a channel flow. *J. Fluid Mech.* **458**, 419.

PROSPERETTI, A. & ZHANG, D. Z. 1995 Finite-particle-size effects in disperse two-phase flows. *Theor. Comp. Fluid Dynamics* **7**, 429–440.

RASHIDI, M. & BANERJEE, S. 1988 Turbulence structure in free surface channel flows. *Phys. Fluids* **31**, 2491.

RASHIDI, M. & BANERJEE, S. 1990*a* The effect of boundary conditions and shear rate on streak formation and breakdown in turbulent channel flow. *Phys. Fluids* **A 2 (10)**, 1827.

RASHIDI, M. & BANERJEE, S. 1990*b* The effect of boundary conditions and shear rate on streak formation and breakdown in turbulent channel flow. *Phys. Fluids* **A 2 (10)**, 1827.

RASHIDI, M., HETSRONI, G. & BANERJEE, S. 1992 Wave–turbulence interaction in free-surface channel flows. *Phys. Fluids* **A 4**, 2727.

REEKS, M. W. 1983 The transport of discrete particles in inhomogeneous turbulence **14**, 729.

RISSO, F. & FABRE, J. 1998 Oscillations and breakup of a bubble immersed in a turbulent field. *Journal of Fluid Mechanics* **372**, 323–355.

ROBINSON, S. K. 1991 Coherent motion in the turbulent boundary layer. *Annu. Rev. Fluid Mech.* **23**, 601.

ROUSON, D. W. I. & EATON, J. K. 2001 On the preferential concentration of solid particles in turbulent channel flow. *J. Fluid Mech.* **428**, 149.

SADATOMI, I., SATO, Y. & SEKOGUCHI, I. 1981 Momentum and heat transfer in two-phase bubbly flow-i. *J. Multiphase Flow* **7**, 167–177.

SAFFMAN, P. G. 1962 On the stability of laminar flow of a dusty gas. *J. Fluid Mech.* **13**, 120–128.

SCHOPPA, W. & HUSSAIN, F. 2002 Coherent structure generation in near–wall turbulence. *J. Fluid Mech.* **453**, 57.

SHAMS, M., AHMADI, G. & RAHIMZADEH, H. 2000 A sublayer model for deposition of nano– and micro–particles in turbulent flows. *Chem. Eng. Sci.* **55**, 6907.

SMAGORINSKY, J. 1963 General circulation experiments with the primitive equations i the basic experiment. *Mon. Weather Rev.* **91**, 99–165.

SMITH, B. 1998*a* On the modelling of a bubble plume in a liquid pool. *Appl. Math. Modelling* **22**, 773–797.

SMITH, B. 1998*b* On the modelling of a bubble plume in a liquid pool. *Appl. Math. Modelling* **22**, 773–797.

SOLDATI, A. & BANERJEE, S. 1998 Turbulence modification by large–scale organized electrohydrodynamic flows. *Phys. Fluids* **10(7)**, 1742.

SOLOVIEV, A. V. & SCHLUESSEL, P. 1994 Parametrization of the temperature difference across the cool skin of the ocean and the air–ocean gas transfer on the basis of modeling surface renewal. *j. Phys. Oceanogr.* **24**, 1319.

SULLIVAN, P. P., MCWILLIAMS, J. C. & MOENG, C. H. 2000 Simulation of turbulent flow over idealized water waves. *J. Fluid Mech.* **404**, 47.

THEOFANOUS, T. G. 1984 Conceptual models for gas exchange. *in GAS TRANSFER AT WATER SURFACES* pp. 271–281, Edited by W. Brutsaert and G. H. Jirka.

TISELJ, I., BERGANT, R., MAVKO, B., BAJSIC, I. & HETSRONI, G. 2001*a* Dns of turbulent heat transfer in channel flow with heat conduction in the solid wall. *ASME J. Heat Transfer* **123**, 849.

TISELJ, I., POGREBNYAK, E., LI, C., MOSYAK, A. & HETSRONI, G. 2001*b* Effect of wall boundary condition on scalar transfer in a fully developed turbulent flume. *Phys. Fluids* **13(4)**, 1028.

TONG, X.-L. & WANG, L.-P. 1999 Two-way coupled particle-laden mixing layer. part 1: Linear instability. *Int. J. Multiphase Flow* **25**, 575–598.

TRAN, M. 1997 *MODELISATION INSTATIONNAIRE DE LA DISTRIBUTION SPATIALE DES PHASES DANS LES ECOULEMENTS DIPHASIQUES EN REGIMES A BULLES*. University of Claude Bernard, Lyon: Doctoral Thesis.

WANG, L. P. & MAXEY, M. R. 1993 Settling velocity and concentration distribution of heavy particles in homogeneous isotropic turbulence. *J. Fluid Mech.* **256**, 27.

WANG, Q., SQUIRES, K. D. & WANG, L.-P. 1998 On the effect of nonuniform seeding on particle dispersion in two–dimensional mixing layers. *Phys. Fluids* **10**, 1700–1714.

WANNINKHOF, R. H. & MCGILLIS, W. R. 1999*a* A cubic relationship between air-sea co_2 exchange and gas speed. *Geophys. Res. Letters* **26**, 1889.

WANNINKHOF, R. H. & MCGILLIS, W. R. 1999*b* A cubic relationship between air-sea co_2 exchange and gas speed. *Geophys. Res. Letters* **26**, 1889.

WEN, F. & EVANS, J. 1994 Linear instability of a two-layer flow with differential particle loading. *Phys. Fluids* **6**, 3893–3905.

WEN, F. & EVANS, J. 1996 Effect of particle inertia on the instability of a particle-laden flow. *Computers & Fluids* **25**, 667–676.

WENGLE, H. & WERNER, H. 1989 Large-eddy simulation of flow over a square rib in a channel. *Proc. TSF-7 (Stanford)* .

YADIGAROGLU, G. 2003 Letter to the editor, cfmd (a brand name) and other acronyms. *Int. J. Multiphase Flow* **29**, 719–720.

YADIGAROGLU, G., DREIER, J., ANDREANI, M. & CODDINGTON, P. 2003 Trends and needs in experimentation and numerical simulation for lwr safety. *Nucl. Eng. Design* **221**, 205–220.

YANG, Y., CHUNG, J. N., TROUTT, T. R. & CROWE, C. T. 1990 The influence of particles on the spatial stability of two-phase mixing layers **2**, 1839–1845.

YOUNG, J. & LEEMING, A. 1997 A theory of particle deposition in turbulent pipe flow. *J. Fluid Mech.* **340**, 129.

YOUNGS, D. 1982 Time-dependent multi-material flow with large fluid distortion. *Numerical Methods for Fluid Dynamics, Ed. K.W. Morton* pp. 273–285.

ZHANG, D. Z. & PROSPERETTI, A. 1997 Momentum and energy equations for disperse two-phase flow and their closure for dilute suspensions. *Int. J. Multiphase Flow* **23**, 425–453.

Résumé de Carrière

CV succint

Djamel Lakehal
Né le 9 novembre 1965 en Algérie
Adresse: ETH Zentrum, CLT, Zurich 8092, Suisse
Tél: +41 01 273 74 32
Courriel: lakehal@iet.mavt.ethz.ch

Diplômes

- 1994. **Doctorat** *de Dynamique des Fluides et des Transferts* de l' Ecole Centrale de Nantes.
  Thème: *Simulation des Ecoulements Turbulents autour de Formes Courbes*.
  Directeurs: Dr. Ch. Sacré et Dr. P.G. Mestayer.
- 1991. **D.E.A** *de Dynamique des Fluides et des Transferts* de l'Ecole Centrale de Nantes.
  Thème: *Simulation Lagrangienne de la Dispersion de Particules dans la Couche de Surface*
  Directeur: Dr. P.G. Mestayer.
- 1990. **Ingénieur** *en Mécanique Energétique* de l'Université de Batna, Algérie.

Prix, Distinctions et Bourses

- 1997. Subside de Recherche de la Foundation Allemande pour la Recherche (DFG).
- 1995. Bourse de Recherche Européene, dans le cadre du programme 'Human Capital & Mobility'.
- 1991. Bourse de Thèse, Centre International des Etudiants & Stagiaires, France.

Spécialités

- Dynamique des Fluides Numérique
- Ecoulements Multiphasiques et Dispersion Particulaire
- Modélisation et Simulation de la Turbulence
- Aérothermodynamique

Carrière

- **[1991-1994] Ingénieur–Doctorant** au CSTB de Nantes. Service Aérodynamique et Climatique (Dr. Jacques Gandemer).
  Recherches: Etudes des (i) effets de la turbulence amont en couche de surface, (ii) des structures tridimensionnelles complexes, et (iii) des effets de rugosité de surface sur la transition des écoulements aux régimes hypercritiques.

- **[1995-1997] Chercheur Associé** à l' Université de Karlsruhe, Institut d'Hydromécanique (Pr. Wolfgang Rodi).
  Recherches: Modélisation de la turbulence dans les écoulements internes et externes. Développement de (i) modèles de turbulence anisotropiques, (ii) de modèles hybrides, bi- ou multi-couches, pour la turbulence pariétale en 3D, et de (iii) modèles algébriques pour les écoulements de fluides non-Newtoniens fortement stratifiés.

- **[1997-1998] Chef de Groupe Calcul** à l' Université Technique de Berlin, Institut de Mécanique des Fluides (Pr. Franke Thiele).
  Recherches: Modélisation des écoulements turbulents avec détachements tourbillonnaires. Etude de la réalisabilité des modèles de turbulence non-linéaires, (ii) analyse de la stabilité des écoulements quasi-laminaires et transitionnels, et (iii) intégration de l'approche PDF pour l'étude de la stabilité des flammes.

- **[1998-2004] Maitre Assistant**, Institut de Génie Energétique de l'ETHZ. Laboratoire de Génie Nucléaire (Pr. George Yadigaroglu).
  Recherches: Initiateur et chef du groupe *CMFD**, Calcul des Ecoulements Multi-Fluides. Entre 2001 et 2003, chef de groupe (Simulation) à temps partiel au Laboratoire de Turbomachines (Pr. R.S. Abhari).

Enseignements

- 1997 - 1998 Travaux dirigés en *Méthodes Numériques*, Hermann-Föttinger Institute for Fluid Mechanics, TU-Berlin. Fréquence: 2H par semaine, soit 40H par année universitiare.
- 1999 - 2003 Cours d'*Analyse Numérique des Ecoulements et des Transferts* (avec notes de cours), ETHZ. Niveau 6/8ème semestre et M.S. (equivalent DEA). Fréquence: 2H équivalent cours par semaine (14 semaines par semestre).
- 1998 - 2003 Cours de Phénoménologie et Modélisation de la Turbulence (avec notes de cours),ETHZ. Niveau 6/8ème semestre et equivalent DEA (1ère année de thèse). Fréquence: 2H équivalent cours par semaine (14 semaines par semestre).
- 1998 - 2003 Travaux Pratiques en Transferts de Chaleur, ETHZ. Niveau 6ème semestre. Total de 10H par semestre.

La charge globale des enseignements (cours, TD et Travaux) s'élève à 80H par année universitaire.

Encadrement (c.f. Paragraphe 2.1)

- **Doctorants** en Allemagne: Martin Armbruster, Jan Erhard, Holger Luebcke.
- **Doctorants** en Suisse, depuis 1998: Chidambaram Narayanan, Marco Fulgosi, Jeffrey Davis, Andre Burdet, Azzi Abbes, Bob Mischo, Thomas Mokulys, Friedrike Mund, Massimo Milelli, Rade Milenkovic, Marco Simiano.
- **Diplomes**: Roxana Machovschi, Andreas Wick, Andreas Arlt, Ryad Mezzour, Christian Gjerloev, Andreas Peter, Lorenzo Botto, Boris Meier, Pascale Buchel.

*www.lkt.iet.ethz.ch/cfmg/

Séjours Scientifiques

- 2000-2003, échanges fréquents avec l'Ecole Centrale de Lyon (Pr. M. Lance).
- 1998, l'Ecole Polytechnique de Salonique, Grèce (Pr. R. Moussiopoulos).
- 1999 et 2000, UC Santa Barbara, USA (Pr. S. Banerjee).

Activitiés de Lecture (Review)

- Physics of Fluids
- Journal of Turbulence
- ASCE Journal of Hydraulic Eng.
- Int. Journal of Multiphase Flow
- Flow, Turbulence & Combustion
- Computers & Fluids

Affiliations

- AIChE
- ERCOFTAC Leonhard Euler Center (Suisse)
- EMSI (European Multiphase Systems Institute)
- IMuST (Institute of Multiphase Science & Technology)

Activités de Recherche Scientifique

Dès mon entrée à l'ETH Zurich en 1998, j'ai constitué une équipe de recherche composée de thésards et de post-doctorands, que je continue encore à diriger.

Les activités de cette équipe sont essentiellement centrées autour de l'étude de la dynamique des écoulements multi-phasiques et des transferts. Les motivations s'inscrivent dans un cadre de recherche fondamentale, ayant pour objectif de faire avancer les connaissances sur les mécanismes microphyisiques qui controllent les échanges interfaciaux, et leur rapport avec le comportement macroscopique des écoulements dans les systemes energétiques. L'élément essentiel de nos recherches porte sur la structure de la turbulence à l'échelle du mélange et à l'échelle interfaciale, ainsi que sur le développement des méthodes de calcul adéquates. L'approche suivie a été élaborée il y a cinq ans dans le cadre de la création du groupe CMFD. Elle consiste à traiter cette classe d'écoulements sur trois fronts complémentaires: faire recours aux méthodes de suivi d'interfaces pour les écoulements interfaciaux, et traiter les mélanges hétérogènes avec l'approche multi-fluide. Dans tous les cas de figures, la turbulence est traitée par la simulation macro-echelles (LES). Les modèles requis pour le traitment des échelles sous-mailles et des échanges interfaciaux sont developpés sur la base de résultats fournis par la simulation directe (DNS) des écoulements stratifiés diphasiques. Ces axes de recherche sont détaillés plus bas.

Recherches en Cours (Thèses et Post-docs)

THESE: Simulation directe de la dispersion particulaire dans les écoulements cisaillés libres
(C. Narayanan, D. Lakehal)
Le projet porte sur l'identification du rôle exacte du couplage particule-turbulence-particule dans ce type de configurations. Une méthode pseudo-spectrale DNS est employée pour la phase porteuse, couplée avec un module Lagrangien pour le suivi de la phase dispersée. L'originalité de la méthode réside dans le fait que la couche limite peut évoluer transversalement de $+\infty$ à $-\infty$, ce qui engendre la désintegration des structures cohérentes (générées

par les instabilités de Kelvin-Helmholtz) en petites échelles dissipatives. Cette thèse vient d'être soutenue; le candidat C. Narayanan s'est fait distingué par la Médaille d'Argent de l'ETHZ (1er Prix).

THESE: Simulation directe des transferts aux interfaces cisaillées déformables
(M. Fulgosi, D. Lakehal, G. Yadigaroglu, S. Banerjee)
L'objective de cette thèse de doctorat est d'aider à clarifier les mécanismes d'échanges interfaciaux (passifs et actifs) aux surfaces libres déformables et cisaillées. Il s'agit de qualifier les effets simultanés de déformations interfaciales (dans la limite de petites perturbations) et de condensation sur le taux globale des échanges. Des corrélations pourraient en être proposées dans un cadre plus générale de modélisation des transferts.

Post-Doc: Simulation macro-echelles des écoulements diphasiques
(D. Lakehal, P. Liovic, M. Lance, P. Sagaut)
Dans ce projet de collaboration Franco-Suisse, nous travaillons au développement d'une méthode de simulation LES pour deux types d'écoulements diphasiques: à bulles et interfaciaux. La première approche, basée sur le modèle deux-fluides étant déja validée et publiée (en collaboration avec l'Ecole Centrale de Lyon, c.f. liste des publications), l'effort est à présent orienté vers l'extension aux fluides immiscibles séparés par une interface cisaillée continue (en collaboration cette fois-ci avec l'université Paris 6 et l'Ecole Polytechnique; nous acceuillerons en 2004 un élève stagiaire). La base du modèle étant dans ce cas la méthode de suivi d'interface VOF. Les deux points restant en suspend sont le traitement près des interfaces, et le modèle sous-maille.

Post-Doc: Microfluidique
(P. Liovic, D. Lakehal)
L'objectif de ce projet est de développer les outils de simulation nécéssaires pour les écoulements et transferts dans les micro-canaux. Ce secteur de pointe ne cesse en effet de se développer dans le sillage des avancées récentes faites en micro- and nano-technologies. L'utilisation des écoulements multi-phasiques avec ébullition pour le refroidissement s'avère être très efficace par rapport aux méthodes classiques. Les applications potentielles étant la micro-éléctronique et l'aérospatiale. Dans ce projet nous utilisons des méthodes de suivi d'interfaces où le changement de phase est basé sur la simulation directe des gradients de température aux interfaces, sans recours à des corrélations empiriques.

Fluides complexes dominés par les tensions de surface
(H.M. Friess, D. Lakehal)
L'écoulement des fluides complexes tels que les suspensions, les polymères, la peinture peuvent fortement dépendre des tensions de surface. Ce projet fait intervenir des méthodes de suivi d'interfaces diffuses telle que l'approche basée sur les équations de Cahn-Hilliard-Navier-Stokes (CHNS). Les examples d'applications comprennent la séparation de phases par cisaillement, la décomposition spinodale, etc. Nous travaillons à l'extension de ce type de modèles et d'autres (VOF) aux écoulements dominés par un angle de contact dynamique (microfluidique).

Accomplissements

Je décrirai mon itinéraire scientifique sur deux périodes distinctes. Avant 1998, je m'intéressais essentiellement aux aspects de modélisation de la turbulence par les méthodes statistiques (modèle k-E, modèle de second ordre, etc.), avec toutefois quelques interventions dans le domaine de la LES des écoulements fortements convectifs. Les applications touchaient à l'aérodynamique et l'hydrodynamique, aux écoulements atmosphériques, au détachement tourbillonaire, aux jets, au refroidissement d'aubes de turbines à gaz, etc. La seconde phase de cet itinéraire coincide avec mon entrée à l'ETH de Zurich en 1998. Elle a été marquée par un interêt pour la simulation (LES et DNS) des écoulements turbulents multi-phasiques et à surfaces libres. Mes accomplissements les plus marquants sont résumés plus bas.

1ère Période: Modélisation de la Turbulence

- Développement de modèles Lagrangiens pour la dispersion de particles dans un champ turbulent isotrope. La méthode fût appliquée au transport des hydrométéores dans la canopée urbaine. Travaux de DEA (article N○ 26).

- Développement de modèle de turbulence pour les écoulements sur des surfaces rugueuses. L'idée en est que la rugosité de surface peut anticiper la transition au règime hypercritique des écoulements autour de cylindres, sans pour autant agir sur le nombre de Reynolds. Travaux de thèse (articles N○ 20, 23 et 24).

- Développement de lois constitutives pour les écoulements non-Newtoniens (Bingham), turbulents avec stratification stable. Le modèle fût employé pour l'optimisation des systèmes d'épuration des eaux. Travaux de recherche à Karlsruhe (article N○ 21).

- Développement de modèles hybrides, bi- ou multi-couches, pour la turbulence pariétale en 3D. Les applications portaient sur l'aérodynamique et sur les écoulements en turbomachines. Travaux de recherche à Karlsruhe (articles N○ 22 and 25).

- Développement de modèles algébriques pour les écoulements avec détachement tourbillonaire. On a demontré que l'énergie cinétique turbulente induite par l'onde fréquencielle dominante separée du champs total ne dépendait pas du modèle de turbulence en soit. Travaux de recherche à l'université de Berlin (article N○ 19).

- Développment d'un modèle anisotrope et d'un modèle de convection turbulente près des parois solides s'appuiyant sur les résultats de la DNS. L'application de ces deux modèles a porté sur les jets parietaux, en l'occurence ceux présents dans les systèmes de refroidissement des aubes de turbines. Travaux de recherche à Karlsruhe (articles N○ 15-à-18).

2ème Période: Simulation des écoulements multiphasiques et à surfaces libres

- Contribution à l'étude de la stabilité des couches de mélange chargées de particules solides. Travaux récents effectués à l'ETH (articles N○ 10 et 13).

- Développement d'une formulation originale pour le filtrage (par produit de convolution) des équations multifluides pour la LES des écoulements dispersés à bulles, en collaboration avec M. Lance. Un modèle sous-maille fut proposé, basé sur l'approche dynamique de Germano, considérant la dissipation induite par le mouvement sous-maille des bulles. Travaux récents effectués a l'ETH (articles N○ 2 et 12; Chapitre d'Ouvrage N○2.).

- Nous avons par le bias de la DNS étudié la turbulence à l'interface d'un écoulement cisaillé gaz-liquide; la surface libre étant libre de se déformer. Travaux récents éffectués à l'ETH (articles N○ 7 et 8; Chapitre d'Ouvrage N○3).

- Nous avons par le bias de la DNS étudié le transfert passif de masse et de chaleur à travers une surface deformable avec variation du nombre de Prandtl et de l'amplitude des vagues. L'étude a été étendue au problème de condensation d'un mélange de vapeur et gaz sur un liquide sous-refroidi. De nouvelles corrélations en ont été déduites, basées sur l'intensité du cisaillement imposé et sur la structure de la surface deformée (modèle dit de *"surface divergence"* de Banerjee). Travaux récents éffectués à l'ETH en collaboration avec l'Université de Santa Barbara, USA (articles N○ 1 et 8).

- Nous avons proposé une nouvelle théorie qui éxplique les mécanismes de déposition de particles sur des parois solides dans un canal turbulent ouvert par le biais de la DNS. (articles N○ 9). Nos résultats ont en l'occurence démontré l'existence et l'organisation de deux groupes de particles pour des nombres de Stokes de 5 et 15: celles se déposant par les effets diffusionnels et celles exécutant une chute libre à partir du centre du canal où la turbulence est très active (*free-flight mechanism*).

- Nous avons ensuite conduit une étude similaire, comparant le taux de déposition de particules sur parois planes et surfaces deformées. L'étude (DNS) a montré que ce taux pouvait être 10 fois plus important dans le deuxieme cas, du fait de la modification de la turbulence par les déformations interfaciales (article N○ 5).

- Nous avons developpé une nouvelle stratégie qui combine la LES aux méthodes de suivi d'interface (VOF et Level Sets) pour les écoulements charactérisés par une déformation massive de la topologie interfaciale. Travaux en cours (articles N○ 2 et 3; Chapitre d'Ouvrage N○1).

- Une nouvelle formulation de la méthode de suivi d'interface VOF applicable en 3D a été proposée dans un cadre d'une coopération avec les Laboratoires de Los Alamos et de Melbourne. Travaux en cours (article N○ 4). La méthode est conservative et précise au 2nd ordre, et offre une excellente conservation des properités et préserve les symmetries des formes.

Montage de Projets

- 1994 - 1995 Source de support: Commission Européenne. Titre du projet: écoulements turbulents autour d'obstacles. Université de Karlsruhe.
- 1995 - 1996 Source de support: DHV Water, Pays Bas. Titre du projet: Modélisation de la sédimentation dans les systèmes d'épuration des eaux. Université de Karlsruhe.
- 1996 - 1997 Source de support: Ministère Allemand de la Science et de la Technologie (TURBOTHERM project). Titre du projet: Modélisation du refroidissment des aubes de turbines. Université de Karlsruhe.
- 1997 - 1999 Source de support: DFG[†] (Allemagne) et CNRS (France). Titre du projet: Simulation de la stabilité des flammes dans la combustion turbulente. TU-Berlin.
- 1999 - 2002 Source de support: Commission de Recherche de l'ETH. Titre du projet: Simulation du suivi d'interface pour la condensation par injection de vapeur. ETH Zurich.
- 2000 Source de support: Berthele Energy Foundation, Suisse. Titre du projet: Etude experimentale d'un jet diphasique. ETH Zurich.
- 2000 Source de support: ERCOFTAC, Centre Suisse. Titre du projet: Simulation directe de dispersion particulaire dans les écoulements cisaillés libres. ETH Zurich.
- 2001 Source de support: Fonds National Suisse pour la Recherche (FNS). Titre du projet: Etude experimentale d'un panache à bulles. ETH Zurich.
- 2004 (en cours d'élaboration) Source de support: EU 6ème cadre. Projet: Thermo-hydraulique Numérique.
- 2004 (en cours d'élaboration) Source de support: l'Agence Spatiale Européenne (ESA). Projet: Ebullition en micro-canaux.

Publications

Articles parus (ou en cours) dans des revues

1. Yadigaroglu G., Lakehal D.: New trends in computational thermal hydraulics, *Nuclear Technology*, (in press), 2004.
2. Liovic P., Lakehal D.: Interface-turbulence interactions in large-scale bubbling processes, *Phys. Fluids*, (in press), 2004.
3. Friess H.M., Lakehal D.: A new modelling concept for surface tension and contact angle dynamics in two-phase flow. (in review), 2004.
4. Simiano M., de Cachard F., Lakehal D., Yadigaroglu G.: Experimental investigation of the hydrodynamics of large-scale bubble plume. (in review), 2004.
5. Lakehal D., Lance M.: Large-eddy simulation of disperse and interfacial turbulent multi-fluid flows, (in review), 2004
6. Liovic P., Rudman M., Liow J.L., Lakehal D., Kothe, D.: A three-dimensional unsplit-advection volume tracking with planarity-preserving interface reconstruction, (in review), 2004.
7. Botto L., Narayanan C., Fulgosi M., Lakehal D.: Turbulent dispersion and deposition of droplets over capillary waves, (in review), 2004.
8. Banerjee S., Lakehal D., Fulgosi M.: Surface divergence models for scalar exchange between turbulent streams, *J. Multiphase Flow*, 30(8), pp. 965-979, 2004.

[†]Deutsche Forschungsgemenischaft. Le partenaire francais etait Mr. M. Buffat de l'ECL.

9. Lakehal D., Narayanan C.: Numerical analysis of the continuum formulation for the initial evolution of mixing layers with particles, *Int. J. Multiphase Flow*, 29(6), pp. 927-941, 2003.

10. Fulgosi M., Lakehal D., Banerjee S., De Angelis V.: Direct numerical simulation of turbulence in a sheared air-water flow with deformable interface, *J. Fluid Mechanics*, 482, pp. 319-345, 2003.

11. Lakehal D., Fulgosi M., Yadigaroglu G., Banerjee S.: Direct numerical simulation of heat transfer at different prandtl numbers in counter-current gas–liquid flows, *ASME J. Heat Transfer*, 125(6), pp. 1129-1140, 2003.

12. Narayanan C., Lakehal D., Botto L., Soldati A.: Mechanisms of particle deposition in a fully-developed turbulent open channel flow, *Phys. Fluids*, 15(3), pp., 763-775, 2003.

13. Narayanan C., Lakehal, D.: Temporal instabilities of a mixing-layer with uniform and non-uniform particle loadings, *Phys. Fluids*, 14(11), pp. 3775-3790, 2002.

14. Lakehal D., Meier M., Fulgosi M.: Interface tracking for the prediction of interfacial dynamics and heat/mass transfer in multiphase flows, *Int. J. Heat & Fluid Flow*, 23(3) pp. 242-257, 2002.

15. Lakehal D., Smith B.L., Milelli M.: Large-eddy simulation of bubbly turbulent shear flows. *Journal of Turbulence*, 3(25), pp. 1-21, 2002.

16. Narayanan C., Lakehal D., Yadigaroglu G.: Linear stability analysis of particle-laden mixing layers using lagrangian particle tracking, *Powder Technology*, 125(3), pp. 122-130, 2002.

17. Lakehal D.: On the modelling of multiphase turbulent flows for environmental and hydrodynamic applications, *Int. J. Multiphase Flow*, 28(5), pp. 823-863, 2002.

18. Azzi A, Lakehal D.: Perspectives in modelling film-cooling of turbine blades by transcending conventional two-equation turbulence models, *ASME J. Turbomachinery*, 124(3), pp. 472-484, 2002.

19. Lakehal D.: Near-wall modelling of turbulent convective heat transport in film cooling of turbine blades with the aid of direct numerical simulation data, *ASME J.Turbomachinery*, 124(3), pp. 485-498, 2002.

20. Theodoridis G., Lakehal D., Rodi W.: Three dimensional calculations of the flow field around a turbine blade with film cooling near the leading edge, *Flow, Turbulence & Combustion*, 66, pp. 57-83 2001.

21. Lakehal D., Theodoridis G., Rodi W.: Three dimensional flow and heat transfer calculations of film cooling at the leading edge of a symmetrical turbine blade model, *Int. J. Heat & Fluid Flow*, 22(2), pp. 113-122 2001.

22. Lakehal D., Thiele F.: Sensitivity of turbulent shedding flows past cylinders to non-linear stress-strain relations and reynolds stress models, *Computers & Fluids*, 30, pp 1-35, 2001.

23. Lakehal D.: Computation of turbulent shear flows over rough-walled circular cylinders, *J. Wind Eng. & Industrial Aerodynamics*, 80, pp. 47-68, 1999.

24. Lakehal D., Krebs P., Krijgsman J., Rodi W.: Computing shear flows and sludge blanket in secondary clarifiers, *ASCE J. Hydraulic Engineering*, 125, pp. 253-262, 1999.

25. Lakehal D., Theodoridis G., Rodi W.: Computation of film cooling of a flat plate by lateral injection from a row of holes, *Int. J. Heat & Fluid Flow*, 19, pp. 418-430, 1998.

26. Lakehal D.: Application of the k-e model to flow over a building placed in different roughness sublayers, *J. Wind Eng. & Industrial Aerodynamics*, 73, 1, pp. 59-77, 1998.

27. Delaunay D., Lakehal D., Barré C., Sacré C.: Numerical and wind-tunnel simulation of gas dispersion around a rectangular building, *J. Wind Eng. & Industrial Aerodynamics*, 68, pp. 198-213, 1997.

28. Lakehal D., Rodi W.: Calculation of the flow past a surface-mounted cube with two-layer turbulence models, *J. Wind Eng. & Industrial Aerodynamics*, 67, pp. 65-78, 1997.

29. Lakehal D., Mestayer P.G., Edson J.B., Anquentin S., Sini J.F.: Eulero-Lagrangian simulation of atmospheric rain-drop trajectories and impacts inside the urban canopy, *J. Atmospheric Environment: part B*, 29, pp. 3501-3518, 1995.

30. Delaunay D., Lakehal D., Pierrat D.: Numerical approach for wind loads on buildings and structures, *J. Wind Eng. & Industrial Aerodynamics*, 57, 307-321, 1995.

Chapitres d'Ouvrages

1. Liovic P., Lakehal D., Liow J.L.: LES of Turbulent Bubble Formation and Breakup by Use of Interface Tracking. *In "Direct and Large-Eddy Simulation - V", ERCOFTAC Series, 9, pp. 261-270, Geurts/Friedrich/Metais (Eds.), Kluwer Acad.* 2004.

2. Milelli M., Smith B.L., Lakehal D.: Large Eddy Simulation of Turbulent Shear Flows Laden with Bubbles. *In "Direct and Large-Eddy Simulation - IV", ERCOFTAC Series, 8, pp. 461-470, Geurts/Friedrich/Metais (Eds.), Kluwer Acad.* 2001.

3. Fulgosi M., Lakehal D., Banerjee S. Yadigaroglu G.: Direct Numerical Simulation of Turbulence and Interfacial Dynamics in Counter-Current Air-Water Flows. *In "Direct and Large-Eddy Simulation - IV", ERCOFTAC Series, 8, pp. 443-452, Geurts/Friedrich/Metais (Eds.), Kluwer Acad.* 2001.

4. Lakehal D., Thiele F, Duchamp de Lagneste L., Buffat M.: Computation of Vortex-shedding Flows past a Square Cylinder Employing LES and RANS. *In Notes on Numerical Fluid Mechanics, Vieweg Verlag, Braunschweig/Wiesbaden, E.H. Hirschel (Eds.)*, 66, pp. 260-277, 1998.

5. Breuer M., Lakehal D., Rodi W.: Flow Around a Surface Mounted Cubical Obstacle: Comparison of LES & RANS-Results. *In Notes on Numerical Fluid Mechanics, Vieweg Verlag, Braunschweig/Wiesbaden, Deville/Gavrilakis/Ryhming (Eds.)*, 53, pp. 22-30, 1996.

"Keynote Lectures" dans Actes de Colloques

1. Lakehal D.: DNS and LES of Turbulent Multifluid Flows. *In Proceedings of 3rd Int. Symp. Two-Phase Flow Modelling and Experimentation*, **Keynote Lecture**, Pisa, Italy, Sep. 22-24, 2004.

2. Lakehal, D.: Multi-Scale Turbulence Modelling for the LES of Interfacial Gas-Liquid Flows. *In Proceedings of IAHR/SIH Symp. Advances in the Modelling Methodologies of Two-Phase Flow*, **Keynote Lecture**, Lyon, France, Nov. 24-26, 2004.

3. Yadigaroglu G., Lakehal D.: New Trends in Computational Thermal Hydraulics. *In Proceedings of 10th Topical Meeting on Nuclear Reactor Thermal Hydraulics* (NURETH-10), **Keynote Lecture**, Seoul, Corea, Oct. 5-9, 2003.

4. Yadigaroglu G., Lakehal D., Smith B.L., Andreani M.: New Trends and Introduction of Multiphase CFD Methods in Nuclear Engineering. *In Proceedings of Int. Conf. Multiphase Systems* (ICMS'2000), **Keynote Lecture**, Ufa, Russia, June 15-17, 2000.

Communications à des colloques

1. Narayanan C., Lakehal D.: Generation of small-scale vorticity and vortex rupture by particles in two-dimensional mixing layers. *In Proceedings of Int. Conf. Multiphase Flows* (ICMF04), Yokohama, Japan, May 22-25, 2004.

2. Simiano M., de Cachard F., Lakehal D., Yadigaroglu G.: Large-scale PIV measurement of the hydrodynamics of large-scale bubble plume. *In Proceedings of Int. Conf. Multiphase Flows* (ICMF04), Yokohama, Japan, May 22-25, 2004.

3. Narayanan C., Lakehal D.: Preferential concentration of particles and mechanisms of particle-phase fluctuation generation in turbulent mixing layers. *In Proceedings of IUTAM Symposium on Computational Approaches to Disperse Multiphase Flow*, Argonne Natl. Labs., USA, Oct. 17-19, 2004.

4. Lakehal D., Liovic P.: Large-eddy simulation of steep water waves. *In Proceedings of IUTAM Symposium on Computational Approaches to Disperse Multiphase Flow*, Argonne Natl. Labs., USA, Oct. 17-19, 2004.

5. Friess H.M., Lakehal D.: A New Method for including Surface Tension and Contact Angle Dynamics in the Simulation of Two-Phase Flow. Computational Heat Transfer 4 (CHT04), Kirkenes, Norway, 19-24, April, 2004. *In ICHMT/Beguel House Inc. Publishers, New York, de Vahl Davis & Leonardi (Eds.), paper 250*.

6. Fulgosi M., Lakehal D., Yadigaroglu G.: DNS of a condensing counter-current steam over subcooled liquid. *In Proceedings of 3rd Int. Symp. Two-Phase Flow Modelling and Experimentation*, Pisa, Italy, Sep. 22-24, 2004.

7. Smith B., Schepel S., Lakehal D.: A Generic study of Phenomena affecting two-phase mixing in BWR suppression pools during passive decay-heat removal, *In Proceedings of 10th Topical Meeting on Nuclear Reactor Thermal Hydraulics* (NURETH-10), Seoul, Corea, Oct. 5-9, 2003.

8. Lakehal D., Fulgosi M., Yadigaroglu G., Banerjee S.: Turbulent scalar Transfer at Deformable Gas-Liquid Interfaces, AIChE Annual Meeting, San Fransisco, Nov. 15-17, 2003.

9. Lakehal D.: Direct Simulation of Interfacial Flows. *Industrial Challenges in the Simulation of Evolvling Interfaces*, European Network MACSI-NET, Brussels, Belgium, Sep. 1-2, 2003.

10. Botto L., Narayanan C., Lakehal D.: DNS of Particle Deposition Over A Sheared Water Surface, AIChE Annual Meeting, San Fransisco, Nov. 15-17, 2003.

11. Liovic P., Lakehal D., Liow J.G.: LES of Turbulent Bubble Formation and Breakup by use of Interface Tracking, Direct & Large Eddy Simulation 5, Munich, Germany, Aug. 27-29 2003.

12. Burdet A., Mischo B., Lakehal D., Kalfas A., Abhari R.: Predicting Vorticity Transport and Loss Generation in a Turbine Annular Cascade, *In Proceedings of 5th European Conf. on Turbomachinery*, Prague, Czech Republic, March 18-21, 2003. In M. Stastny, Ch. Sieverding, G. Bois (Eds.), pp. 995-1006.

13. Fulgosi M., Lakehal D., Banerjee S., Yadigaroglu G.: Direct Numerical Simulation of Turbulence and Interfacial Dynamics in Counter-Current Air-Water Flows, Direct & Large Eddy Simulation 4, Twente, Enschede, Holland, July 18-20, 2001.

14. Milelli M., Smith B.L., Lakehal D.: Large-Eddy Simulation of Turbulent Shear Flows Laden with Bubbles, Direct & Large Eddy Simulation 4, Twente, Enschede, Holland, July 18-20, 2001.

15. Azzi A. Lakehal D.: Perspectives in Modelling Film-Cooling of Turbine Blades by Transcending Conventional Two-Equation Turbulence Models, *In Proceddings ASME-IMECE01, CD/Rom, paper no. IMECE2001/HTD-24317*, New York, Nov. 11-16, 2001.

16. Milelli M., Smith B.L., Lakehal D.: Subgrid Scale Modelling in LES of Turbulent Bubbly Flows. *In Proceedings of Turbulent Shear Flows & Phenomena 2*, Stockholm, Vol. II, pp. 181-186, Lindborg/Johansson/Eaton (Eds.), June 27-29, 2001.

17. Milelli M., Smith B.L., Lakehal D.: Some New Approaches to Bubble Plume Modelling using CFD, *In Proceddings ASME-IMECE'01, CD-Rom, paper no. IMECE2001/HTD-24173*, New York, Nov. 11-16, 2001.

18. Narayanan C., Lakehal D., Yadigaroglu G.: Temporal Instabilities of a Particle-Laden Mixing Layer: A Numerical Investigation, *In Proceedings of Int. Conf. Multiphase Flows* (ICMF01), New-Orleans, USA, May 27- June 1, 2001.

19. Lakehal D., Meier M., Davis J., Smith B.L., Yadigaroglu G.: Interface Tracking for the Prediction of Interfacial Dynamics and Heat/mass Transfer in Multiphase Flows, Comp. Heat Transfer 2001, Palms-Cove, Australia, May 21- 25, 2001. *In ICHMT/Beguel House Inc. Publishers, New York, de Vahl Davis & Leonardi (Eds.)*, 2, pp. 1267-1274, 2001.

20. Lakehal D., Theodoridis G., Rodi W.: Computation of Film cooling by Lateral Injection Using a Multi-block Technique, *In Proceedings of Turbulent Shear Flows 11*, Grenoble, France, Sep. 1997.

21. Lakehal D., Rodi W.: Computation of a Flow Around a Surface Mounted Cube in a Channel, 6th ER-COFTAC/IAHR Workshop on Refined Flow Modelling, Delft, K. Hanjalic and S. Obi (Eds.), pp. 152-154, 1997.

22. Lakehal D., Rodi W.: Modelling of the Impinging Flows Over Bluff-bodies Using Statistical Turbulence Models, *In Proceedings of Math.& Num. Models for the Simulation of Turbulent & Reactive Flows*, Ottrot, Mt. St Odile, France, 1996.

23. Lakehal D., Rodi W.: Prediction of a 2D-Wall Jet Using Two-layer Turbulence Models, 5th ERCOFTAC/IAHR Workshop on Refined Flow Modelling, Paris, D. Laurence and G. Pot (Eds.), pp. 24-26, 1996.

24. Lakehal D.: Prévision Numérique d'un Ecoulement Turbulent autour d'une Jonction Cylindre-plaque Plane. *In Actes du 12e Congres Francais de Mécanique*, Strasbourg, 1995.

25. Lakehal D., Solliec C.: Numerical Simulation and Wind-tunnel Measurements of Wind Flow Past Round Shaped Buildings, *In Proceedings of 9th Int. Conf. Wind Eng.*, New-Delhi, India, Jan. 9-13, 1995.

26. Lakehal D., Barré C., Sacré C.: Simulation of Turbulent Flows Around 3D Structures With Complex Geometries, *In Proceedings of Turbulence, Heat & Mass Transfer I*, Lisboa, Portugal, Aug. 13-16, 1994. *In ICHMT/Beguel House Inc. Publishers, New York, Hanjalic & Pereira (Eds.)*, pp. 526-534, 1995.